Modeling, simulation and robust control of an electro-pneumatic actuator for a variable geometry turbocharger

Adeel Mehmood

SPIM

Thèse de Doctorat

école doctorale **sciences pour l'ingénieur et microtechniques**

UNIVERSITÉ DE TECHNOLOGIE BELFORT-MONTBÉLIARD

Modeling, simulation and robust control of an electro-pneumatic actuator for a variable geometry turbocharger

Adeel MEHMOOD

SPIM

Thèse de Doctorat

école doctorale **sciences pour l'ingénieur et microtechniques**

UNIVERSITÉ DE TECHNOLOGIE BELFORT-MONTBÉLIARD

N° 1 8 8

THÈSE présentée par

Adeel MEHMOOD

pour obtenir le

Grade de Docteur de
l'Université de Technologie de Belfort-Montbéliard

Spécialité : **Automatique**

Modeling, simulation and robust control of an electro-pneumatic actuator for a variable geometry turbocharger

Soutenue le 22 Novembre 2012 devant le Jury :

Xavier BRUN	Rapporteur	Professeur à l'Université de Lyon 1 INSA-Lyon
Houcine CHAFOUK	Rapporteur	Professeur à ESIGELEC de Rouen
Abdellah EL MOUDNI	Examinateur	Professeur à l'Université de Technologie de Belfort-Montbéliard
Michel BASSET	Examinateur	Professeur à l'Université de Haute Alsace
Mohammed EL BAGROURI	Directeur de thèse	Professeur à l'Université de Technologie de Belfort-Montbéliard
Salah LAGHROUCHE	Co-Directeur	Maitre de Conferences à l'Université de Technologie de Belfort-Montbéliard

Contents

Acknowledgements

This work has been performed at the System and Transports (SeT) laboratory, under the supervision of Prof. M. El Bagdouri and Dr. S. Laghrouche. This work would not have been possible without their motivation, enthusiasm and immense knowledge. First, I would like to thank both of my supervisors for all the support and encouragement they have provided during this work. I would also like to thank them for providing me an opportunity to work with project partners of SIMBA (SIMulation de la Boucle d'Air) from industry.

I would like to thank the jury members: Prof. X. Brun and Prof. H. Chafouk for reviewing my thesis and giving me very useful remarks on the report. I am also very thankful to Prof. A. El Moudni and Prof. M. Basset for their participation as examiners in the jury.

This project was realized with collaboration of Faurecia Emissions Control Technologies, Honeywell Turbo Technologies and Mark IV. I am also grateful to Mr. D. Ragot from Faurecia, Mr. D. Guyon from Mark IV and Mr. J. S. Roux from Honeywell for their guidance and technical support which helped me to solve technical issues related to my thesis.

My colleagues certainly deserve a mention since they have significantly contributed not only to my work but also to my social life. Special thanks to Mr. F. S. Ahmed for his help for conducting experiments on the test bench, Mr. M. Harmouche for helping me to sort out bugs in control theory, Mr. I. Matraji, A. El Amroui and K. Dar for their moral support and organizing the outdoor activities which made my stay very memorable in Belfort.

Last but not the least, I would like to say special thanks to my parents and other family members for their continues support and love throughout my life. They were always

there to celebrate my success and to overcome the fear of failures in my life. Their unconditional support helped me to accomplish this objective with courage and enthusiasm.

Nomenclature

F	force	N	Angular speed
V	volume	I	Moment of inertia
R	gas constant for air	A	area
R_n	universal gas constant	U/C	Blade speed ratio
C_p	Specific heat at constant pressure	ρ	Density
C_v	Specific heat at constant volume	P	Power
γ	specific heat ratio ($\gamma = \frac{C_p}{C_v}$)		
T	temperature	η	Efficiency
C_r	vanes angle	m	mass
λ_0	Air to fuel ratio		
ψ	Dimensionless head parameter		
b	damping coefficient		
k	spring constant		
$\dot{m}$	mass flow rate		
v_s	stribeck velocity		
p	pressure		
e	error signal		
$\dot{e}$	derivative of error signal		
λ	polynomial parameter		
τ	Torque		
M	Mach number		
$\dot{m}_{cr}$	Corrected mass flow rate		

α	fluid inlet and outlet angle	h^0	total enthalpy
β	blade inlet and outlet angle	k	blade clearance
β_{metal}	camber line angle	m	arc length
$\delta\beta$	stagger angle	M	Mach number
δi	incidence	o	length of blade opening
ρ	fluid density	p	pressure
ζ	pressure loses	p^0	total pressure
ζ_p	pressure loses due to profile	Q	source terms
ζ_t	pressure loses due to play	Q_{ext}	external forces
ζ_s	pressure loses due to secondary effects	r	radius
$\overrightarrow{\overrightarrow{\sigma}}$	tenser of constraints	R	perfect gas constant
$\overrightarrow{\overrightarrow{\tau_f}}$	tenser of viscous constraints	R_e	Reynolds number
a	velocity of sound	R_{eref}	reference Reynolds number
A_n	channel cross section	S	cross sectional area.
A_s	channel cross section at start	s	distance between vanes
A_o	channel cross section at exit	Δs	variation in entropy
c	vane comber length	t	static temperature
C_L	lift coefficient	t^0	total temperature
C_D	drag coefficient	Δt	time interval
C_p	specific heat at constant pressure	$\overrightarrow{u}$	normal to $\overrightarrow{m}$
e	energy	$\overrightarrow{V}$	velocity vector
ep	maximum thicknesses of the blade	V_m	meridional velocity
e^0	total energy	V_u	tangential velocity
E_c	kinetic energy	$\overrightarrow{W}$	velocity vector in reference frame
$\overrightarrow{F}$	external force on the fluid	v	volume
h	enthalpy		

SUBSCRIPTS AND ABBREVIATIONS

$aero$	aerodynamic	EPC	Electro-pneumatic
e	Engine		Pressure Converter
ref	reference	VGT	Variable Geometry
tc	Turbocharger		Turbocharger
r	ratio	VNT	Variable Nozzle Turbine
p	plunger	PWM	Pulse Width Modulation
act	actuator	AFR	Air to Fuel Ratio
atm	atmospheric	SI	Spark Ignition
$atm-act$	atmosphere to	MAP	Manifold Absolute
	actuator		Pressure
res	reservoir	CI	Compression Ignition
$act-res$	actuator to	MAF	Mass Air
	atmosphere		Flow
d	diaphragm	EGR	Exhaust Gas Recirculation
0	initial condition	TDC	Top Dead Center
mag	magnetic	BDC	Bottom Dead Center
$s1$	plunger spring	ECU	Electronic Control Unit
f	friction	FPGA	Field-Programmable Gate Array
mem	membrane	PID	Proportional, Integral
trb	Turbine		and derivative
ft	total friction	SISO	Single Input Single Output
s	static friction	MIMO	Multiple Input Multiple Output
c	coulomb friction	SMC	Sliding Mode Control
sm	diaphragm spring		
cr	corrected value		
im	Intake manifold		

Introduction

Personal automobiles are an indispensable means of transportation in our every-day life. However, they cause environmental pollution and are associated with safety risks. Hence, besides fuel consumption, driving performance and safety, the optimization of automobile engines with respect to emissions is of paramount importance as well. According to the latest reports of the Health Journal, road vehicles are responsible for about 73% of the total emission of pollutants in the world [41]. Throughout the history of automobiles, governments have continued to place stringent regulations on engine emissions. Such current and future standards for the light duty diesel engine, as defined in the European Union, are shown in Fig. 0.1. The amount of toxic gases which can be produced in grams per kilometers by a light diesel vehicle are shown in the form of euro emission standards.

The major pollutants in vehicular exhaust are carbon monoxide, nitrogen and sulphur oxides, unburned hydrocarbons (from fuel and crankcase oil), particulate matter, polycyclic aromatic hydrocarbons, and other organic compounds that derive from combustion [28]. Although, carbon dioxide is the major source of air pollution which causes the imbalance in the greenhouse effects, but it is not as harmful as many other particles and gases emitted from the engine burning process. The emission levels, which are already tightly regulated by legislature in key markets, will become even more stringent as time progresses. This is a big challenge for automotive companies, especially in the diesel engine sector, which suffers from heavy particulate matter and NO_x emissions by virtue of its design. The main factors to obtain the required emission levels are the fuel economy and reduction in the emission of the toxic exhaust gases, which are increasing day by day due to the ever increasing demand for new vehicles. The automotive industry has found solutions in the diesel engine air path to improve engine performance and to reduce NO_x emissions. Turbocharging increases the engine intake air mass using a turbo-compressor run by the engine's exhaust gas. Excess air in the engine cylinder ensures lean fuel burn and improves the engine's power to weight

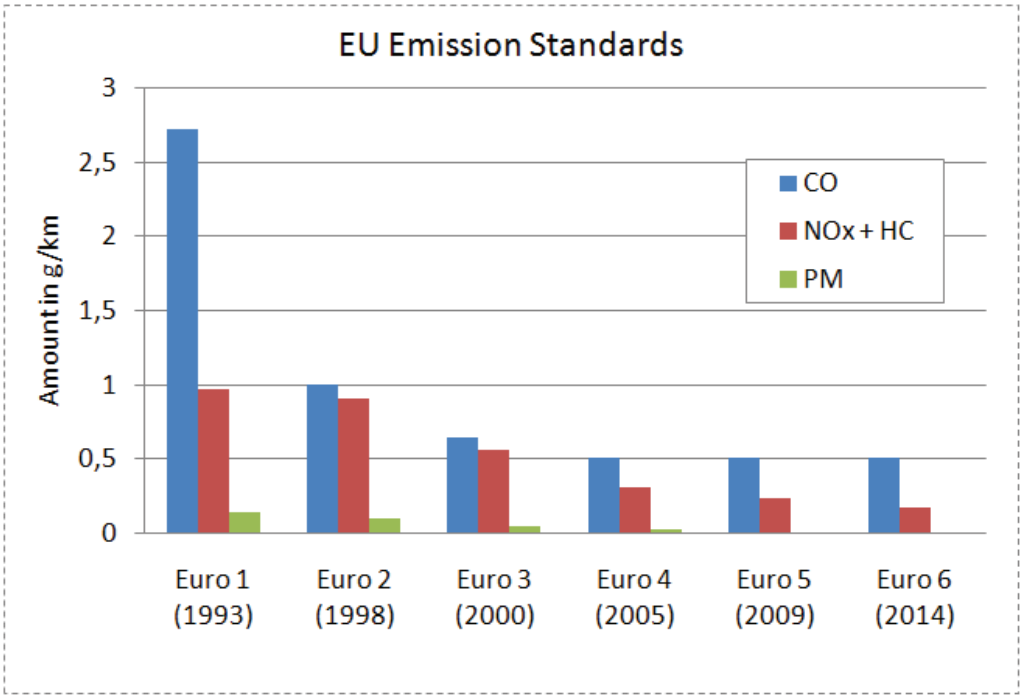

FIGURE 0.1. *European standard cycles to control the air pollution*

ratio. Exhaust Gas Recirculation (EGR) reintroduces the exhaust gas into the air intake manifold. The presence of exhaust gas in the cylinder cools the combustion process down, reducing NO_x production. It also allows some unburnt hydrocarbons in the exhaust air to be re-burnt.

The modern diesel engine air path improves the engine's performance as well as reduces pollution. However the existence of complex interdependent sub-systems results in precise and accurate control requirements. For example, the use of EGR means there is less air to run the turbocharger. This results in less fresh air for combustion, hindering the engine operation. To attain better performance of the engine, electronic engine control units (ECUs) and mechatronic actuators are playing an important role in the modern vehicles [89]. Therefore, the need of studying each sub-system in detail, as well as the impact of their performance on the entire air path and the engine, can no longer be ignored.

It is in this spirit, that partners from the automobile industry and academics joined hands under the banner of project SIMBA (SIMulation de la Boucle d'Air). This project was launched by the Pôle Véhicule du Futur Alsace Franche-Comté, which organizes particular competencies and solutions for future vehicles and their mobility. The objective of the project SIMBA, is to better understand the phenomena of air flow around

a diesel engine, by studying the influence of each air path sub-system on other systems and on the global air path performance. In this regard, the laboratory SeT of the UTBM focused on influence of the actuator dynamics and nonlinearities in the engine air path. We need the accurate control strategies to meet performance requirements, which in turn depend on actuators. In this thesis, we have studied the electropneumatic actuator used for Variable Geometry Turbocharge (VGT) control. Our focus in this thesis is the nonlinear effects in these actuators and their compensation using control techniques for improved control of the engine air path.

MOTIVATION

As described earlier, the efforts to enhance engine performance have led the way to exhaust gas after-treatment to improve combustion efficiency and to reduce NO_x emission [61]. Most after-treatment methods contain exhaust gas recirculation, variable geometry turbo-charging and reduction of toxic exhaust emissions through catalytic converter. The exhaust gas after-treatment is the special focus of current research. Electro-pneumatic actuators continue to generate significant research interest due to their advantages over common electric actuators. Their high power to weight ratio, high speed, excellent compliance, high force capabilities, low cost and simple operational mechanism make them more useful for the automotive industry (See for example [24], and [93]), and many other industrial applications such as robotics [8] and automation [74]. In the automotive industry, such actuators are commonly found in the engine air path for exhaust gas recirculation [52], [40], the position control of the VGT [59] and air brake systems [84]. Therefore, our focus is on the control of a VGT powered by an electro-pneumatic actuator. However, the existence of nonlinearities such as air compressibility, pre-compression and friction, limit their role in precise control applications. Additionally, the hysteresis phenomenon, caused by friction force, increases with the influence of the nonlinear aerodynamic forces on the VGT actuator.

The nonlinearities in pneumatic actuators, degrade the actuator performance by causing the backlash and hysteresis phenomenon. Therefore, fixed gain linear controllers cannot satisfy tracking requirement in these actuators, in presence of undesirable characteristics [12]. To remedy this we require a precise model for nonlinear robust control techniques to compensate for these phenomena. Different nonlinear robust control approaches for the control of a double acting pneumatic actuator have been discussed in the literature (see for example [10], [79], [43] and [80]).

In this study, we address the problem of VGT actuator modeling for detailed air path study as well as for control. These modeling problems are distinct, as the behavioral study of the air path requires precise dynamic modeling of the actuator, in order to quantify its influence on the overall system. On the other hand, control purposes require simplified models which do not possess heavy computational constraints and can be implemented on embedded systems. We first develop a detailed dynamic model of the actuator, which takes into account the nonlinear phenomena associated with the actuator as well as the effect of aerodynamic forces exerted by the exhaust gas passing through the VGT turbine. Then we propose simplification methods to make this academic model suitable for control purposes, and present different control methods designed on the simplified model.

ORGANIZATION OF THE THESIS

The thesis is organized as follow

Chapter 1: State of the art

Chapter 1 begins by describing the formation of NO_x and PM during the diesel combustion process, after this an overview of diesel emission reduction and the state of the art in engine emission control is presented. Exhaust gas recirculation and turbocharging are not only a well established mean to reduce NO_x emissions, but they also play a key role to fulfil the boost pressure requirement in the engine. The subsequent work on the air path is ultimately aimed at improving the boost pressure requirement through the precise control of the VGT actuators.

Chapter 2 : VGT Actuator System modeling

In chapter 2 the modeling of the electro-pneumatic actuator used for the control of the variable geometry of the turbocharger is presented. The pressure inside the actuator chamber is regulated with an electro-pneumatic pressure converter (EPC). The pressure dynamics inside the actuator chamber are modeled by taking into account the variation of mass, temperature and volume. To obtain these dynamics, orifice flow equations are used along with identified flow area through the pressure regulator. Moreover, the attenuation and delay in the air mass flow due to pneumatic lines are also considered with the help of wave propagation and Navier-Stokes equations. At the end, the complete actuator's model is validated with experiments.

Chapter 3 : Modeling with Nonlinearities

In chapter 3 the modeling of the electro-pneumatic actuator used in the VGT system is rectified with the special focus on the nonlinear phenomena, such as the friction and aerodynamic forces. The friction phenomenon possess hysteresis which is modeled with the help of LuGre model. Furthermore, the hysteresis effect changes with the impact of external aero-dynamic forces. The aerodynamic force, being an important nonlinear effect on the actuator, is studied with three different approaches. In the first approach, Navier-Stockes equations for compressible fluid are used to obtain this force. Two other approaches, which are based on actuator characteristics and force sensor, are also discussed in this chapter to describe these nonlinear forces. Ultimately, an adaptive LuGre model is developed and compared with the experimental results obtained from the DV6TED4 type diesel engine.

Chapter 4 : Sensitivity analysis of parameters

In chapter 4 we have studied the sensitivity factor of the actuator parameters. The sensitivity analysis assists in the study of the variation in the output of a model. In this chapter, input parameter variation method and variance based analysis are performed to see their influence on the output. Secondly, a production tolerance analysis is performed on the actuators having same characteristics. The results are obtained with collaboration of Honeywell Turbo Technologies (HTT). At times it is impossible to find accurate model of an actuator due to uncertainties and sometimes we need generalized tolerance models for the actuators of similar types. This analysis will help us to provide an evaluation of the confidence in the model.

Chapter 5 : Robust Control Design

In Chapter 5, a complete physical model of an electro-pneumatic actuator with an adaptive LuGre model described in chapter 3, has been simplified to obtain two empirical models for control. One of the simplified models is used to design robust backstepping and sliding mode controllers. We have shown different techniques to compensate the nonlinear effects to guarantee an accurate position tracking of the VGT actuator by taking into account its nonlinear behavior in the engine. We have developed nonlinear observer for friction compensation which depends on the adaptive LuGre friction model. Furthermore, to reduce the controller cost, a sliding mode pressure observer is also designed in this chapter.

Chapter 6 : Conclusions

The conclusions and contributions of the presented work are discussed and potential areas for further research are highlighted.

Chapter 1 State of the art

1.1 Introduction

The diesel engine, named after its inventer Rudolf Diesel (March 18, 1858 − September 29, 1913), is an internal combustion engine in which ignition of injected fuel is initiated by the heat generated during compression of the working fluid (air). Torque is generated by varying the quantity of injected fuel, thereby varying the air-fuel ratio. This principle contrasts with Spark-Ignition (SI) engines, in which an electric spark ignites a premixed air-fuel mixture of a fixed ratio, which acts as the working fluid. Diesel engines or Compression-Ignited (CI) engines generate ignition temperature by compressing air at much high compression ratios as compared to SI engines. The high temperature and pressure present in the cylinder result in improved fuel efficiency, higher than any other internal or external combustion engine [32].

Compression ratio in SI engines is limited by the self-ignition temperature of the air-fuel mixture. In CI engines, the high compression ratio is achieved by separately introducing air and fuel into the cylinder. Air is compressed in the cylinder and fuel is injected at the exact moment at which ignition is required. Since diesel fuel does not evaporate at ambient temperatures, modern injection systems use pressurized rails and fine nozzle injectors to inject the fuel as a very fine spray. As the temperature and pressure at the time of injection are at the fuel's self-ignition level, the droplets in the outer part of the spray burn immediately, however the inner part takes time to mix with the surrounding air [30]. This requires the engine to run in 'lean conditions', i.e. with air-fuel ratios much higher than the stoichiometric ratio. This excess air not only guarantees that the fuel burns completely, but provides other desirable advantages as well. The need of large amounts of excess air means that the engine can run un-throttled, and the intake manifold pressure can even be boosted to achieve very high air mass-flow rates. This in turn means that more fuel can be burned as compared to SI engines, inside a cylinder of

the same volume, giving higher power to weight ratio. However, excess air and locally high temperatures increase the amount of produced NO_x [30, 14]. Unfortunately, the pollution control methods which have proved very successful with the fixed air-fuel ratio combustion of SI engines (e.g. Three-Way Catalyzers), do not work efficiently in the case of diesel engines [30].

In this chapter, we will discuss how the issues of pressure boosting and NO_x reduction are addressed in modern diesel systems. The mechanisms employed in the air path to achieve these objectives will be discussed briefly, to develop a basis of understanding the importance of the rest of the work presented in the thesis.

1.2 DIESEL ENGINE AIR PATH

Fig. 1.1 shows the equivalent graphical representation of a modern diesel engine, with exhaust and admission paths and all the actuators required for the operation of the air path. The diesel engine air path is designed to attain the two objectives mentioned before, i.e. pressure boosting for fuel-efficient combustion and NO_x emission control to keep pollution levels under government regulations. The air path structure presented in Fig. 1.1 is being used in most renowned vehicle brands e.g. Citroen, Ford, Mazda, Mini, Peugeot, Volvo etc. There are two key systems employed in this air path, namely 'Turbocharging' for boost pressure and 'Exhaust Gas Recirculation (EGR)' for NO_x reduction [14].

The elements of the air path, as illustrated in Fig. 1.1 are described in detail in the following sections. The main systems and their working are presented first. Then, the auxiliary systems and actuators are discussed.

1.2.1 PRESSURE BOOSTING

The maximum power that an engine can deliver is limited by the amount of fuel that can be burned efficiently inside the engine cylinder. The latter depends upon the amount of air present in the cylinder. The power output can be increased by increasing the air charge density in the engine by some means, i.e. forcing more air into the cylinder so that more fuel can be burnt in the same volume at high Air to Fuel ratio (AFR) [33]. This can also be interpreted as reduction in Brake Specific Fuel Consumption (BSFC). There are two basic methods used to accomplish this objective, known as supercharging and turbocharging [32].

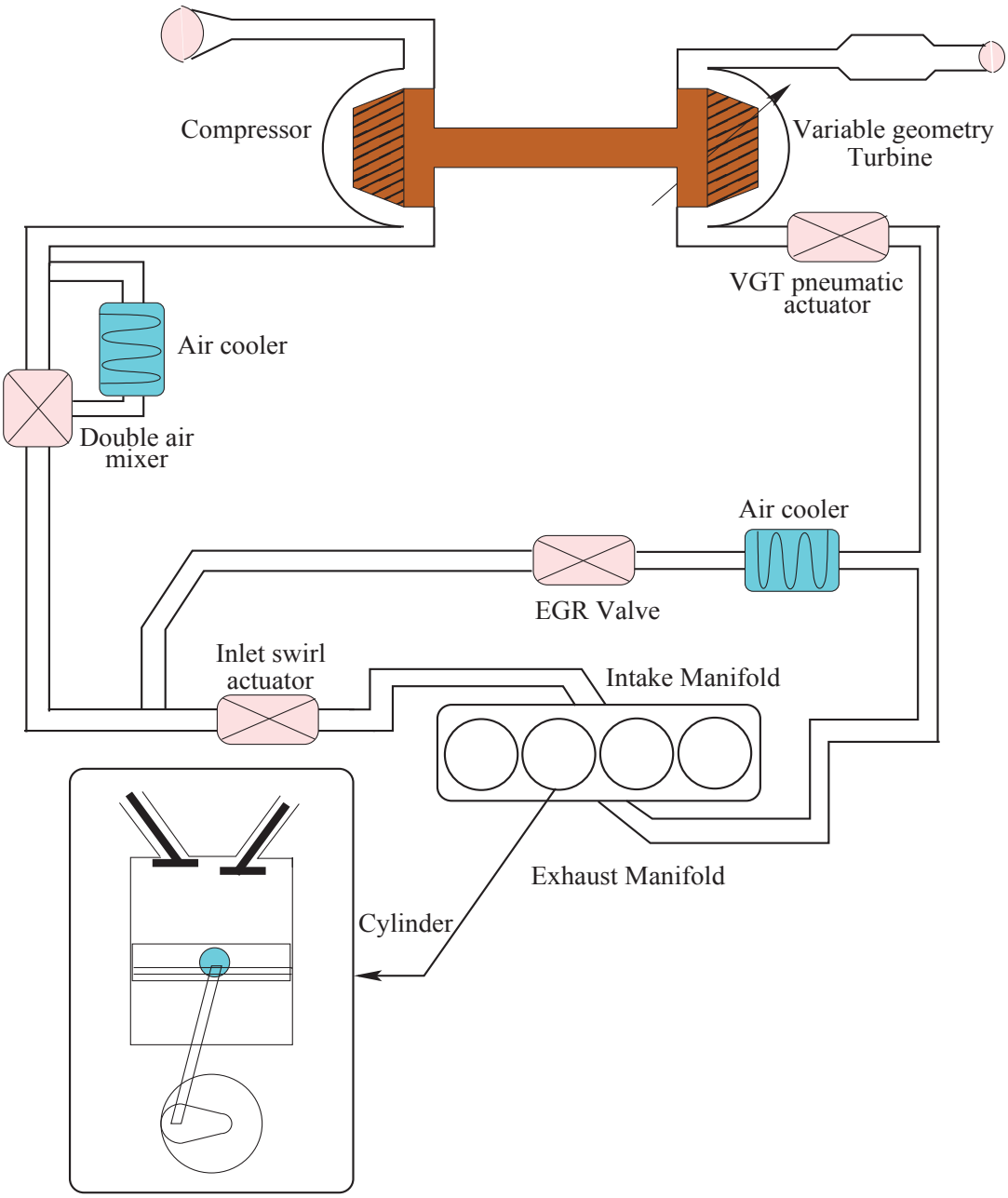

FIGURE 1.1. *Engine diagram with all the actuators for the air path modeling of the diesel engine*

1.2.1.1 SUPERCHARGING

Mechanically driven superchargers are air compressors, connected directly to the engine crankshaft. They are generally positive displacement compressors running at speeds about the same as engine speed. The major advantage of a supercharger is very quick response to throttle changes. Being mechanically linked to the crankshaft, any engine speed change is immediately transferred to the compressor [72]. However, the power to drive the compressor is a parasitic load on the engine output and because of more

mechanical linkages more space is required to instal these superchargers. Other disadvantages include higher cost, greater weight, chances of mechanical failure and greater noise. However, the drawbacks of supercharging can be overcome by new state-of-the-art techniques, such as exhaust gas turbocharging.

1.2.1.2 TURBOCHARGING

Exhaust gas turbochargers consist of a compressor and a turbine, joined by a shaft. The turbine is installed in the exhaust path and runs on the energy that would otherwise be wasted in the exhaust gas. The turbine, in turn, powers the compressor in the admission path, providing the pressure boost. The advantage of this technique is that no extra load is put on the engine, and the wasted energy is reused to improve the engine's performance. In addition to better power output, the reduce energy waste results in better overall efficiency as well. The main advantages of turbocharging as compared to naturally aspirated and supercharged engines are as follows [72, 62, 30]:

- Due to the lower volumetric displacement required in a turbocharged engine, the power-to-weight ratio of the engine is higher than naturally aspirated engines and frictional and thermal losses are less.
- Compared with a naturally aspirated or supercharged engine of identical power output, the fuel consumption of a turbo engine is lower, as some of the normally wasted exhaust energy contributes to the engine′s efficiency.
- The turbo engine′s installation space requirement is smaller than that of a naturally aspirated engine with the same power output.
- The high-altitude performance of a turbocharged engine is significantly better. Because of the lower air pressure at high altitudes, the power loss of a naturally aspirated engine is considerable. In contrast, turbine′s performance improve at altitude as a result of the greater pressure difference between the virtually constant pressure upstream of the turbine and the low ambient pressure at outlet. The lower air density at the compressor inlet is largely equalized. Hence, the engine has barely any power loss.

In the past, turbochargers were avoided as the additional feedback path introduced by the exhaust-admission linkage complicated the dynamic behavior of the entire engine system [30]. With advances in embedded electronics and control theory, this is no longer a problem and turbochargers are now a common feature in diesel engine automobiles [14].

1.2.2 EXHAUST GAS RECIRCULATION (EGR)

Diesel engines are inherently more fuel-efficient than gasoline engines due to high compression and lean burning, but they cannot use the pollutant abatement systems that have proved to be very successful in gasoline engines [30]. In fact, the torque output of diesel engines is controlled by changing the air-fuel ratio in the combustion chamber, which can be as high as ten times the stoichiometric ratio. However, the fuel mixture is heterogeneous because combustion occurs as the fuel is injected; there is no time for the fuel to mix evenly in the air. The prevailing flame temperature therefore, is high at localized points in the cylinder. Hence, on a power generation basis, the decrease in overall mixture strength does not reduce the specific rate of NO_x generation [100]. EGR was proposed to alter combustion in spark ignition engines for knock suppression [35]. Kopa et al. first demonstrated that reintroducing exhaust gas into the cylinder could lower flame temperature and reduce the concentration of NO_x in the exhaust gas [39]. Recently, EGR has emerged as a necessary means to meet the United States Environmental Protection Agency (EPA) NO_x regulations [35].

There are two methods of returning exhaust gas back into the cylinder; internal and external. Internal EGR uses variable valve timings to retain a fraction of exhaust from the previous engine cycle. External EGR uses piping to route the exhaust gas to the intake system, where it is inducted into the cylinder. While internal EGR provides very short response time, its practical application is not possible without camless technology [35]. Furthermore, exhaust gas needs to be cooled before it can be reintroduced into the cylinder, which is not possible with internal EGR. Cooling the residual improves fuel economy and engine performance and enables further reduction of NOx [30]. Therefore, external EGR is the preferred method in the automobile industry today.

1.3 AIR PATH ACTUATORS

In the previous section, we discussed the important tasks performed by the air path. We will now consider the components of the air path through which these tasks are achieved.

1.3.1 TURBOCHARGERS

The principle, characteristics and advantages of turbochargers have been discussed in the previous section. Unfortunately, small turbochargers are inefficient at loads and the high backpressure increases the pumping work of the engine. There exist two types of turbochargers which address this problem.

Waste-gate Turbocharger

A waste-gate is a valve that diverts exhaust gases away from the turbine wheel in a tur-

bocharged engine system. Diversion of exhaust gases regulates the turbine speed, which in turn regulates the rotating speed of the compressor. The primary function of the waste-gate is to regulate the maximum boost pressure in turbocharger system and to limit the turbine speed to protect the turbocharger. One advantage of installing a remote mount waste-gate to a free-float (or non-WG) turbo includes allowance for a smaller A/R turbine housing, resulting in less lag time before the turbo begins to spool and create boost. However, a substantial fraction of the exhaust gas has to bypass the turbine through a waste gate and at a certain point, not enough enthalpy can be extracted from the exhaust gas, leading to a lack in boost pressure and thus constraining the entire engine system.

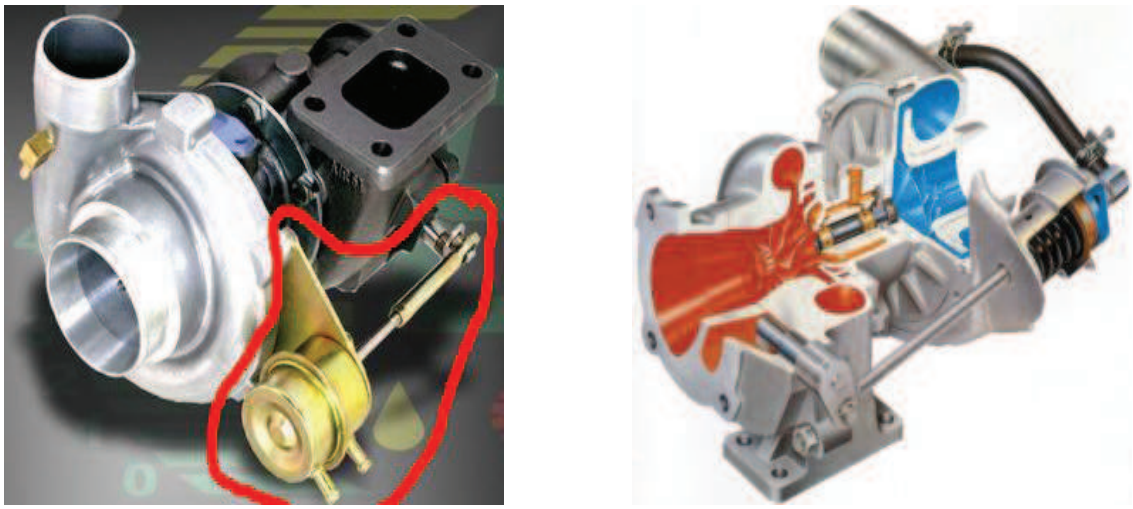

FIGURE 1.2. *A turbocharger with a waste-gate actuator that bypass the exhaust gases*

Variable Geometry Turbocharger

The variable geometry of the turbine allows the turbine flow cross-section to be varied in accordance with the engine operating point. It has moveable vanes located around the exhaust turbine. When the vanes are closed, the exhaust gases speed up (since they are passing through a smaller orifice) and the turbine spins faster. When they open, the gases slows down but there is a larger amount of gasses to spin through turbine and give it more pumping power. This allows the entire exhaust gas energy to be utilized and the turbine flow cross-section to be set optimally for each operating point. As a result, the efficiency of the turbocharger and the engine is higher than that achieved with the waste-gate. Both intake and exhaust pressures are dependent upon VGT, the intake being regulated by the compressor and the exhaust by VGT vanes. In Fig. 1.3 a mechanical assembly of a turbocharger is shown along with the moving mechanism. In Fig. 1.5 the VGT vanes are shown in their closed position. A variable geometry turbocharger with its vanes in open position are shown in Fig 1.4.

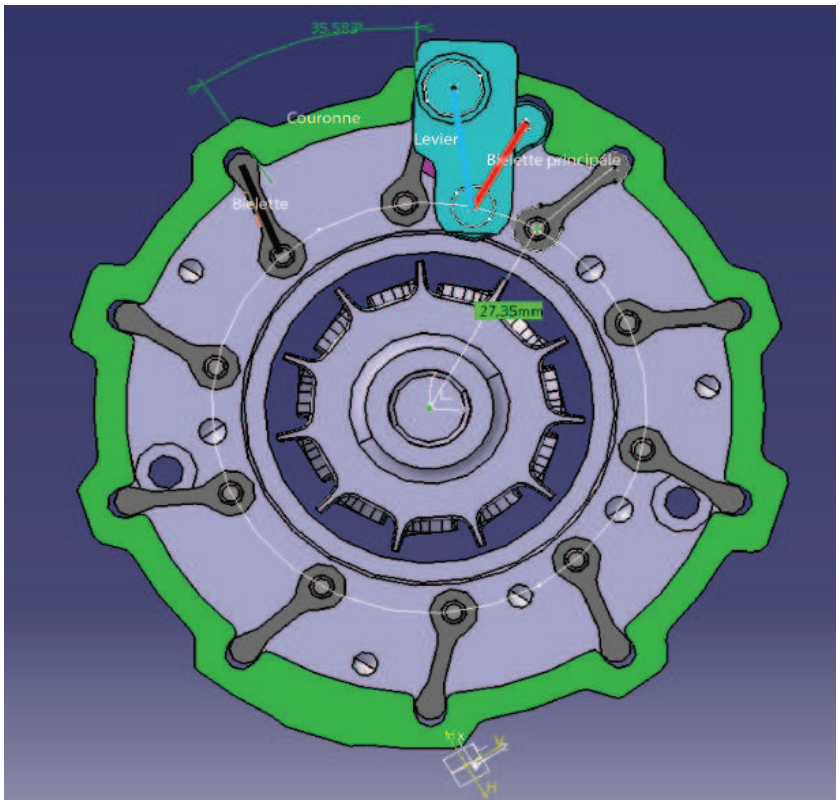

FIGURE 1.3. *Mechanical diagram of a variable geometry turbocharger*

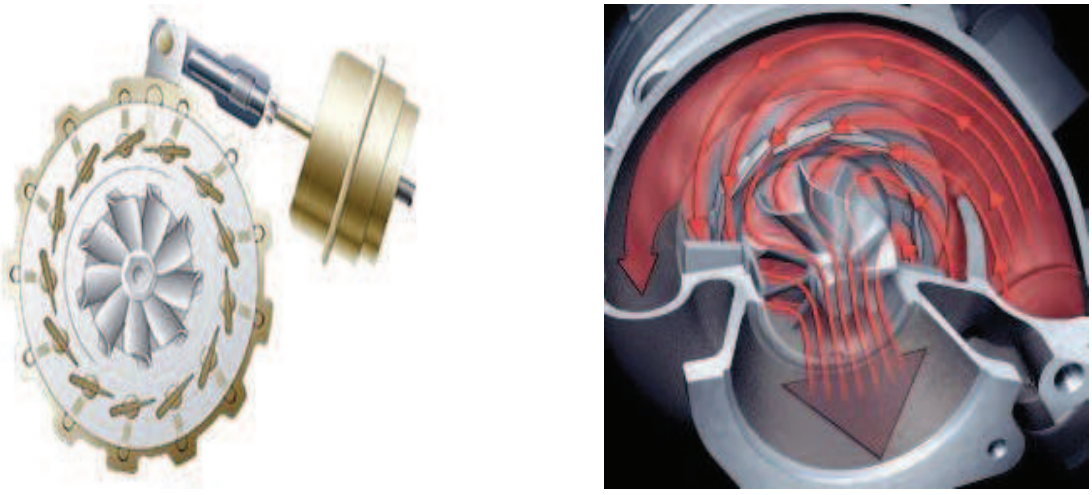

FIGURE 1.4. *A variable geometry turbocharger with the actuator at its initial position*

1.3.2 VGT ACTUATOR

A geometry of a VGT is usually controlled by a linear actuator. The actuator is connected to the vanes through a rack and pinion crankshaft and a unison ring which moves all the vanes together. Hence, with the actuator′s movements all the vanes moves together to change the angle of attack of the exhaust air [49] and the area of flow to the radial or

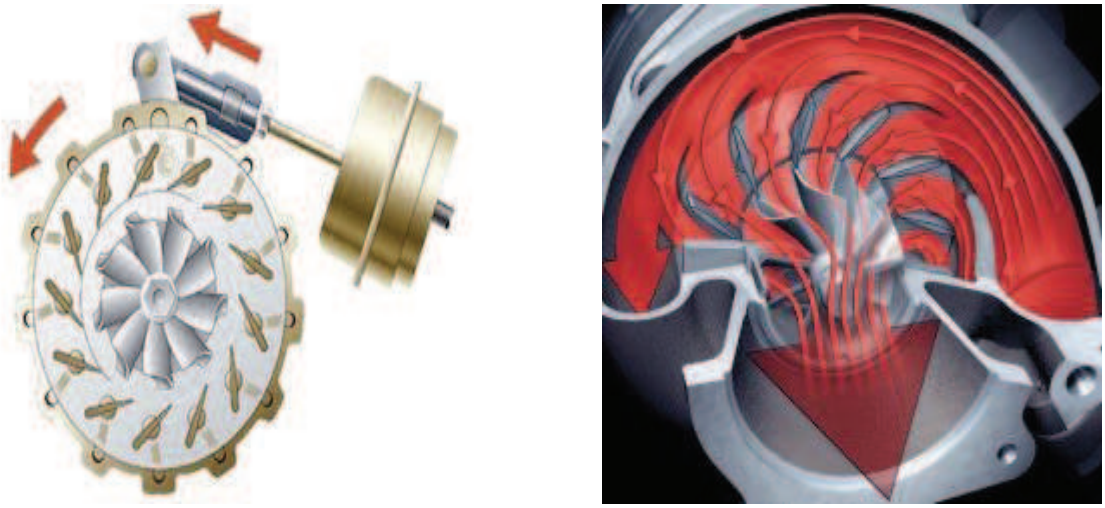

FIGURE 1.5. *A variable geometry turbocharger with the actuators when all the vanes are close*

mixed flow impeller of the turbine. As mentioned in the introduction, this actuator is the subject of the thesis.

In the automotive industry, electro-pneumatic actuators are widely used for the control of VGT. The electro-pneumatic actuator used in the air path is a unit that contains a pneumatic actuator and an electromechanical distributor. In this study, the distributer is of solenoid type, also known as Electro-pneumatic Pressure Converter (EPC). The pneumatic actuator is a single-action diaphragm actuator which is connected to the vanes of the VGT through a linear linkage. The pneumatic actuator chamber is separated into two parts via an elastic membrane. The EPC reduces the pressure in one of the actuator chambers to vacuum, which generates a force on diaphragm due to pressure difference. A spring action is used to bring the diaphragm back to its position. A detailed explanation of this actuator is presented in the subsequent sections. In Fig. 1.6 a complete VGT pneumatic actuator along with a turbocharger and its structural diagram are shown to understand VGT actuator working principle.

1.3.3 EGR ACTUATOR

While the EGR process appears complex, it is controlled simply by a valve present in the routing between exhaust and intake. The actuator typically consists of a linear (globe) valve with a torque or PMDC motor and a cam or screw drive to convert rotary motion to linear motion. The EGR actuator used in the DV6 type engine is a torque motor shown in Fig. 1.7. The advantage of torque motors over others is that they can provide high load torque, which is required to sustain the heavy forces acting on the EGR valve due to high

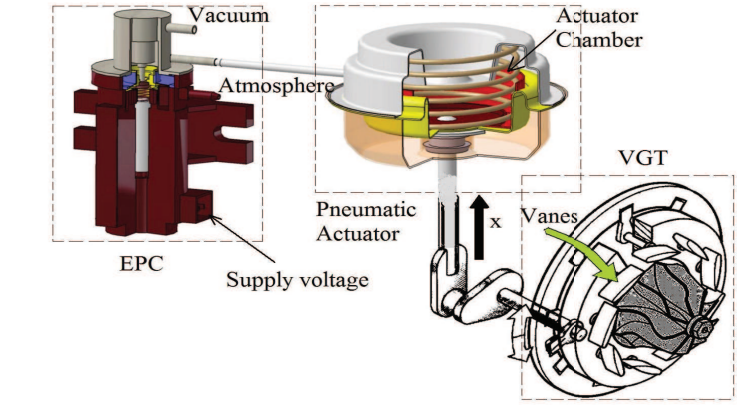

FIGURE 1.6. *A variable geometry turbocharger with an electro-pneumatic actuator system*

exhaust air pressure.

1.3.4 DOUBLE AIR MIXER

As it has been mentioned before that the intake air coming from the compressor is hot and needs to be cooled down before entering the manifold. The temperature is often controlled using Double Air Mixers (Fig. 1.8). The objective of this actuator is to maintain the temperature of the fresh air entering the intake manifold. It combines the hot and cool fresh air to maintain the air temperature. It can also bypass the charge air cooler, if no cooling is required. This actuator consists of two separate motorized butterfly valves.

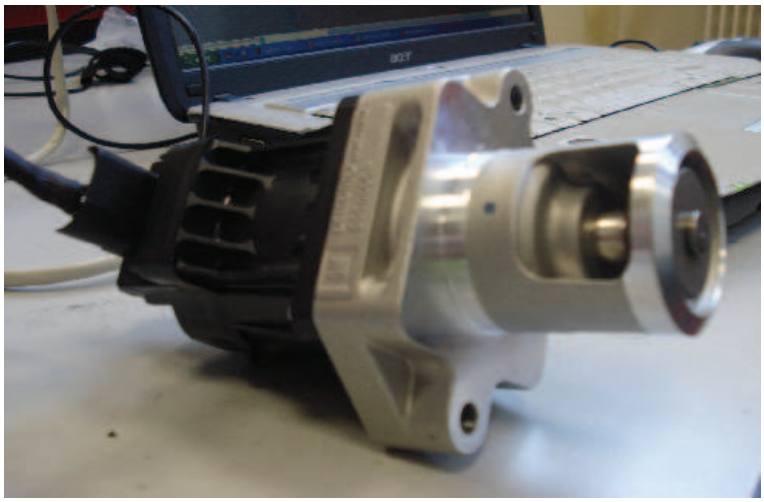

FIGURE 1.7. *EGR actuator used in the diesel engine air path for exhaust gas recirculation*

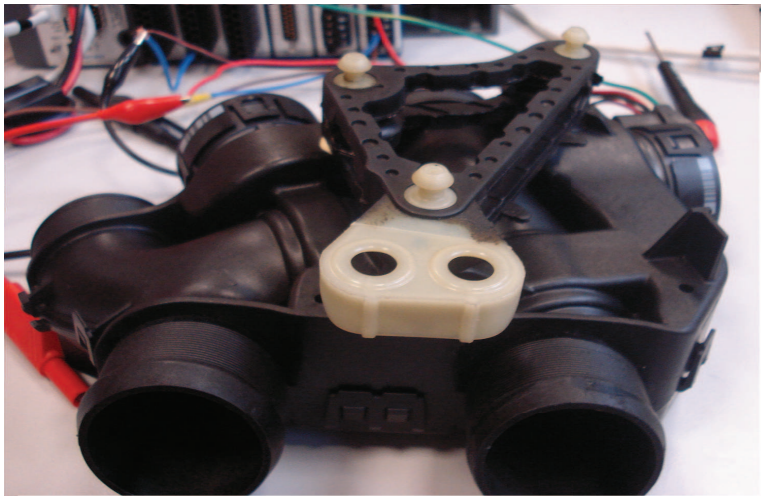

FIGURE 1.8. *Double air mixer used to mix the air coming from the compressor*

1.3.5 INLET SWIRL ACTUATORS

Adding turbulence to the air entering the cylinder results in better fuel mixing at injection time. In modern diesel engines, a swirl actuator is integrated in the air inlet manifold (Fig. 1.9). The manifold consists of two air ducts for each cylinder, which are one letting the air directly into the cylinder and the other allowing swirled air into the cylinder, the amount of which is controlled by the actuator [1]. Air is swirled or perturbed by the geometry of the inlet path leading to the second duct.

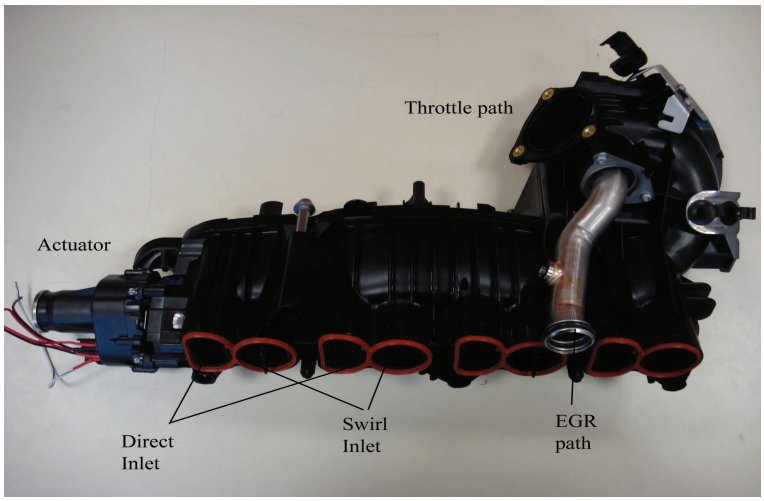

FIGURE 1.9. *Inlet swirl actuator for the use of swirling the air which is entering the cylinder*

1.4 CONCLUSION

In this chapter we have presented a concise study of the diesel engine air path, its principle tasks and its components. It is clear that VGT and EGR have now become an essential part of a CI engine. One interesting feature of the set-up in Fig. 1.1 is that both the EGR and VGT are driven by the exhaust gas and are therefore strongly coupled [20]. Both the EGR and VGT introduce feedback paths around the cylinders which open up several system issues that need to be addressed. Most importantly, the high efficiency of modern turbochargers establishes conditions where the intake manifold pressure is higher than the exhaust manifold pressure, rendering EGR impossible. As the VGT regulates both intake and exhaust pressures, precise VGT control is necessary for achieving pressure boost and EGR. At the same time the performance of VGT depends upon the engine performance, therefore a complex control problem arises in which all engine and air path processes appear interdependent. In this thesis, we focus on one aspect of this problem, i.e. VGT control. Specifically, we will concentrate on precise modeling of the VGT actuator, taking into account its nonlinearities and the aerodynamic effects of exhaust gas on the VGT vanes, which have repercussions on the actuator. Then we will propose robust control techniques that guarantee the performance of the VGT actuator under varying conditions, such as variations in exhaust pressure and load demand. In chapter 2 the complete modeling of the pneumatic actuator will be presented with the proportional solenoid pressure control valve.

Chapter 2 VGT Actuator System modeling

2.1 Introduction

The subject of this thesis concerns physical modeling of electro-pneumatic actuation systems for VGT control. The main objective of this work is to provide a detailed mathematical model of a commercial VGT electro-pneumatic actuator which

- accurately represents the behavior of a real actuator, including the nonlinear characteristics due to friction and varying aerodynamic force on the VGT vanes and
- can be simplified in terms of computability, to be suitable for control purposes.

A detailed nonlinear model which accurately describes different behavior at different operating points is required during engine design, for simulating the effects of actuator dynamics on the overall engine and air path performance. This helps engineers to identify possible shortcomings and problems during the design phase. On the other hand, the extensive computation required to calculate the output of these models limits their applicability for control design and implementation. Therefore detailed models require simplification, such as state reduction, to be suitable for use in controllers. This chapter deals with the base of the first part of the problem. In this chapter, we introduce the VGT actuator under consideration and the mathematical description of the physical phenomena which govern its working. The scope of this chapter is limited to a base model, which describes the different dynamics of the actuation system. This model will be completed in the next chapter, with the integration of nonlinear phenomena.

2.2 System description and modeling

As mentioned in the previous chapter, electro-pneumatic VGT actuation systems generally comprise of two sub-systems, a linear pneumatic actuator and an electro-magnetic

system which regulates the pressure inside the pneumatic actuator, to control its position. The focus of this study is a commercial actuator, used with the VGT of the DV6TED4 engine. The block diagram of this pneumatic actuator system is shown in Fig. 2.1. The pneumatic actuator is a single acting actuator which is connected to a pressure regulator or Electropneumatic Pressure Converter (EPC) through a pneumatic line, and to the unison ring of the VGT via a mechanical linkage. It consists of a diaphragm which is connected to the VGT′s vanes through this linkage. The diaphragm along with a membrane splits the inner space of the actuator into two chambers. The solenoid EPC connects the pneumatic actuator chamber with a source reservoir (vacuum) when it is energized, and to the atmosphere when it is de-energized. The pressure difference so obtained inside the two actuator chambers results in diaphragm motion. The actuator stem linking the diaphragm with the VGT vanes hence moves the vanes to vary the turbine geometry. The spring action inside the pneumatic actuator brings the vanes back to their original position. The diaphragm inside the pneumatic actuator moves in response to the pressure difference created inside the chamber. It should be noted that single acting actuators are preferred over double acting actuators due to their simpler pneumatic circuitry.

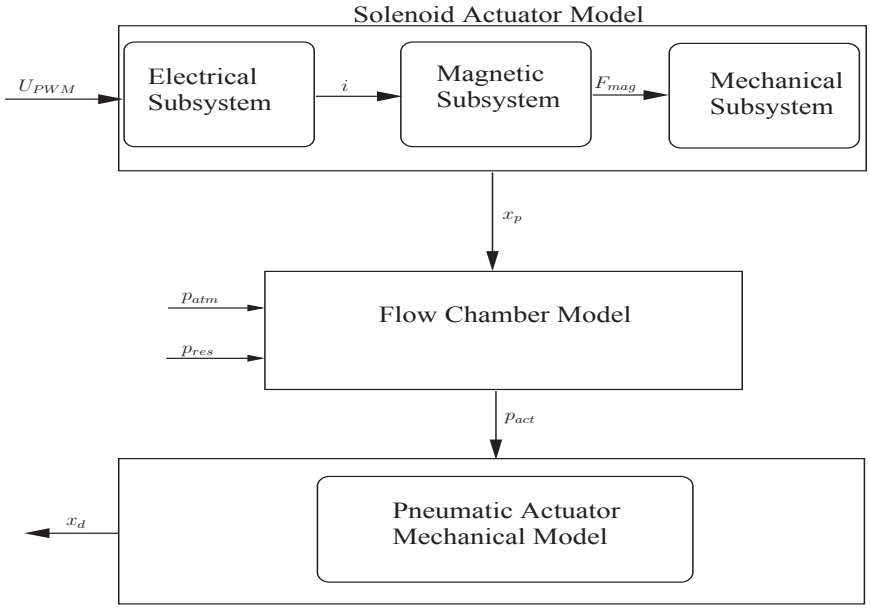

FIGURE 2.1. *Block diagram of the complete VGT system containing an EPC and a pneumatic actuator*

In this section, a physical model of the electro-pneumatic pressure converter is presented, and the magnetic force acting on its plunger is identified. Then, physical modeling of the pneumatic actuator is also presented. While, in the modeling procedure, the pressure dynamics in the pneumatic actuator are considered by taking into account the compressible flow equation along with pressure and temperature losses in the pneumatic lines. Both the system (i.e. electro-pneumatic pressure converter and the pneumatic actuator) are

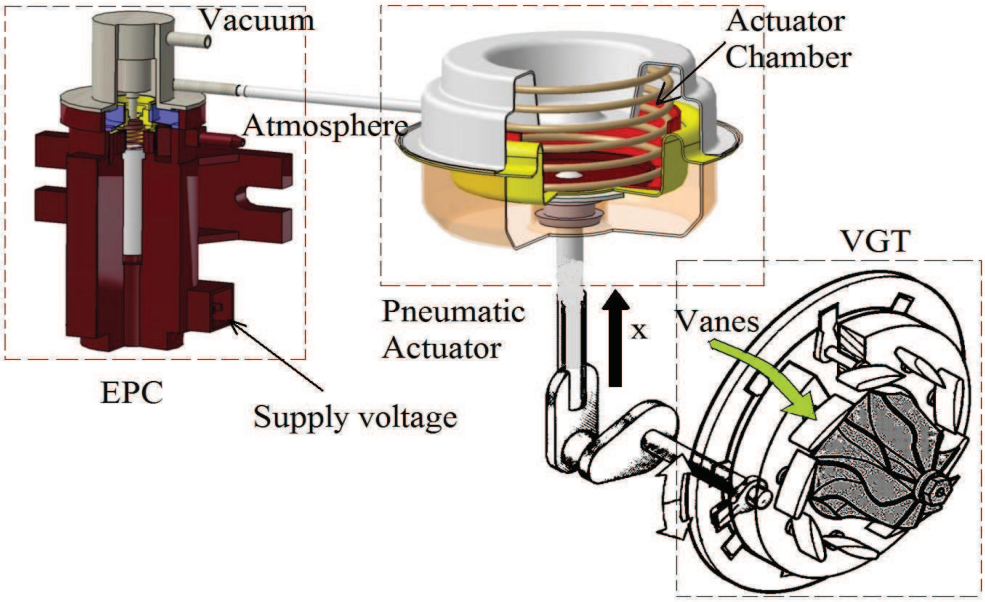

FIGURE 2.2. *A complete system with EPC and pneumatic actuator*

combined together to obtain a base model of an electro-pneumatic actuator. The physical model is compared and validated with experimental data obtained from a laboratory test bench.

2.2.1 ELECTRO-PNEUMATIC PRESSURE CONVERTER MODELING

Physical modeling of the EPC, as a current carrying solenoid valve, has been addressed in the literature e.g. [48], [85], [86], and [90]. In most of the cases its magnetic and pneumatic models are discussed separately. Some mathematical models, which incorporate the magnetic hysteresis effect in the solenoid, have been presented by Eyabi [21] and Zevarehi [99] by assuming a lumped parameter hysteresis model. Another approach to model the hysteresis has been proposed in [71] by using the magnetization curve. In this approach, relatively simple magnetic models for the pressure converters are considered with special focus on the pressure variation within these actuators. For example, Galindo et al. [24] have proposed a static model for magnetic force which is acting on the EPC, in order to avoid parameter identification. The models which deal with the pressure variation due to air mass flow to the actuator chamber have been discussed in [24], [74], [59] and [97]. The authors in [74] have also proposed a model for the pneumatic line using wave propagation and Navier-Stokes equations. Physical modeling of the EPC through electro-magnetic circuit, however, was not their focus. Kotwicki et al. [40] have developed an adiabatic thermodynamic vacuum actuator model for a pneumatic actuator without considering its interaction with the EPC and with special focus on

the temperature dynamics inside the pneumatic actuator. Similarly, Carneino et al. [13] have also compared different thermodynamic models for pneumatic actuator chamber (See also [95]), without considering physical models for the EPC and the pneumatic actuator. Next, we will present both the magnetic and pneumatic model of the EPC.

Solenoid valves can be divided into two categories i.e proportional solenoid valve [48] and ON/OFF solenoid valve [92, 78, 58]. The proportional valve uses a damper or a spring and its advantage over conventional ON/OFF solenoid valve is that it can attain more than two positions with different input voltages. The EPC used in the VGT actuator under consideration however, has mixed characteristics. It has a spring and damper mechanism but without air pressure it acts as an ON/OFF solenoid valve. The reason for this mixed design is that in the pressure converter, the force due to air pressure plays a significant role. The second part of the system is a single acting pneumatic actuator. It can be modeled as a spring damper mechanism with input as pressure difference across both the chambers of pneumatic actuator [24].

In Fig. 2.3, two schematic diagrams of the servo pneumatic pressure regulator are shown. Pierburg servo actuator can be represented symbolically, with the actuator shown in Fig. 2.3(a). It has 3 ports and 3 positions and it permits the bidirectional air flow. It regulates the static pressure inside the pneumatic actuator by either connecting it with the atmosphere or with the vacuum. The third position is equilibrium position. In this position, no air flow through these ports and, therefore, the pressure inside the pneumatic actuator remains constant.

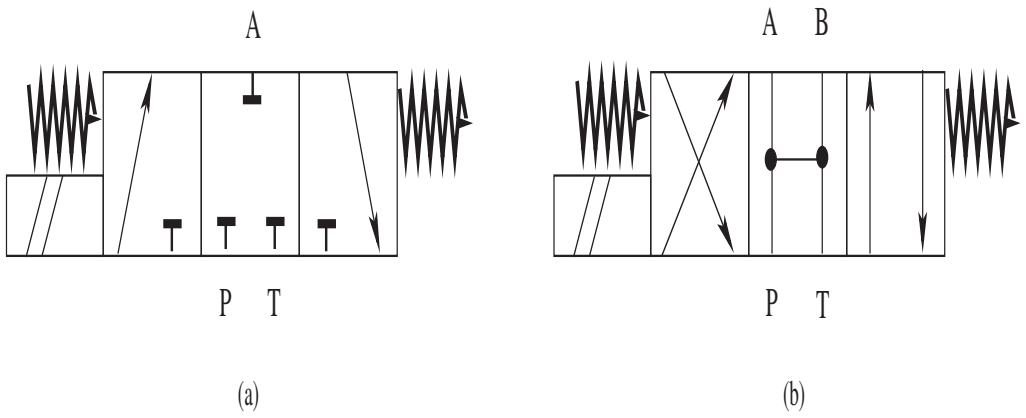

FIGURE 2.3. *Symbolic representation of a pressure converter (a) 3 port 3 position servo valve (b) 4 port 3 position servo valve*

The EPC converts electromagnetic force into plunger movement when the solenoid coil is

energized. The produced magnetic force pushes the plunger (armature) in the downward direction to reduce magnetic resistance. When it is de-energized, a membrane brings the plunger back to its original position. A spring is also present in the actuator, which acts only when the plunger moves up from its equilibrium position. This happens when a pressure difference created across two chambers, separated by the membrane, push the plunger in the upward direction. All the components in the solenoid actuator are shown in Fig. 2.4.

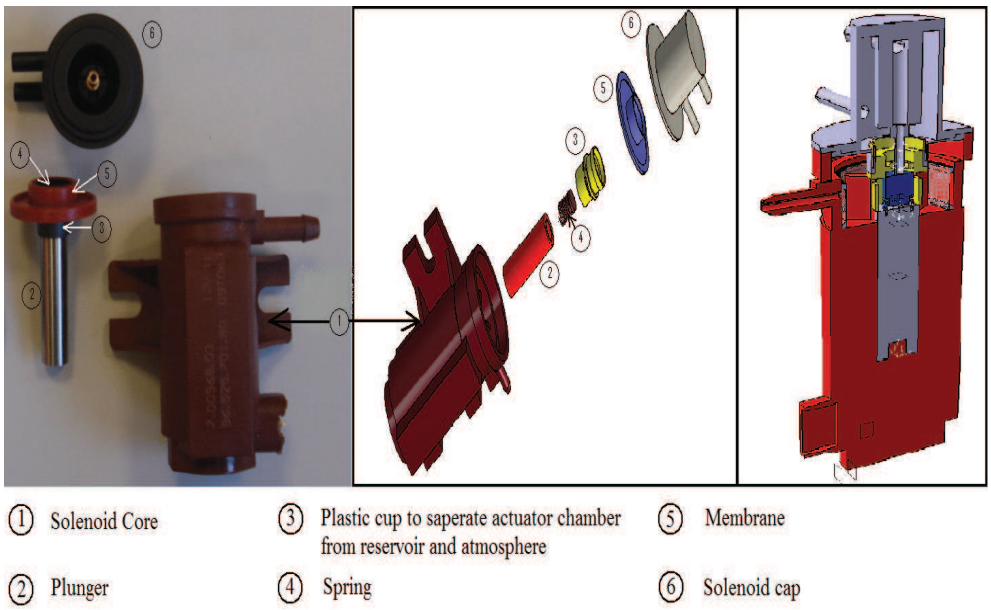

FIGURE 2.4. *Solenoid actuator with three dimensional view*

The solenoid valve has three ports, one outlet port and two inlet ports. The outlet port is connected to the pneumatic actuator and two inlet ports are connected to a vacuum supply and the atmosphere.

The EPC has three positions shown in the Fig. 2.5. The illustration in the center shows that the actuator chamber is connected to the vacuum. The figure on the left shows that the plunger is in equilibrium. The figure on the right shows that actuator chamber is connected to atmosphere. The equivalent electrical circuit of the EPC is a current carrying wire with resistance R_i and variable inductance L; dependent on plunger position. Fig. 2.6 shows equivalent circuit diagram of EPC. From Kirchhoff's voltage law, the equation of the electric circuit can be written as

$$U_{PWM} = R_i i + L\frac{di}{dt} + i\frac{dL}{dt} \tag{2.1}$$

The variable inductance L can be written as a function of plunger position using the relationship $L = \frac{NBA}{i}$ and $B = \frac{Ni\mu_c}{x_{eq}}$

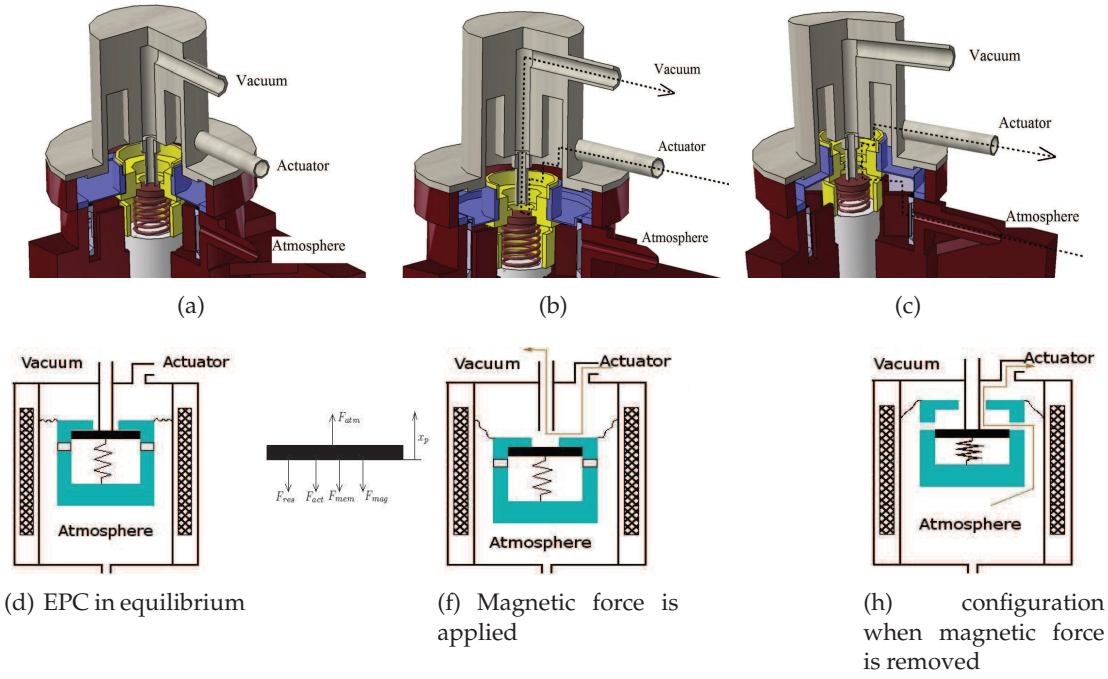

FIGURE 2.5. *EPC is shown in three different working configurations*

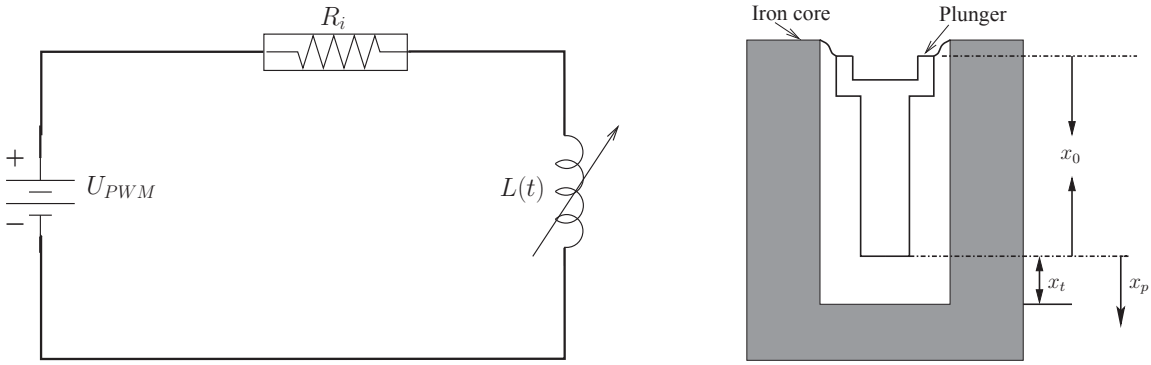

FIGURE 2.6. *Electrical circuit of the EPC (left) and its cross sectional view along with the plunger (right)*

$$L = \frac{N^2 A \mu_c}{x_{eq}} \tag{2.2}$$

Here μ_c is the permeability of the core, N and A are the number of coil turns and cross sectional area of the magnetic flux through plunger respectively. The term x_{eq} is the total length of the magnetic lines through the iron core and the air gap between plunger and iron core.

$$x_{eq} = x_0 + \mu_r (x_t - x_p) \tag{2.3}$$

where x_0, x_t and x_p are the length of the plunger, maximum displacement of plunger and its position, respectively. Here the term μ_r is the relative permeability of the core. Substituting equation (2.3) into equation (2.2) and taking the derivative

$$\frac{d}{dt}L = \frac{\mu_r N^2 A \mu_c}{\left[x_0 + \mu_r (x_t - x_p)\right]^2} \dot{x}_p \tag{2.4}$$

The magnetic force acting on the solid bar plunger inside the solenoid can be determined from the magnetic field density B, cross sectional area of magnetic field lines passing through plunger A and permeability of air μ_0. Equation for magnetic force is given by

$$F_{mag} = \frac{B^2 A}{2\mu_0} \tag{2.5}$$

By using the relationship for magnetic flux density $B = \frac{Li}{NA}$, equation (2.5) for the magnetic force can be written as a function of current i, variable inductance L and number of coil turns N.

$$F_{mag} = \frac{L^2 i^2}{2\mu_0 A N^2} \tag{2.6}$$

The mechanical equation of the plunger can be written as a sum of all the forces acting on it.

$$m_p \ddot{x}_p = F_{atm} - F_{res} - F_{act} - F_{mem} - F_{mag} - b_p \dot{x}_p - F_s^* \tag{2.7}$$

Where m_p and b_p are the plunger mass and its damping constant. The terms F_{atm}, F_{res} and F_{act} are forces on the plunger due to atmospheric pressure p_{atm}, reservoir pressure p_{res} and pressure within the actuator chamber p_{act}, respectively.

$$\begin{aligned} F_{atm} &= p_{atm} A_{atm} \\ F_{act} &= p_{act} A_{act} \\ F_{res} &= p_{res} A_{res} \end{aligned}$$

Here, A_{atm}, A_{act} and A_{res} are the corresponding cross sections of the EPC, towards atmosphere, actuator and reservoir chamber, respectively (See Fig. 2.5). F_{mem} is the force due to the elasticity of the membrane and is given below

$$F_{mem} = k_{mem} x_p$$

Where k_{mem} is the stiffness constant of membrane. $F_s^*(= k_{s1}^* x_p)$ is the spring force that only acts when the plunger is displaced in the upward direction.

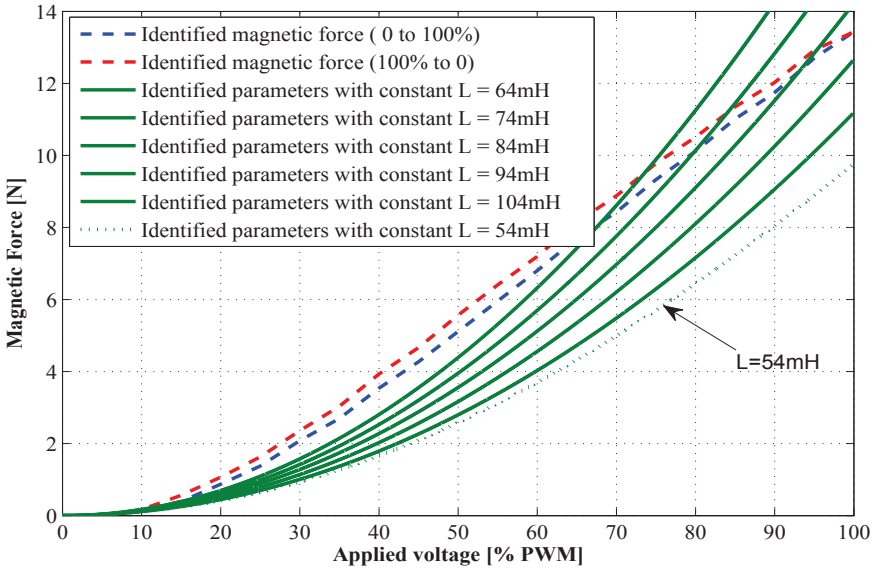

FIGURE 2.7. *The curves for magnetic force with constant inductance and its identified value with variable inductance*

The magnetic force acting on the EPC is difficult to be determined, because it depends on the solenoid characteristics and its complex geometry. However, we have obtained the curves between the magnetic force and the applied voltage with available parameters for the solenoid and considering that the inductance is constant. The curves of magnetic force are shown for different inductance values in Fig.2.7. The above method does not accurately calculate the magnetic force because it also depends on the actuator, the reservoir and the atmospheric pressure. Therefore, a method to identify magnetic force is introduced below, where the magnetic force is represented as a static function of applied voltage [24].

2.2.1.1 MAGNETIC FORCE IDENTIFICATION

The problem with the above model is related to parameter identification which is hard or impossible to measure, especially when it comes to magnetic properties of materials. Therefore, the magnetic force is identified from the force balance equation for the plunger. Moreover, this approach reduces the number of states of the system. The EPC always returns back to its equilibrium position when magnetic force is applied. This is due to the fact that in equilibrium condition air does not flow through the EPC and pressure is constant in the actuator chamber. The balance attained due to the applied magnetic force

and pressure across plunger permits us to identify magnetic force. Equation (2.7) can be simplified to the following equation. This equation is obtained by putting acceleration, velocity and position of the plunger to zero at equilibrium position.

$$F_{mag} = F_{atm} - F_{res} - F_{act} \tag{2.8}$$

Applied magnetic force, calculated for different step inputs, is plotted against the input voltage in Fig. 2.8. Since the actuator was energized using pulse width modulation, the voltage has been expressed as the percentage of duty cycle.

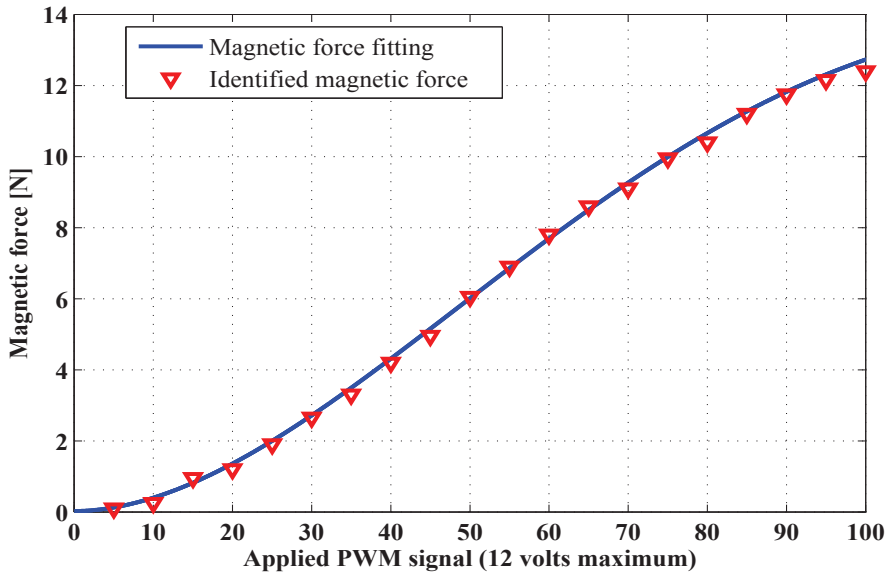

FIGURE 2.8. *Magnetic force acting on the plunger for the duty cycle input voltage*

The magnetic force shown in Fig. 2.8 is parameterized as a function of input PWM duty cycle. Using the least squares method, a polynomial is obtained that approximates the static characteristics of the magnetic force.

$$\begin{aligned} F_{mag} = &\left(9.135e-8\langle pwm\rangle^4\right) - \left(3.573e-5\langle pwm\rangle^3\right) + \left(0.0039\langle pwm\rangle^2\right) + \\ &\left(0.00226\langle pwm\rangle\right) + 0.02173 \end{aligned} \tag{2.9}$$

2.2.1.2 IDENTIFICATION OF THE PLUNGER'S PARAMETERS

The physical parameters e.g. plunger area towards atmosphere A_{atm}, actuator A_{act}, reservoir A_{res} and plunger mass m_p are measurable. These parameters are given in appendix B. The EPC plunger is equivalent to a mass-damper system, and can be represented by a second order system with a transfer function between the plunger position and the applied force.

$$\frac{x_p}{F_u} = \frac{\left[1/\left(k_{mem} + k_{s1}^*\right)\right]}{\frac{m_p}{k_{mem}+k_{s1}^*}s^2 + \frac{b_p}{k_{mem}+k_{s1}^*}s + 1} \tag{2.10}$$

Where F_u is the sum of magnetic force and all other forces caused by the actuator, reservoir and atmospheric pressure

$$F_u = F_{mag} - F_{atm} + F_{act} + F_{res} \tag{2.11}$$

Considering the general form of the second order transfer function $T_r(s)$, in terms of damping ratio ζ and natural frequency of the system ω_n:

$$T_r(s) = \frac{K}{\frac{1}{\omega_n^2}s^2 + 2\frac{\zeta}{\omega_n}s + 1} \tag{2.12}$$

From the data obtained for applied magnetic force and plunger position, we applied nonlinear least square method to obtain the unknown parameters k_{mem}, k_{s1}^* and b_p of the EPC. The identified parameters are also provided in appendix B.

2.2.2 AIR MASS FLOW

The air mass flow can be modeled as air passing through the duct towards actuator. A path is formed between actuator chamber and reservoir when the plunger moves down due to applied magnetic force and the air flows from actuator to vacuum reservoir ($\dot{m}_{act-out}$).

$$\dot{m}_{act-out} = A_{eff(act-res)}\, p_{act} \sqrt{\frac{\gamma}{RT_{act}}}.\Phi\left(\frac{p_{res}}{p_{act}}\right) \tag{2.13}$$

The path between actuator chamber and atmosphere is attained when applied magnetic force on solenoid valve is removed and plunger moves up from its equilibrium position. In this configuration air mass ($\dot{m}_{act-in}$) flows from atmosphere to actuator chamber.

$$\dot{m}_{act-in} = A_{eff(atm-act)}\, p_{atm} \sqrt{\frac{\gamma}{RT_{atm}}}\Phi\left(\frac{p_{act}}{p_{atm}}\right) \tag{2.14}$$

Here $A_{eff(act-res)}$ is the effective flow area between actuator chamber and reservoir, which depends upon the plunger position. $A_{eff(atm-act)}$ is the effective flow area between atmosphere and actuator chamber. $\Phi(p_r)$ is a function which depends on the pressure ratio p_r of the upstream and down stream pressure. Air mass flow is choked when this ratio is $p_r \leq 0.528$ (See for example [32] and [66]) air mass flow becomes constant at

this point. At this point air velocity is equal to the velocity of sound (Mach number = 1). This expression is given in the following equation

$$\Phi(p_r) = \begin{cases} \sqrt{\left\{(p_r)^{2/\gamma} - (p_r)^{(\gamma+1)/\gamma}\right\}\frac{2}{\gamma-1}}, & p_r > \left(\frac{2}{\gamma+1}\right)^{\gamma/\gamma-1} \\ \sqrt{\left(\frac{2}{\gamma+1}\right)^{\gamma+1/\gamma-1}} & , p_r \leq \left(\frac{2}{\gamma+1}\right)^{\gamma/\gamma-1} \end{cases} \tag{2.15}$$

A detailed derivation of the mass flow equation is given in appendix A. The tube connecting the EPC with the pneumatic actuator may have two impacts on the flow. First, the pressure drop because of tube resistance and second, the delay in the flow due to the wave travel time through the long tube. Based on the mass continuity and equilibriums for one dimensional flow, the two basic differential equations governing transient flow in tubes are given below (see e.g. [4])

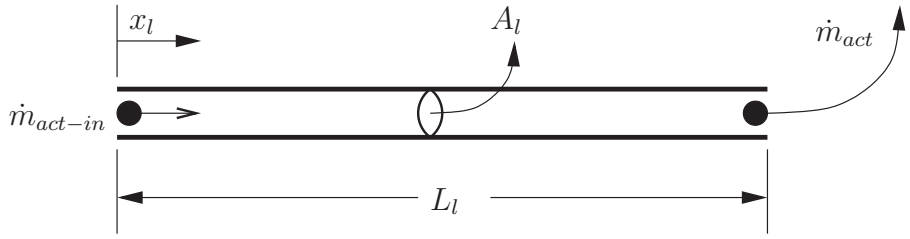

FIGURE 2.9. *The air mass flow through pneumatic tube line*

$$\begin{aligned} \frac{\partial v}{\partial x_l} &= -\frac{1}{\rho c^2}\frac{\partial p}{\partial t} \\ \frac{\partial p}{\partial x_l} &= -R_t v - \rho\frac{\partial v}{\partial t} \end{aligned} \tag{2.16}$$

Where R_t, v and c are tube resistance, velocity of air and velocity of sound respectively. Replacing the velocity of air by introducing mass flow equation $\dot{m} = \rho A_l v$.

$$\frac{\partial \dot{m}}{\partial x_l} = -\frac{A_l}{c^2}\frac{\partial p}{\partial t} \tag{2.17}$$

$$\frac{\partial p}{\partial x_l} = -\frac{R_t \dot{m}}{\rho A_l} - \frac{1}{A_l}\frac{\partial \dot{m}}{\partial t} \tag{2.18}$$

Where ρ and A_l are air density and tube cross sectional area. Now by taking the partial derivative of equation (2.17) with respect to x_l and partial derivative of equation (2.18) with respect to t

$$\begin{aligned}\frac{\partial^2 \dot{m}}{\partial x_l^2} &= -\frac{A_l}{c^2}\frac{\partial^2 p}{\partial x_l \partial t} \\ \frac{\partial^2 p}{\partial x_l \partial t} &= -\frac{R_t}{\rho A_l}\frac{\partial \dot{m}}{\partial t} - \frac{1}{A_l}\frac{\partial^2 \dot{m}}{\partial t^2}\end{aligned} \tag{2.19}$$

Combining equations in (2.19) to get mass flow through pipe

$$\frac{\partial^2 \dot{m}}{\partial t^2} - c^2\frac{\partial^2 \dot{m}}{\partial x_l^2} + \frac{R_t}{\rho}\frac{\partial \dot{m}}{\partial t} = 0 \tag{2.20}$$

This equation represents a generalization of a wave equation, with an additional dissipative term. The proposed mass flow equation can be solved by using the following form (see [74]):

$$\dot{m}(x_l, t) = \chi(t)\Gamma(x_l, t) \tag{2.21}$$

Introducing equation (2.21) into equation (2.20) we get

$$\begin{aligned}&\ddot{\chi}(t)\Gamma(x_l,t) + 2\dot{\chi}(t)\frac{\partial \Gamma(x_l,t)}{\partial t} + \chi(t)\frac{\partial^2\Gamma(x_l,t)}{\partial t^2} - c^2\chi(t)\frac{\partial^2\Gamma(x_l,t)}{\partial x_l^2} + \frac{R_t}{\rho}\dot{\chi}(t)\Gamma(x_l,t) + \\ &\frac{R_t}{\rho}\chi(t)\frac{\partial\Gamma(x_l,t)}{\partial t} = 0\end{aligned} \tag{2.22}$$

$$\begin{aligned}&\left(\ddot{\chi}(t) + \frac{R_t}{\rho}\dot{\chi}(t)\right)\Gamma(x_l,t) + \left(2\dot{\chi}(t) + \frac{R_t}{\rho}\chi(t)\right)\frac{\partial\Gamma(x_l,t)}{\partial t} + \chi(t)\frac{\partial^2\Gamma(x_l,t)}{\partial t^2} - \\ &c^2\chi(t)\frac{\partial^2\Gamma(x_l,t)}{\partial x_l^2} = 0\end{aligned} \tag{2.23}$$

In order to simplify the equation for Γ, we determine $\chi(t)$ such that, after substitution in equation (2.23), the remaining equation in Γ contains no term related to $\chi(t)$,

$$2\dot{\chi}(t) + \frac{R_t}{\rho}\chi(t) = 0 \tag{2.24}$$

Solving first order differential equation (2.24) with $\rho = \frac{p_{act}}{RT_{act}}$, we get

$$\chi(t) = e^{-\frac{R_t R T_{act}}{2p_{act}}t} \tag{2.25}$$

By substituting the solution obtained in equation (2.25) into equation (2.23)

$$\frac{R_t^2 R^2 T_{act}^2}{4p_{act}^2}\Gamma(x_l,t) + \frac{\partial^2\Gamma(x_l,t)}{\partial t^2} - c^2\frac{\partial^2\Gamma(x_l,t)}{\partial x_l^2} = 0 \tag{2.26}$$

Above equation is dispersive wave equation in 1D. The tubes under consideration are not very long, so we assumed that the dispersion caused by the factor $\frac{R_t^2 R^2 T_{act}^2}{4p_{act}^2}$ is very small, and hence can be neglected.

$$\frac{\partial^2 \Gamma(x_l,t)}{\partial t^2} - c^2 \frac{\partial^2 \Gamma(x_l,t)}{\partial x_l^2} = 0 \tag{2.27}$$

Equation (2.27) is non dispersive wave equation. We assume that there is no flow through the tube at $t = 0$, the flow at the inlet $(x_l = 0)$ is a time dependent function $\dot{m}_{act-in}$ and there is no reflection from the end connected at the pneumatic cylinder. Solution of the non dispersive wave equation with initial boundary problem is given by

$$\Gamma(x_l,t) = \begin{cases} 0 & ,\texttt{if} \quad t < x_l/c \\ \dot{m}_{act-in} & ,\texttt{if} \quad t > x_l/c \end{cases} \tag{2.28}$$

The input wave will reach the end of the tube in a time period $\tau = L_l/c$. Where L_l is length of the tube. Replacing t by L_l/c in equation (2.25), the mass flow at the outlet of the tube $x_l = L_l$ is,

$$\dot{m}(L_l,t) = \begin{cases} 0 & ,\texttt{if} \quad t < L_l/c \\ \Gamma(x_l,t) e^{-\frac{R_t R T_{act}}{2 p_{act}} \frac{L_l}{c}} & ,\texttt{if} \quad t > L_l/c \end{cases} \tag{2.29}$$

The tube resistance R_t can be obtained from the expression for the pressure drop along the tube (see Richer and Hurmuzlu [74]).

$$\Delta p = f \frac{L_l \rho v^2}{2D} = R_t v L_l \tag{2.30}$$

where f is the friction factor and D is the inner diameter of the tube. As the flow is turbulent, friction factor f can be computed using the Blasius formula $f = \dfrac{0.316}{R_e^{1/4}}$. Here R_e is the Reynolds number and its value is grater than 4000 for turbulent flow. The tube resistance for turbulent flow is given by

$$R_t = 0.158 \frac{\mu}{D^2} R_e^{3/4} \tag{2.31}$$

where μ is dynamic viscosity of the air. Total mass flow to the actuator is the difference of air mass flowing out from the actuator to reservoir and air mass flowing toward the actuator from atmosphere through pneumatic line

$$\dot{m}_{act}(x_l,t) = \dot{m}_{act-in} \chi_{in}(x_l,t) - \dot{m}_{act-out} \chi_{out}(x_l,t) \tag{2.32}$$

2.2.2.1 EFFECTIVE FLOW AREA

It is important to calculate effective flow area of the gas to determine air mass flow entering or leaving the actuator. One method of modeling the effective flow area is to define a function between the plunger position and the known internal geometry of the EPC [59]. However, the effective flow area has also been modeled and identified using a mass flow

sensor as a function of plunger position of the EPC in [24]. To avoid the use of mass flow sensor, we have used the dynamics of actuator pressure using sensors with high bandwidth. By using the ideal gas equation, air mass flow can be determined after considering the constant volume. Knowing actuator pressure, reservoir pressure, atmospheric pressure and air mass flow; we can determine effective flow area between atmosphere and actuator or between actuator and reservoir using following equation.

$$A_{eff} = \frac{\dot{p}_{act} V_{act}}{T_{act}} \sqrt{\frac{T_0}{R\gamma}} / \left(p_0 \Phi\left(p_r\right)\right) \tag{2.33}$$

where T_0 and p_0 are upstream temperature and pressure. Fig. 2.10 shows the effective flow area as a function of the plunger position. The figure shows the actuator-reservoir effective flow area when the plunger position is negative; and the actuator-atmosphere effective flow area when the plunger moves up and its position is positive. At equilibrium, the actuator chamber is neither connected to the reservoir nor to the atmosphere.

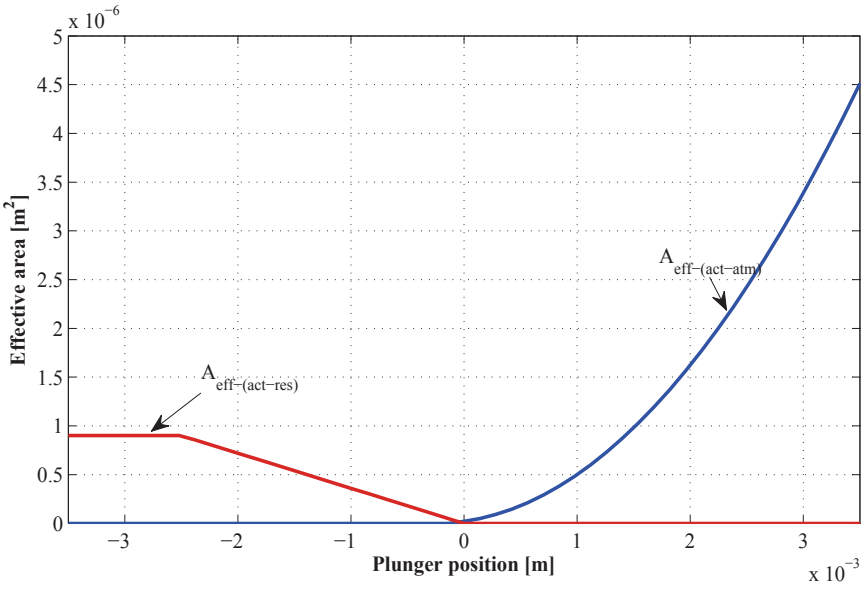

FIGURE 2.10. *Effective flow area vs plunger position*

The function of effective area is not linear as it can be seen from the complex geometry of EPC in Fig. 2.5. The relative plunger position is determined after solving point by point the mechanical equation (2.7) for all known input parameters.

2.2.3 PNEUMATIC ACTUATOR MODEL

The pneumatic actuator controls the VGT vanes position. As mentioned before, it consists of two chamber, separated by a membrane and a diaphragm. One side of the diaphragm

is open to the atmosphere. The EPC controls the pressure on the other side of the diaphragm. Pressure difference between the sides causes the diaphragm to move back and forth. The diaphragm is connected to the vanes of the VGT through a linear linkage. The linkage moves a crank in the VGT to which the vanes are connected. The crank turns the vanes all together and hence, varies the amount of the exhaust gas reaching the impeller of the turbocharger's turbine. Fig. 2.11 shows an industrial pneumatic actuator and its schematic diagram, with all the subparts in it.

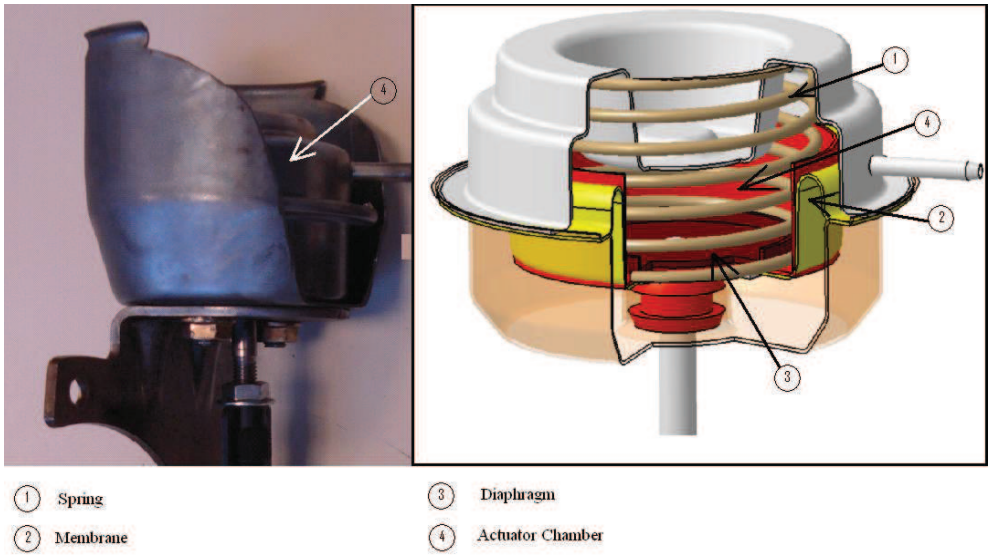

FIGURE 2.11. *Pneumatic actuator and its subparts*

The mechanical subsystem for the diaphragm can be modeled as a mass, spring and damper system under the effect of forces due to pressure difference across actuator chamber. Using Newton's second law of motion.

$$m_d \ddot{x}_d = F_{act} - b_d \dot{x}_d - F_s - F_{aero} - F_f \tag{2.34}$$

Where m_d, x_d and F_{act} are diaphragm mass, its position and the forces due to pressure difference across diaphragm of pneumatic actuator, respectively. F_s is the sum of pre-compressed spring force and the position dependent spring (and membrane) force. Damping force is the product of diaphragm velocity and damping coefficient b_d.

$$\begin{aligned} F_{act} &= (p_{atm} - p_{act})\, A_d \\ F_s &= F_0 + (k_{mem2} + k_{s2})\, x_d = F_0 + k_{sm} x_d \end{aligned}$$

Here A_d is the area of the diaphragm. Pressure in one of the actuator chambers is considered as atmospheric pressure p_{atm}. The term F_{aero} represents the external perturbation

force on the actuator due to the influence of the exhaust gases acting on the VGT. As, we have conducted these tests in cold conditions (no exhaust gas), we will not consider this force for the time being. F_f is the force of friction, and it is, here, described as a simple classical model. However, in chapter 3 it will be presented as a velocity dependent dynamic model.

$$F_f = F_c sign(\dot{x}_d) \tag{2.35}$$

where F_c is the coulomb force of friction.

2.2.3.1 SPRING CONSTANT IDENTIFICATION

The pneumatic actuator contains a spring and a membrane. The purpose of membrane is to separate two chambers of the pneumatic actuator. But it also has elastic properties, which can be modeled as spring. Combined stiffness of both spring and membrane can be determined using the force balance equation at equilibrium. The characteristic curve shown in Fig. 2.12 was obtained for different values of x_d, by discarding the pre-compression force. Equivalent spring constant was obtained using the following equation:

$$k_{sm} = \left[\left(p_{atm} - p_{act}\right) A_d - F_0\right] / x_d \tag{2.36}$$

The above equation has been obtained from the dynamic equation of the diaphragm, considering the force balance for all diaphragm positions at rest ($\dot{x}_d = 0$).

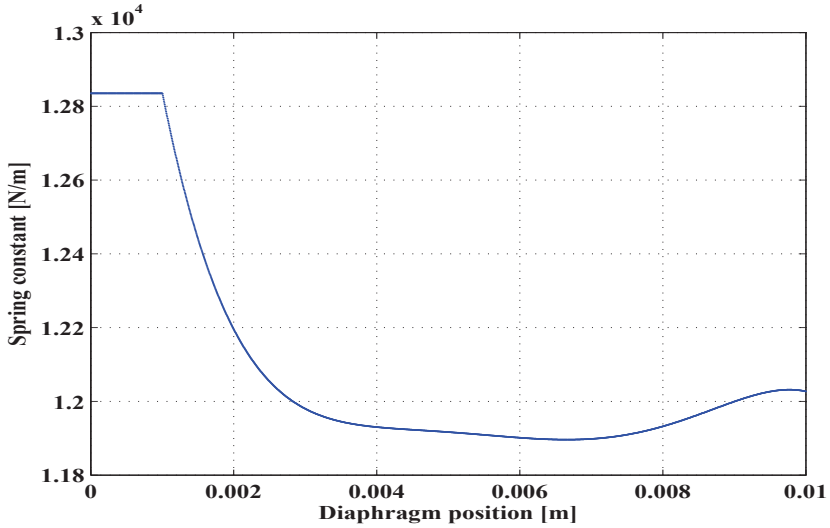

FIGURE 2.12. *Spring constant as a function of the diaphragm position*

2.2.3.2 MASS AND DAMPING CONSTANT

The diaphragm equation is equivalent to a second order transfer function between diaphragm position and pressure difference across the diaphragm. Now by repeating the same steps for diaphragm instead of plunger we get

$$T_r(s) = \frac{x_d}{p_{act}^{'}} = \frac{A_d}{m_d s^2 + b_d s + k_{sm}} \tag{2.37}$$

Where $p_{act}^{'} = p_{act} - p_0$, is the equivalent input to the system. $p_0 = (F_0/A_d)$ is the pressure that compensates the pre-compression and friction. Now, considering again the general form of the second order transfer function $T_r(s)$

$$T_r(s) = \frac{K}{\frac{1}{\omega_n^2} s^2 + 2\frac{\zeta}{\omega_n} s + 1} \tag{2.38}$$

By applying the least square approach we have determined the unknown parameters k_{sm}, b_d and m_d. The identified parameters are shown in Table. B.2. Furthermore, Fig. 2.13 shows the comparison between simulation and experimental results for a step input of $60mBar$. It is shown that identified parameters predict the experimental results with accuracy.

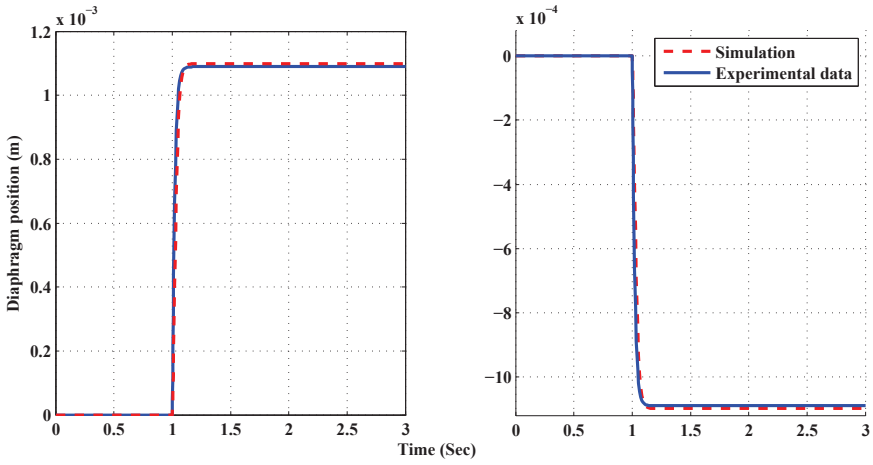

FIGURE 2.13. *Step response of the second order system for 60mBar step up and step down input*

2.2.3.3 ACTUATOR PRESSURE MODEL

The pressure inside the actuator chamber can be modeled from the air mass flow equation entering or leaving the actuator chamber, variation in volume and variation in temperature of the chamber. The flow model is obtained using following assumptions [66].

- Air is thermally a perfect gas
- Pressure is homogeneously distributed throughout the chamber
- No heat loss occurs from the walls of the actuator
- There is no leakage flow from the walls of the actuator

Using the ideal gas equation, the pressure inside the actuator can be modeled as a function of the air gas constant, volume, temperature and mass inside the actuator chamber.

$$p_{act} = \frac{RT_{act}}{V_{act}} m_{act} \tag{2.39}$$

The variation in volume of the gas, temperature and mass flow to or from the pneumatic actuator chamber cause variation in pressure inside the actuator chamber. Using ideal gas equation and taking the partial derivative of the pressure with respect to time would give us the relationship between pressure and time dependent variables temperature, volume and air mass flow of the gas.

$$\frac{dp}{dt} = \frac{RT}{V}\frac{dm}{dt} + \frac{mR}{V}\frac{dT}{dt} + mRT\frac{d}{dt}\left[\frac{1}{V}\right] \tag{2.40}$$

2.2.3.4 VOLUME OF THE ACTUATOR CHAMBER

The volume of the actuator chamber varies with the change in position of the diaphragm. Let us consider the actuator chamber as a cylinder with volume V_0 at initial position. Volume of the chamber reduces as the diaphragm moves from its initial position. The displaced volume depends on the diaphragm position x_d and diaphragm disk area A_d. The volume of the actuator can be calculated by the following equation

$$V_{act} = V_0 - A_d x_d \tag{2.41}$$

Change in volume of the actuator chamber with respect to time is the product of diaphragm area and its velocity

$$\dot{V}_{act} = -A_d \dot{x}_d \tag{2.42}$$

2.2.3.5 TEMPERATURE IN THE ACTUATOR CHAMBER

Temperature inside the actuator chamber varies due to the energy flowing from atmosphere to the actuator or from actuator to the reservoir. From the first law of thermodynamics and considering that mass inside the system is not constant we can write the sum of all energies added to the system by the following energy equation (See [13], [30] and [40]).

$$\frac{d}{dt}E + \frac{d}{dt}W_x = \frac{d}{dt}Q + \dot{H}_{in} - \dot{H}_{out} \tag{2.43}$$

- E is total energy of the air inside the chamber, we may assume that no substantial changes in potential or kinetic energy in the flow occurs, hence $E = U$ (Internal energy).
- dW_x is the mechanical work
- Q is the heat transfer across actuator boundary. We assume no heat or mass transfer through the walls.
- $\dot{H}_{in}$ is the change in enthalpy of the air mass when it flows towards the actuator
- $\dot{H}_{out}$ is the change in energy due to change in enthalpy when air flows out of the actuator

Equation (2.43) can be simplified, by considering the assumptions explained above to calculate the variation in temperature when air is flowing in or out of pneumatic actuator chamber.

$$\frac{d}{dt}U = -\frac{d}{dt}W_x + \dot{m}_{act-in}h_{in} - \dot{m}_{act-out}h_{out} \tag{2.44}$$

where h_{in} and h_{out} are the specific enthalpy of air. The total change in the air mass is the difference of air flow in the chamber

$$\frac{d}{dt}m_{act} = \dot{m}_{act} = \dot{m}_{act-in} - \dot{m}_{act-out} \tag{2.45}$$

and by the caloric relations

$$\begin{aligned} U &= m_{act}c_v T_{act} \\ h_{in} &= c_p T_{atm} = (c_v + R)\, T_{atm} \\ h_{out} &= c_p T_{act} = (c_v + R)\, T_{act} \end{aligned} \tag{2.46}$$

where c_p and c_v are specific heat ratios at constant pressure and constant volume, respectively. R is the gas constant. Substituting above equations into (2.44) we get the following equation

$$\frac{d}{dt}\left(m_{act}c_v T_{act}\right) = -\frac{d}{dt}W_x + \dot{m}_{act-in}\left(c_v + R\right)T_{atm} - \dot{m}_{act-out}\left(c_v + R\right)T_{act} \tag{2.47}$$

Internal energy U is the function of air mass inside the actuator chamber and the temperature, so its derivative can be written in the form given below.

$$\frac{d}{dt}\left(m_{act}c_v T_{act}\right) = c_v \dot{T}_{act} m_{act} + c_v T_{act}\dot{m}_{act-in} - c_v T_{act}\dot{m}_{act-out} \tag{2.48}$$

Mechanical work done by the actuator diaphragm is the product of pressure inside the pneumatic actuator and change in the volume of the actuator chamber. It is given in the equation

$$\frac{d}{dt}W_x = p_{act}\frac{d}{dt}V_{act} \tag{2.49}$$

Using equations (2.48) and (2.49) and substituting into equation (2.47) we get

$$\begin{aligned} c_v \dot{T}_{act} m_{act} + c_v T_{act}\dot{m}_{act-in} - c_v T_{act}\dot{m}_{act-out} = -p_{act}\dot{V}_{act} + (c_v T_{atm} + \\ RT_{atm})\,\dot{m}_{act-in} - (c_v T_{act} + RT_{act})\,\dot{m}_{act-out} \end{aligned} \tag{2.50}$$

Simplifying equation (2.50), by discarding equal terms on the both sides we get

$$\begin{aligned} c_v \dot{T}_{act} m_{act} + c_v T_{act}\dot{m}_{act-in} = -p_{act}\dot{V}_{act} + (c_v T_{atm} + RT_{atm})\,\dot{m}_{act-in} - \\ RT_{act}\dot{m}_{act-out} \end{aligned} \tag{2.51}$$

Using the ideal gas equation

$$p_{act}V_{act} = m_{act}RT_{act} \tag{2.52}$$

Using the expression for actuator volume and its derivative, as described in equation (2.41) and (2.42), and rewriting the above equation we get

$$p_{act}\dot{V}_{act} = -\frac{m_{act}RT_{act}}{V_0 - A_d x_d}A_d \dot{x}_d \tag{2.53}$$

Rearranging equation (2.51) for $\dot{T}_{act}$ and replacing the expression of work given in equation (2.53) we get the following equation

$$\begin{aligned} \dot{T}_{act} = \frac{m_{act}RT_{act}}{c_v m_{act}\left(V_0 - A_d x_d\right)}A_d \dot{x}_d + \left[\left(1 + \frac{R}{c_v}\right)T_{atm} - T_{act}\right]\frac{\dot{m}_{act-in}}{m_{act}} \\ -\frac{R}{c_v}T_{act}\frac{\dot{m}_{act-out}}{m_{act}} \end{aligned} \tag{2.54}$$

Equation (2.54) can be further simplified to the following equation by replacing the terms with specific heat at constant volume by specific heat ratio $\frac{c_v + R}{c_v} = \gamma$

$$\dot{T}_{act} = T_{act}\left[\frac{(\gamma-1)A_d\dot{x}_d}{(V_0 - A_d x_d)}\right] + \left(\gamma T_{atm} - T_{act}\right)\frac{\dot{m}_{act-in}}{m_{act}} - \left[\left(\gamma-1\right)T_{act}\right]\frac{\dot{m}_{act-out}}{m_{act}} \tag{2.55}$$

By combining equations (2.40), (5.10), (2.41), (2.42) and (2.55) the actuator pressure dynamics can be determined.

$$\begin{aligned}\dot{p}_{act} = {} & \frac{RT_{act}}{V_{act}}\dot{m}_{act-in} - \frac{RT_{act}}{V_{act}}\dot{m}_{act-out} + \frac{p_{act}}{V_{act}}\dot{V}_{act} + \frac{m_{act}R}{V_{act}}\left\{ T_{act}\left[\frac{(\gamma-1)A_d\dot{x}_d}{(V_0 - A_d x_d)}\right] + \right. \\ & \left.\left(\gamma T_{atm} - T_{act}\right)\frac{\dot{m}_{act-in}}{m_{act}} - \left[\left(\gamma-1\right)T_{act}\right]\frac{\dot{m}_{act-out}}{m_{act}} \right\}\end{aligned} \tag{2.56}$$

After eliminating the similar terms

$$\dot{p}_{act} = \frac{\gamma R}{V_0 - A_d x_d}\left(T_{atm}\dot{m}_{act-in} - T_{act}\dot{m}_{act-out}\right) - \frac{\gamma p_{act}}{V_0 - A_d x_d}A_d\dot{x}_d \tag{2.57}$$

The complete model of the system, after combining equations (2.7), (2.32), (2.34), (2.55) and (2.57) is given by

$$\begin{aligned}
\dot{x}_1 &= x_2 \\
\dot{x}_2 &= \left[\left(p_{atm}A_{atm} - F_{mag} - b_p x_2 - x_6 A_{act} - k_{mem}x_1 - p_{res}A_{res} - k^*_{s1}x_1\right)/m_p\right] \\
\dot{x}_3 &= x_4 \\
\dot{x}_4 &= \left[\left(\left(p_{atm} - x_6\right)A_d - b_d x_4 - \left(F_0 + k_{sm}x_3\right) - F_c sign(x_4)\right)/m_d\right] \\
\dot{x}_5 &= \left[x_5\frac{(\gamma-1)A_d x_4}{(V_0 - A_d x_3)} + \left(\left(\gamma T_{atm} - x_5\right)\frac{\dot{m}_{act-in}}{x_7}\right) - \left(x_5\left(\gamma-1\right)\frac{\dot{m}_{act-out}}{x_7}\right)\right] \\
\dot{x}_6 &= \frac{\gamma R x_5}{V_0 - A_d x_3}\left(\dot{x}_7\right) - \frac{\gamma x_6}{V_0 - A_d x_3}A_d x_4 \\
\dot{x}_7 &= \chi_{in}(x_l, t)A_{eff(atm-act)}p_{atm}\sqrt{\frac{\gamma}{RT_{atm}}}\Phi\left(\frac{x_6}{p_{atm}}\right) - \chi_{out}(x_l, t)A_{eff(act-res)}x_6\sqrt{\frac{\gamma}{Rx_5}}\Phi\left(\frac{p_{res}}{x_6}\right)
\end{aligned}$$

$$\texttt{where}\quad \Phi\left(p_r\right) = \begin{cases} \sqrt{\left\{\left(p_r\right)^{2/\gamma} - \left(p_r\right)^{(\gamma+1)/\gamma}\right\}\frac{2}{\gamma-1}}, & p_r \geq \left(\frac{2}{\gamma+1}\right)^{\gamma/\gamma-1} \\ \sqrt{\left(\frac{2}{\gamma+1}\right)^{\gamma+1/2(\gamma-1)}} & , p_r < \left(\frac{2}{\gamma+1}\right)^{\gamma/\gamma-1} \end{cases} \tag{2.58}$$

A complete state space model of the electro-pneumatic actuator system is presented in the model (2.58). Here x_1, x_2, x_3, x_4, x_5, x_6 and x_7 are state variables for the plunger position, the plunger velocity, the diaphragm position, the diaphragm velocity, the temperature, pressure and the air mass inside the pneumatic actuator, respectively.

2.3 Simulation and Experimental Validation of the Model

The mathematical model developed in the last section is implemented with AMESim simulation software. The advantage of using AMESim is that a set of validated libraries can be used for pneumatic, electric and hydraulic components. Such an example of an electro-pneumatic actuator is given in Fig. 2.14. However, some times existing components does not fulfil user requirement. As in our case, the pressure converter due to its unique characteristics can not be modeled with existing libraries. But the user can develop his own component based on its mathematical model. Therefore, we have programmed the whole system with AMESim without using existing components in its libraries. The complete AMESim model is shown in Fig. 2.15

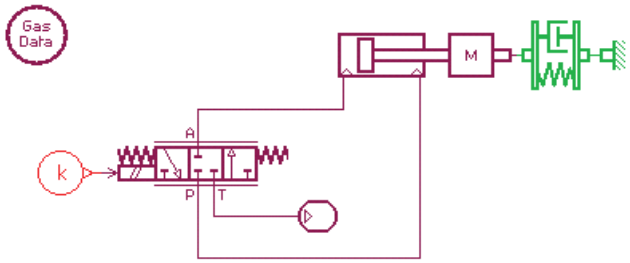

Figure 2.14. *An electro-pneumatic actuator with AMESim*

The experiments were conducted on a pneumatic valve and EPC used with the DV6TED4 commercial engine. Experimental results were obtained using the test bench shown in the Fig. 2.16. National Instruments (NI) Compact RIO system was used for data acquisition. The test bench is equipped with two PTX druck 600-1176 pressure sensors with output from $20mA$ to $4mA$. These sensors measure relative gauge pressure with range from 0 to $-1Bar$. One sensor measures the actuator chamber pressure while the other measures source reservoir pressure. The position of the diaphragm is measured using a potentiometer mounted on the pneumatic actuator. Data is acquired using Compact-RIO modules (NI-9215) for analog input. EPC, Pierburg device, is energized with H-Bridge DC servo drive module (NI-9505). The sampling frequency for the CompactRio is fixed to $1KHz$.

The electro-pneumatic actuator model shown in equation set (2.58) have been simulated in matlab/simulink using the identified parameters given in appendix B for an industrial actuator. In Fig. 2.17 measured and simulation values of the actuator pressure and source reservoir pressure are shown for duty cycle input for (0-100)% and then for (100-0)%. Time response for the pressure rise is $0.2sec$ and fall time is $1.2sec$ inside the actuator.

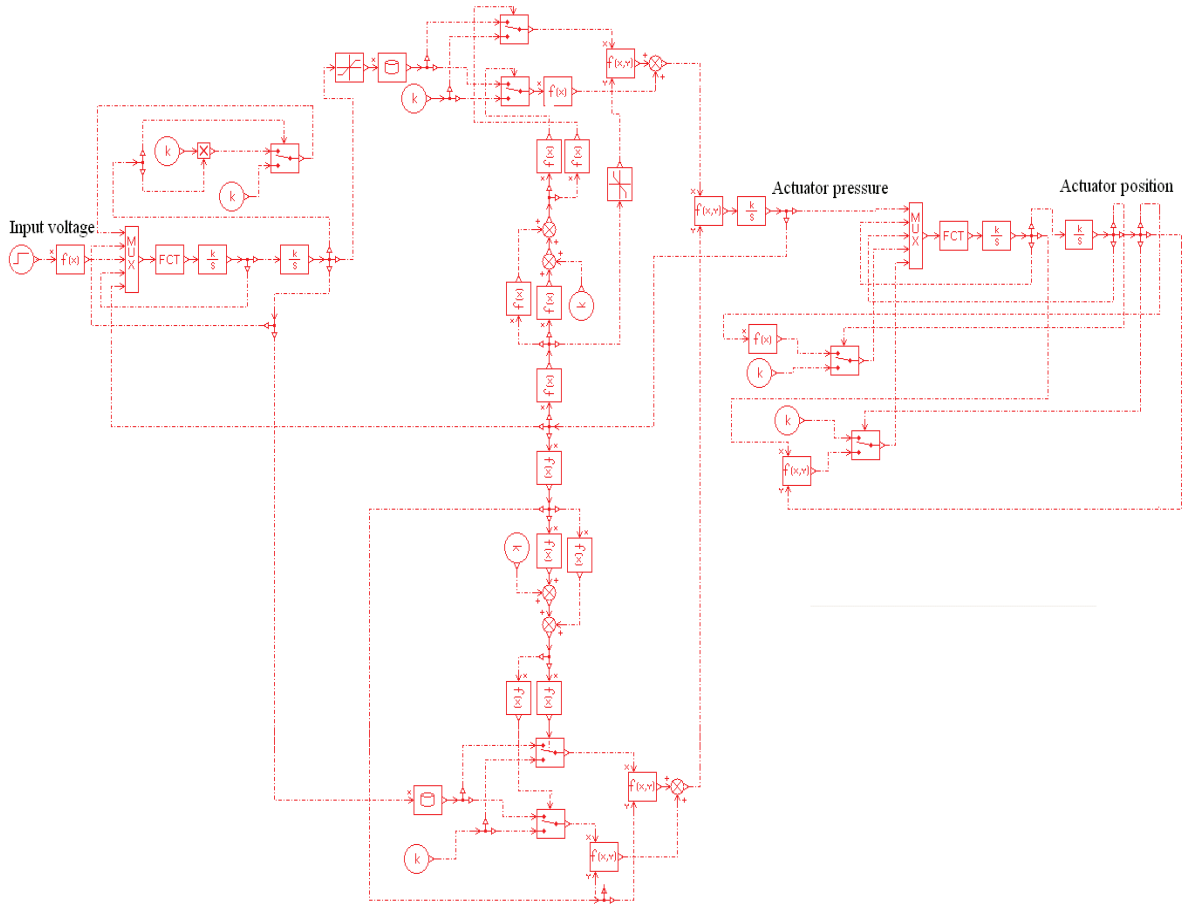

FIGURE 2.15. *The complete actuator system modeled in AMESim*

This difference is due to the effective flow area of actuator-to-reservoir and actuator-to-atmosphere. Steady state error between simulations and experimental results is in between $\pm 10 mBar$.

In Fig. 5.4 measured and simulation values of the actuator pressure and diaphragm position are shown for duty cycle input of 80%. Time response of the system for the pressure fall is $0.3 sec$ inside the actuator. All the three models follow dynamics of pressure with steady state error of $\pm 5 mBar$. Diaphragm position for applied pressure is shown with time response of $0.35 sec$. Steady state error for the simulation models is $\pm 0.3 mm$.

In Fig. 5.5 measured and simulation values of the actuator pressure and diaphragm position are shown for duty cycle input 50%. The model follows dynamics of the pressure with steady state error of $\pm 8 mBar$, and $\pm 0.3 mm$ for diaphragm position.

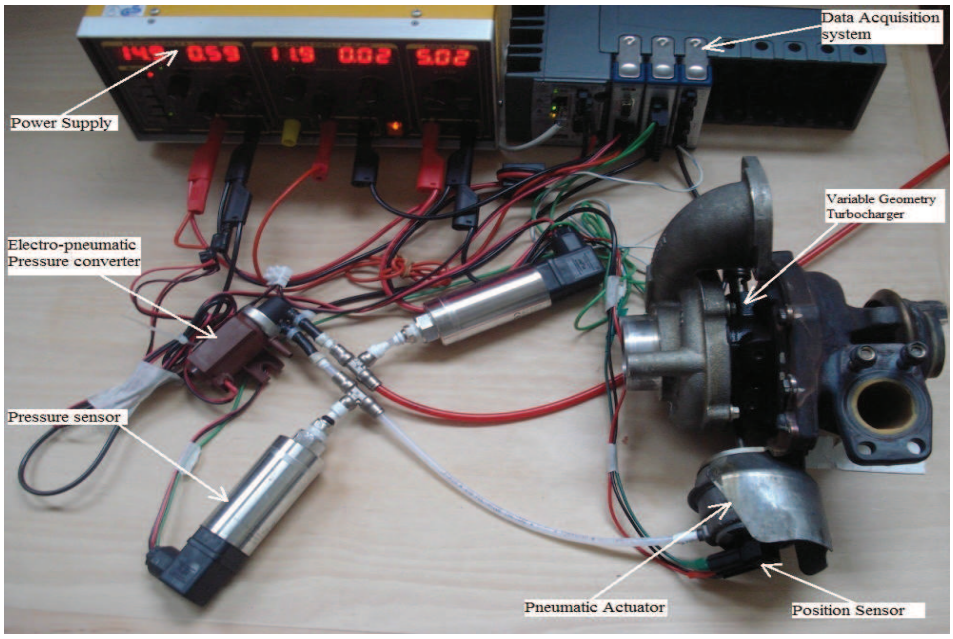

FIGURE 2.16. *Test bench for the experimental tests*

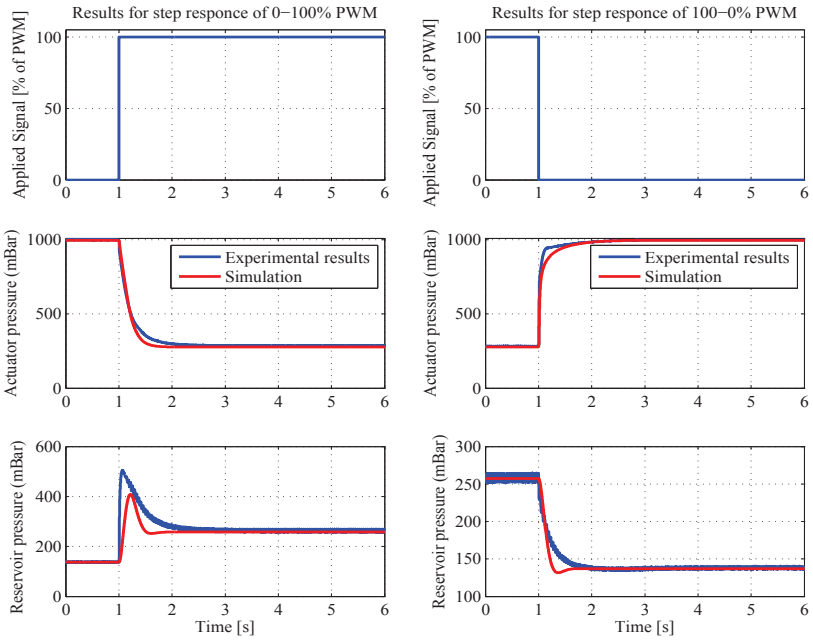

FIGURE 2.17. *System response to 100% PWM input voltage signal*

2.4 CONCLUSION

In this study, we have presented a detailed model for a commercial VGT actuator. The pressure dynamics inside the actuator chamber are modeled by taking into account the

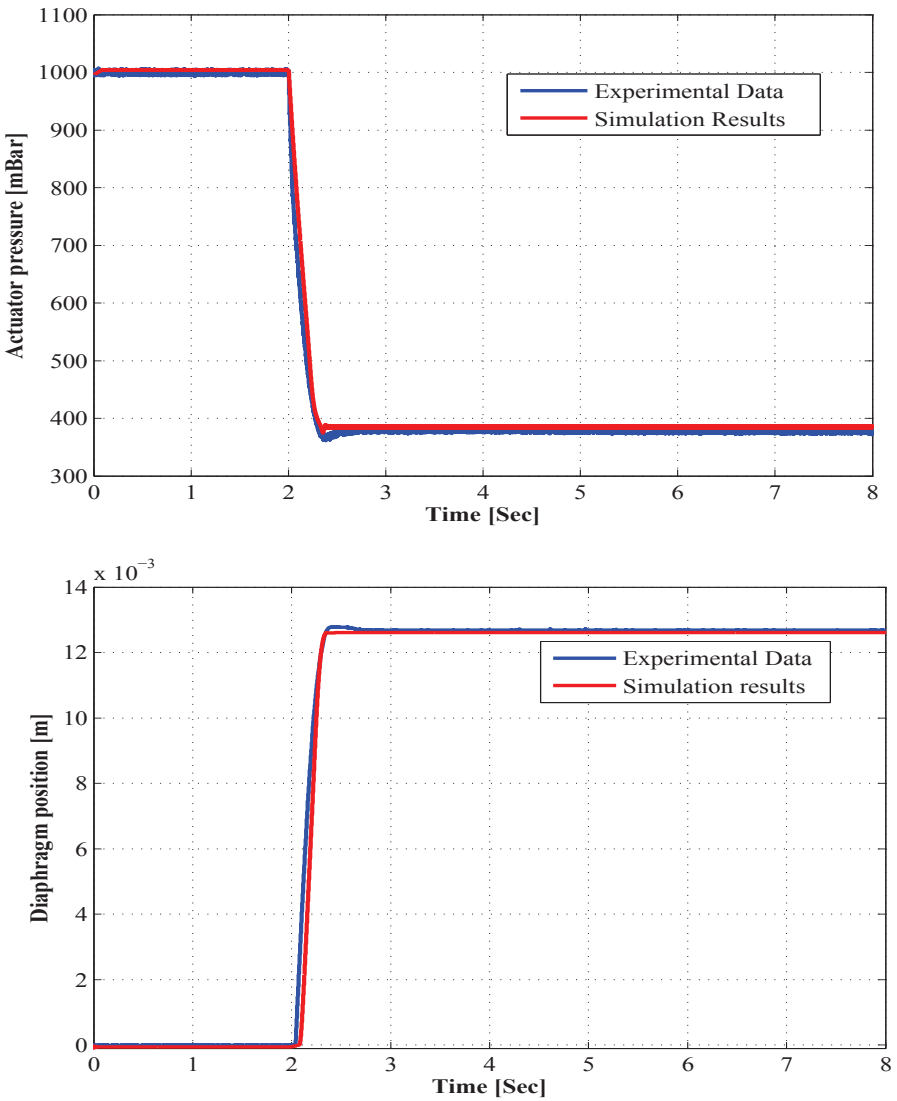

FIGURE 2.18. *Validation of the proposed model for actuator pressure and diaphragm position, for 80% applied PWM signals*

variation of mass, temperature and volume. Moreover, the attenuation and delay in the air mass flow due to pneumatic lines, is also considered with the help of wave propagation and Navier-Stokes equations. This model has been implemented in AMESim, a well-known platform for energy-based modeling of physical systems. The model so obtained is validated with the experiments carried out on the laboratory test bench.

The presented model describes the electro-mechanical phenomena inside the actuator. However, a complete model requires friction to be considered as well. Also, the varying aerodynamic force exerted on the VGT vanes by the exhaust gas passing through the turbine, has a significant influence on the actuator's performance. In the next chapter, these two forces, i.e. friction and aerodynamic force will be modeled and integrated, to

auspicious

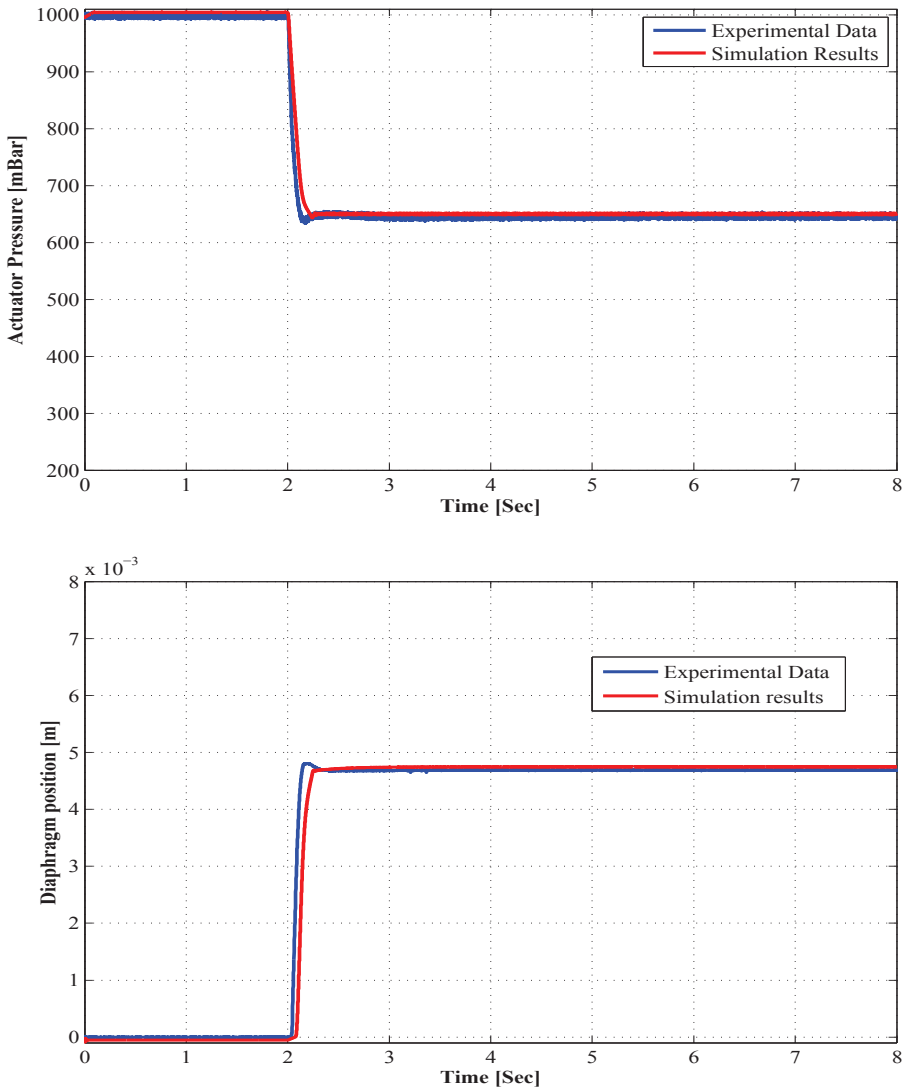

FIGURE 2.19. *Validation of three proposed models for actuator pressure and diaphragm position, for 50% applied PWM signals*

develop a complete detailed model. Then we will proceed to control design, where the model will be sufficiently simplified and control algorithms will be designed for actuator control, ranging from classical PID algorithms with nonlinearity compensation to advanced methods such as backstepping control.

Chapter 3 Modeling with Nonlinearities

3.1 Introduction

So far, we have developed a basic physical model of the VGT actuator. Laboratory bench tests have validated the behavior of this model under cold conditions i.e. with maximum lubrication and no exhaust gas. In fact, this model remains incomplete until two important resistive forces, namely friction and turbine aerodynamic force, have been modeled and integrated into the actuator dynamics. These forces have a strong influence on the working of the VGT Actuator during operation on a running engine. Therefore, it is important that these forces be represented in the model to study the global effect of VGT actuator dynamics and nonlinearity on the performance of the turbocharger, air path and engine.

In real life, friction needs to be minimized in most engineering applications, since its highly nonlinear behavior affects the performance of the system. It causes energy loses, wear and tear, hysteresis, heat generation and material deformation etc [5]. Friction is one of the historic fields of scientific study, considered by classical scientists such as de Vinci, Amonton and Coulomb. The physicist Amonton defined two basic laws for friction: friction is directly proportional to the applied load and it is independent of the apparent area of contact [9]. Coulomb published one of the most famous and comprehensive studies about friction also known as the Coulomb friction law. Friction was then considered to be independent of the velocity. Stribeck [83] improved Coulomb's model by taking into account velocity dependent nonlinear phenomena like the Stribeck effect, Stick-slip friction and stiction. Modern studies on friction are essentially based on the work of Stribeck.

The other important factor which adds nonlinear effects in the VGT actuator is the aerodynamic force. The high pressure exhaust gases passing through the turbine significantly increase the hysteresis in the actuator. The analysis of aerodynamic force, despite its great significance, has not been addressed in the literature on small turbomachinery systems like VGT. However, we can find such models for the multistage compressors and turbines

used in the heavy industry [2]. There are three common methods to determine the aerodynamic force. Two of them are based upon the characteristic maps obtained through experimentation and the third method depends on the 1D flow model of the exhaust air. This model depends upon the pressure losses in the exhaust air flow channel [98]. Analytical and lumped volume (0D) models are simple but not so accurate. On the contrary 2D or 3D models are too complex to be solved for analysis [46] [19].
In this chapter our focus will be on the detailed modeling of the VGT actuator system with nonlinearities, by including friction and aerodynamic force in the physical model presented in the previous chapter. Friction is presented with static and dynamic friction models. The reaction of engine's exhaust gases on the actuator is studied with aerodynamic force, which increases the hysteresis in the actuator. Therefore, a 1D model of the air flow through a turbocharger is proposed in this work with special focus on the aerodynamic force acting on the VGT actuator. Our main objective is to opt these models for the single stage mixed flow turbocharger used in a diesel engine. The most accurate models of friction and aerodynamic force are then included in the physical VGT actuator model and the detailed model so obtained is validated with experimental data.

3.2 NONLINEARITIES IN THE SYSTEM

The static friction models, obtained on the basis of the theory explained in the previous section, are discontinue at zero velocity [5]. The main disadvantage when using a static model is that it does not work for simulation and control. Karnopp [36] proposed a first static model which considered finite continuous interval around zero velocity. The main drawback of this model is that the zero velocity interval, however, does not agree with real friction. In Fig. 3.1, all the static friction models are represented with velocity friction diagram.

3.2.1 HYSTERESIS

During the experiments on the pneumatic actuators, we have observed the nonlinear hysteresis. It is obvious that the primary cause of this hysteresis is friction. Fig. 3.2 shows the hysteresis curve between applied actuator pressure and diaphragm position. The applied pressure is given in $mBar$, and it represents the differential pressure across actuator's diaphragm.

In the following sections, we will see that the primary cause of the hysteresis is the sudden change in friction with change in direction of actuator motion. The aerodynamic force further complicates the problem of dealing with hysteresis as the opening and closing characteristics of the actuator become different.

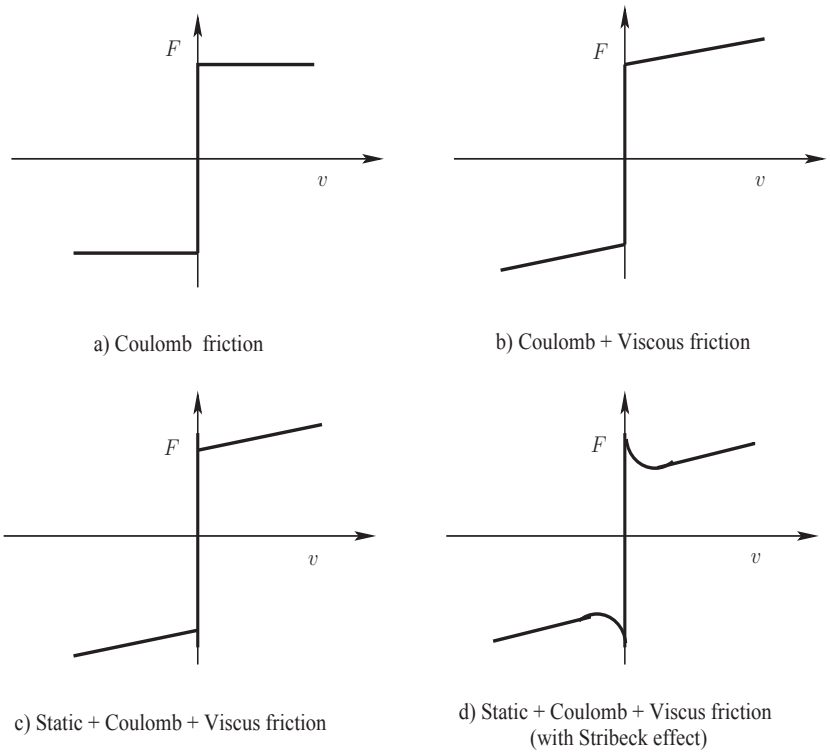

FIGURE 3.1. *Static fiction models with all type of frictions*

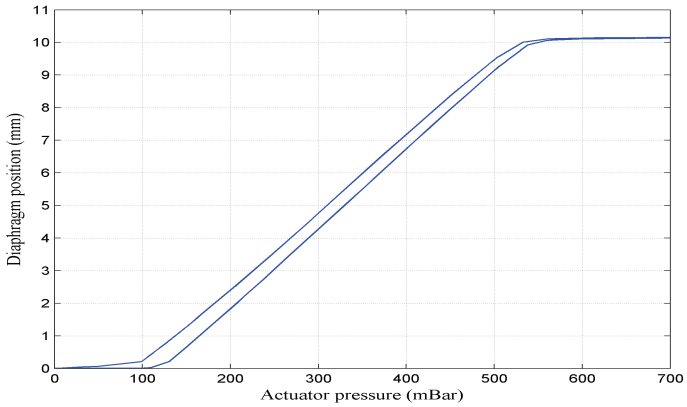

FIGURE 3.2. *The experimental curve between actuator pressure and diaphragm position for slowly ramped up and down actuator pressure*

3.3 FRICTION MODELING

Friction is a natural force that arises essentially from surface irregularities or asperities [17, 50]. It is in fact a complex phenomenon and can be divided into two components. The first is static friction F_s which keeps the bodies at rest. It has to be overcome to start the relative motion between two surfaces [65]. The second component is dynamic

friction which manifests itself during motion. It further comprises of two components i.e. Coulomb and Viscous friction. Coulomb friction F_c is the minimum value friction can take while the object moves, it depends upon the materials in contact. The viscous friction is a linear function of velocity and is attributed to lubricants. When a body starts from zero velocity, i.e. breaks away from static friction, the transition between static friction (or break-away force) and dynamic friction is called Stribeck effect [17]. Stribeck effect is generally described as a composite of two different processes: the static process when an object is stationary (no sliding is involved) and likely to move under certain applied force, and the dynamic process when sliding is involved. The static process is characterized by the maximum static force (or breakaway force) under which body remains in stationary condition. In the slipping process, the friction force decreases with increasing velocity in certain velocity regimes. In practice, the downward bend of friction force at low velocity is due to Stribeck effect [81].
The discontinuity induced in the system by static friction is especially difficult to model and simulate on the computer [36]. Different models have been proposed to overcome this problem. These models are generally classified as static and dynamic models. The terms static and dynamic models must not be confused with static and dynamic friction forces, here the terms are used in the context of systems and modeling. Static friction models consider friction to be a static function of the system's velocity. Whereas, dynamic friction models represent friction to be dynamic with respect to velocity, and hence, are formed using differential equations. A survey of all friction models have been described in [65] and [5]. Next, we will describe some of the known friction models and their identification procedure for the pneumatic actuator.

3.3.1 Static Friction Models

A static friction model is a piece-wise continuous function used to model friction in different regions. The Karnopp friction model is the most popular static friction model. It was developed in 1985 to handle the discontinuity due to static friction and to provide a friction model that can be simulated on the computer. The Karnopp model reforms the discontinuity by a small region between two very small values of velocity, replacing the discontinuity characteristic with a linear relationship between force applied to the system and static friction force [36, 25]. The Karnopp friction model is shown in the equation below [45, 78]

$$F_f = \begin{cases} F_c.\mathrm{sgn}(\dot{x}_d) & ,\dot{x}_d \neq 0 \\ F_p & ,\dot{x}_d = 0, F_p < F_s \\ F_s.\mathrm{sgn}(F_p) & ,\dot{x}_d = 0, F_p > F_s \end{cases} \tag{3.1}$$

where F_f, F_c, F_p, F_s are friction force, coulomb friction force, applied force and static friction force respectively. Static friction model is discontinuous, hence not suitable for control and simulation. Some modifications on this basic friction model however make it suitable for simulation.

3.3.2 Dynamic Friction Model

The static models cover most of the friction behavior, however, they neither explain hysteretic behavior when studying friction for non-stationary velocities nor small displacements that occur at the contact interface during stiction [65]. As static models, such as the Karnopp model, are still piece-wise continuous, they are problematic in simulation of dynamic systems as well. The dynamic friction models have now been developed which cover not only these nonlinear phenomena but also are continues near zero velocity. This property makes the dynamic models useful for computer simulations and control [12]. Many dynamic models have been proposed so far. Some examples are the Dahl model [18], the Bouc-Wen model [75] and the LuGre model [12] etc.

3.3.2.1 Dahl Friction Model

Dahl developed a comparatively simple model that was used extensively to simulate systems with ball bearing friction. One of his findings was that bearing friction behaves very similar to solid friction. This model also covers the phenomenon of hysteresis within the moving bodies due to the friction. Dahl [65] proposed a dynamic friction model, in which he considered the surface irregularities or asperities (main cause of friction) as elastic springs, thereby replacing the discontinuity with spring dynamics. In Fig. 3.3, the bristles are shown between the sliding surfaces. The length of these bristles is represented by z, whereas, σ represents the stiffness coefficient of these bristles.
The Dahl model is described here as the function of stiffness coefficient and direction of the velocity v [65].

$$\frac{dF_f}{dx} = \sigma \left(1 - \frac{F_f}{F_c}.sgn(v)\right)^{\alpha} \tag{3.2}$$

where F_f is the friction of the system. σ is the stiffness constant and α is the constant that determines the shape of stress strain curve [65]. Its value is taken as one in most cases [6]. Equation (3.3) specifies that friction force is the function of sign of velocity and position of the body and is independent of time. This important property of the model makes it possible to use it for hysteresis modeling. See for example [18], [65] and [82]. Simplified Dahl model is shown below.

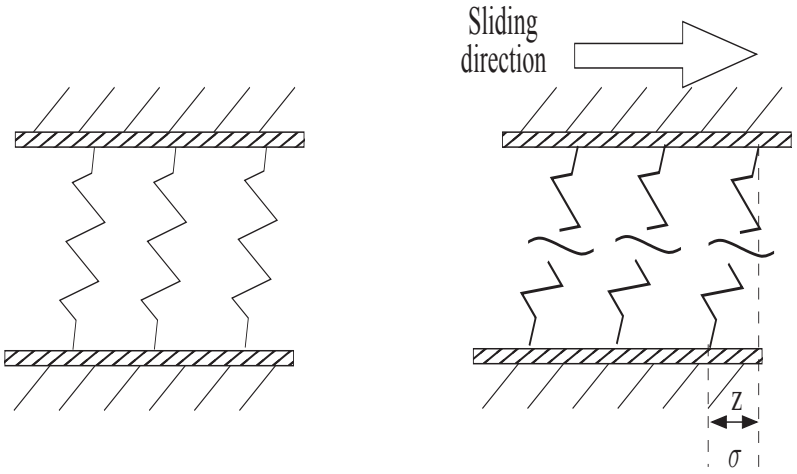

FIGURE 3.3. *Dahl friction model with stiffness coefficient between the sliding bodies*

$$\frac{dF_f}{dt} = \frac{dF_f}{dx}\frac{dx}{dt} = \sigma\left(1 - \frac{F_f}{F_c}.sgn(v)\right).v \tag{3.3}$$

Further simplifying the equation (3.3) by replacing $sgn(v).v = |v|$, Dahl model in the time domain will become,

$$\frac{dF_f}{dt} = \sigma\left(v - \frac{F_f}{F_c}.|v|\right) \tag{3.4}$$

This model is relatively easy to identify as compared to other friction models. This model generalizes the ordinary coulomb plus viscous friction model. Dahl model is represented in the state space form with the parameters σ, F_c and state variable z.

$$\begin{aligned} \dot{z} &= v - \frac{\sigma|v|}{F_c}z \\ F_f &= \sigma z \end{aligned} \tag{3.5}$$

The identification procedure for the parameters of the Dahl model, F_c and σ, is derived below.

3.3.2.2 DAHL MODEL IDENTIFICATION

Hysteresis in the pneumatic actuator system can be modeled using Dahl friction model with parameters σ and F_c. Fig. 3.4 shows the simulation results for friction within the actuator. The curve is obtained, for each value of diaphragm position, by discarding the rest of the forces in the actuator. The model's parameters are identified by analyzing the friction position curve and making the following two synthesis

- The stiffness constant σ is equal to the slope of the friction curve at the point when the friction is zero.

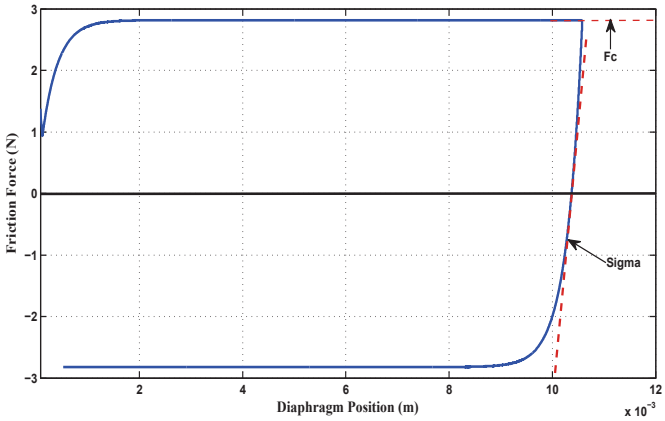

FIGURE 3.4. *Identification of friction parameters of the Dahl model*

- The maximum coulomb friction F_c is the point on the friction line when derivative of the curve dF_f/dx is zero. The values of the identified parameters are $F_c = 2.8N$ and $\sigma = 42150$.

3.3.2.3 THE LUGRE MODEL

The LuGre Friction model is a dynamic model, in the same direction as the Dahl model. It treats asperities as elastic bristles instead of springs. Motion, according to this model, occurs when the bristles start slipping [12]. It allows for the static friction to be modeled separately, and also incorporates Stribeck effect in the model [17, 65, 16]. The LuGre model considers friction as a function of the bristle displacement, bristle velocity and the system velocity.

$$\begin{aligned} F_f &= \sigma_0 z + \sigma_1 \dot{z} + f(v) \\ \dot{z} &= v - \sigma_0 \frac{|v|}{g(v)} z \end{aligned} \tag{3.6}$$

where z is the average deflection of the bristles before slipping, σ_0 is their stiffness coefficient and σ_1 is the damping coefficient which stabilizes the dynamics in the Stribeck region [12]. σ_2 is the coefficient of viscous friction. The $g(v)$ function models the Stribeck effect as a function of velocity. If v_s is the velocity at which stribeck effect takes place (Stribeck velocity), then $g(v)$ can be expressed as:

$$g(v) = \left(F_c + (F_s - F_c)\exp^{-(|v|/v_s)}\right) \tag{3.7}$$

v_s is the sliding speed coefficient which determines the stribeck curve and $g(v)$ is such that $F_c \leq g(v) \leq F_s$. As it can be seen that the LuGre friction model is the most comprehensive friction model, in our study we have used this model for simulation and modeling.

In Fig. 3.5, the friction force F_f and the function $g(v)$ are shown as a function of velocity. The LuGre model parameters, that form an arbitrary spring and damper system due the deflection of bristles between sliding surfaces, are shown in Fig. 3.5(b).

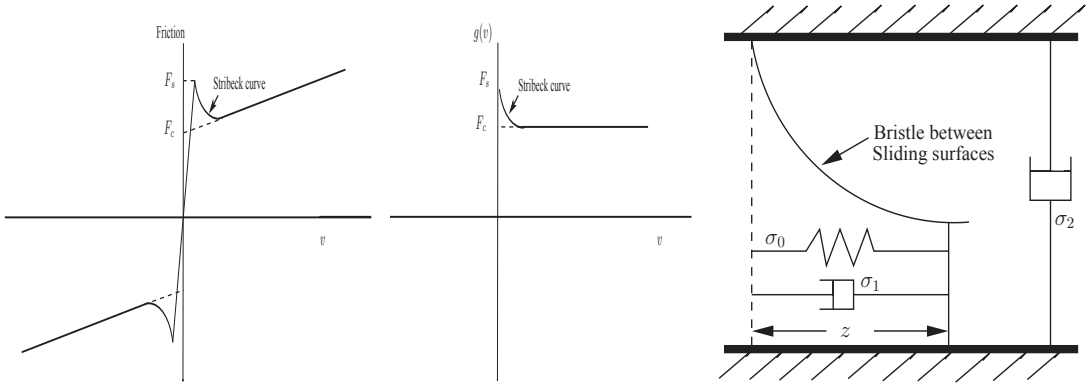

(a) (i) Friction vs. velocity, (ii) Function $g(v)$ that captures coulomb and stribeck friction (b) Parameters of the LuGre friction model

FIGURE 3.5. *LuGre friction model for diaphragm velocity (See equation* (3.6)*)*

3.3.2.4 LUGRE MODEL IDENTIFICATION

The identification of the LuGre model parameters requires some experiments. Considering the actuator force balance equation (2.34) in chapter 2 at the steady state ($\ddot{x}_d = 0$) and simplifying the LuGre model i.e $\dot{z} = 0$ (See [88] and [94] for more details), we obtain

$$F_{act} - F_{sm} = F_f = \sigma_0 z + \sigma_2 v \tag{3.8}$$

where F_{act} and F_{sm} are the applied force and spring equivalent force respectively. σ_0 and σ_2 are the only LuGre model parameters that act in this operation phase. Equation (3.6) can be simplified for $\dot{z} = 0$

$$\frac{dz}{dt} = v - \frac{\sigma_0}{g(v)} z|v| = 0 \tag{3.9}$$

Using above equation with equation (3.7), $g(v)$ can be eliminated and we obtain

$$\sigma_0 z = g(v) = \left(F_c + (F_s - F_c)\exp^{-(|v|/v_s)}\right)\frac{v}{|v|} \tag{3.10}$$

Applying to equation (3.8), the force balance equation can be re-written as

$$
\begin{aligned}
\dot{x}_1 &= x_2 \\
\dot{x}_2 &= \left[\left(p_{atm}A_{atm} - F_{mag} - b_p x_2 - p_{act}A_{act} - k_{mem}x_1 - p_{res}A_{res} - k^*_{s1}x_1\right)/m_p\right] \\
\dot{x}_3 &= x_4 \\
\dot{x}_4 &= \left[\left(\left(p_{atm} - x_7\right)A_d - b_d x_4 - \left(F_0 + k_{sm}x_3\right) - \sigma_0 x_5 - \sigma_1 \dot{x}_5 - \sigma_2 x_4 - F_{aero}\right)/m_d\right] \\
\dot{x}_5 &= x_4 - \sigma_0\left(|x_4|/g(x_4)\right)x_5 \\
\dot{x}_6 &= \left[x_6\frac{(\gamma-1)A_d x_4}{(V_0 - A_d.x_3)} + \left(\left(\gamma T_{atm} - x_6\right)\frac{\dot{m}_{act-in}}{x_8}\right) - \left(x_6\left(\gamma-1\right)\frac{\dot{m}_{act-out}}{x_8}\right)\right] \\
\dot{x}_7 &= \frac{Rx_6}{V_0 - A_d x_3}\left(\dot{x}_8\right) + \frac{x_7}{V_0 - A_d x_3}A_d x_4 \\
\dot{x}_8 &= \chi_{in}A_{eff(act-res)}x_7\sqrt{\frac{\gamma}{Rx_6}}.\Phi\left(\frac{p_{res}}{x_7}\right) - \chi_{out}A_{eff(atm-act)}p_{atm}\sqrt{\frac{\gamma}{RT_{atm}}}.\Phi\left(\frac{x_7}{p_{atm}}\right)
\end{aligned}
$$

$$
Where\ \Phi\left(p_r\right) = \begin{cases} \sqrt{\left\{\left(p_r\right)^{2/\gamma} - \left(p_r\right)^{(\gamma+1)/\gamma}\right\}\frac{2}{\gamma-1}}, & p_r \geq \left(\frac{2}{\gamma+1}\right)^{\gamma/\gamma-1} \\ \sqrt{\left(\frac{2}{\gamma+1}\right)^{\gamma+1/\gamma-1}} & , p_r \leq \left(\frac{2}{\gamma+1}\right)^{\gamma/\gamma-1} \end{cases} \tag{3.13}
$$

$$
F_{act} - F_{sm} = \left(F_c + \left(F_s - F_c\right)\exp^{-\left(|v|/v_s\right)}\right)\frac{v}{|v|} + \sigma_2 v \tag{3.11}
$$

Performing the test at two constant speeds, such that $v \gg v_s$, the above equation can be solved to find F_c and σ_2

$$
F_{act} - F_{sm} = F_c\frac{v}{|v|} + \sigma_2 v \tag{3.12}
$$

Once F_c and σ_2 have been identified through equation (3.12), equation (3.11) is used to determine F_s and v_s. The remaining two parameters (σ_0 and σ_1) are determined using non linear least squares approach. All parameters are given in appendix B.

A complete state space model of the electro-pneumatic actuator system is presented in the equation set (3.13). Here x_1, x_2, x_3, x_4, x_5, x_6, x_7 and x_8 are state variables for plunger position, plunger velocity, diaphragm position, diaphragm velocity, friction state, temperature, pressure and air mass inside the pneumatic actuator respectively.

3.4 AERODYNAMIC FORCE

The performance of the pneumatic actuator degrades when it is operated at different engine conditions. The reason of this behavior is the varying exhaust air pressure, which produces the aerodynamic force that acts as external perturbation. This force is then

transferred from turbocharger vanes to the pneumatic actuator via mechanical linkages. It is important to see its influence on the actuator performance. The significance of this force is that it increases the hysteresis loop of the actuator as a function of exhaust air pressure. Fig. 3.6 shows the experimental results for actuator hysteresis which are obtained at different exhaust air pressures.

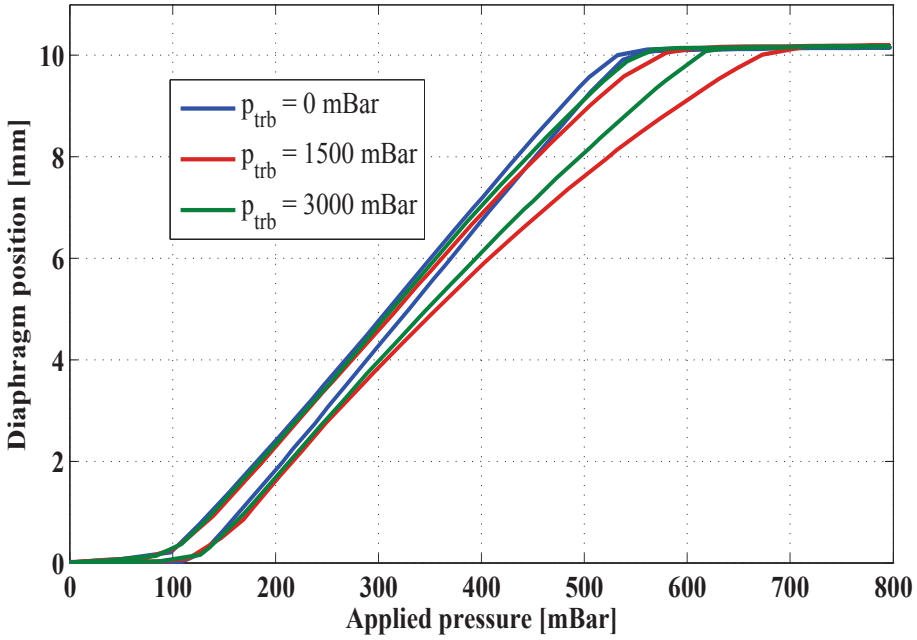

FIGURE 3.6. *The experimental results for the hysteresis observed in the pneumatic actuator for different exhaust air pressures*

Modeling of the aerodynamic force has not been addressed in the available literature, however some work has been done by Namba et al. [63] to predict the aerodynamic force on the oscillating blades. Before we address the modeling of this force, it is necessary to understand complex geometry of turbocharger. The vanes of the VGT are connected to a unison ring that moves them together. The unison ring is connected to the actuator linkage via the crank. This forms the transformation from linear to rotary motion. As the actuator diaphragm moves, the linear motion of the linkage rotates the crank, which in turn moves the unison ring. Fig. 3.7 shows a variable geometry turbocharger system with all the vanes and the reactional aerodynamic force.

The aerodynamic force depends on the vane angle as well as pressure of the exhaust gas entering and leaving the turbine. The turbocharger's vanes angle and actuator diaphragm displacement are related by a constant $\psi_{x_d} = 3.12$, which represents the vane angle for unit millimeter of the diaphragm displacement. Crank angle C_r is the sum of ψ_{x_d} times diaphragm position and minimum offset angle θ_{offset}. Equation (3.14) shows

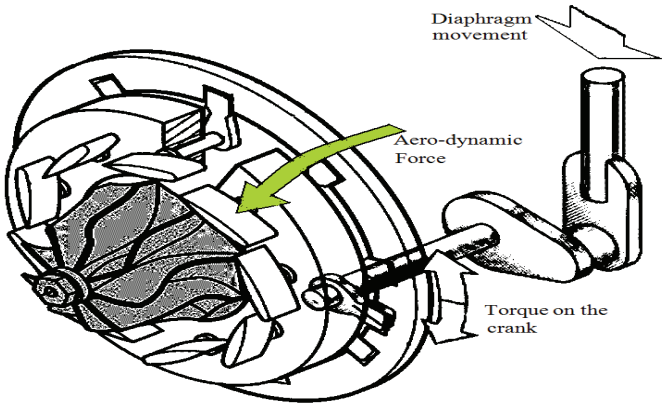

FIGURE 3.7. *A VGT system with vane and crank that convert translational diaphragm movement to rotational movement of the vanes*

the total crank angle for diaphragm position x_d.

$$C_r = \left[(x_{d-max} - x_d)\,\psi_{x_d} + \theta_{offset}\right] \tag{3.14}$$

The vanes are in open state at initial diaphragm position. The proposed approaches to determine aerodynamic force acting on these vanes are given below.

3.4.1 METHOD 1: AERODYNAMIC FORCE ESTIMATION USING FORCE SENSOR

In the first approach, a force sensor is used to determine aero-dynamic force. A force sensor is placed between diaphragm and unison ring. Force is determined at different vane/crank angles and pressure ratios across turbine. Experimental data is used to determine two dimensional polynomial to obtain this force using curve fitting technique. Surface fitting toolbox in Matlab is used to obtain polynomial function for aero-dynamic force. The polynomial function for the crank angle C_r and pressure ratio across the turbine p_{te} is shown in equation (3.15).

$$\begin{aligned} F_{aero}(C_r, p_{te}) = {} & 191 + 2.065C_r - 408.3p_{te} - 1.192C_r^2 + 14.65C_r.p_{te} + 261.5p_{te}^2 + \\ & 0.0385C_r^3 + 0.7C_r^2.p_{te} - 16.06C_r.p_{te}^2 - 47.88p_{te}^3 - 0.00029C_r^4 - 0.029C_r^3 p_{te} + 0.162C_r^2 p_{te}^2 + \\ & 3.38C_r p_{te}^3 - 7.78e-7C_r^5 + 2.25e-4C_r^4 p_{te} + 2.29e-3C_r^3 p_{te}^2 - 0.057C_r^2 p_{te}^3 \end{aligned} \tag{3.15}$$

Fig. 3.8 shows the relationship between the aero-dynamic force, crank angle and pressure ratio across turbine obtain through curve fitting technique.

The proposed model given in equation set (3.13) has been simulated in Matlab/Simulink along with the aerodynamic force provided in equation (3.15), which is a polynomial function of crank angle C_r and turbine inlet pressure p_{te}. Here, the crank angle must not be confused with crank shaft angle, which determines the engine speed. It is a linkage

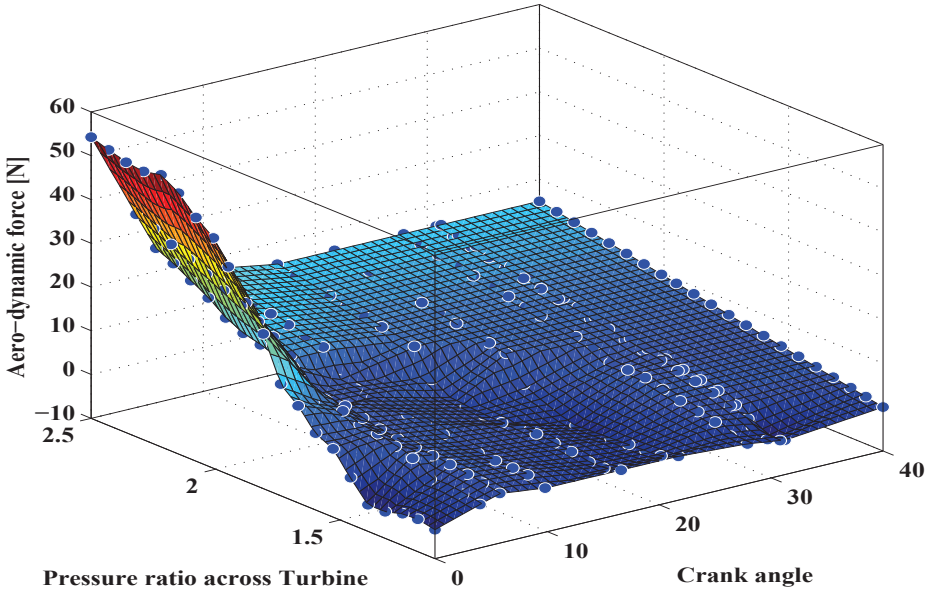

FIGURE 3.8. *Three dimensional plot showing the equivalent force on the vanes as a function of vane opening and pressure ration across turbine*

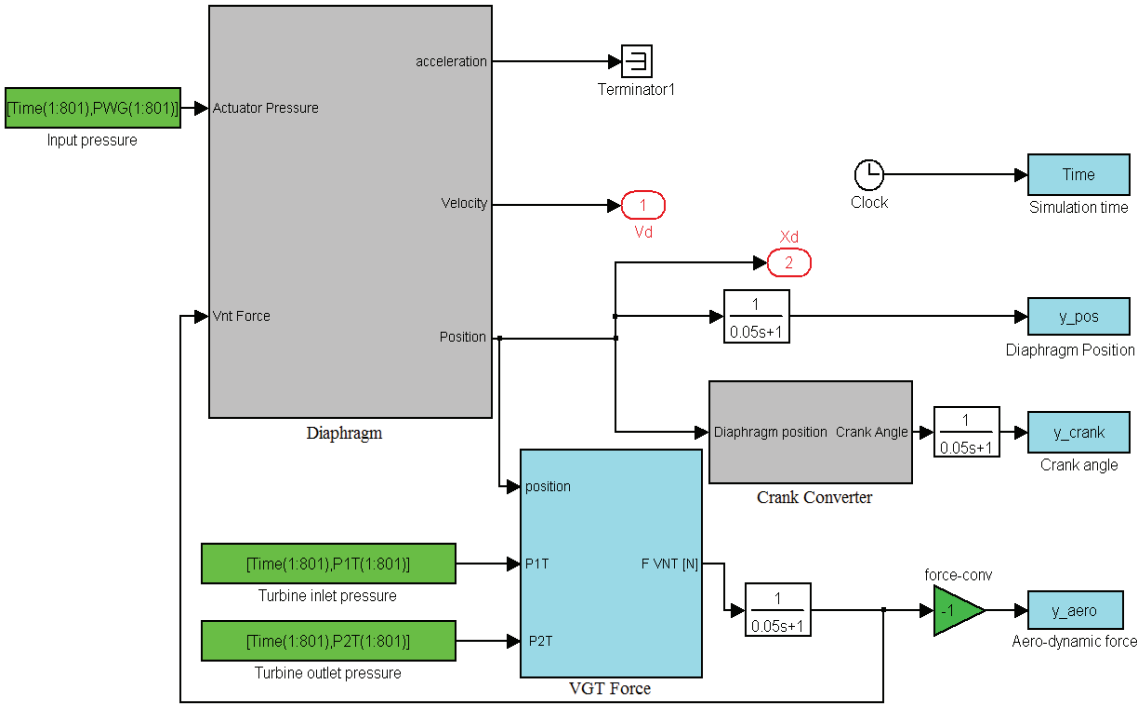

FIGURE 3.9. *Complete simulation model of electro-pneumatic actuator with aerodynamic forces*

between pneumatic actuator diaphragm and the turbocharger's unison ring. A simulation model is shown in the Fig. 3.9. The model contains three main blocks which are diaphragm, crank converter block and VGT force. The diaphragm block contains a pressure converter model, a pneumatic actuator model and the LuGre friction model. The LuGre friction model requires diaphragm velocity and it provides friction force as output. The pneumatic actuator model determines actuator position. The inputs to the block are applied pressure to the pneumatic actuator and aerodynamic force. The diaphragm block gives position as output which is provided to the crank converter block and VGT force block. The crank converter block determines the vanes angle from diaphragm position through a linear relationship, which is provided by constructor. The VGT force block calculates aerodynamic force acting on the actuator with two proposed methods i.e the polynomial function provided in equation (3.15) and aerodynamic force estimation by analyzing actuator's characteristics. The second method is explained in the next section. The input of the VGT force block are diaphragm position, turbine inlet and outlet pressures. At the end this simulator gives the diaphragm position, the crank angle and the aerodynamic force as final output. The output signals are filtered to improve the signal quality by passing them through a low pass filters.
It is observed that relationship between the aero-dynamic force, the crank angle and the pressure ratio is linear at higher values of the crank angle and different pressure ratios. The aero-dynamic force increases with increase in pressure ratio across turbine. Aerodynamic force is maximum when crank angle is zero i.e. the vanes are close and small amount of air can pass through the turbine impeller (blades).

3.4.2 METHOD 2: AERODYNAMIC FORCE ESTIMATION FROM HYSTERESIS

Aerodynamic force is represented here as a function of pressure at the inlet of the turbine and the crank angle. Experiments were carried out, on twenty different turbochargers for different inlet turbine pressures varying between $0mBar$ and $3000mBar$ gauge pressures. We determined the difference of hysteresis, for both back and forth movement of actuator diaphragm. This difference was determined in the form of pressure difference for same diaphragm position, at all available turbine pressures ($p_{trb} = XmBar$) and reference turbine pressure ($p_{trb} = 0mBar$) at the inlet. Moreover, this pressure difference is also determined for all diaphragm positions for a range of 0 to $10mm$. The diaphragm position is converted to vanes angle via a linear relationship provided in equation (3.14). The difference in actuator pressure at different exhaust gas conditions i.e. $\left[p_{act}(p_{trb} = XmBar) - p_{act}(p_{trb} = 0mBar)\right]$, multiplied with diaphragm area A_d gives us the aerodynamic force. The data so obtained is two dimensional. In Fig. 3.10 pressure difference Δp, is shown for corresponding crank angle and turbine pressures for both

opening and closing positions of the vanes.

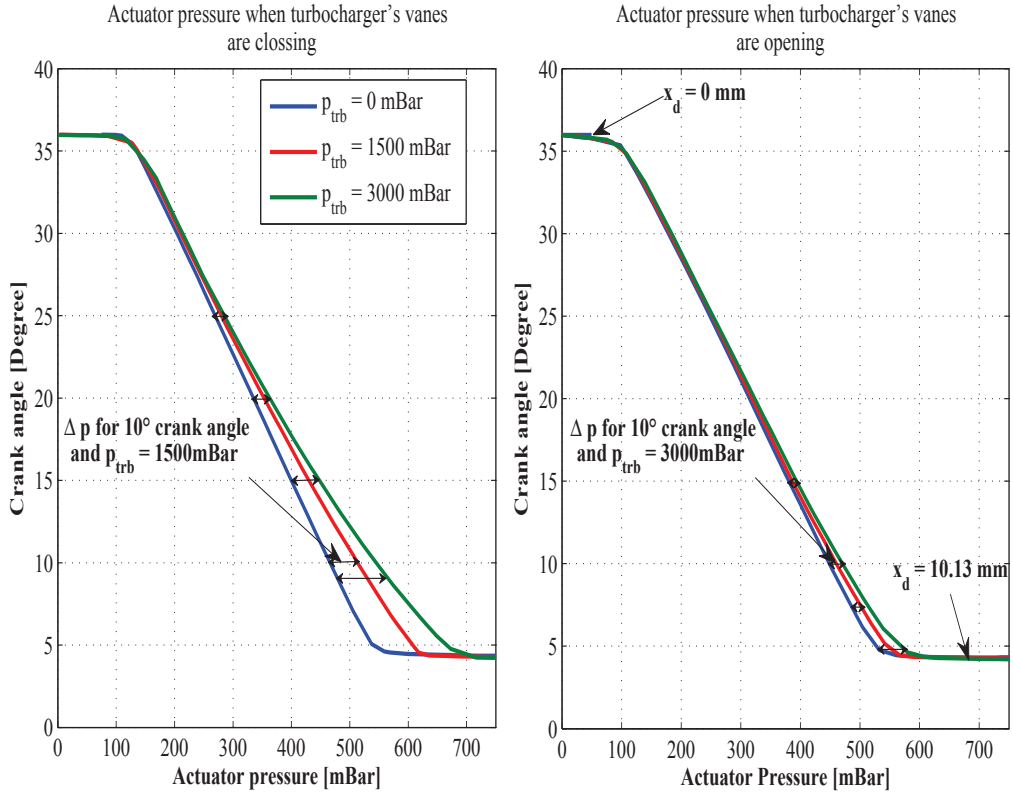

FIGURE 3.10. *Figure explaining Δp for all crank angles at different turbine pressures (a) when vanes are closing, (b) when vanes are opening*

The mathematical expression to determine aerodynamic force is given below

$$F_{aero} = \left[p_{act}(p_{trb} = XmBar) - p_{act}(p_{trb} = 0mBar)\right] * A_d = \Delta p * A_d \tag{3.16}$$

As explained above, aerodynamic force is a function of turbine pressure and crank angle. It depends on the direction of diaphragm movement, as well. Fig. 3.11 represents the force, when VGT vanes are closing from their open positions. Impact of aerodynamic force is different and more influential when vanes are closed than when they are opening (See Fig. 3.10(a)). This fitting is applied to the physical model to determine the change in actuator position for applied pressure.

Fig. 3.11 represents the aerodynamic force when vanes are closing. Similar procedure, as explained in equation (3.14), is followed to determine this force for turbocharger's vanes when they are opening from their closed position (See Fig. 3.10(b)). Fig. 3.12 shows the the fitting for aerodynamic force for this case.

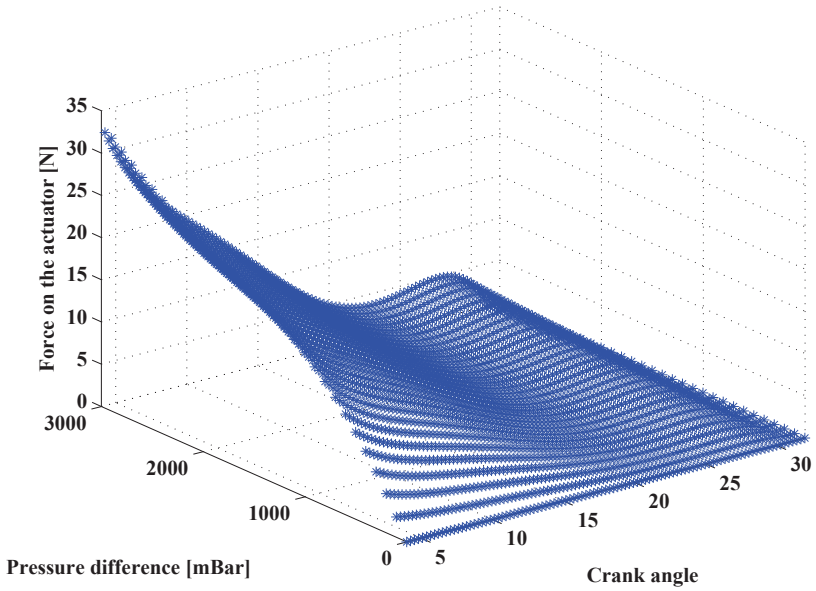

FIGURE 3.11. *Force acting on the diaphragm when vanes are closed from their opening position at equilibrium*

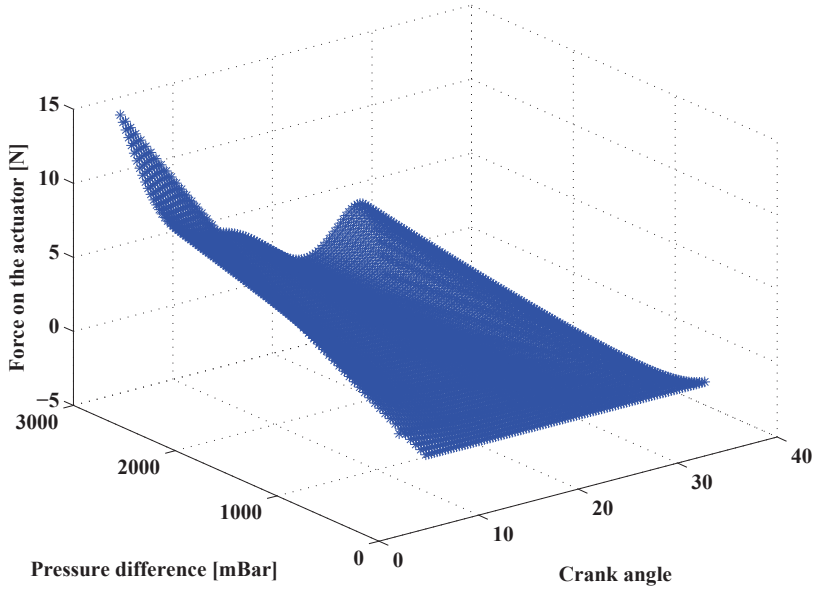

FIGURE 3.12. *Force on the diaphragm when vanes of VGT are opened from closed position*

Thence, an empirical model for aerodynamic force is developed for both back and forth motion of the turbocharger vanes, that depends upon the turbine pressure, crank angle and the sign function of diaphragm velocity.

$$F_{aero} = \Delta p\left(p_{trb}, C_r\right) * A_d * sign(\dot{x}_d) \tag{3.17}$$

3.4.2.1 ADAPTIVE LUGRE MODEL

As described above, partially known LuGre model parameters do not depict the cause of increase in hysteresis. Moreover, aerodynamic force acts as a viscus friction force on the actuator. Canudas et al. [11] introduced adaptive mechanism to deal with structured normal force and temperature variation. Inspired from their work, an adaptive LuGre model is proposed which is given in equation (3.18).

$$F_{f_t} = \hat{\theta} F_f \tag{3.18}$$

where $\hat{\theta}$ represents variation in the model parameters. We have obtained this adaptive friction model by considering that the aerodynamic force is a part of friction and it can be characterized by the variation in the LuGre model parameters.

$$F_{f_t} = F_f + F_{aero} = \left[1 + \frac{F_{aero}}{F_f}\right] F_f \tag{3.19}$$

where F_f $\left(\left(\sigma_0 z + \sigma_1 \dot{z} + f(v)\right)\right)$ is the friction force obtained from LuGre model. In the problem under discussion, an adaptive model is proposed as function of aerodynamic force. This model copes with variation of the full set of parameters. Furthermore, this variation is also the function of turbine pressure p_{trb} and vanes angle C_r.

$$\hat{\theta} = f\left(F_{aero}\right) = \left[1 + \frac{f\left(p_{trb}, C_r\right) sign(\dot{x}_d)}{F_f}\right] \tag{3.20}$$

Fig. 3.13 shows estimated friction for for different ramp signals when exhaust gas at the inlet of the turbocharger is varied from $0mBar$ to $3000mBar$.

3.5 METHOD 3: ONE DIMENSIONAL CFD MODEL

The aerodynamic force models obtained previously, are based on the experiments or characteristic maps provided by the constructor. Therefore, we require a model which can be generalized for all type of turbochargers. The objective of this work is to obtain a one dimensional flow model of the exhaust gas entering into the turbine, which can predict the aerodynamic force without performing expensive tests on the turbocharger.

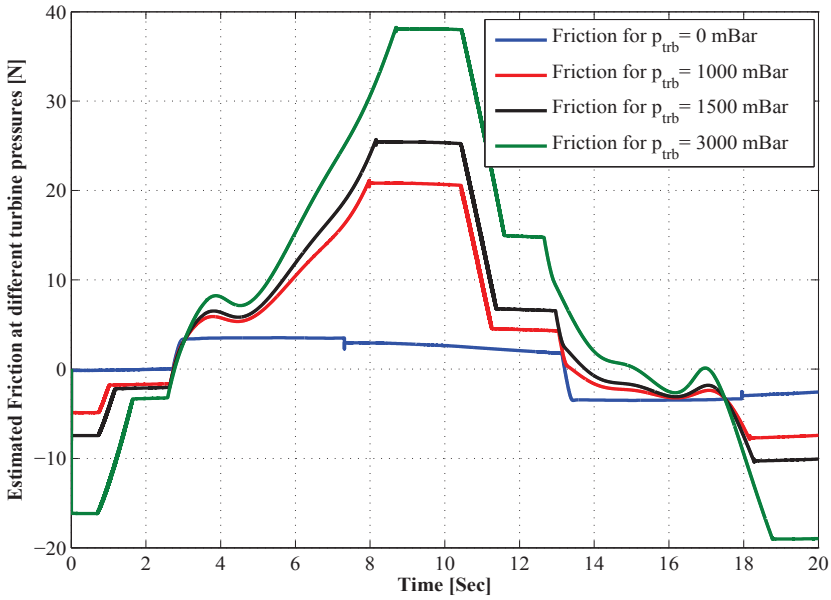

FIGURE 3.13. *The estimated friction force using adaptive LuGre model for a ramp test*

3.5.1 HYPOTHESIS AND PROBLEM FORMULATION WITH NAVIER-STOKES EQUATION

The Navier-Stokes equations can be used to model the aerodynamic force exerted by the exhaust gases coming from the exhaust manifold and passing through the turbocharger. These equation represents the conservation laws for mass, energy and momentum of the fluid in all directions. The Navier-Stokes equations can be reformed to obtain 1D model of the fluid with some assumptions on the fluid's direction of flow. The velocity vector for fluid is $\overrightarrow{V} = [V_m\, V_u\, V_l]^T$ with condition that the velocity of the fluid in the vertical direction is zero $V_l = 0$. Henceforth, we can apply following simplification to consider the one dimensional fluid flow.

$$\iiint dv = \int S dm \tag{3.21}$$

Here m, u and l are the axis representing the meridional, tangential and vertical direction of the fluid, respectively. The term S is the cross section of the channel through which fluid is passing and $dv = dm\,du\,dl$

For the perfect gas the tenser for the viscus forces can be consider as equal to zero i.e. $\overrightarrow{\overrightarrow{\tau_f}} = \overrightarrow{\overrightarrow{0}}$.

Additionally, for initial development of Navier-Stokes equations, it is consider that external source terms $Q_{ext} = 0$. But, later they will be considered to obtain final matrix

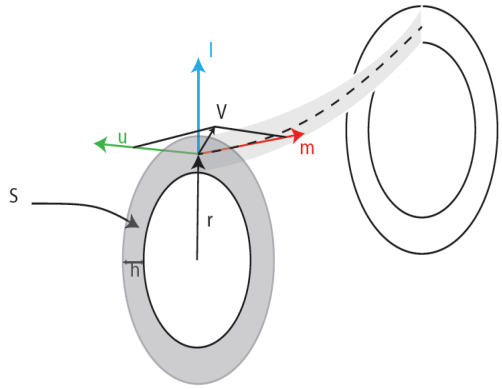

FIGURE 3.14. *Flow of air through a vein with all 3 dimensional velocity components*

form. With the assumptions about the velocity vector $\vec{V}$ described above, the following equation set can be obtained

$$
\begin{aligned}
div(\vec{V}) &= \frac{1}{S}\frac{\partial S V_m}{\partial m} \\
\overrightarrow{grad}(x) &= \begin{bmatrix} \frac{\partial x}{\partial m} \\ 0 \\ 0 \end{bmatrix} \\
\overrightarrow{rot}(\vec{V}) \wedge \vec{V} &= \begin{bmatrix} -\frac{V_u}{r}\frac{\partial r V_u}{\partial m} \\ \frac{V_m}{r}\frac{\partial r V_u}{\partial m} \\ 0 \end{bmatrix} \\
\overrightarrow{grad}(\frac{V^2}{2}) &= \begin{bmatrix} V_u\frac{\partial V_u}{\partial m} + V_m\frac{\partial V_m}{\partial m} \\ 0 \\ 0 \end{bmatrix} \\
\frac{d\phi}{dt} &= \frac{\partial \phi}{\partial t} + \vec{V}\cdot\overrightarrow{grad}(\phi) \\
\frac{d\vec{V}}{dt} &= \frac{\partial \vec{V}}{\partial t} + rot(\vec{V}) \wedge \vec{V} + \overrightarrow{grad}\left(\frac{V^2}{2}\right)
\end{aligned}
\tag{3.22}
$$

3.5.2 MODEL DERIVATION

A physical interpretation of the 1D equations is the study of fluid flow in a thin tube or a narrow channel. It also permit us to analyze the properties of the fluid; velocity, density and energy change only along the tube or the channel. The law of conservation of mass for a fluid can be derived from the Navier-Stokes equation. The equation is also known

as the continuity equation and it is given below [34]

$$\iiint \left(\frac{\partial \rho}{\partial t} + div\left(\rho \vec{V}\right) \right) dv = 0 \tag{3.23}$$

By using the assumption (3.21)

$$\int \left(\frac{\partial S\rho}{\partial t} + Sdiv\left(\rho \vec{V}\right) \right) dm = 0 \tag{3.24}$$

In the differential form, the above equation will become

$$\frac{\partial S\rho}{\partial t} + \frac{\partial S\rho V_m}{\partial m} = 0 \tag{3.25}$$

The terms ρ and V_m are the density and meridional velocity of the fluid, respectively. The momentum equation is based on the principle of conservation of momentum, i.e. the time rate of change of momentum in a region is equal to the sum of the forces on that region.

$$\iiint \rho \frac{d\rho \vec{V}}{dt} dv = \iiint \rho \vec{F} dv + \iiint \frac{1}{\rho} \overrightarrow{grad}(p) + \frac{1}{\rho} div(\vec{\tau_f}) dv \tag{3.26}$$

Above equation is rewritten into one dimensional form by using assumption (3.21)

$$\int \frac{d\rho S\vec{V}}{dt} dm = \int S\rho \vec{F} dm - \int \overrightarrow{grad}(Sp) dm \tag{3.27}$$

By integrating the above equation and writing it in the differential form

$$\frac{\partial S\rho \vec{V}}{\partial t} = -S\rho.rot(\vec{V}) \wedge \vec{V} - \rho S.\overrightarrow{grad}\left(\frac{V^2}{2}\right) - S.\overrightarrow{grad}(p) - \vec{V}\frac{\partial S\rho}{\partial t} \tag{3.28}$$

In the derivation it is also assumed that the fluid have only tangential V_u and meridional V_m components of the velocity. Therefore, the momentum equation obtained by the equivalent meridian velocity (velocity of fluid in the direction of fluid flow) is given below

$$\frac{\partial S\rho V_m}{\partial t} + \frac{\partial S\rho \left(p/\rho + V_m^2\right)}{\partial m} = S\rho \frac{V_u^2}{r} \frac{\partial r}{\partial m} + p\frac{\partial S}{\partial m} \tag{3.29}$$

The momentum equation (3.28) can be rewritten for the tangential component of the velocity. This expression is given by the following equation

$$\frac{\partial S\rho V_u}{\partial t} + \frac{\partial S\rho V_m V_u}{\partial m} = -S\rho \frac{V_m V_u}{r} \frac{\partial r}{\partial m} \tag{3.30}$$

Fig. 3.15 shows the direction of fluid through a variable geometry turbocharger. Cartesian components of the velocity are also shown in this figure. The direction of air flow

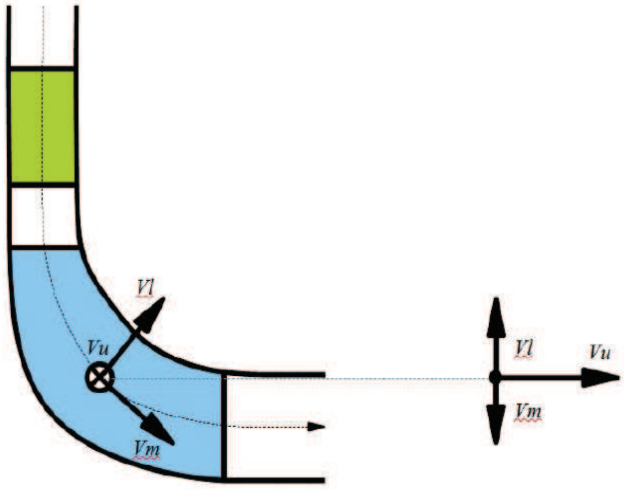

FIGURE 3.15. *Flow of air through a turbocharger, with all velocity components*

at the turbine outlet is perpendicular to the flow at inlet, which indicate that the VGT is mixed flow type turbocharger.

where m represents the unit distance of fluid in the direction of flow and r is the reditus of the fluid channel. The conservation of energy, like conservation of mass and momentum, represents that total energy in a fluid remain constant. The total energy of the fluid can be obtained by integrating it in all three directions

$$\iiint \rho \frac{de^0}{dt} dv = \iiint \rho \vec{F}.\vec{V}\, dv + \iiint -div\left(p\vec{V}\right) - \overrightarrow{grad}(p).\vec{V} + div(\vec{\tau}_f).\vec{V} + \vec{\tau}_f.\overrightarrow{\overrightarrow{grad}}(\vec{V}) dv + Q_{ext} \tag{3.31}$$

The energy balance equation for one dimensional fluid flow can be obtained by using assumption (3.21)

$$\int \rho S \frac{\partial e^0}{\partial t} dm = \int \rho S\vec{F}.\vec{V}\, dm - \int S.div\left(p\vec{V}\right) + S\overrightarrow{grad}(p).\vec{V}\, dm - \int \rho S\overrightarrow{grad}(e^0).\vec{V}\, dm \tag{3.32}$$

Writing the above equation in the differential form by using the mathematical derivations given in equation set (3.22)

$$\frac{\partial}{\partial t}\left(S\rho e^0\right) + S\rho V_m \frac{\partial e^0}{\partial m} + e^0 \frac{\partial S\rho V_m}{\partial m} + V_m S \frac{\partial p}{\partial m} + S\frac{\partial pV_m}{\partial m} = 0 \tag{3.33}$$

With further simplifications

$$\frac{\partial}{\partial t}\left(S\rho e^0\right) + \frac{\partial S\rho V_m\left(\frac{p}{\rho} + e^0\right)}{\partial m} = 0 \tag{3.34}$$

Finally, by simplifying the above equation we get the following equation for energy of the fluid

$$\frac{\partial S e^0 \rho}{\partial t} + \frac{\partial S \rho V_m h^0}{\partial m} = -S\rho\Omega \frac{V_m V_u \partial r}{\partial m} \tag{3.35}$$

where e^0 and h^0 are the total energy and enthalpy of the fluid. Equations (3.25), (3.29), (3.30) and (3.35) can be combined together and can be written in the non-dimensional vector form

$$\frac{\partial U}{\partial t} + \frac{\partial E}{\partial m} = Q \tag{3.36}$$

where U, E and Q are conservative variable vector, flux vector and the source term vectors, respectively. In the vector from these terms are given as

$$U = \begin{bmatrix} \rho S \\ \rho V_m S \\ \rho V_u S \\ \rho e^0 S \end{bmatrix}, \quad E = \begin{bmatrix} \rho V_m S \\ \left(p + \rho V_m^2\right) S \\ \rho V_m V_u S \\ \rho V_m h^0 S \end{bmatrix}, \quad \text{and} \quad \mathrm{Q} = \begin{bmatrix} 0 \\ S\rho \dfrac{V_u W_u}{r} \dfrac{\partial r}{\partial m} + p \dfrac{\partial S}{\partial m} \\ -S\rho \dfrac{V_m V_u}{r} \dfrac{\partial r}{\partial m} \\ -S\rho V_m V_u \Omega \dfrac{\partial r}{\partial m} \end{bmatrix} \tag{3.37}$$

Let $U = [U_0\, U_1\, U_2\, U_3]^T$, then the conservative flux vector E can be written as a function of components of the vector U. By rewriting the flux vector

$$\begin{aligned} E_0 &= U_1 \\ E_1 &= (\gamma - 1)\left(U_3 - \frac{1}{2}\left(\frac{U_1^2}{U_0} + \frac{U_2^2}{U_0}\right)\right) + \frac{U_1^2}{U_0} \\ E_2 &= \frac{U_1 U_2}{U_0} \end{aligned}$$

The last term of vector E needs some development. The total enthalpy h^0 of the fluid can be written as a function of its total kinetic energy at that particular point

$$h^0 = e^0 + \frac{p}{\rho} \tag{3.38}$$

with total energy e^0

$$e^0 = C_v t + \frac{1}{2} V^2 \tag{3.39}$$

where C_v, t and V are the specific heat at constant volume, temperature of the gas and the sum of its meridional and tangential velocities, respectively. By using the perfect gas equation $\frac{p}{\rho} = r t$ and $C_v = \frac{r}{\gamma - 1}$, with γ and r are specific heat ratio and universal gas constant

$$e^0 = \frac{1}{(\gamma - 1)} \frac{p}{\rho} + \frac{1}{2}(V_m^2 + V_u^2) \tag{3.40}$$

by introducing the expression for speed of sound $a^2 = \frac{\gamma p}{\rho}$, in equation (3.40), the total energy will become

$$e^0 = \frac{a^2}{\gamma(\gamma-1)} + \frac{1}{2}(V_m^2 + V_u^2) \tag{3.41}$$

Finally, the total kinetic energy of the fluid for the both tangential and meridional components of velocities is given by

$$\frac{1}{2}(V_m^2 + V_u^2) = \frac{1}{2}\left(\left(\frac{U_1}{U_0}\right)^2 + \left(\frac{U_2}{U_0}\right)^2\right) \tag{3.42}$$

The term for pressure, by using perfect gas and equation $h^0 = e^0 + \frac{p}{\rho}$

$$p = (\gamma-1)\left(U_3 - \frac{1}{2}\left(\frac{U_1^2}{U_0} + \frac{U_2^2}{U_0}\right)\right) \tag{3.43}$$

Finally the conservative flux vector E can be represented as a function of U by the following expression

$$E = \begin{bmatrix} U_1 \\ (\gamma-1)\left(U_3 - \frac{1}{2}\left(\frac{U_1^2}{U_0} + \frac{U_2^2}{U_0}\right)\right) + \frac{U_1^2}{U_0} \\ \frac{U_1 U_2}{U_0} \\ \left(\gamma U_3 - \frac{\gamma-1}{2}\left(\frac{U_1^2}{U_0} + \frac{U_2^2}{U_0}\right)\right)\frac{U_1}{U_0} \end{bmatrix} \tag{3.44}$$

The main objective to write the flux vector E as a function of U is to obtain the Jacobian flux vector A. This vector will help us to find the numerical solution of equation (3.36). The Jacobian vector is obtained by taking the partial derivative of E with respect to U [46], i.e $A = \frac{\partial E}{\partial U}$

$$A = \begin{bmatrix} 0 & 1 & 0 & 0 \\ \frac{(\gamma-3)V_m^2 + (\gamma-1)V_u^2}{2} & -(\gamma-3)V_m & -(\gamma-1)V_u & \gamma-1 \\ -V_m V_u & V_u & V_m & 0 \\ \left(\frac{\gamma-2}{2}(V_m^2+V_u^2) - \frac{a^2}{\gamma-1}\right)V_m & \frac{a^2}{\gamma-1} - \frac{2\gamma-3}{2}V_m^2 - \frac{V_u^2}{2} & -(\gamma-1)V_m V_u & \gamma V_m \end{bmatrix} \tag{3.45}$$

3.5.3 SOURCE TERMS

The source terms in the Euler equations are used to represent the influence of the blade rows and the flow-path on the fluid. The source terms vector Q is the vector of all contributions which were initially neglected in the derivation. It may be further divided into four distinct categories by their physical meanings

$$Q = Q_g + Q_b + Q_f + Q_c \tag{3.46}$$

where Q_c is the cooling source term and it is neglected in this derivation i.e. $Q_c = 0$. The other terms, for example Q_g, Q_b and Q_f are the source terms due to the geometry of the volute, impeller blade force and viscus friction, respectively. These terms are described below

3.5.3.1 GEOMETRY OF THE FLOW-PATH

The source term Q_g, represents the variation in fluid velocities and pressure drop across the exhaust air flow-path. The air flow direction through the vein between the exhaust manifold and the turbocharger is shown in Fig. 3.15, where r represents the mean-line radius. This term can be obtained by considering the right hand side of equations (3.25), (3.29), (3.30) and (3.35). The final form of geometrical source term is given by

$$Q_g = \begin{bmatrix} 0 \\ S\rho \dfrac{V_u V_u}{r} \dfrac{\partial r}{\partial m} + p \dfrac{\partial S}{\partial m} \\ -S\rho \dfrac{V_m V_u}{r} \dfrac{\partial r}{\partial m} \\ 0 \end{bmatrix} \tag{3.47}$$

3.5.3.2 BLADE SOURCE TERMS

This term is implemented to represent the isentropic influence of blade rows. The force applied by the blades onto the fluid can be deduced from the knowledge of the velocity triangles. An angular momentum balance over the blade row provides the tangential component of the blade force. Here we use the tangential velocities along the blade deflection induced by the given component for $\tilde{V}_u$.

$$\tilde{V}_{u\,i} = \frac{V_{m\,i}}{tan(\alpha_i)} \tag{3.48}$$

where α_i is the angle of the fluid with respect to blade comber line. By writing the Euler equation and the equation of variation in energy, we get

$$r_i F_{bu\,i} \Omega = \left(r_i \Omega \tilde{V}_{u\,i} - r_{i-1} \Omega V_{u\,i-1} \right) \frac{q_m}{S_i (m_i - m_{i-1})} \tag{3.49}$$

where Ω is the angular velocity of the blades. The blade force in the tangential direction is given by

$$F_{bu\,i} = \left(r_{i1} \tilde{V}_{u\,i} - r_{i-1} V_{u\,i-1} \right) \frac{q_m}{S_i r_i (m_{i+1} - m_{i-1})} \tag{3.50}$$

The forces acting on the blade are perpendicular to the referential velocity $\overrightarrow{W}$. Henceforth, it can be assumed that the axial and tangential forces do not generate losses

$$F_{bmi}W_{mi} + F_{bui}W_{ui} = 0 \tag{3.51}$$

where W_m is the relative velocity vector. By analyzing the velocity triangles for the fluid through the single stage turbocharger, it can be deduced that in the meridional direction relative meridional velocity is equal to the absolute velocity, thence $W_m = V_m$. Therefore, the blade force in the meridional direction is given by

$$F_{bmi} = -F_{bui}\frac{W_{ui}}{V_{mi}} \tag{3.52}$$

The source term related to the action of impeller blade on the turbocharger vanes is given below

$$Q_{bi} = \begin{bmatrix} 0 \\ F_{bmi}S_i \\ F_{bui}S_i \\ r_i\Omega F_{bui}S_i \end{bmatrix} \tag{3.53}$$

3.5.3.3 FRICTION SOURCE TERMS

In the Euler equations, the entropy production is due to a separate distributed friction force F_f in the momentum equations. This force causes the loss in fluid pressure when it moves through the channel. The pressure drop due to this friction may cause the variation in momentum and energy loss in the fluid. This friction force is aligned with the relative velocity by the following expression. The negative sign indicate that it has the opposite direction

$$\overrightarrow{F_f} = -\left|\overrightarrow{F_f}\right|\frac{\overrightarrow{W}}{\left|\overrightarrow{W}\right|} \tag{3.54}$$

The change in entropy of the fluid can be represented by the following formula

$$\Delta s = -R\,ln\,(1-\zeta) \tag{3.55}$$

where R is the gas constant and ζ represents the pressure losses due to profile, play in the turbine geometry and secondary effects. The force related to these losses can be evaluated from the Gibbs relation, which is given below

$$\left|\overrightarrow{F_f}\right| = \rho\, t\frac{\Delta s}{\Delta m} \tag{3.56}$$

To obtain the source term that contains the momentum and energy equations can be determined from the axial and tangential components of the friction force.

$$F_{fm} = \rho t \frac{R\,ln\,(1-\zeta)}{\Delta m} \frac{V_m}{\sqrt{V_m^2 + (V_u - r\Omega)^2}} \tag{3.57}$$

where Δm is the small step size in the meridional direction. The tangential component of the force is given by

$$F_{fu} = \rho t \frac{R\,ln\,(1-\zeta)}{\Delta m} \frac{V_u - r\Omega}{\sqrt{V_m^2 + (V_u - r\Omega)^2}} \tag{3.58}$$

The source term related to friction forces is given by the following expression

$$Q_{fi} = \begin{bmatrix} 0 \\ F_{fmi} S_i \\ F_{fui} S_i \\ r_i \Omega F_{fui} S_i \end{bmatrix} \tag{3.59}$$

3.5.3.4 PRESSURE LOSSES

As described previously, the source term obtained from friction depends upon the pressure losses in the turbocharger. These losses are mainly due to the turbine geometry, play in its components and some secondary effects. In reference [2] two different methods are presented to determine these losses. These methods are described below

INTERPOLATION BASED METHOD

The pressure losses in the vanes increase The losses due to tip clearance in a blade row of a turbine increases , which results in a decrease of turbine efficiency. The gas mass flow and the power output corresponding to a fixed turbine speed and pressure ratio also change. Typical profile losses on conventional blades intermediate between nozzle and impulse blades may be interpolated in the following manner

$$\zeta_p = \left(Y_{p(\beta_1=0)} + \left(\frac{\beta_1}{\alpha_2} \right)^2 \left(Y_{p(\beta_1=-\alpha 2)} - Y_{p(\beta_1=0)} \right) \right) \left(\frac{ep}{0.2c} \right) \tag{3.60}$$

where ep is the pitch to chord ratio. The term Y_p represents the profile losses at different inlet angles for blades. These losses are determined through the mapping between inlet and outlet angles for both the blade and fluid: and the profile. Stodola quoted a simplified method to determine the losses associated with the tip clearance. The formula to determine clearance losses is given by

$$\zeta_t = 6.26\frac{k^{1.4}}{h_c} \tag{3.61}$$

where h_c is the blade hight and k is the radial clearance. In this approach the secondary losses are neglected, therefore we considered that

$$\zeta_s = 0 \tag{3.62}$$

ANGLE RATIO BASED METHOD

In this method, the profile losses are determined with more sophisticated and more precise model. It depends upon the ratio of angles α_2 and β_1 (See [98] and [2] for more detail)

$$\zeta_{p(\delta i=0)} = \left(Y_{p(\beta_1=0)} + \left(\frac{\beta_1}{\alpha_2}\right)^2 \left(Y_{p(\beta_1=-\alpha 2)} - Y_{p(\beta_1=0)}\right)\right)\left(\frac{ep}{0.2c}\right)^{-\frac{\beta_1}{\alpha_2}} \tag{3.63}$$

with $Y_{p(\beta_1=0)}$ and $Y_{p(\beta_1=-\alpha_2)}$ are obtained from the maps between pitch to chord ratio and profile loss coefficient. The pressure losses due to blade tip clearance ζ_t is given by the following equation

$$\zeta_t = 0.5\frac{k}{h_c}\left(\frac{C_L}{\frac{s}{c}}\right)^2 \frac{cos(\alpha_2)^2}{cos(\alpha_m)^3} \tag{3.64}$$

where C_L is the lift coefficient. The term α_m is the mean gas angle. Its expression for this angle is given in [34]

$$\zeta_s = \lambda\left(\frac{C_L}{\frac{s}{c}}\right)^2 \frac{cos(\alpha_2)^2}{cos(\alpha_m)^3} \tag{3.65}$$

with $\lambda = f\left(\frac{\left(\frac{A_2}{A_1}\right)^2}{1+\frac{I.D}{O.D}}\right)$ is the ratio of drag and lift coefficient. It can also be mapped by the ratio of inlet and outlet flow area
Here $I.D = r - \frac{h_c}{2}$ and $O.D = r + \frac{h_c}{2}$. The inlet and outlet flow area depends on the blade inlet and the fluid outlet angle

$$\begin{aligned} A_1 &= A_{n0}cos(\beta_1) \\ A_2 &= A_{n2}cos(\alpha_2) \end{aligned} \tag{3.66}$$

The ratio $\frac{C_L}{\frac{s}{c}}$ can also be represented as a function of fluid inlet, outlet and mean angle. So, its expression in equation (3.65) can be replaced by following equation

$$\frac{C_L}{\frac{s}{c}} = 2\left(tan(\alpha_1) - tan(\alpha_2)\right)cos(\alpha_m) \tag{3.67}$$

3.5.4 EQUATION SOLVER

Equation (3.36) represents one dimensional fluid flow equation in the form of a matrix, which can be transformed into discrete domain to obtain its numerical solution. For the numerical simulations explicit or implicit approaches may be used to solve time-dependent partial differential equations. The only difference between both the approaches is that explicit method calculates the solution of a system at a later time from its state at the current time, while implicit methods find a solution by involving both the current state of the system and the later one [60]. Therefore, the implicit method require extra calculation, however it solve the equations with minimal error. Thence, the implicit form of the equation (3.36) has been used to solve the problem (see [34] for more details),

$$\frac{\Delta U}{\Delta t} + \left(\frac{\partial E}{\partial m}\right)^{(n+1)} - Q^{(n+1)} = 0 \tag{3.68}$$

Using the Taylor series expansion, equation (3.68) can be simplified to obtain the following equation

$$\frac{\Delta U}{\Delta t} + \frac{\partial}{\partial m}\left(E^{(n)} + \frac{\partial E^{(n)}}{\partial U}\Delta U\right) - \left(Q^{(n)} + \frac{\partial Q^{(n)}}{\partial U}\Delta U\right) = 0 \tag{3.69}$$

Considering the jacobian of Q, i.e. $B = \dfrac{\partial Q}{\partial U}$, and separating the terms to obtain the implicit form of equation. This form can be rearrange to obtain the block triangle form of the equation (3.70)

$$\left(I + \Delta t\left(\frac{\partial A^{(n)}}{\partial m} - B^{(n)}\right)\right)\Delta U = \Delta t\left(\frac{\partial E^{(n)}}{\partial m} - Q^{(n)}\right) \tag{3.70}$$

For a steady state simulation, a time marching solver allows the system to evolve toward a stationary solution [98]. By considering the initial conditions for density ρ, meridian V_m and tangential velocities V_u and total pressure p_0 of the fluid, we can determine the meridional and tangential forces acting on the vanes by the following equation. The terms h and s are the hight and distance between two vanes.

$$\begin{aligned}\frac{dF_u(m)}{dm} &= \rho(m)V_m(m)hs(m)\frac{\partial V_u}{\partial m}\\ \frac{dF_m(m)}{dm} &= \rho(m)V_m(m)hs(m)\frac{\partial V_m}{\partial m}\end{aligned} \tag{3.71}$$

These forces can transferred to the crank which is joining the mechanical part of turbocharger with actuator's stem. The following illustration shows that how the torque generated on the vanes is transformed to the aerodynamic force, acting on the actuator.

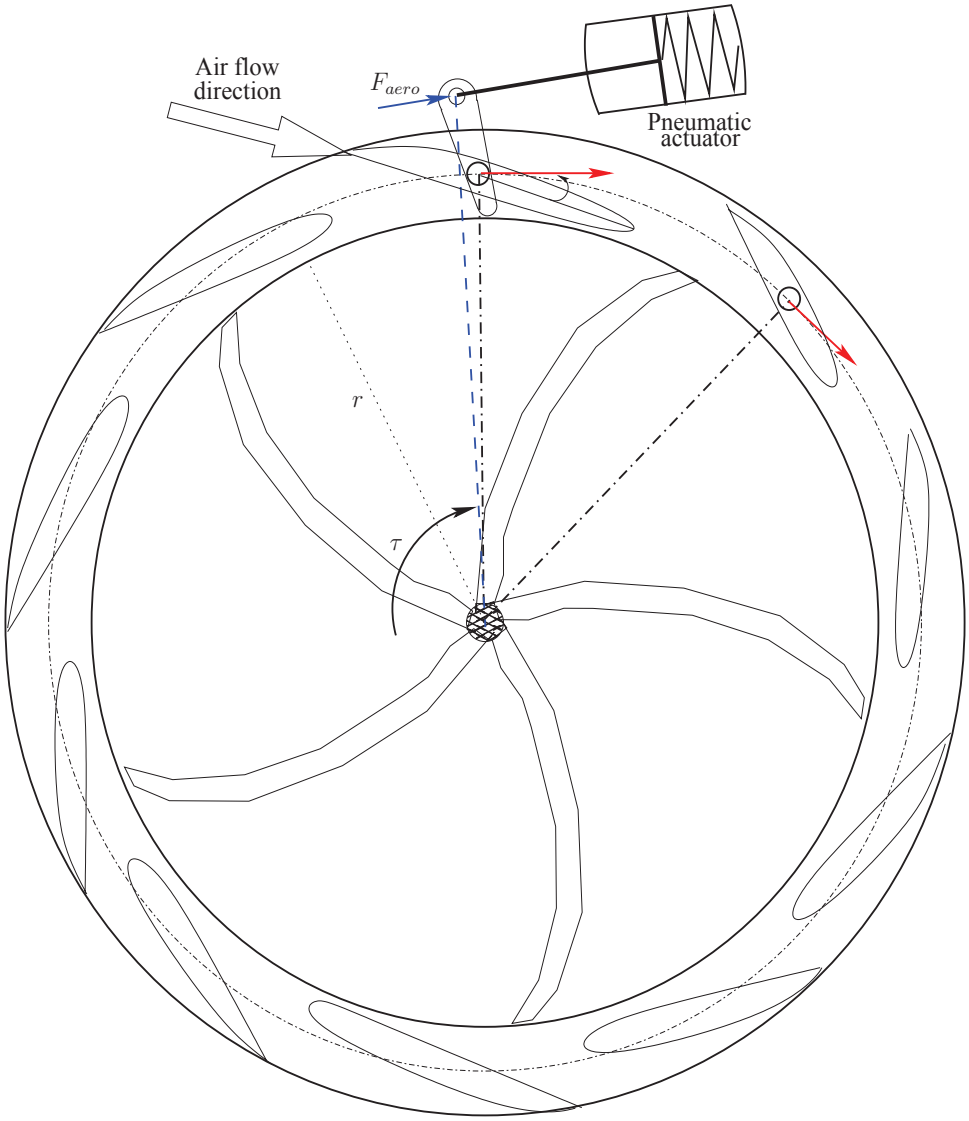

FIGURE 3.16. *A mixed flow turbocharger with aerodynamic force as a sum of torque acting on each vane*

The total torque acting on the crank is the sum of all the torques acting on the each vane. Torque on each vane is the vector product of displacement vector $\vec{r}$ and vector sum of meridional and tangential forces $\vec{F}$.

$$\vec{\tau} = \sum_{i=1}^{n} \vec{r}_i \Lambda \vec{F}_i \tag{3.72}$$

The mechanistic model developed here may need more refinement, because we have considered some assumptions while deriving this model. Moreover, the loses due to cooling source term are neglected. The development of this new one dimensional model is currently in progress. The results for the aerodynamic forces will be included in the future work. However, we have shown the results for two different techniques to estimate the

aerodynamic force which are based upon the actuator characteristics or force sensor information.

3.6 COMPLETE MODEL VALIDATION

In the previous chapter, tests were carried out in cold conditions to rule out the effects of aerodynamic force. In order to validate the complete model with friction and aerodynamic force, tests were carried out on an industrial diesel engine test bench, installed with Honeywell Garrett (GTB1244VZ) turbocharger. The complete test bench of commercial diesel engine DV6TED4, is shown in Fig. 3.17 where VGT system is shown, separately. The maximum displacement of this actuator is $10.13mm$, which allows movement of the vanes in the range of 48^o. This bench is used for the tests at different engine load and speeds, e.g. working of the turbocharger for engine speed of $1000RPM$ with maximum torque an engine can support i.e. $280Nm$. The second test was performed at $2000RPM$ engine speed with half of load torque applied to it i.e. $140Nm$ and the third test was pyramid tests when engine is in working condition. For these tests EGR valve is kept close and VGT can operate only in a limited predefine range. Some other tests were also performed to see the impact of aero-dynamic force on the actuator for all ranges of VGT opening in engine off condition. However, these tests involve an external source to generate the exhaust air pressure. The advantage of new setup is that all the VGT vanes' angles can be tested unlike the previous test performed on the running engine.

The complete turbocharger system is shown in the Fig. 3.18(a). This system comprises of an industrial pneumatic actuator and a variable geometry turbocharger. The pressure in the pneumatic actuator is measured with Druck PTX 610-1176 pressure sensors with output range from 0 to $-1Bar$ gauge pressure. The position of the diaphragm is measured with position sensor mounted on the pneumatic actuator. The system shown in Fig. 3.18(a) is also tested, separately, in the laboratory for characterizing the actuator system.

The experiments have been carried out at two different engine operating conditions. These tests were carried out on a test bench capable of measuring the actuator pressure, diaphragm position, pressure at the turbine inlet and outlet and the torque acting on the crank due to aerodynamic force.

Fig. 3.19 shows the simulation and experimental results for the actuator at $1000RPM$ engine speed when it is operated at full load. The maximum load for the DV6 engine is $280Nm$. The pressure coming from the pressure regulator is the input of the simulator which is shown in Fig. 3.19(a). The applied pressure is actually the differential pressure

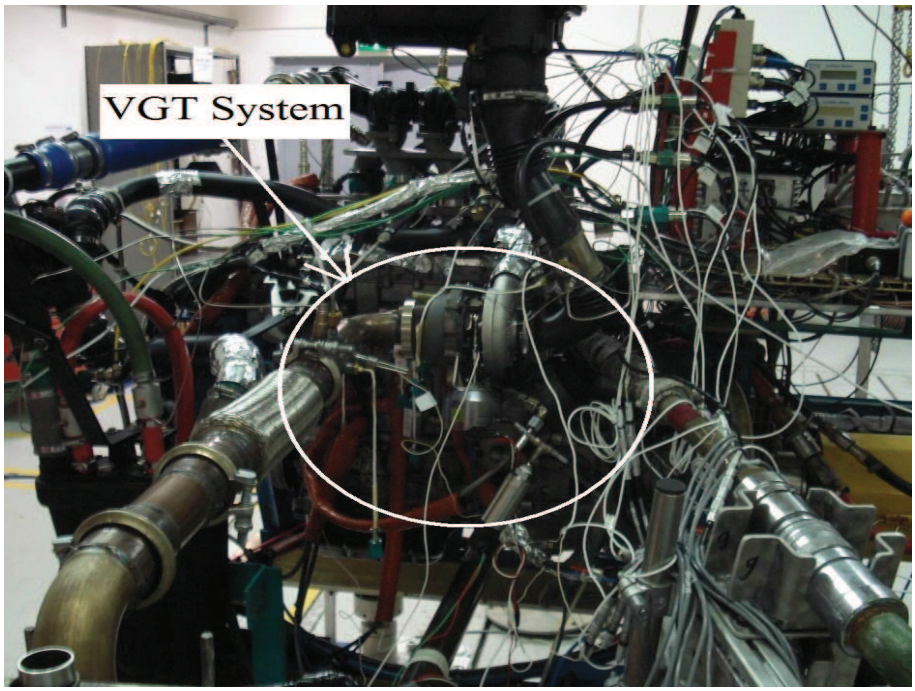

FIGURE 3.17. *A complete test bench for diesel engine with pneumatic actuator and VGT system*

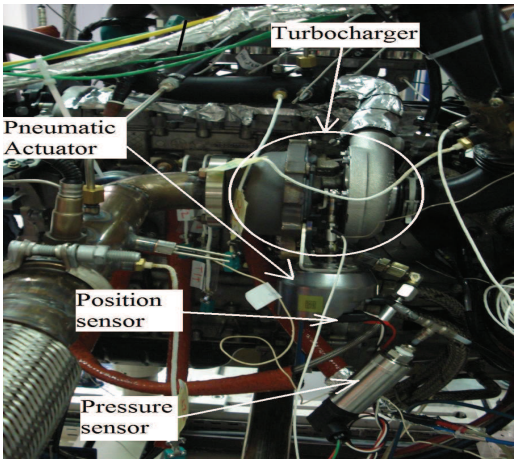

(a) A complete turbocharger system with pneumatic actuator

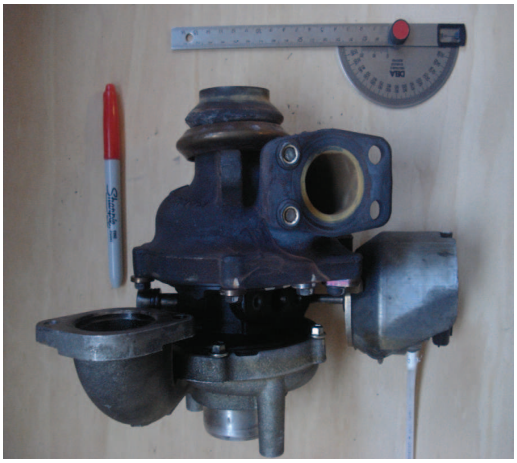

(b) A variable geometry turbocharger

FIGURE 3.18. *Variable geometry turbocharger as a part of diesel engine*

across diaphragm. The spring inside the actuator is pre-compressed and about $120kPa$ of applied pressure is required to compensate its compression. Fig. 3.19(b) shows the diaphragm position for the applied pressure. Fig. 3.19(c) represents the vanes opening angle for different diaphragm positions. Crank angle has the minimum offset of 4^o. The corresponding aero-dynamic force is shown in Fig. 3.19(d) which is maximum when vanes are close.

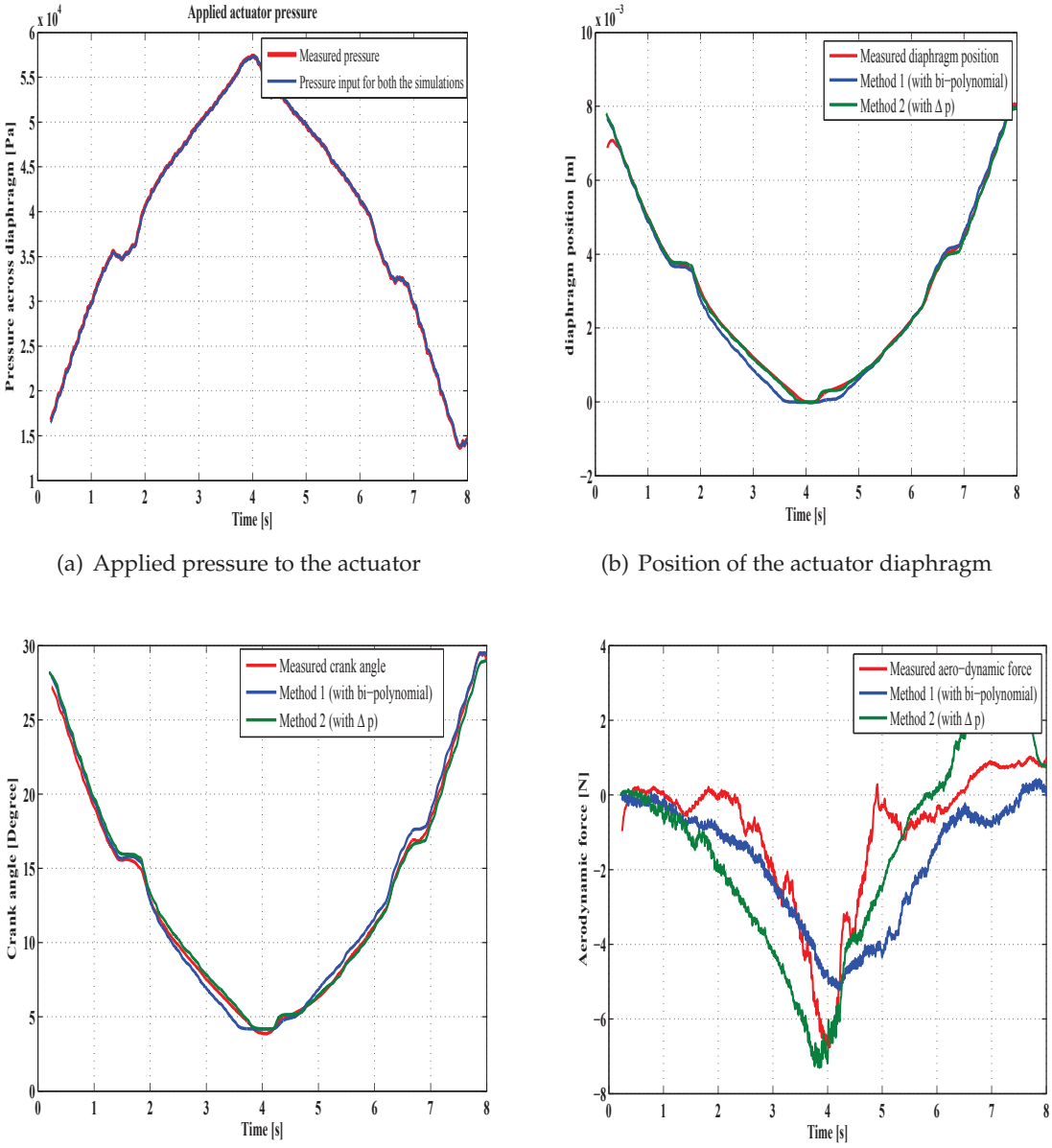

(a) Applied pressure to the actuator

(b) Position of the actuator diaphragm

(c) Crank angle at different positions

(d) Aero-dynamic force acting on the vanes

FIGURE 3.19. *Tests for the actuator for applied PWM signal at full load and 1000 RPM.*

Fig. 3.20 shows the simulation and experimental results for the actuator at the engine speed of 2000RPM and when it is operated at 50% of full load. The pressure coming from the pressure regulator is the input to the simulator as shown in Fig. 3.20(a). The maximum applied pressure is 350$mBar$ as we do not want to close the vanes completely. Fig. 3.20(b) shows the diaphragm position for the applied pressure. Diaphragm movement is limited to 4mm in this particular case. Fig. 3.20(c) represents the vanes opening angle for the different diaphragm positions at 2000RPM. The range of crank angle is 16degree to

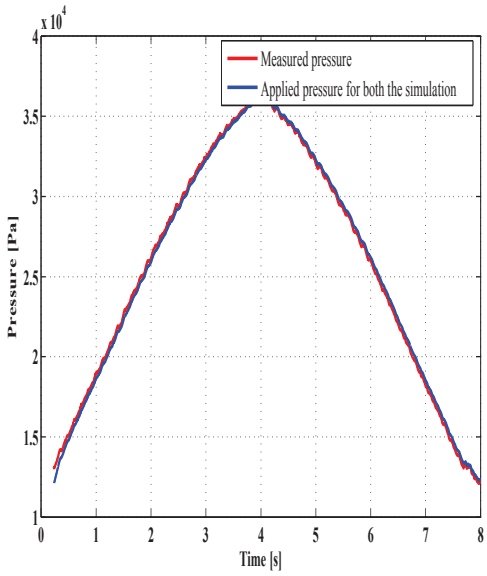

(a) Applied pressure to the actuator

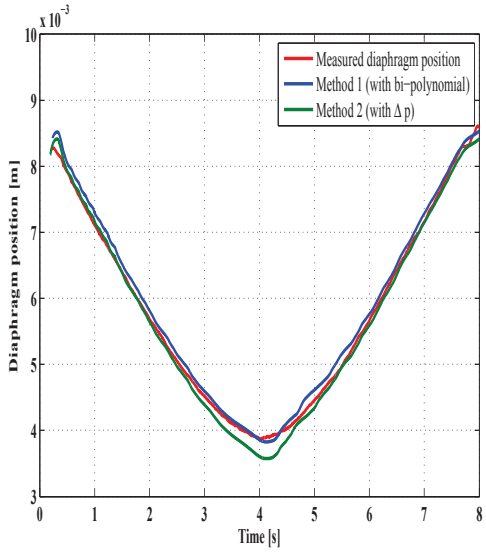

(b) Position of the actuator diaphragm

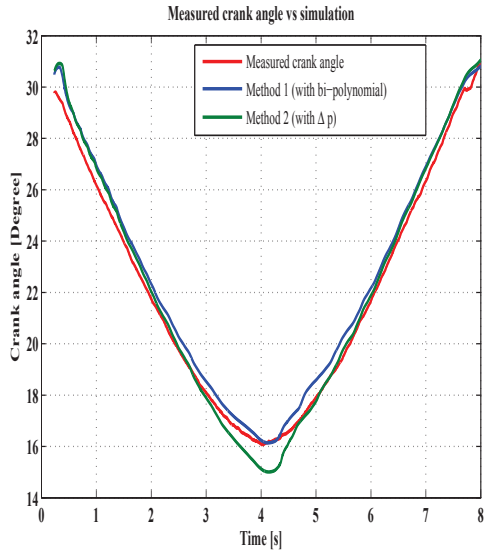

(c) Crank angle for different diaphragm positions

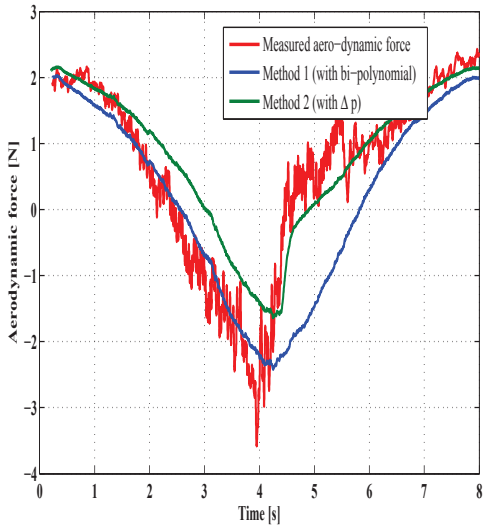

(d) Aero-dynamic force acting on the vanes

FIGURE 3.20. *Tests for the actuator for applied PWM signal at half load and* 2000RPM

32degree in this case. Corresponding aero-dynamic force is shown in Fig. 3.20(d) which is maximum when vanes are close.

In Fig. 3.21 hysteresis effect has been shown for applied pressure and diaphragm position. Where as both the models are compared with the experimental results which are obtained at two different operating points. Figure on the left 3.21(a) represents the hysteresis curve for engine speed of 1000RPM with full load. While, figure on the right 3.21(b) shows the results when engine is rotating at 2000RPM with 50% of the full load.

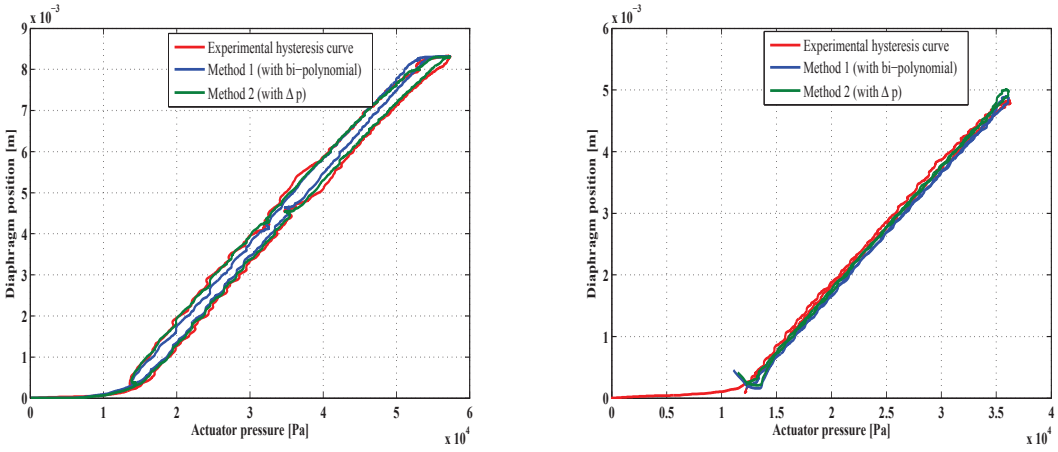

(a) Applied pressure to the actuator

(b) Position of the actuator diaphragm

FIGURE 3.21. *Hysteresis in the actuator at two operating points i.e.* $1000RPM$ *with full load and* $2000RPM$ *with* 50% *load*

Comparison between simulation models and experiments confirms the effectiveness of these models with very lean hysteresis effect at $2000RPM$. The reason is that the maximum course for the actuator is only $3.5mm$. Therefor, the actuator does not experience a large aerodynamic force on its diaphragm.

Fig. 3.22 shows the simulation and experimental results for the actuator when the pressure is applied in the form of a pyramid. The applied pressure is shown in Fig. 3.22(a) with variable step sizes. Fig. 3.22(b) shows the diaphragm position for the applied pressure. The crank angle and aero-dynamic force which corresponds to this test are shown in Fig. 3.22(c) and 3.22(d), respectively.

The tests for characterizing hysteresis were performed on a slightly different actuator for different operating conditions. In this actuator the maximum displacement is kept to $10.13mm$ instead of $8.8mm$ which was used in the previous actuator. The spring used in the pneumatic actuator is also slightly different from the previous one. In Fig. 3.23, the hysteresis effect has been shown for applied pressure and diaphragm position when the turbine is in working conditions. The gauge pressure at the inlet of turbine is $1500mBar$. It can be seen that the hysteresis increases when the turbocharger's vanes are moving towards their closed position. The closed position corresponds to the maximum diaphragm position and minimum crank angle.

In Fig. 3.24, a comparison of the hysteresis effect between the simulation and experiments has been shown for applied pressure and diaphragm position when the gauge

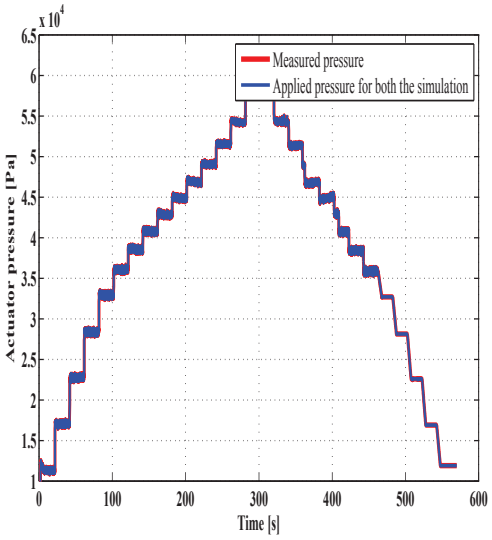

(a) Applied pressure to the actuator

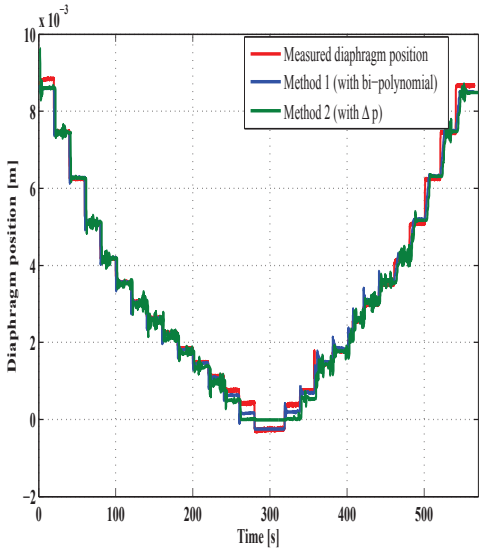

(b) Position of the actuator diaphragm

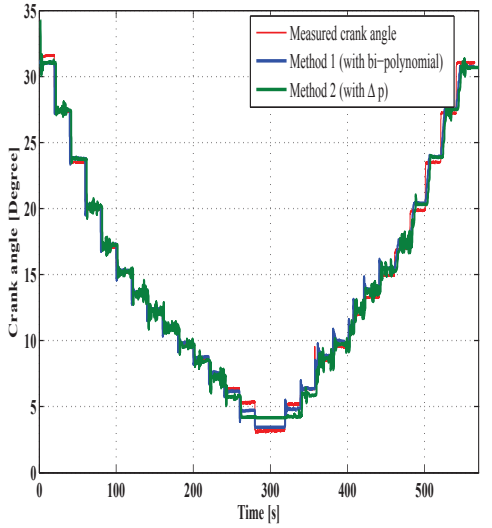

(c) Crank angle for different diaphragm positions

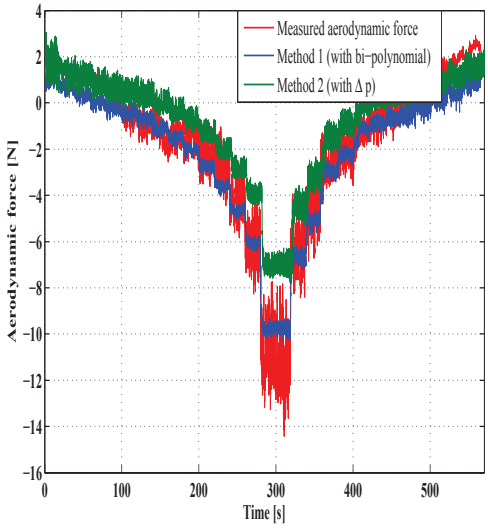

(d) Aero-dynamic force acting on the vanes

FIGURE 3.22. *Tests for the actuator when the applied pressure signal is a pyramid*

pressure entering in the turbine inlet is $3000mBar$. The hysteresis curve for $3000mbar$ pressure is wider than the curve for $1500mBar$. The maximum actuator pressure required to close these vanes completely, also increases with the increase in turbine pressure.

As it can be seen, the simulation adheres to the experimental data with only a slight deviation at the vanes closed position. The information of the force sensor is not

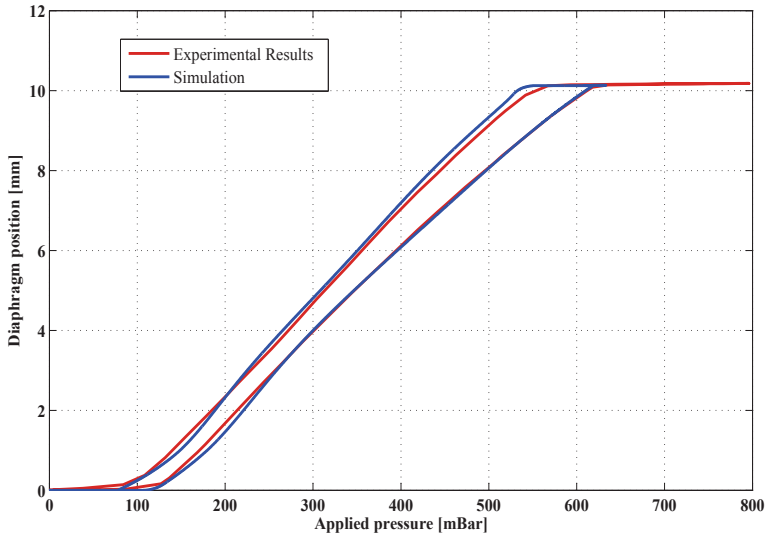

FIGURE 3.23. *Comparison between experiments and simulation results for hysteresis observed when pressure entering in the turbine is 1500mBar*

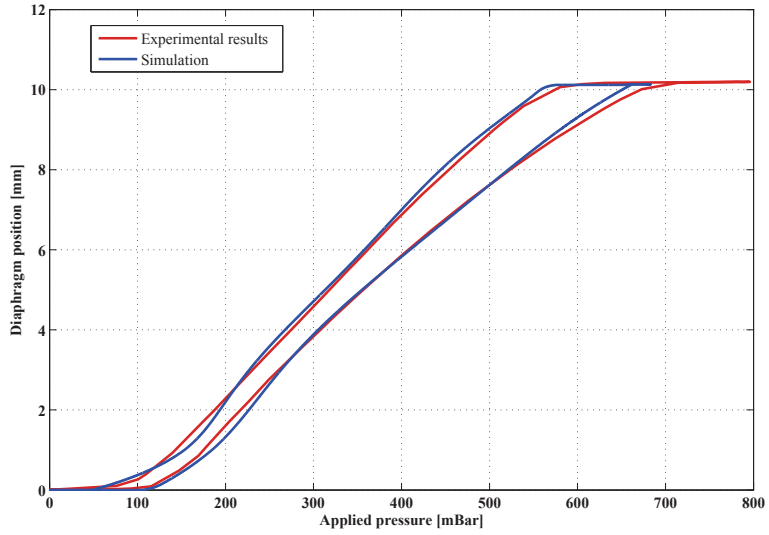

FIGURE 3.24. *Comparison between experiments and simulation results for hysteresis observed when pressure entering in the turbine is 3000mBar*

available for this actuator, therefore, we have only validated the experimental results in figures 3.23 and 3.24 with method2 for aerodynamic forces.

3.7 CONCLUSION

In this chapter, we have completed the VGT Actuator model, by integrating two important nonlinear forces in the physical model. A comprehensive study of different friction models is presented. The LuGre model has been preferred because it is most detailed and comprehensive in terms of friction related phenomena. The effects of external aerodynamic force have been modeled using three different approaches as well. However, only two of them are tested and validated for the instant. The complete model is validated with the experiments performed on the DV6TED4 diesel engine. To conclude the modeling effort, we will perform sensitivity analysis on the actuator model in chapter 4, to evaluate the effect of variation in model parameters upon its characteristics.

Chapter 4 Sensitivity analysis of parameters

4.1 Introduction

In this chapter, we have developed a quantified understanding towards the role of model parameters an their influence on the actuator dynamics. In model development there exist some constrains due to computational limitations, estimation errors and knowledge gaps on system parameters. Sensitivity analysis (SA) is a useful tool to see the impact of system parameters on the model. Especially, when parameters are difficult to identify or there is uncertainty due to lack of knowledge about the system. Design sensitivity also plays a critical role in identification studies as well as numerical optimization and reliability analysis.

Different techniques for sensitivity and uncertainty analysis are detailed in [23]. A simple approach to study the influence of the parameters on the overall global system is the method of varying each parameter and then observing its impact on the system. Such a method for the sensitivity analysis of electro-hydraulic actuator has been studied in [15] by using the parameter variation. Another approach is the method of derivation in which the slope of the derivative of a mechanistic model is analyzed [38]. Both these methods require a prior knowledge of the model and are characterized as the direct and local sensitivity analysis techniques. On the other hand, the techniques based on the variance and covariance of more complex dynamical systems are proposed in [69] and [68]. Some of well known variance based techniques are the sensibility index (SI), Standardized Regression Coefficient (SRC), Fourier Amplitude Sensitivity Test (FAST) and Anova methods.

In this chapter, we have performed sensitivity test for both the actuator and friction models. The actuator parameters are analyzed with Standardized Regression Coefficient and

parameter variation technique. This study will help us to understand the variation in actuator′s response with respect to its parameters. Furthermore, the VGT′ open and close vanes effects have been studied on the actuators. With this approach we can obtain an accurate model of the VGT actuator with bounds on the incertitude in its parameters.

4.1.1 SENSITIVITY ANALYSIS OF PARAMETERS

It is important to understand that how closely a model approximates a real system which can not be depicted by comparing model results with experimental data alone. There are certain analysis which should be carried out, to improve model performance. Two main approaches for model analysis are the sensitivity and uncertainty analysis. Sensitivity analysis involves studying how changes in a model input values or assumptions affect its output or response. Uncertainty analysis investigates how a model might be affected by the lack of knowledge about a certain population or the real value of model parameters. VGT actuator model involves two types of parameters, i.e. the actuator's parameters and the friction model parameters. Next, we will present two simple techniques for parameters sensitivity.

4.1.2 ACTUATOR PARAMETERS

The use of the regression technique allows the sensitivity ranking to be determined based on the relative magnitude of the regression coefficients. The coefficients are indicative of the amount of influence the parameter has on the model as a whole. The variance factor might be very helpful to determine the sensibility index of each parameter with respect to the output. Variance based methods, normally calculate sensibility index (SI) by calculating the variance and covariance between the input and output. Standardized Regression Coefficient (SRC) is a variance based method which is used for the sensitivity test by calculating the sensibility index.

$$SRC(x_i) = \left[\frac{Cov(x_i, y)}{\sqrt{Var(x_i)Var(y)}} \right]^2 \tag{4.1}$$

The value of SRC of the parameter x_i varies between 0 and 1. A parameter with SRC near to 1 means that the output is heavily dependent on that particular parameter and its responsiveness is very high. Similarly, for the SRC value approaching to zero means that the variation in the parameter is insignificant to the output. The formula to calculate the variance is given below

$$Var(x_i) = \sum_{i=1}^{n} \frac{\left(x_i - \mu\right)^2}{n} \tag{4.2}$$

Here μ is the expected or mean value of the variable x_i. Using this technique, we will now determine the SRC of the actuator's parameters. As described in the chapter 2, the second order equation of the pneumatic actuator is given by the following equation

$$m_d \ddot{x}_d = (p_{atm} - p_{act}) A_d - b_d \dot{x}_d - F_0 + k_{sm} x_d - F_{ft} \tag{4.3}$$

Equation (4.3) is simplified by avoiding the friction and constant forces acting on the actuator for the sensitivity analysis of the actuator. The solution of the remaining second order equation is given by

$$x_d = p_{act} K \left[1 + \frac{1}{2\sqrt{\zeta^2 - 1}} \left(\frac{1}{\zeta - \sqrt{\zeta^2 - 1}} exp^{-\omega_n \left(\zeta - \sqrt{\zeta^2 - 1}\right) t} + \frac{1}{\zeta + \sqrt{\zeta^2 - 1}} exp^{-\omega_n \left(\zeta + \sqrt{\zeta^2 - 1}\right) t} \right) \right] \tag{4.4}$$

with

$$\omega_n = \sqrt{\frac{k_{sm}}{m_d}} \quad K = \frac{A_d}{k_{sm}} \quad \zeta = \frac{b_d}{2\sqrt{m_d k_{sm}}} \tag{4.5}$$

As the equation (4.4) is time dependent, therefore we have determined the output at a fixed value of time $t = 0.02sec$, by varying input parameters diaphragm position A_d, diaphragm mass m_d, spring constant k_{sm} and damping coefficient b_d. The input and output data used to determine the SRC of the diaphragm area is shown in Table. 4.1.

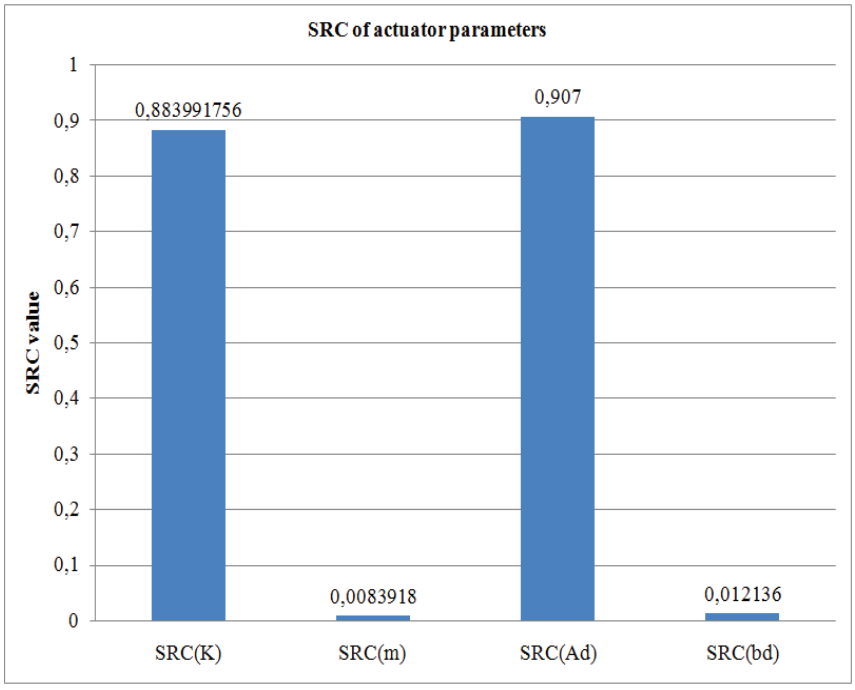

FIGURE 4.1. *sensitivity analysis data graph*

TABLE 4.1: *Variation in parameter values for the actuator*

m_d	k_{sm}	b_d	A_d	P_{act}	K	ζ	ω	x_d
0.53	7400	166	0.002372	19800	3.949E-07	1.362	108.382	0.03159
0.63	7700	186	0.002922	20000	3.795E-07	1.335	110.554	0.03036
0.73	8000	206	0.003525	20200	3.653E-07	1.3099	112.687	0.02922
	8300				3.521E-07	1.286	114.781	0.02817
	8600				3.398E-07	1.2635	116.836	0.02718
	8900				3.283E-07	1.2419	118.857	0.02627
	9200				3.176E-07	1.2216	120.843	0.02541
	9500				3.076E-07	1.202	122.798	0.02461
	9800				2.982E-07	1.183	124.722	0.02386
	10100				2.893E-07	1.1658	126.616	0.02315
	10400				2.810E-07	1.1489	128.483	0.02248
	10700				2.731E-07	1.1327	130.323	0.02185
	11000				2.656E-07	1.117	132.137	0.02125
	11300				2.586E-07	1.1022	133.927	0.02069
	11600				2.519E-07	1.087	135.693	0.02015
	11900				2.455E-07	1.0740	137.436	0.01964
	12200				2.395E-07	1.0607	139.158	0.01916
	12500				2.337E-07	1.0479	140.859	0.0187
	12800				2.283E-07	1.0356	142.539	0.01826
	13100				2.230E-07	1.0237	144.2	0.01784
	13400				2.180E-07	1.0122	145.842	0.01745
							SRC(K_{sm})	0.884

In Fig. 4.1, SRC of all the inputs are shown. From this result, it can be concluded that the parameters A_d and k_{sm} are more sensitive for the output than the parameters m_d and b_d.

Another effective approach to determine the parameter sensitivity is the partial derivative method in which partial derivative of output is analyzed with respect to all inputs. Since, the actuator's model discussed here is nonlinear and complex, we have preformed only the parameter variation method. As, the equation relating the inputs to the output is in time domain, thence we have shown the impact of variation in each parameter as a function of time. The results obtained with SRC method can be reasserted at fixed value of time. Furthermore, it is seen that only the parameter A_d influences the steady state response. While parameters k_{sm}, b_d and m_d only influence the transient response of the output.

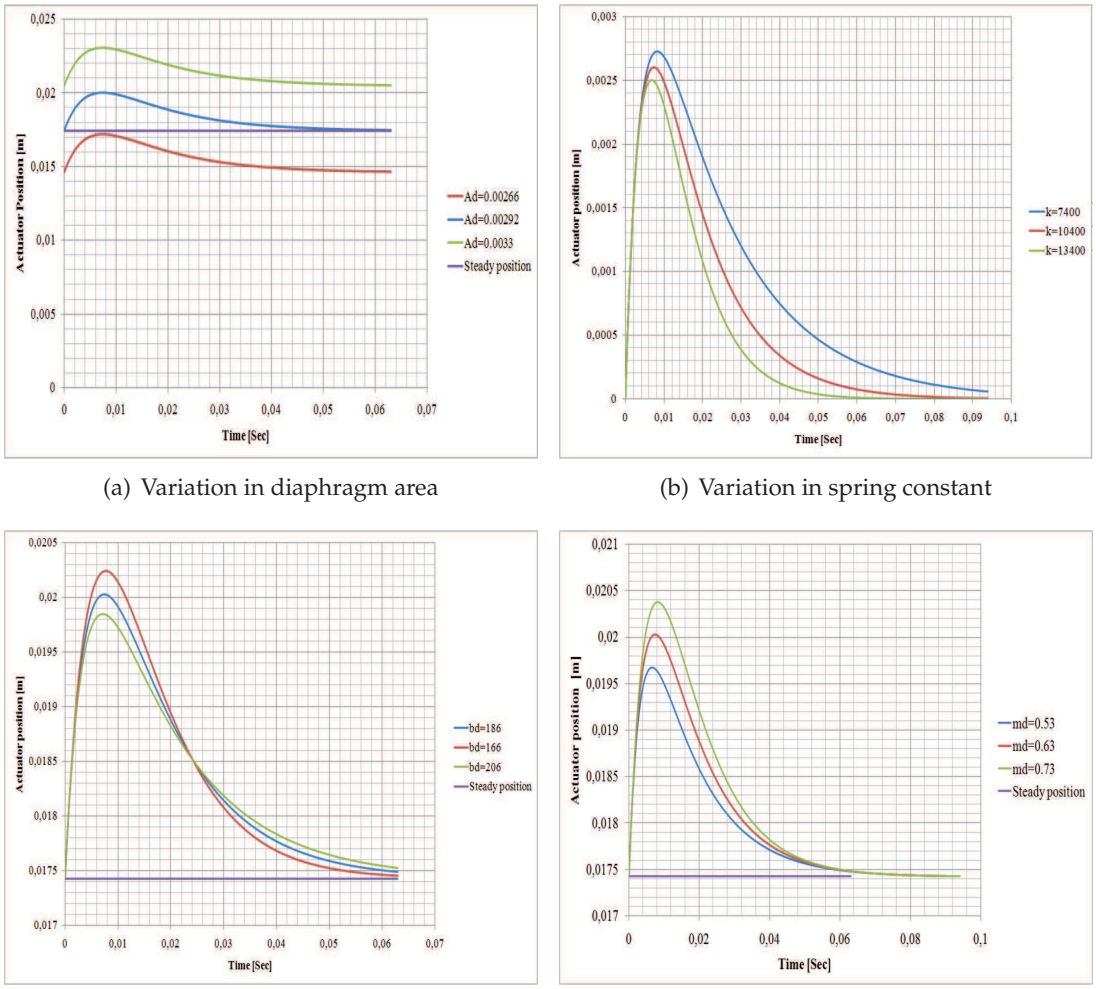

(a) Variation in diaphragm area

(b) Variation in spring constant

(c) Variation in damping coefficient

(d) Variation in diaphragm mass

FIGURE 4.2. *Actuator's parameters test in the transient region*

4.1.3 FRICTION MODEL PARAMETERS

LuGre model identification procedure has been described in chapter 3. The identification procedure depends upon the tests performed under low velocity conditions. Unmodeled process dynamics increases the uncertainty related to the estimated parameter values [3]. Moreover, friction model is identified using nonlinear least square method, which gives approximate parameters for the system. Thus it is important to perform sensitivity tests to affirm the identification procedure. The sensitivity analysis has been performed on the actuator to obtain accurate friction model [57]. The mathematical form of LuGre model is given in the following equation

$$\begin{aligned} F_f &= \sigma_0 z + \sigma_1 \dot{z} + f(v) \\ \dot{z} &= v - \sigma_0 \frac{|v|}{g(v)} z \end{aligned} \tag{4.6}$$

with

$$g(v) = \left(F_c + (F_s - F_c)\exp^{-(|v|/v_s)}\right) \tag{4.7}$$

The formalization of the variation in model's parameters is stated as

$$\begin{aligned} &\sigma_{0x} = \sigma_0 + \delta_{\sigma_0}\,,\ \sigma_{1x} = \sigma_1 + \delta_{\sigma_1} \\ &\sigma_{2x} = \sigma_2 + \delta_{\sigma_2}\,,\ v_{sx} = v_s + \delta_{v_s} \\ &F_{sx} = F_s + \delta_{F_s}\,,\ F_{cx} = F_c + \delta_{F_c} \end{aligned} \tag{4.8}$$

TABLE 4.2: *Variation in the parameters values for the friction model*

F_c	F_s	v_s	σ_0	σ_1	σ_2	F_f
1.6	2.6	0.001	10000	1000	180	3.12437
1.65	3.2	0.0001	100000	1200	160	3.15273
1.7	3.8	0.0005	314567	800	200	3.13912
1.75						3.13694
1.8						3.12016
1.85						3.13653
1.9						3.14267
1.95						3.13882
2						3.120923
2.05						3.13546
2.1						3.13146
2.15						3.12983
2.2						3.12872
2.25						3.140013
2.3						3.122054
2.35						3.13342
2.4						3.128341
2.45						3.13901
2.5						3.14385
2.55						3.14237
2.6						3.13874
					SRC(F_c)	0.3945

where δ_{σ_0}, δ_{σ_1}, δ_{σ_2}, δ_{v_s}, δ_{F_s} and δ_{F_c} are variation in the all six friction model parameters. Model's response after changing different input parameters is shown in Fig. 4.4 where identified parameters are varied one by one and there impact on the model is studied. In Table. 4.2, data analysis of the coulomb friction F_c with respect to the total friction F_f is provided. Similar procedure is repeated to calculate the SRC of each term.

Fig. 4.3 shows the SRC factor of all the friction model parameters. It is observed that model parameters F_s and F_c are more sensitive as compared to other parame-

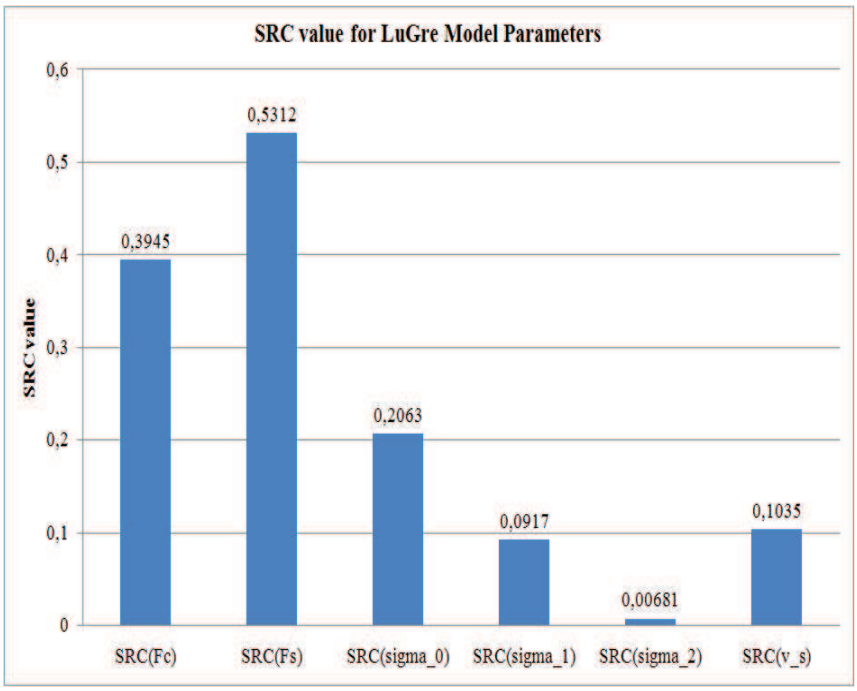

FIGURE 4.3. *Sensitivity analysis data graph for friction parameters*

ters. As this model is velocity dependent, therefore, we have performed this analysis at $v = 0.005m/Sec$.

Continuing to the same procedure as depicted in previous section we have performed sensitivity tests on the LuGre model. Here, actuator velocity is changed in both directions and the friction model is plotted for all the parameters. It is observed that model parameters, for example, σ_0, σ_1 and v_s only have an impact on the pre-sliding region. Whereas the other three parameters influence both the pre and post sliding regimes.

In Fig. 4.4 all the parameters are characterized by variation in their nominal value to see their impact on the over all friction model. It is seen that parameters σ_0, σ_1 and v_s have influence on the dynamics of the friction model. Whereas, other parameters effect the steady state error of the friction model. It can be seen that variation in the value of σ_0 is significant only if we increase its value above 50%. σ_1 is less sensitive as compared to σ_0 as the variation up to 68% has little significance on the results. Effect of σ_2 is negligible as by changing its value up to 90% produces little variation in the results. The coulomb friction is varied up to 15.36% to see its impact on the friction model. The static friction is the most important parameter as a 16% variation in its values has a significant impact on the hysteresis curve. The effect of stribeck velocity on the model is shown in Fig. 4.4(f). Increase or decrease in the stribeck velocity effects only the transient region of the friction velocity curve.

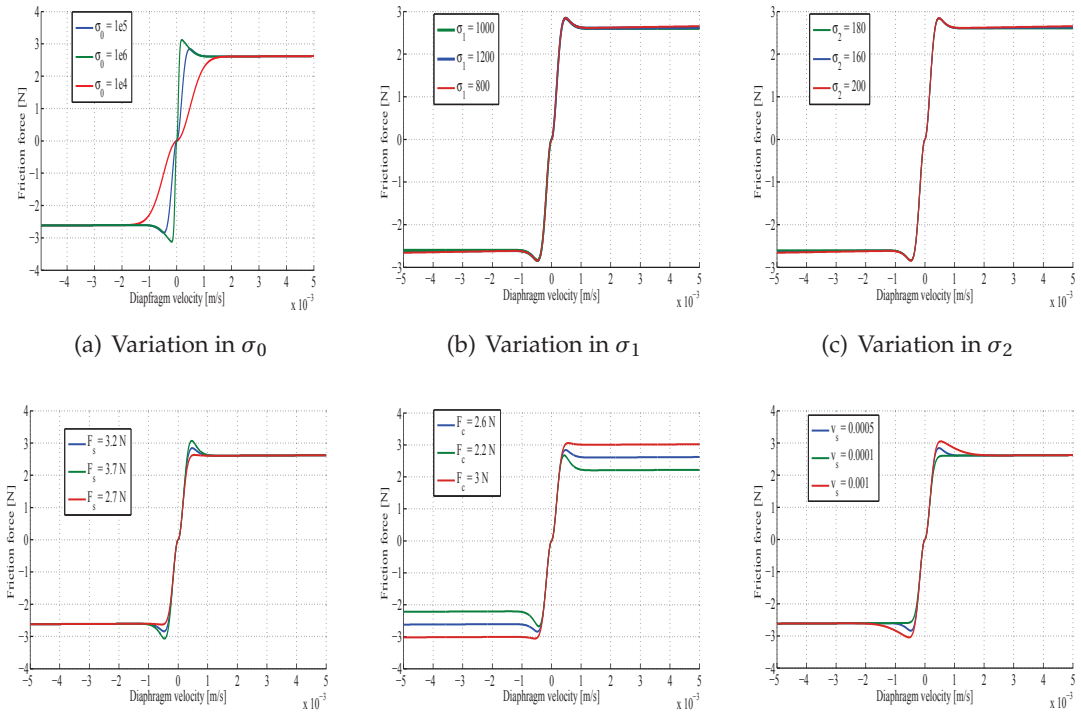

(a) Variation in σ_0 (b) Variation in σ_1 (c) Variation in σ_2

(d) Variation in static friction F_s (e) Variation in coulomb friction F_c (f) Variation in stribeck velocity v_s

FIGURE 4.4. *LuGre friction model for diaphragm velocity*

4.2 TOLERANCE ANALYSIS

The range between the upper and lower limits of the variation of a parameter from the nominal dimension is called tolerance. In ideal case tolerance should be set close to zero. However, high precision is usually associated with high manufacturing cost. Here, twenty turbochargers of the same kind are tested for hysteresis analysis. It is found that each actuator performs in a different way. Fig. 4.5 shows all the hysteresis curves obtained from these twenty actuators at $0mBar$ gauge pressure at the turbine inlet.

As in the sensitivity analysis it is shown that the parameters A_d and k_{sm} have high sensibility indexes. Thus, the variation in the actuator performance indicates that the main cause of this variation is the actuator's diaphragm and the spring used inside it. The variation in diaphragm area is very trivial because all actuators belong to the T3 type series. Thence, it is concluded that this variation is because of the springs used inside the actuator. Next, we have performed the same tests on these turbochargers but in different working conditions. Fig. 4.6 shows all the hysteresis curves obtained from these actuators at $1500mBar$ gauge pressure at the turbine inlet. It can be seen that the hysteresis curves not only become wider as compared to the curves for $0mBar$, but also the

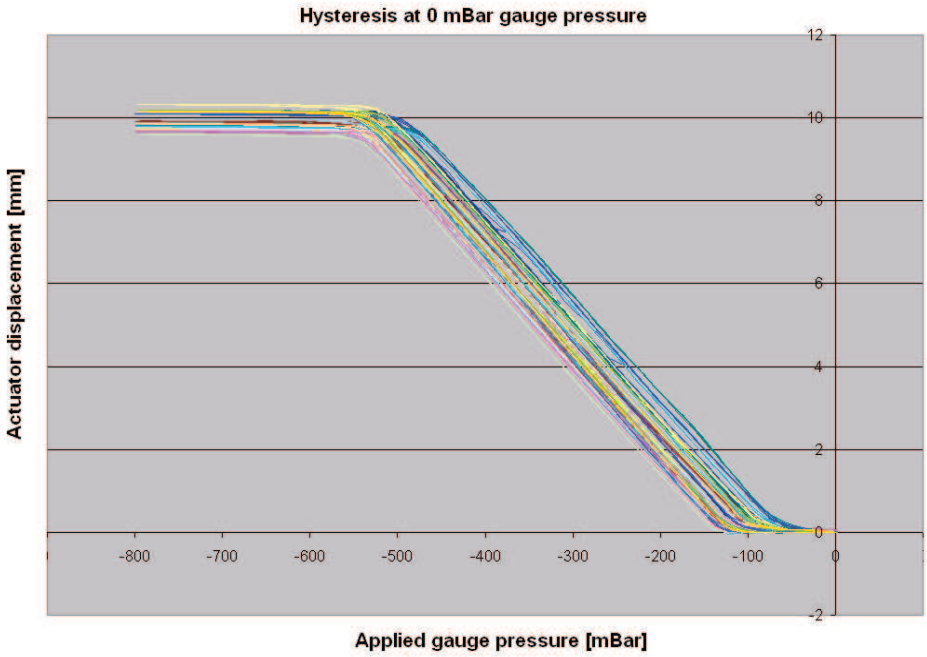

FIGURE 4.5. *Hysteresis curves of the VGT actuators with no turbine inlet pressure*

saturation point for the applied pressure has been shifted.

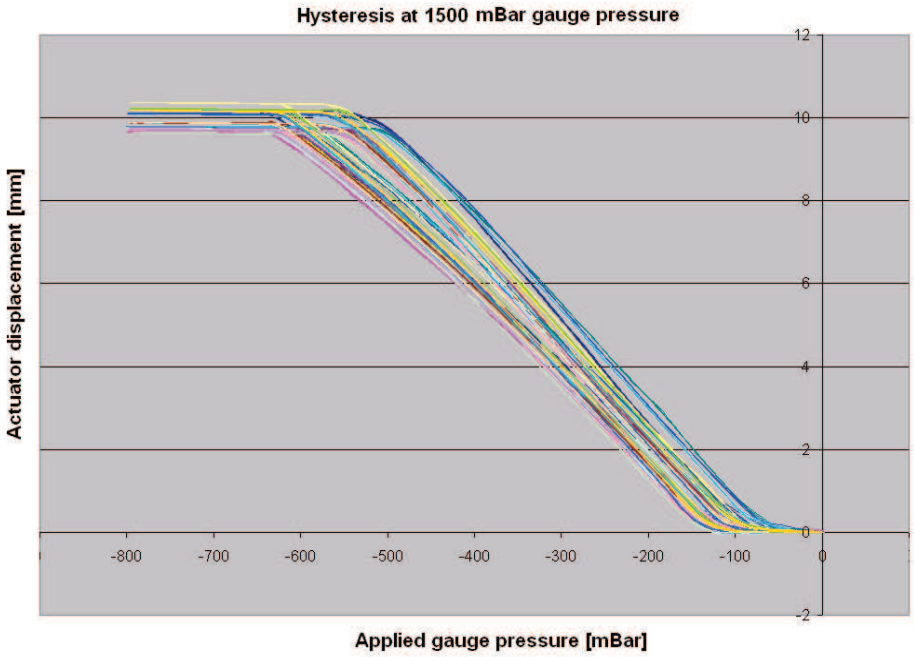

FIGURE 4.6. *Hysteresis curves of the VGT actuators with gauge pressure of* $1500mBar$ *at the turbine inlet*

The trend of hysteresis curves caused by the turbine pressure of $3000mBar$ has been

shown in Fig. 4.7. The hysteresis curves have become more wider, as well as the saturation point has also been shifted. This means that now we have to apply extra pressure to completely close the turbochargers vanes compared to the case of low turbine pressures. From the sensitivity analysis on the friction parameters it is concluded that with the applied aerodynamic force caused by the exhaust air pressure the static F_s and coulomb friction F_c parameters varies, as they have highest sensitivity indexes.

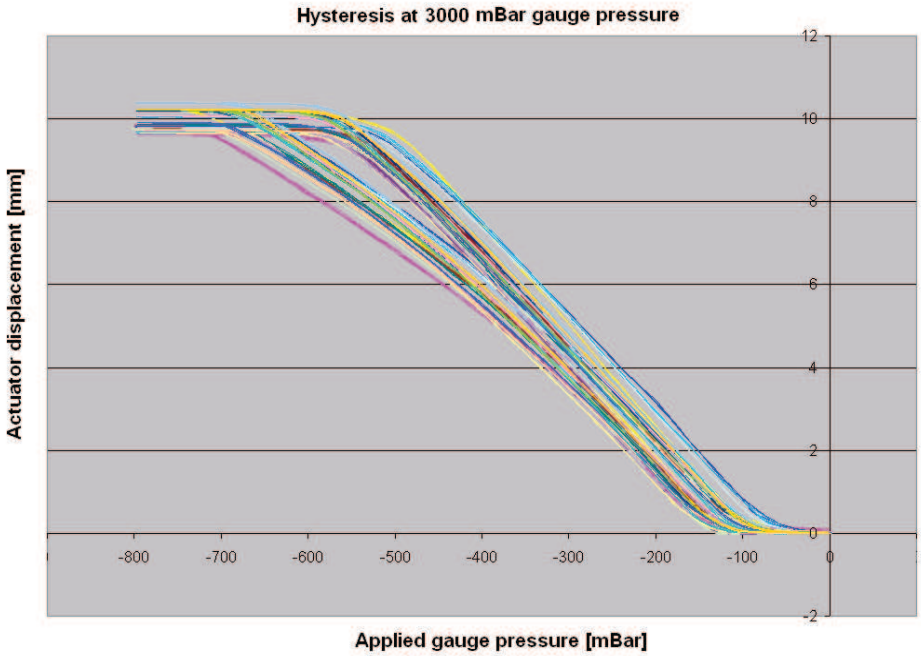

FIGURE 4.7. *Hysteresis curves of the VGT actuators with* $3000mBar$ *gauge pressure at the turbine inlet*

This increase in hysteresis is due to effect of aerodynamic forces which act differently when vanes are opening or closing. However, in [49] it is claimed that this increase is due to the aging factor of the turbocharger. The hysteresis is presented as open valve effect in Fig. 4.8 in which input pressure difference is determined for three points of operation, when the actuator valve is opening. The same procedure is repeated for all actuators when the vanes are opening from their closed position.

Fig. 4.9 shows the closed vanes effect for different actuators. In closed vanes effect input pressure is determined at three points of operation i.e. $0mBar$, $1500mBar$ and $3000mBar$ when the vanes are closing from their opened positions. The closed valve effect is determined by taking one point of operation as reference point when turbine inlet pressure is $0mBar$.

We determined the difference of hysteresis, for both back and forth movement of these twenty actuators. This difference is determined by considering $0mBar$ turbine pressure as a reference (for the same diaphragm position). Furthermore, this pressure difference

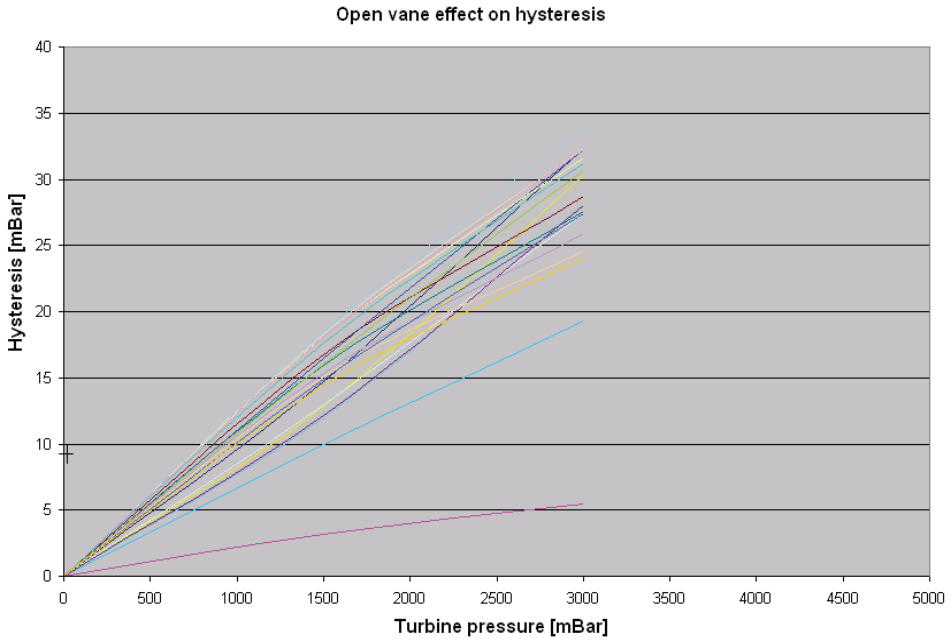

FIGURE 4.8. *Hysteresis lines* $[mBar]$ *as a function of turbine pressure, when the vanes are opening*

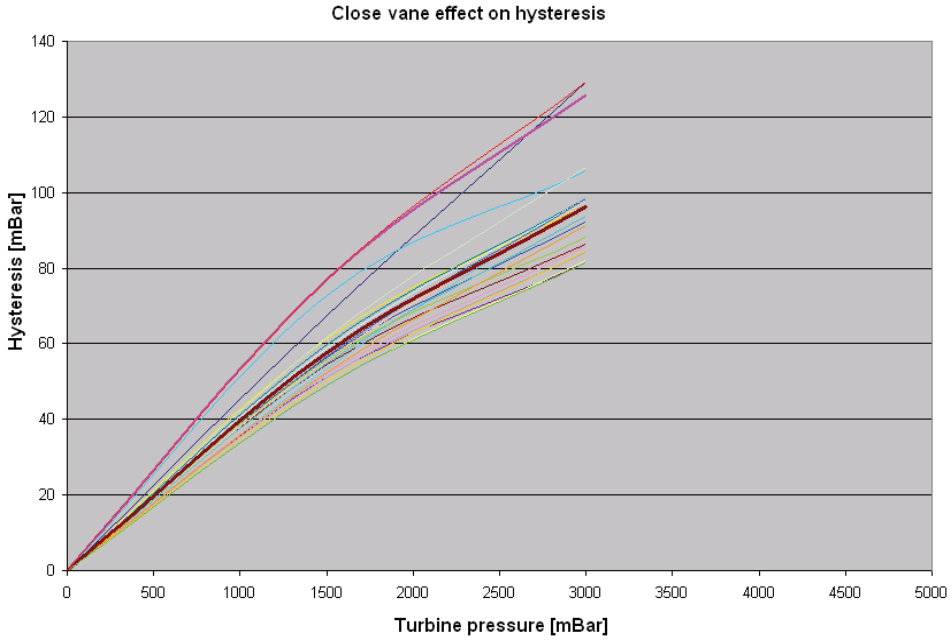

FIGURE 4.9. *Hysteresis lines* $[mBar]$ *as a function of turbine pressure, when the vanes are closing*

(hysteresis in $mBar$) is also determined for different diaphragm positions (Crank angles). The open and closed vanes effects depict that aerodynamic effect adds up extra force in the turbocharger's vanes when they are opening as compared to the case when they are

closing.

4.3 CONCLUSION

A comprehensive analysis of the actuator's parameters sensitivity has been performed in this chapter, along with the friction model. This analysis helped us to study the general trend of the turbocharger's performance, and its dependence on each parameter. These tests were performed on twenty turbochargers at three operating points for turbine inlet pressure. Sensitivity analysis has shown that actuator parameters A_d, k_{sm}, F_s and F_c are of great significance in the turbocharger performance. It can be deduced that turbocharger performance depends upon the actuator size and the spring installed in it. This chapter concludes the detailed modeling of the VGT actuator. In the next chapter, our focus will on the nonlinear robust control of the VGT pneumatic actuator.

Chapter 5 Robust control design

5.1 Introduction

In the previous two chapters, a detailed analytical model of the VGT electro-pneumatic actuator was developed. This model describes the dynamic behavior and hysteresis of friction in the actuator and the effect of aerodynamic force acting on the VGT vanes [55]. Comparison between model simulations and experimentally obtained data shows that the model behavior fits accurately to that of the real actuator. In this chapter we will use this knowledge of the friction effects and aerodynamic force to develop controllers that can counteract the negative effects of these forces.

In the first step, the study is carried out using conventional control techniques and compensation methods. These methods usually consider control and compensation separately. Unfortunately, to the best of our knowledge, aerodynamic force has not been studied in the context of control in contemporary literature, therefore this study is limited to friction compensation only. In the second step, advances in the field of robust and adaptive control are used to develop comprehensive controllers, using which, friction and aerodynamic force compensation are integrated at the level of control design. These controllers are based on backstepping method.

While detailed models are useful for understanding and simulating the behavior of systems, they are not suitable for control design. This is because complex dynamics make control calculations difficult and controller hardware is usually limited in computing capability. Therefore, it was necessary to simplify the model for control design. We have presented two simplification methods based on certain assumptions, that can be justified in real life. The simplified models have been validated by comparing their simulation results with experimental data, to verify that the simplifications do not affect the major

behavioral characteristics of the real actuator, such as its response time and hysteresis.

In this chapter, the model simplifications and their constraints are presented first. Then, conventional control and friction compensation methods are discussed, and the result of their implementation are presented. In the end, Lyapunov-based advanced control methods are developed, in which, friction and aerodynamic force compensation methods are incorporated right from the beginning in the control design. These methods are based on observers and backstepping control design method. The experimental performance of the advanced controllers, based on tests conducted on the engine test bench, are presented in the end.

5.2 MODEL SIMPLIFICATION FOR CONTROL

Model simplification of pneumatic actuators has been studied by many researchers. Sesmat [77] have replaced the mass-flow equation by pressure and servo valve position mapping. A similar strategy can be found in [26], [27] and [73] where the dynamics of the pressure regulator were considered to be very rapid with respect to overall actuator behavior. The commonality in all these works is that pressure distributors are proportional and contain the servomechanism. In our study, we have considered two successive simplifications, which result in a model that is suitable for control purpose. First, air mass flow is mapped as a function of plunger (EPC) position and actuator pressure. Then, a static mapping between applied PWM signal to the EPC, air mass flow and a pressure difference factor is developed to determine the direction of air flow. This results in a simple model with the minimum dynamics required to define the behavior of the actuator.

5.2.1 AIR FLOW AS FUNCTION OF ACTUATOR PRESSURE AND PLUNGER POSITION

Methods for simplification of nonlinear servo pneumatic actuators models, based on simplification of air mass-flow dynamics, have been addressed in the literature (See for example [77], [26] and [73]). For example Belgharbi et al. [7] have proposed a simplified model by using static relationship between air mass-flow, applied signal U and actuator pressure. This fitting is possible because plunger position is linearly proportional to the applied signal. Also, it is considered that the response time of the spool to the input signal is faster than the valve dynamics. The actuator model is simplified for air mass flow

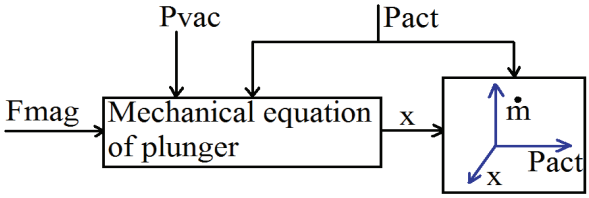

FIGURE 5.1. *Cartography for mass flow equation as a function of actuator pressure and EPC plunger position*

using cartography for control input U and pressure in the actuator chamber, to apply non linear control. Fig. 5.1 shows schematic diagram to simplify the model for further use in control.

In our case the EPC plunger position is not proportional to the applied signal because the plunger always returns to the equilibrium position. So, we have mapped mass-flow as a function of actuator pressure and plunger position, as shown in Fig. 5.2. This map was curve-fitted to find a polynomial function.

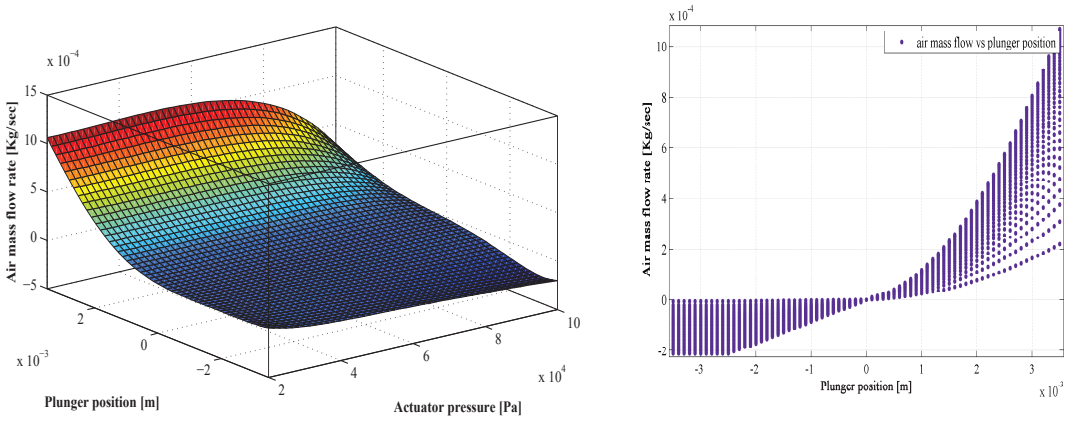

FIGURE 5.2. *Cartography for mass flow as a function of plunger position and actuator pressure for both 2D and 3D view*

Fitting in Fig. 5.2, is obtained as follows

- The air mass flow is determined for different actuator pressures and different applied signals by using actuator pressure dynamics (measured with high bandwidth pressure sensor), under the assumption that the gas is ideal and incompressible.

- The plunger position is obtained using its mechanical equation. As plunger always returns back to its equilibrium position ($x_p = 0$); Therefore, we have considered only its peak value and the value of the air mass flow correspond to this position.

- A Bi-polynomial function of the air mass-flow is determined using surface fitting toolbox in Matlab which depends upon the pressure and plunger position

$$\dot{m}_{act} = \lambda\left(x_p, p_{act}\right) \tag{5.1}$$

By replacing equation (5.1) in the equation set (3.13) in chapter 3 we obtain a simplified state space model, given in equation set (5.2). It is also assumed that the dynamics of the actuator are independent of variation in temperature and the precess is isothermal. Here x_1, x_2, x_3, x_4, x_5 and x_6 are state variables for the plunger position and its velocity, the diaphragm position and its velocity, internal state of the friction model and the pressure inside the actuator chamber, respectively.

$$\begin{aligned}
\dot{x}_1 &= x_2 \\
\dot{x}_2 &= \left[\left(F_{mag} - b_p x_2 + x_6 A_{act} - p_{atm} A_{atm} + p_{res} A_{res} - k_{mem} x_1 - k^*_{s1} x_1\right)/m_p\right] \\
\dot{x}_3 &= x_4 \\
\dot{x}_4 &= \left[\left(\left(p_{atm} - x_6\right) A_d - b_d x_4 - \left(F_0 + k_{sm} x_3\right) - \hat{\theta}\left(\sigma_0 x_5 + \sigma_1 \dot{x}_5 + \sigma_2 x_4\right)\right)/m_d\right] \\
\dot{x}_5 &= x_4 - \frac{\sigma_0 |x_4|}{g(x_4)} x_5 \\
\dot{x}_6 &= \frac{R T_{act}}{V_0 - A_d x_3}\left(\lambda(x_1, x_6)\right) + \frac{x_6}{V_0 - A_d x_3} A_d x_4
\end{aligned} \tag{5.2}$$

Although, this simplification technique has reduced the order of the actuator system, but the model (5.2) is still complex for control application. Moreover, it is not possible to measure the plunger position in current scenario. Therefore, the actuator's model is further simplified to reduce its order.

5.2.2 Air flow as function of applied signal and PWM dependent equilibrium pressure

The order of the system is further reduced by neglecting the EPC plunger dynamics. In fact, the plunger response time ($0.02sec$) is seventeen times faster than the response time of the diaphragm ($0.35sec$). Moreover, it is considered that the variation in the temperature inside the actuator chamber is insignificant.

The mapping for estimated mass flow, as a function of the input signal and pressure inside the actuator, is presented in [73] and [26]. As explained earlier that mostly, in the available literature, the directions of the air mass flow depends upon the sign of the applied signal of the servo device. On the contrary, in the case of the EPC in current discussion, the amount of air flowing from the actuator chamber does not depend on the sign of the applied signal, but the variation in the applied signal. This means that the flow may be positive (from the atmosphere to the actuator chamber) or negative (from the actuator

chamber to the vacuum reservoir) for the same voltage value, depending upon its previous value. Therefore, we have established a static characteristic between the applied PWM signal (0 – 100%) and the actuator equilibrium pressure $f(PWM) = p_{eq-(PWM)}$ to incorporate air flow in both directions [53]. The mass flow is then mapped as a function of the applied voltage U as percentage of PWM, the difference of actual actuator pressure and PWM dependent equilibrium pressure $\Delta p = p_{act} - p_{eq-(PWM)}$. Fig. 5.3 shows estimated air mass flow as function of applied signal and pressure difference Δp. From curve fitting of this map, we obtain

$$\dot{m}_{act} = \lambda\left(U, \Delta p\right) \tag{5.3}$$

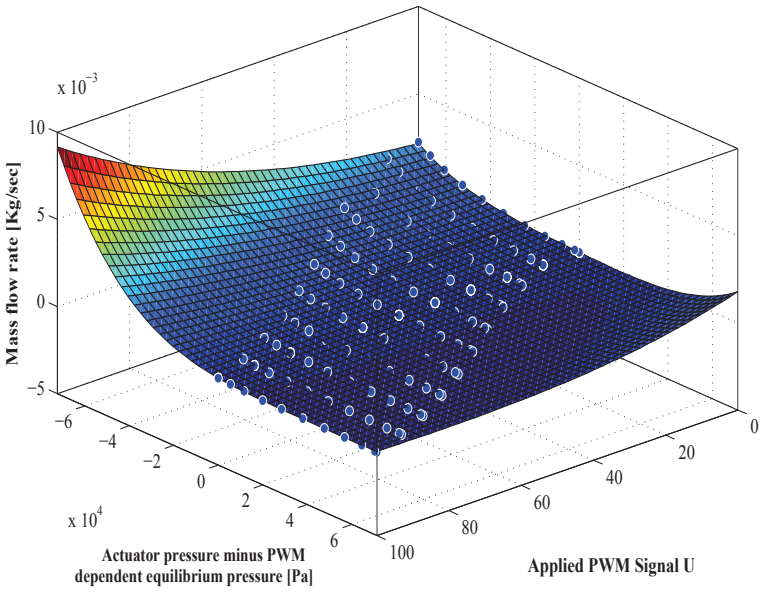

FIGURE 5.3. *Cartography for mass flow as a function of applied signal and pressure difference*

By replacing equation (5.3) in the model we get the simplified model which is shown in equation set (5.4). The plunger dynamics are neglected to reduce system order. Here x_1, x_2, x_3 and x_4 are state variables for the diaphragm position and its velocity, internal state of the friction model and the pressure inside the actuator chamber, respectively.

$$\begin{aligned}
\dot{x}_1 &= x_2 \\
\dot{x}_2 &= \left[\left(\left(p_{atm} - x_4\right) A_d - b_d x_2 - \left(F_0 + k_{sm} x_1\right) - \hat{\theta}\left(\sigma_0 x_3 + \sigma_1 \dot{x}_3 + \sigma_2 x_2\right)\right) / m_d\right] \\
\dot{x}_3 &= x_2 - \frac{\sigma_0 |x_2|}{g(x_2)} x_3 \\
\dot{x}_4 &= \frac{R T_{act}}{V_0 - A_d x_1}\left(\lambda(U, \Delta p)\right) + \frac{x_4}{V_0 - A_d x_1} A_d x_2
\end{aligned} \tag{5.4}$$

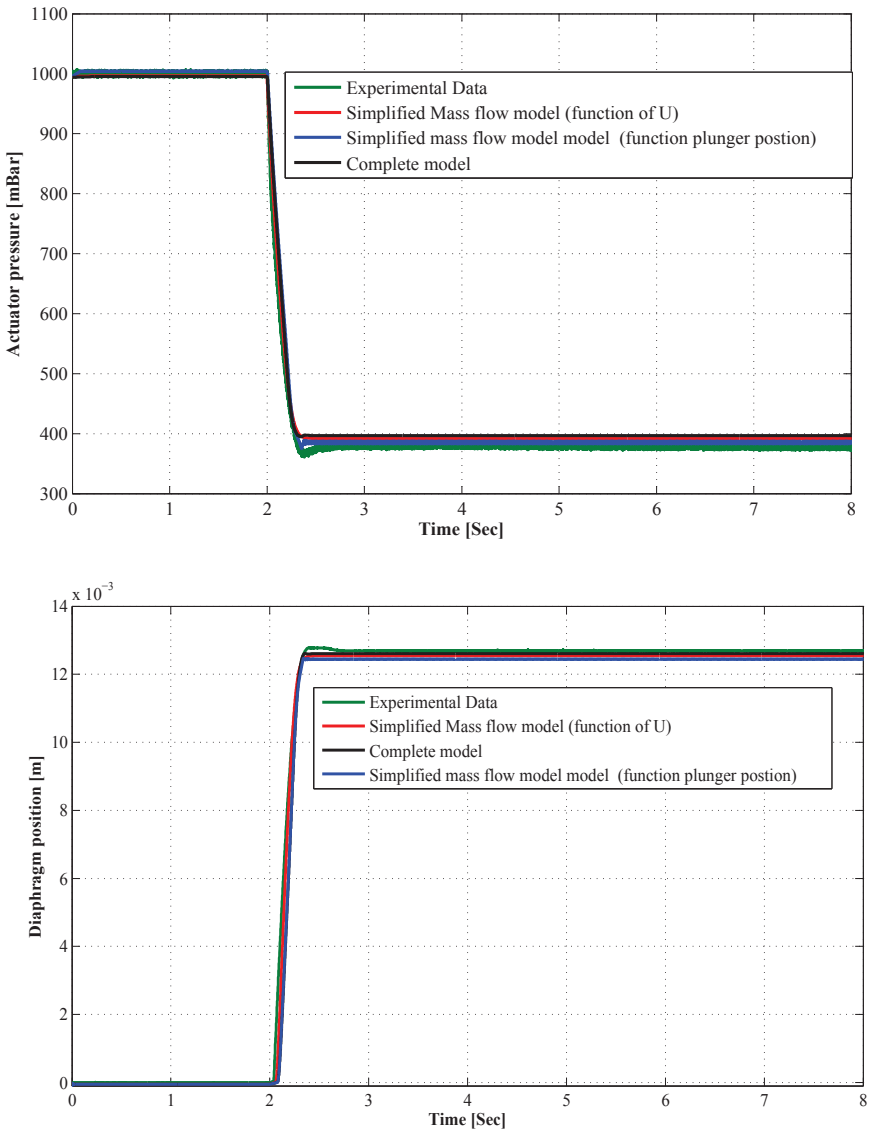

FIGURE 5.4. *Validation of three proposed models for actuator pressure and diaphragm position, for 80% applied PWM signals*

5.2.3 EXPERIMENTAL VALIDATION OF SIMPLIFIED MODELS

The electro-pneumatic actuator models shown in equation sets (5.2) and (5.4) have been simulated in matlab/simulink using the identified parameters given in Table. B.1 and Table. B.2, using the same laboratory test bench as described in chapter 2. In Fig. 5.4 measured and simulation values of the actuator pressure and diaphragm position are shown for duty cycle input of 80%. Time response of the system for the pressure fall is $0.3sec$ inside the actuator. All the three models follow dynamics of pressure with steady state error of $\pm 5mBar$. Diaphragm position for applied pressure is shown with time

response of $0.35sec$. Steady state error for the simulation models is $\pm 0.3mm$.

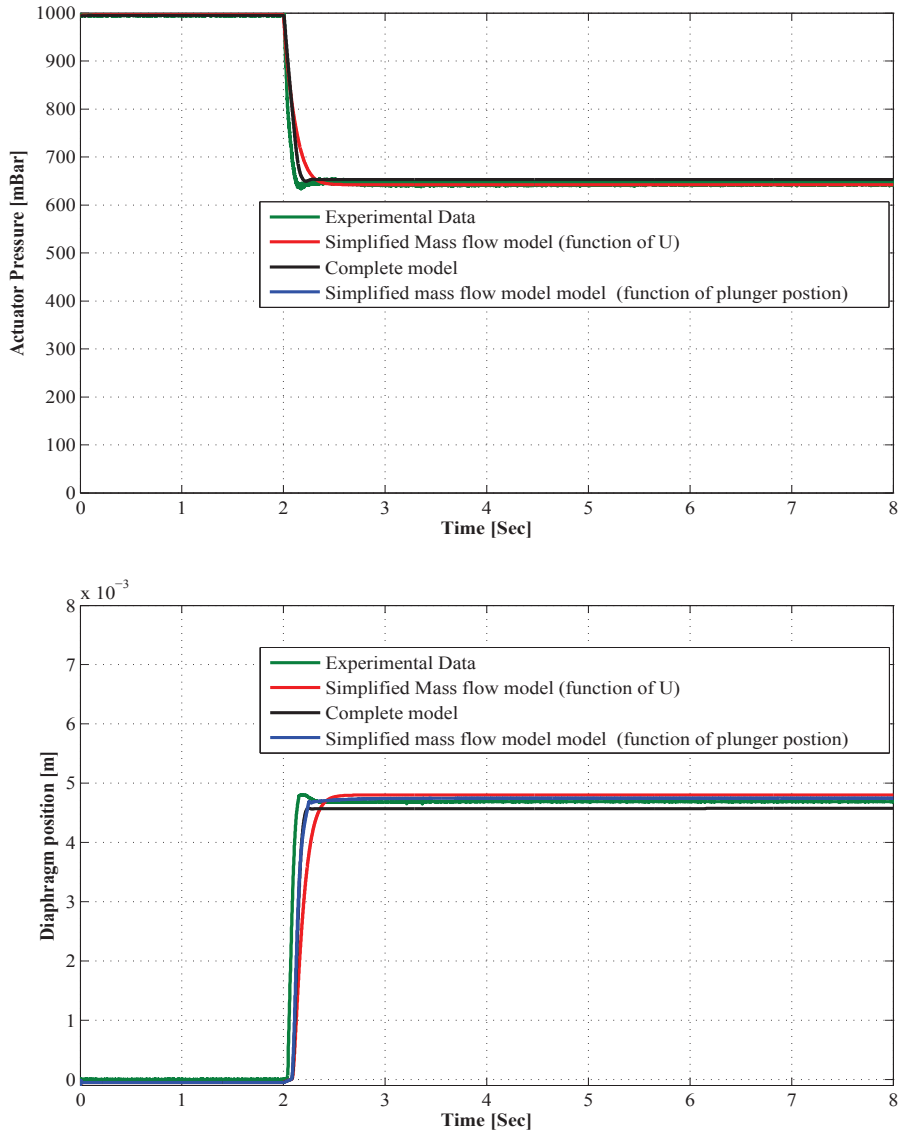

FIGURE 5.5. *Validation of three proposed models for actuator pressure and diaphragm position, for 50% applied PWM signals*

In Fig. 5.5 measured and simulation values of the actuator pressure and diaphragm position are shown for duty cycle input 50%. All the three models follow dynamics of pressure with steady state error of $\pm 8mBar$ for actuator pressure, and $\pm 0.3mm$ for diaphragm position. The incertitude in the error, for different applied signals, is due to the reason that fitted polynomials are determined with goodness fit of 95%. So, there can be an incertitude of $\pm 5\%$ in the pressure and position of diaphragm.
In Fig. 5.6 measured and simulation values of the actuator pressure and diaphragm position are shown for applied ramp signal.

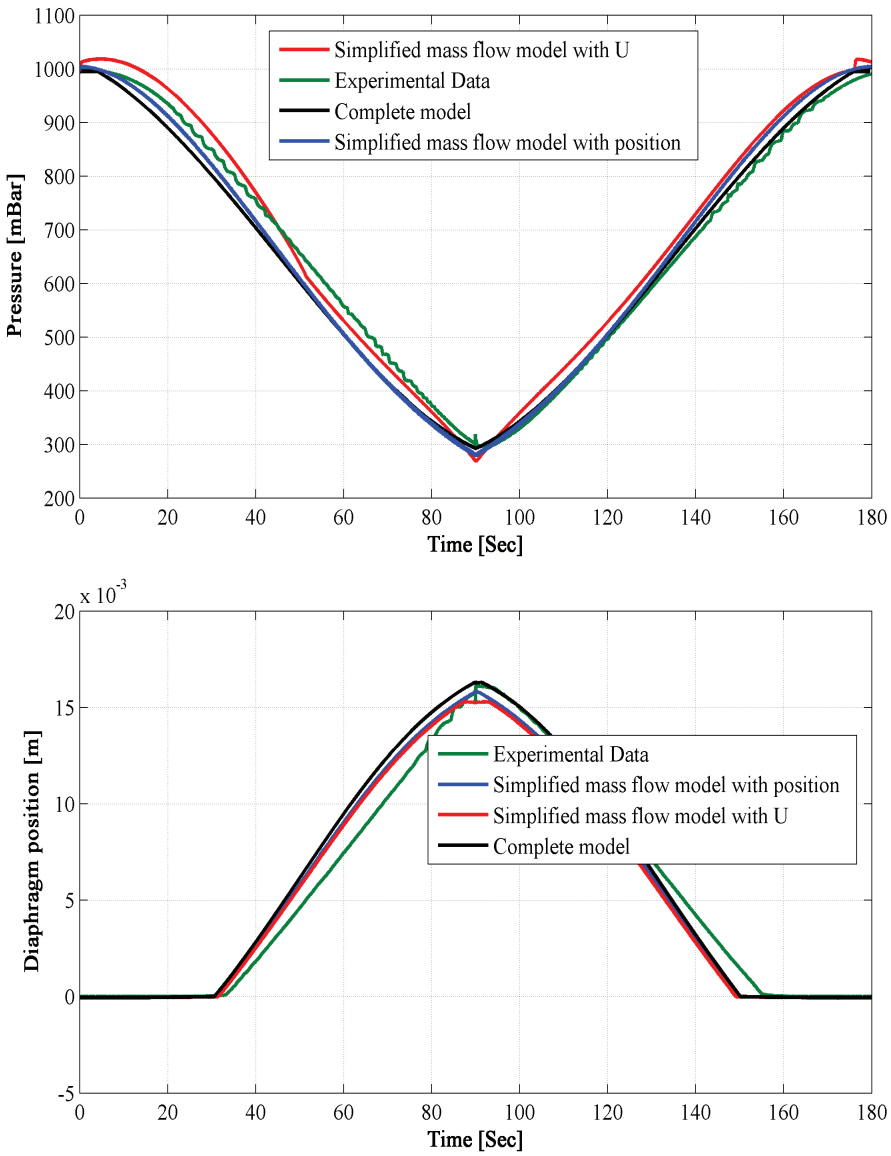

FIGURE 5.6. ***Actuator*** *pressure and diaphragm position for the ramp test*

Fig. 5.7 compares the three models with experimental data. Actuator does not move all of a sudden when input signal is applied in the form of pressure. This phenomenon can be observed in the hysteresis curve which intervenes due to the pre-loaded spring force and the friction force that must be compensated before actuator start its movement.

It can be seen that simplified models do not differ greatly from the detailed mechanistic model. Deviation in the transient response is almost insignificant. In the next sections, equation set (5.4) will be used for control design.

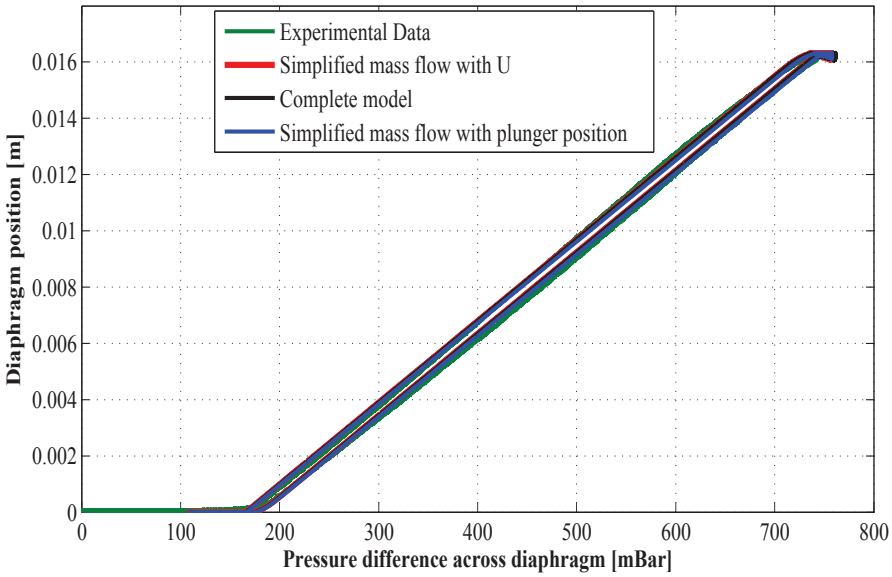

FIGURE 5.7. *Hysteresis in the actuator due to friction*

5.3 CONVENTIONAL FEEDBACK CONTROL WITH FRICTION COMPENSATION

Standard linear fixed gain controllers have been proven to be unsatisfactory in systems with friction [5]. Friction is one of the main factors affecting the positioning accuracy of the actuator system. Specially, when controlled with common PID controllers (which are considered as standard controller in the industry), limit cycles and steady state positioning errors can be observed in the actuator position [12]. To illustrate this point further, Fig. 5.8 shows hunting phenomenon in the experiments with the simple PI control. This phenomenon consists of finite-amplitude oscillations or limit cycles which result from the integral action in presence of friction, which is shown in Fig. 5.9.

To overcome the problems that rise due to friction, knocker [31] and friction observers [96] based control techniques have been presented for friction compensation. A brief review about different friction compensation techniques is presented in [65]. In this section, two methods for friction compensation have been discussed. They have been implemented for the control of the actuator under consideration, and their effectiveness has been shown through experiments.

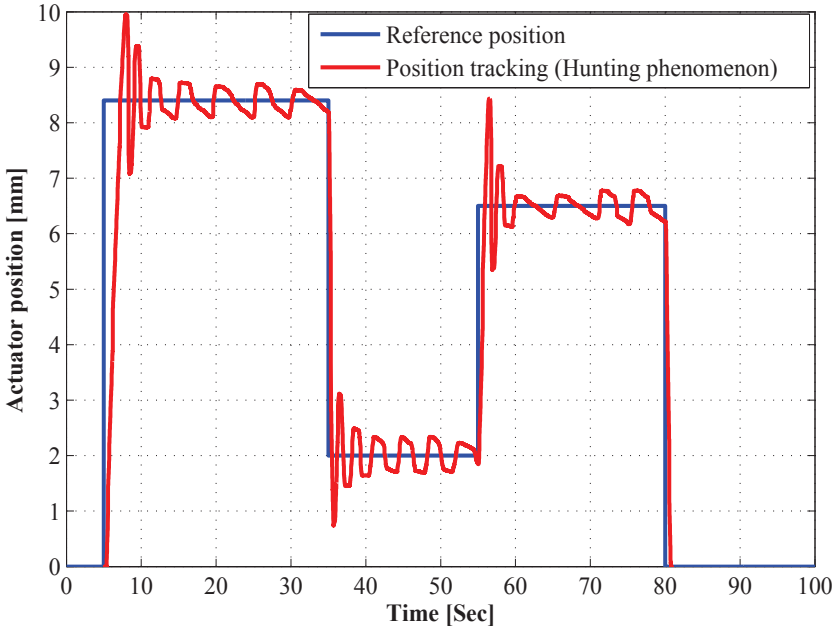

FIGURE 5.8. *Position tracking with linear PID controller, hunting phenomenon is also shown in the figure*

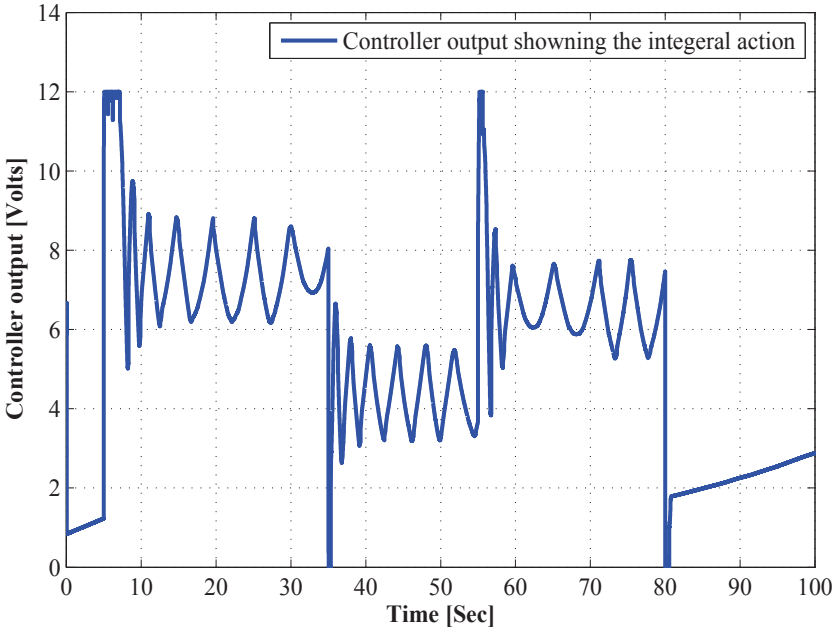

FIGURE 5.9. *Controller output showing the integral action*

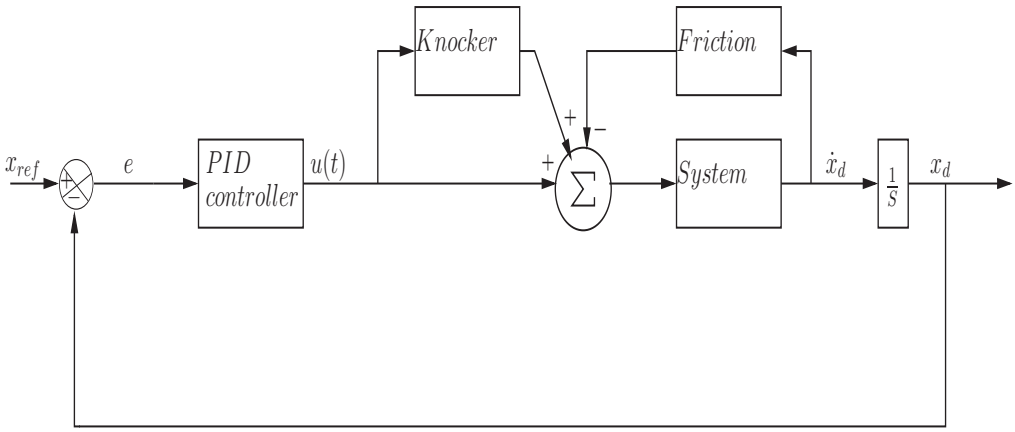

FIGURE 5.10. *Block diagram illustrating the knocker used in the control loop*

5.3.1 KNOCKER

The techniques for friction compensation discussed in the literature are mainly model-based. However, a very simple way to eliminate some effects of friction is to use a dither signal, i.e. a high frequency signal added to the control input. The dither signal, also known as knocker, introduces an extra force which is used to eliminate nonlinearities like stiction in the model. The concept of friction compensation with the help of a knocker is shown in Fig.5.10. The output from the knocker is a pulse sequence. It has three parameters: the amplitude of the pulse α, time between each pulse t_k and the pulse width τ. See, e.g. [31] to understand knocker design and its parameters selection.
Consider that the PI controller output is $u(t)$. The knocker output u_k, is a signal derived from the controller output and is given by the following relation

$$u_k = \begin{cases} -\alpha sign(u(t) - u(t_p)) & , for \;\; t \leq t_p + t_k + \tau \\ 0 & , for \;\; t > t_p + t_k + \tau \end{cases} \tag{5.5}$$

where t_p is the time of onset of previous pulse. As described above, the knocker has three parameters α, τ and t_k, that determine the characteristics of the pulse sequence. These parameters have to be chosen suitably. The pulses should be sufficiently large to compensate the stiction in the actuator. In this experiment, the following parameters have been used for the knocker

$$\alpha = 2\% \;\; \texttt{of the maximum input signal,}$$
$$\tau = 0.02Sec, \; t_k = 2\tau = 0.04sec$$

Due to simple structure and easy implementation, this technique is widely implemented in the industry.

5.3.2 OBSERVER BASED FRICTION COMPENSATION

The disadvantage of using knocker is that controller output switches to compensate friction, which causes fatigue of mechanical parts. It is of course more appealing to use model-based control that uses the model to predict the friction to compensate its nonlinear behavior. Since friction is dynamic and its state is unmeasurable, an observer is necessary to obtain its value. By considering the friction model presented in equation (3.6) and (3.7) given in chapter 3 and assuming that the parameters σ_0, σ_1 and σ_2 and the function $g(v)$ in equation (3.7) are known. The state z is, however, not measurable and hence has to be observed to estimate the friction force. For this we use a nonlinear friction observer given by

$$\dot{\hat{z}} = v - \sigma_0 \frac{|v|}{g(v)} \hat{z} - ke \tag{5.6}$$

where k is a positive constant and $e = x_d - x_{ref}$, is the error between actual and reference position. The friction force obtained from the state observer is given by equation (5.7) where $\hat{\theta}$ describes the adaption of external nonlinear forces.

$$\hat{F}_{f_t} = \hat{\theta}\left(\sigma_0 \hat{z} + \sigma_1 \dot{\hat{z}} + f(v)\right) \tag{5.7}$$

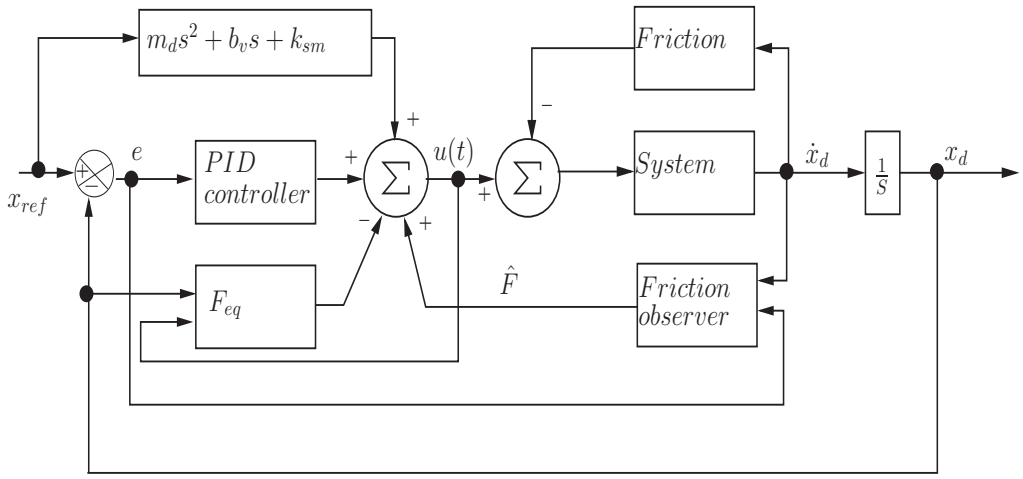

FIGURE 5.11. *Block diagram illustrating the friction observer used in the control loop*

A block diagram of the complete system with position control and correction based friction observer is shown in the Fig. 5.11.

Control input to the system is calculated using feedback linearization with following control law

$$u = -H(s)e + \hat{F}_{f_t} + m_d\ddot{x}_{ref} + b_v\dot{x}_{ref} + k_{sm}x_{ref} - F_{eq} \tag{5.8}$$

$$\texttt{with} \qquad F_{eq} = F_{atm} - F_{act} - F_0$$

where x_{ref} and $H(s)$ represent the reference position and the linear PID controller (with parameters k_p, k_i and k_d as proportional, integral and differential gains for controller), respectively. If we chose $H(s)$ such that the transfer function

$$G(s) = \frac{\sigma_1 s + \sigma_0}{m_d s^2 + b_v s + k_{sm} + H(s)} \tag{5.9}$$

is strictly positive real function (SPR), then observer error $\tilde{F_{f_t}} = F_{f_t} - \hat{F}_{f_t}$, and the position error $e = -G(s)\tilde{z}$, will asymptotically go to zero. Where $\tilde{z}$ is the difference between the observer state and the real friction state. Using the Kalman-Yakubovitch Lemma and LaSalle's theorem it is proven that above system is asymptotically stable, for $\tilde{z} \to 0$ this means that the error e will tends to zero. The proof of the theorem is detailed in [12] and [37]. The only disadvantage with observer based friction compensation is that we need a precise friction model which does not require in case of knocker based compensation.

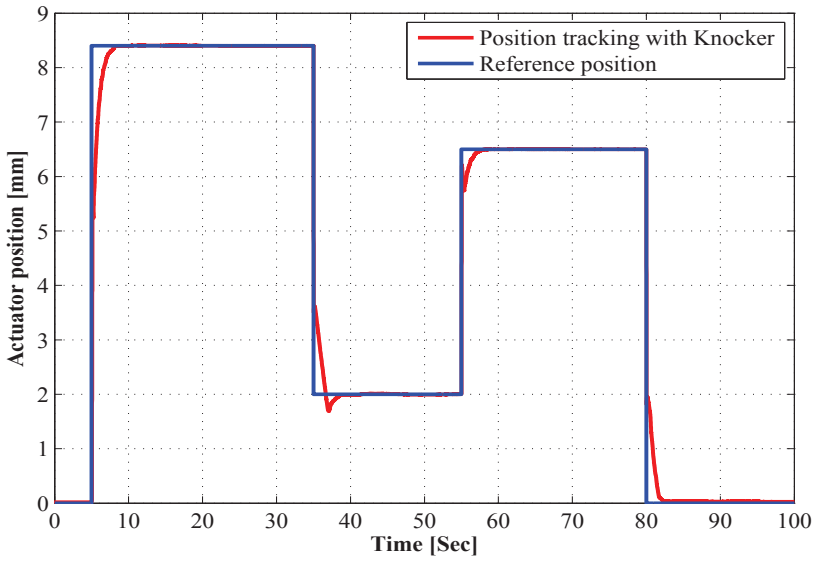

FIGURE 5.12. *Position tracking with knocker*

5.3.3 VALIDATION WITH FRICTION COMPENSATORS

In Fig. 5.12, the output results for the position tracking of the VGT pneumatic actuator are shown using the knocker as a compensation tool. It can be seen that the oscillation in

the actuator have successfully been removed. The controller output is shown in Fig. 5.13. The error difference with the knocker can be seen in the Fig. 5.14. The position error is reduced to $0.067mm$ which is ten times less than its value $0.82mm$ with PI controller.

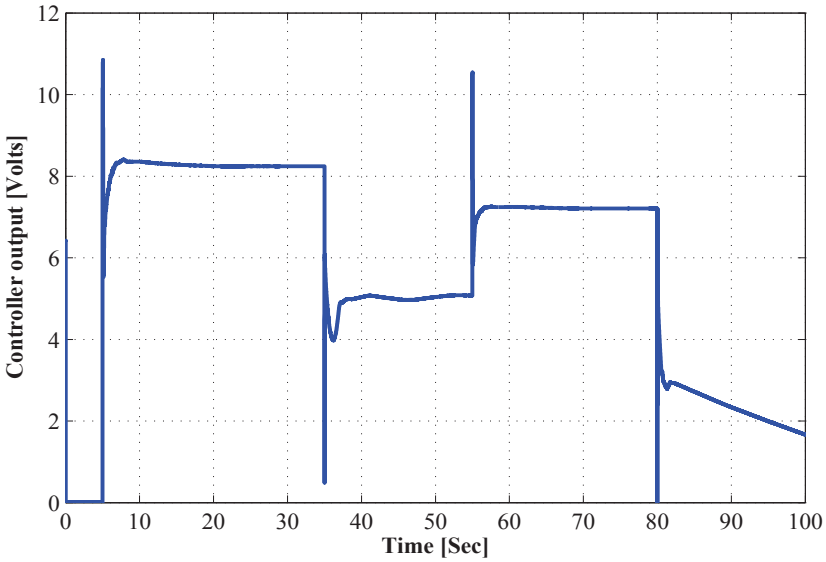

FIGURE 5.13. *Control signal applied to the actuator*

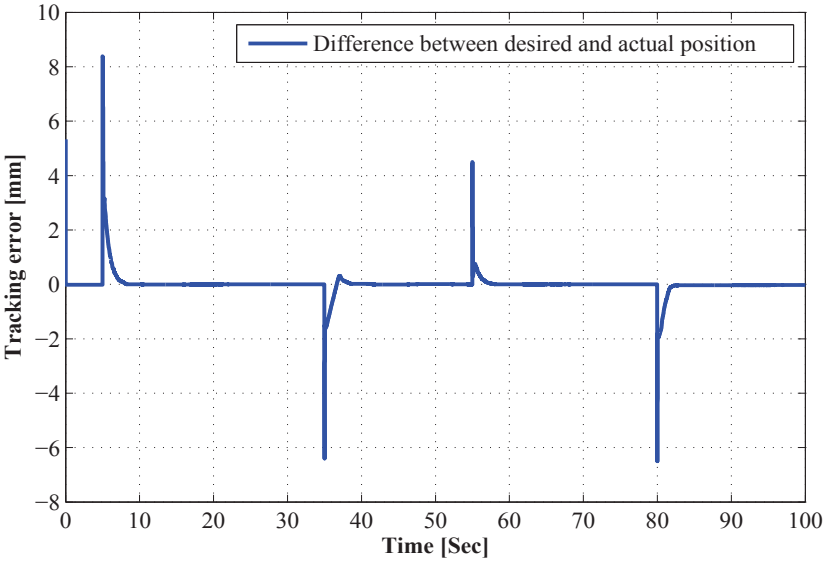

FIGURE 5.14. *Error in the position tracking with and without knocker*

In Fig. 5.15, the output results for the position tracking of the VGT pneumatic actuator are shown for friction observer. The controller output is shown in Fig. 5.16. The error difference with the friction observer is provided in Fig. 5.17. The position error is also

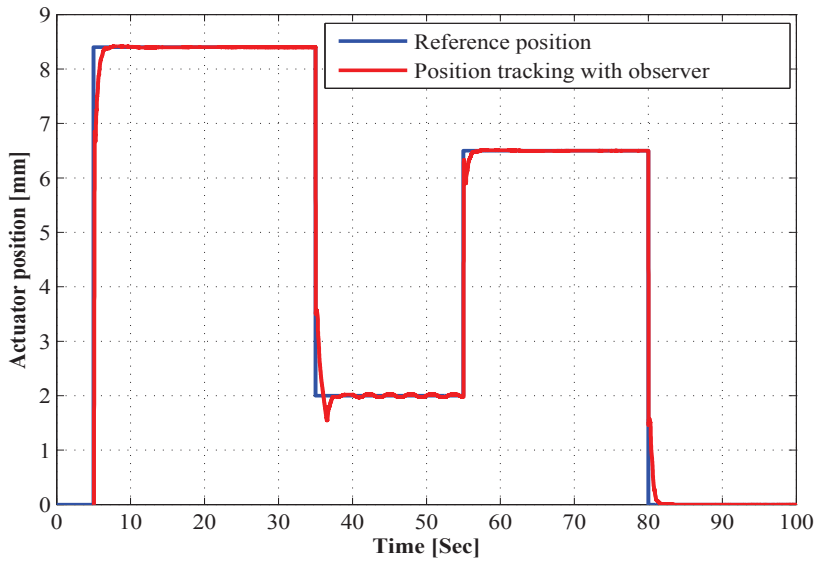

FIGURE 5.15. *Friction compensation with feedback observer*

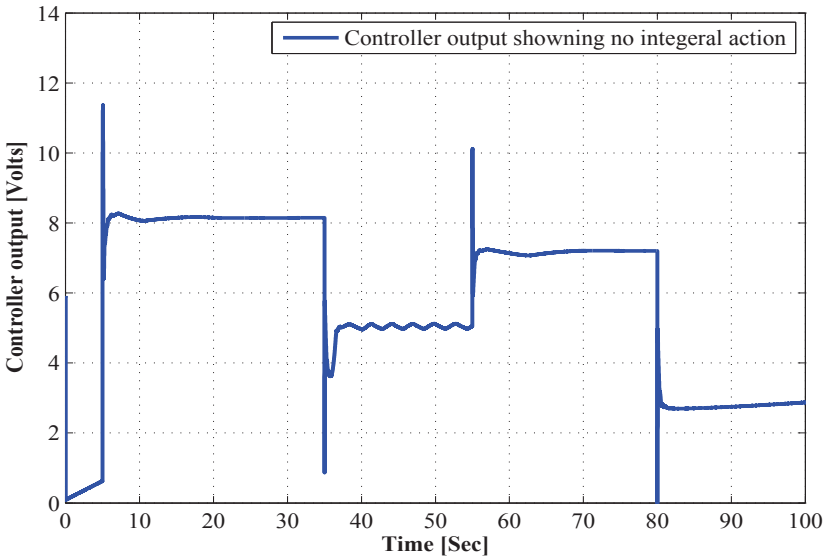

FIGURE 5.16. *Control signal applied to the actuator*

reduced in this case which shows the effectiveness of this approach.

The experimental results shown above are performed on the real system with $\hat{\theta} = 1$. This implies that there is no external force due to exhaust gas pressure. For the time being, validation of controller with external perturbation forces is not possible because of test bench limitations. So, to validate our controller, the aerodynamic force is induced in the system, using adaptive LuGre model when exhaust gas pressure at the inlet of turbine is kept at $1500mBar$. The estimated aerodynamic force is added as an external perturbation

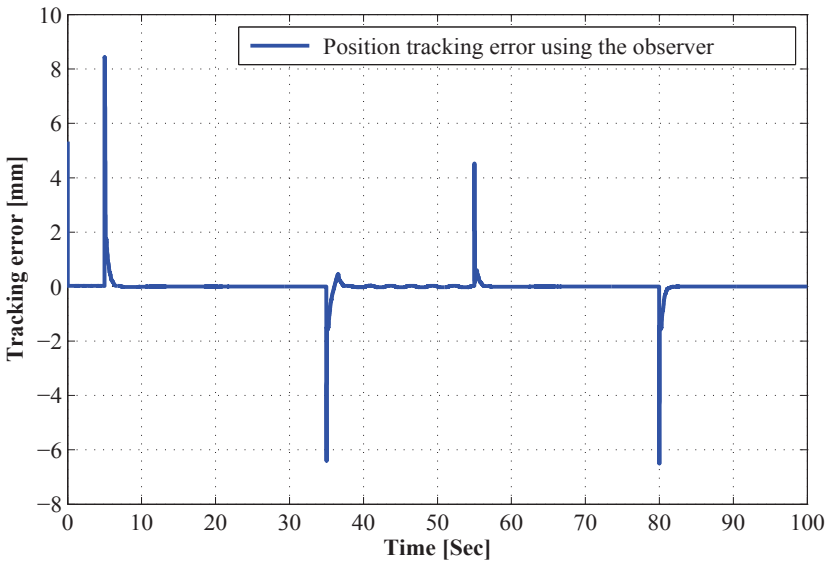

FIGURE 5.17. *Error in the position tracking with and without feedback observer*

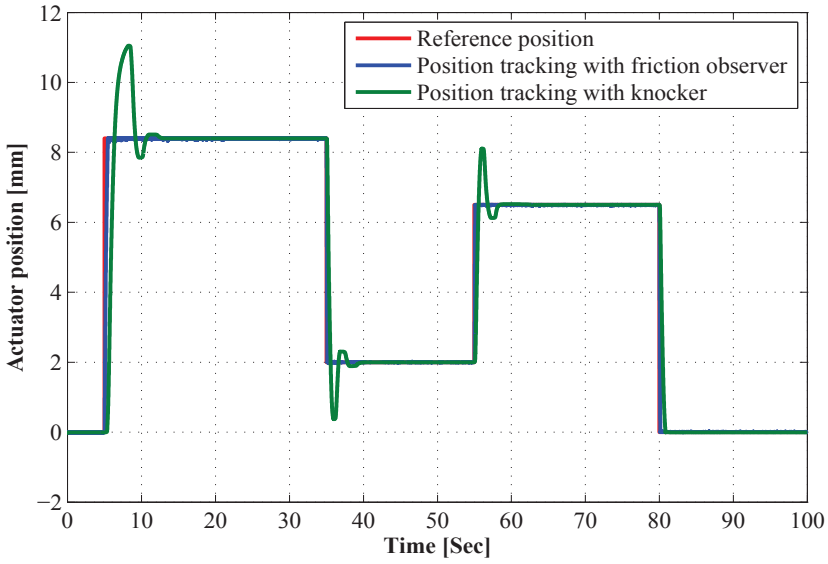

FIGURE 5.18. *Simulation results with friction compensation techniques when exhaust gas produces aerodynamic force*

force. So, the performance of the controller with external force is shown in Fig. 5.18 for both knocker and friction observer. The simulation results prove that model based friction observer is more robust and give better performance as compared to the knocker.

5.4 ADVANCED CONTROL DESIGN

In the previous section, we saw that conventional methods of friction compensation are not integrated in control design, and are external to the control algorithm. This means that the desired closed-loop characteristics that were considered during control design, may not appear in actual implementation. For this problem, alternative control strategies based on fuzzy logic, sliding mode and backstepping control have been proposed in many publications, such as [51, 10, 80, 44, 73]. Amongst advanced techniques, Girin et al. [26] have proposed Higher-Order Sliding-mode controllers for electro-pneumatic actuators, which ensure finite time convergence, high accuracy and robustness. Adaptive gain Sliding Mode Control has been recently used for this control problem [70]. Backstepping has emerged as an effective method, in which friction compensation is considered during control design itself.

In the research works mentioned above, all system states are considered to be known. Unfortunately this is not the case in practical applications, as the control of pneumatic actuators depends upon precise pressure measurements. The cost of high-speed pressure sensors does not permit manufacturers to integrate them in actuators. As friction is also dynamic in nature [65], its dynamics need to be taken into account in control design. These dynamics cannot be measured and require estimation from other means. Some attempts were made to use Position-Velocity-Acceleration (PVA) control methods for pneumatic actuator control with friction compensation (for example, [64]), however Pandian et al. [67] demonstrated clearly that the use of pressure states is essential for precise and robust control. In contemporary literature, observer based friction compensation has been studied in many works for similar applications. Canudas et al. [12] were the first to propose LuGre model based friction observer for second order mechanical systems. The LuGre friction model is the most comprehensive dynamic model available today and it is widely used for developing models suitable for control purpose. In the seminary work [12], the authors have also highlighted that friction needs to be observed from the system error and control effort. In [22], the authors have presented new insights into the numerical real-time implementation of LuGre model based compensation. Their approach is based on High Gain Observers. In [76], the authors have proposed an adaptive cascaded controller with LuGre observer, using backstepping method. A LuGre based dual-observer has been developed in [87], which is also used in [71] for friction compensation.

The problem of pressure observer design has been the subject of many publications, with the motivation of developing controllers that are robust and do not offset the economic interest of using pneumatic actuators. Pandian et al. [67] have presented an

observer-controller using two observer schemes, the first based on continuous gains and the second based on sliding mode. The nonlinear mass-flow functions are assumed to be constant in the control and observer design, under certain hypotheses. While the application in this paper is on a double chamber actuator, the pressure of only one chamber is observed. The pressure in the second chamber is measured in the case of continuous observer and numerically estimated in the case of sliding mode observer. This partial observation implies that the observer error dynamics can guarantee ultimate boundedness only. Friction is not taken into consideration in either case. To compensate the observation error and friction, robust sliding mode controller is used to guarantee the overall system convergence. As friction is not modeled, the robust controller compensates it as well. Gulati et al. [29] have presented a globally stable Lyapunov based pressure observer for a similar system. The convergence of this observer is proven and shown experimentally. However, since other nonlinearities have not been taken into account, the authors have again used a robust Sliding-Mode controller to compensate for friction and other unmodeled phenomena.

In this section, we present two backstepping control methods for the electro-pneumatic actuator. The control objective is to force the actuator position x_1 to precisely track a reference trajectory x_{ref} in presence of friction and varying aerodynamic forces and with the position variable as the only available measurement. Therefore this is an output-feedback control problem. The control design is based on the simplified model given in equation (5.4) and the Adaptive LuGre model based friction and aerodynamic force model presented in Chapter 3. The first controller is of output feedback type, in which both friction and pressure states have been observed. The second controller is based on an adaptive friction compensation design. The advantage of using the composite friction and aerodynamic force model is that it is simple in its structure, therefore suitable for control purpose. Also, it allows both friction and aerodynamic force to be treated as a single composite resistive force in control design. The convergence of both controllers is proven through Lyapunov analysis and their performance is validated experimentally.

5.4.1 Control Design with Pressure Observation

In this section, we present a Lyapunov-based backstepping output feedback controller for a pneumatic actuator. A similar method has been successfully applied to our system in [56] and [42]. The main contribution of this controller is that both pressure and the resistive force have been observed, and the controller requires position feedback only. In comparison with contemporary research, both pressure and friction observation problems have been treated together in this work, to develop a comprehensive output

feedback control. The convergence of the controller-observer closed-loop system is demonstrated through Lyapunov analysis, which proves global exponential convergence. To evaluate practical performance, the controller is applied on a turbocharger installed on an industrial engine test bench. The experimental results show the effectiveness of the controller-observer system.

5.4.1.1 SLIDING MODE OBSERVER

While commercial actuators are equipped with position sensors only, velocity can easily be estimated by using robust differentiators or finite time observers. In this work, we have estimated velocity from measured position using the robust differentiator given in [47]. Considering the model equation (5.4), this differentiator guarantees $\hat{x}_2$ will converge to x_2 in finite time t_i, for all $t > t_i$, and for all subsequent time instances, the derivative can be considered as the actual velocity. With the assumption that the motion states are known, in this section, we present the observers for pressure and friction state. Moreover, the pressure dynamics are represented with the following mass-flow function for Lyapunov analysis

$$f(u, x_4) = \dot{m}_{act} = a_0 + b_1 u + a_1 x_4 + a_2 x_4^2 + b_2 u^2. \tag{5.10}$$

To design the observer for pressure, the error of function $f(u, x_4)$ for observed and actual pressure is given by the following equation

$$\bar{f} = (a_1 + a_2 (x_4 + \hat{x}_4)) \varepsilon_4 = \tilde{f} \varepsilon_4, \tag{5.11}$$

where $\bar{f} = f(u, x_4) - f(u, \hat{x}_4)$ and it can be shown using equation (5.10) that $\tilde{f} < 0$ for all values of the PWM control input u. The observer is designed using sliding mode, as follows:

$$\begin{aligned}
\dot{\hat{x}}_1 &= \hat{x}_2 + \alpha_1 \varepsilon_1 + K_1 sign(\varepsilon_1), \\
\dot{\hat{x}}_2 &= \left[\left(\left(p_{atm} - \hat{x}_4\right) A_d - b_d \hat{x}_2 - (F_0 + k_{sm} x_1) - \hat{\theta}\,(\sigma_1 + \sigma_2)\,\hat{x}_2 - \hat{\theta}\,(\sigma_0 - \sigma_0 \sigma_1 |x_2| \alpha(x_2))\,\hat{x}_3\right) / m_d\right] \\
&\quad + \alpha_2 \varepsilon_2 + K_2 sign(\varepsilon_2), \\
\dot{\hat{x}}_3 &= \hat{x}_2 - \sigma_0 \alpha(x_2) |x_2| \hat{x}_3 + \alpha_3 \varepsilon_1 + \alpha_4 \varepsilon_2 + K_3 sign(\varepsilon_1) + K_4 sign(\varepsilon_2), \\
\dot{\hat{x}}_4 &= \frac{R T_{act}}{V_{act}} \left(\hat{f}(u, \hat{x}_4)\right) + \frac{A_d x_2}{V_{act}} \hat{x}_4 + \alpha_5 \varepsilon_1 + \alpha_6 \varepsilon_2 + K_5 sign(\varepsilon_1) + K_6 sign(\varepsilon_2),
\end{aligned} \tag{5.12}$$

where K_i and α_i $(i = 1..6)$ are constants, the conditions on which would determined later. The estimation errors $\varepsilon_i = x_i - \hat{x}_i$ $(i = 1..4)$ are obtained by subtracting equation (5.12) from (5.4), as

$$\begin{aligned}
\dot{\varepsilon}_1 &= -\alpha_1\varepsilon_1 + \varepsilon_2 - K_1 sign(\varepsilon_1), \\
\dot{\varepsilon}_2 &= \left[\left(A_d\varepsilon_4 - b_d\varepsilon_2 - k_{sm}\varepsilon_1 - \hat{\theta}\left(\sigma_1+\sigma_2\right)\varepsilon_2 - \hat{\theta}\left(\sigma_0 - \sigma_0\sigma_1|x_2|\alpha(x_2)\right)\varepsilon_3\right)/m_d\right] - \\
&\quad -\alpha_2\varepsilon_2 - K_2 sign(\varepsilon_2), \\
\dot{\varepsilon}_3 &= \varepsilon_2 - \sigma_0\alpha(x_2)|x_2|\varepsilon_3 - \alpha_3\varepsilon_1 - \alpha_4\varepsilon_2 - K_3 sign(\varepsilon_1) - K_4 sign(\varepsilon_2), \\
\dot{\varepsilon}_4 &= \left(\tilde{f} - \frac{A_d x_2}{V_{act}}\right)\varepsilon_4 - \alpha_5\varepsilon_1 - \alpha_6\varepsilon_2 - K_5 sign(\varepsilon_1) - K_6 sign(\varepsilon_2).
\end{aligned} \tag{5.13}$$

The error dynamics can be written in the matrix form given in (5.14).

$$\begin{bmatrix} \dot{\varepsilon}_1 \\ \dot{\varepsilon}_2 \\ \dot{\varepsilon}_3 \\ \dot{\varepsilon}_4 \end{bmatrix} = \begin{bmatrix} -\alpha_1 & 1 & 0 & 0 \\ \dfrac{-k_{sm}}{m_d} & \dfrac{-b_d}{m_d} - \dfrac{\hat{\theta}\left(\sigma_1+\sigma_2\right)}{m_d} - \alpha_2 & \dfrac{\hat{\theta}\left(\sigma_0 - \sigma_0\sigma_1|x_2|\alpha(x_2)\right)}{m_d} & \dfrac{-A_d}{m_d} \\ -\alpha_3 & 1-\alpha_4 & -\sigma_0\alpha(x_2)|x_2| & 0 \\ -\alpha_5 & -\alpha_6 & 0 & \tilde{f} - \dfrac{A_d x_2}{V_{act}} \end{bmatrix} \begin{bmatrix} \varepsilon_1 \\ \varepsilon_2 \\ \varepsilon_3 \\ \varepsilon_4 \end{bmatrix} - \begin{bmatrix} K_1 & 0 \\ 0 & K_2 \\ K_3 & K_4 \\ K_5 & K_6 \end{bmatrix} \begin{bmatrix} sign(\varepsilon_1) \\ sign(\varepsilon_2) \end{bmatrix}. \tag{5.14}$$

Here K_3 and K_5 are positive arbitrary constants and α_i are positive constants chosen such that the eigenvalues of the 4×4 matrix are at desired locations in the left-half of the complex plain. For large positive values of K_1 and K_2, we obtain

$$\begin{aligned}
-\alpha_1\varepsilon_1 + \varepsilon_2 - K_1 sign(\varepsilon_1) &< 0, \\
-\frac{-k_{sm}}{m_d}\varepsilon_1 - \left(\frac{b_d}{m_d} - \frac{\hat{\theta}\left(\sigma_1+\sigma_2\right)}{m_d} - \alpha_2\right)\varepsilon_2 + \frac{\hat{\theta}\left(\sigma_0 - \sigma_0\sigma_1|x_2|\alpha(x_2)\right)}{m_d}\varepsilon_3 - \frac{A_d}{m_d}\varepsilon_4 - K_2 sign(\varepsilon_2) &< 0.
\end{aligned} \tag{5.15}$$

Then the errors ε_1 and ε_2 would converge in finite time to the sliding surface $\varepsilon_1 = \varepsilon_2 = 0$. Using the concept of equivalent control [91], we obtain the following equations

$$\begin{aligned}
sign(\varepsilon_1) &= 0, \\
sign(\varepsilon_2) &= -\frac{1}{K_2}\left[\frac{\hat{\theta}\left(\sigma_0 - \sigma_0\sigma_1|x_2|\alpha(x_2)\right)}{m_d}\varepsilon_3 - \frac{A_d}{m_d}\varepsilon_4\right].
\end{aligned} \tag{5.16}$$

By putting the values of $sign(\varepsilon_1)$ and $sign(\varepsilon_2)$ in the error dynamics of friction and pressure observer we obtain the following system

$$\begin{bmatrix} \dot{\varepsilon}_3 \\ \dot{\varepsilon}_4 \end{bmatrix} = \begin{bmatrix} \frac{K_4}{K_2}\frac{\hat{\theta}\sigma_0}{m_d} & \frac{K_4}{K_2}\frac{A_d}{m_d} \\ \frac{K_6}{K_2}\frac{\hat{\theta}\sigma_0}{m_d} & \tilde{f}_0 + \frac{K_6}{K_2}\frac{A_d}{m_d} \end{bmatrix} \begin{bmatrix} \varepsilon_3 \\ \varepsilon_4 \end{bmatrix} + \begin{bmatrix} \Delta_1 \\ \Delta_2 \end{bmatrix}, \tag{5.17}$$

with

$$\Delta_1 = \left(\sigma_0 |x_2| \alpha(x_2) - \frac{K_4}{K_2}\frac{\hat{\theta}\sigma_0\sigma_1 |x_2| \alpha(x_2)}{m_d}\right)\varepsilon_3, \quad \Delta_2 = \left(\tilde{f}_1 - \frac{A_d x_2}{V_{act}} - \frac{K_6}{K_2}\frac{\hat{\theta}\sigma_0\sigma_1 |x_2| \alpha(x_2)}{m_d}\right)\varepsilon_4. \tag{5.18}$$

Equation (5.17) has the following form,

$$\dot{\varepsilon} = A\varepsilon + \Delta. \tag{5.19}$$

It is clear that for $K_2 > 0$, $K_6 > 0$ and $K_4 < 0$, the matrix A is Hurwitz. Then there exists a symmetric, positive definite matrix P, satisfying Lyapunov Equation:

$$PA + A^T P = -I.$$

We define the following Lyapunov function for the observer,

$$\begin{aligned} V_O &= \varepsilon^T P \varepsilon, \\ \dot{V}_O &\leq -\|\varepsilon\|^2 + c\|\varepsilon\|^2, \end{aligned} \tag{5.20}$$

where c is a positive constant. Then according to [37] (Chapter 9), for sufficiently large values of K_4 and K_6 we obtain $c < 1$ and $\dot{V}_O \leq -\bar{c} V_O$, where $\bar{c} = 1 - c$. This assures exponential convergence of the observer error ε to zero. Then the derivative becomes

$$\dot{V}_O \leq -\bar{c}\|\varepsilon\|^2. \tag{5.21}$$

5.4.1.2 BACKSTEPPING CONTROL DESIGN

The controller has been developed using backstepping method, which is a recursive procedure based on Lyapunov's stability theory. In this method, system states are chosen as virtual inputs to stabilize the corresponding subsystems.

Step1: According to the control objective given in Section 2, the following error function is chosen:

$$s_1 = \lambda e_1 + \dot{e}_1, \tag{5.22}$$

Where $e_1 = x_1 - x_{ref}$ is the tracking error. The term λ is a positive constant and x_{ref} is the reference signal to be tracked. The error function dynamics are given as

$$\dot{s}_1 = \dot{x}_2 - \left[\ddot{x}_{ref} - \lambda\left(x_2 - \dot{x}_{ref}\right)\right], \tag{5.23}$$

which can be rewritten using equation (5.4), as

$$\begin{aligned}\dot{s}_1 = \lambda\left(x_2 - \dot{x}_{ref}\right) - \ddot{x}_{ref} + \frac{1}{m_d}\left[p_{atm}A_d - F_0 - x_4 A_d - k_{sm}x_1 - b_d x_2 - \ddot{x}_{ref}\right. \\ \left. -\hat{\theta}\left(\sigma_1 + \sigma_2\right)x_2 - \hat{\theta}\left(\sigma_0 - \sigma_0\sigma_1|x_2|\alpha(x_2)x_3\right)\right].\end{aligned} \tag{5.24}$$

We choose a virtual control, x_4^*, as follows

$$\begin{aligned}x_4^* = \frac{-1}{A_d}\left[k_{sm}x_1 + b_d x_2 + F_0 - p_{atm}A_d + \hat{\theta}\left(\sigma_1 + \sigma_2\right)x_2 + \right. \\ \left. \hat{\theta}\left(\sigma_0 - \sigma_0\sigma_1|x_2|\alpha(x_2)\right)\hat{x}_3 + m_d\left(\ddot{x}_{ref} - \lambda\left(x_2 - \dot{x}_{ref}\right)\right) - k_d s_1\right],\end{aligned} \tag{5.25}$$

where k_d is a positive constant. In this case,

$$\dot{s}_1 = -K_d s_1 - \frac{A_d}{m_d}s_2 - \frac{1}{m_d}\hat{\theta}\left(\sigma_0 - \sigma_0\sigma_1|x_2|\alpha(x_2)\right)\varepsilon_3, \tag{5.26}$$

where $s_2 = x_4 - x_4^*$ **Step 2:** The dynamics of s_2 is given as

$$\begin{aligned}\dot{s}_2 &= \dot{x}_4 - \dot{x}_4^*, \\ &= \frac{RT_{act}}{V_{act}}\left(f(u, x_4)\right) - \frac{x_4}{V_{act}}A_d x_2 - \dot{x}_4^*.\end{aligned} \tag{5.27}$$

By adding the expression for the pressure dynamics and introducing the virtual control input x_4^* into equation (5.27), we get

$$\begin{aligned}\dot{s}_2 = \frac{RT_{act}}{V_{act}}\left(f(u, x_4)\right) - \frac{x_4}{V_{act}}A_d x_2 + \frac{1}{A_d}\left[k_{sm}x_2 + b_d\dot{x}_2 + \hat{\theta}\left(\sigma_1 + \sigma_2\right)\dot{x}_2 + \right. \\ \left. \left[\hat{\theta}\left(\sigma_0 - \sigma_0\sigma_1|x_2|\alpha(x_2)\right)\hat{x}_3\right]' + m_d\left(\dddot{x}_{ref} - \lambda\left(\dot{x}_2 - \ddot{x}_{ref}\right)\right) - k_d\dot{s}_1\right].\end{aligned} \tag{5.28}$$

Equation (5.28) can be rearranged as

$$\begin{aligned}\dot{s}_2 = \frac{RT_{act}}{V_{act}}\left(f(u, x_4)\right) - \frac{x_4}{V_{act}}A_d x_2 + \frac{1}{A_d}\left[k_{sm}x_2 + \left(b_d + \hat{\theta}\left(\sigma_1 + \sigma_2\right) - \lambda m_d\right)\dot{x}_2 \right. \\ \left. + \left[\hat{\theta}\left(\sigma_0 - \sigma_0\sigma_1|x_2|\alpha(x_2)\right)\hat{x}_3\right]' + m_d\dddot{x}_{ref} + m_d\lambda\ddot{x}_{ref} - k_d\dot{s}_1\right].\end{aligned} \tag{5.29}$$

By introducing the values of derivative terms, we obtain

$$\begin{aligned}\dot{s}_2 = \frac{RT_{act}}{V_{act}}\left(f(u, x_4)\right) - \frac{x_4}{V_{act}}A_d x_2 + \frac{1}{A_d}\left[k_{sm}x_2 + \left(b_d + \hat{\theta}\left(\sigma_1 + \sigma_2\right) - \lambda m_d\right)\right. \\ \left[\left(\left(p_{atm} - x_4\right)A_d - b_d x_2 - \left(F_0 + k_{sm}x_1\right) - \hat{\theta}\left(\sigma_1 + \sigma_2\right)x_2 - \left[\hat{\theta}\left(\sigma_0 - \sigma_0\sigma_1|x_2|\alpha(x_2)\right)\hat{x}_3\right]'\right)/m_d\right] \\ \left. + m_d\dddot{x}_{ref} + m_d\lambda\ddot{x}_{ref} - k_d\left(-K_d s_1 - \frac{A_d}{m_d}s_2 - \frac{1}{m_d}\hat{\theta}\left(\sigma_0 - \sigma_0\sigma_1|x_2|\alpha(x_2)\right)\varepsilon_3\right)\right].\end{aligned} \tag{5.30}$$

Let us now redefine s_2 in terms of $\hat{x}_4$,

$$s_2 = \varepsilon_4 + \bar{s}_2, \tag{5.31}$$

where $\bar{s}_2$ is defined as $\hat{x}_4 - \hat{x}_4^*$. Then, $\dot{s}_2$ becomes

$$\begin{aligned}\dot{s}_2 = \frac{RT_{act}}{V_{act}}\left(f(u, x_4)\right) - \frac{x_4}{V_{act}}A_d x_2 + \frac{1}{A_d}\left[k_{sm}x_2 + \left(b_d + \hat{\theta}\left(\sigma_1 + \sigma_2\right) - \lambda m_d\right)\right. \\ \left[\left(\left(p_{atm} - x_4\right)A_d - b_d x_2 - \left(F_0 + k_{sm}x_1\right) - \hat{\theta}\left(\sigma_1 + \sigma_2\right)x_2 - \left[\hat{\theta}\left(\sigma_0 - \sigma_0\sigma_1|x_2|\alpha(x_2)\right)\hat{x}_3\right]'\right)/m_d\right] \\ \left. + m_d\dddot{x}_{ref} + m_d\lambda\ddot{x}_{ref} - k_d\left(-K_d s_1 - \frac{A_d}{m_d}\left(\varepsilon_4 + \bar{s}_2\right) - \frac{1}{m_d}\hat{\theta}\left(\sigma_0 - \sigma_0\sigma_1|x_2|\alpha(x_2)\right)\varepsilon_3\right)\right].\end{aligned} \tag{5.32}$$

Let us recall $f(u, x_4) = a_0 + b_1 u + a_1 x_4 + a_2 x_4^2 + b_2 u^2$. We define

$$U = a_0 + b_1 u + b_2 u^2. \tag{5.33}$$

U is chosen such that for a sufficiently large positive constant K_U,

$$\begin{aligned}\frac{RT_{act}}{V_{act}} U = &-K_U \bar{s}_2 - \frac{RT_{act}}{V_{act}} \left(a_1 \hat{x}_4 + a_2 \hat{x}_4^2\right) + \frac{x_4}{V_{act}} A_d x_2 - \frac{1}{A_d} \left[k_{sm} x_2 + \left(b_d + \hat{\theta}\left(\sigma_1 + \sigma_2\right) - \lambda m_d\right)\right. \\ &\left.\left[\left(\left(p_{atm} - \ hat x_4\right) A_d - b_d x_2 - \left(F_0 + k_{sm} x_1\right) - \hat{\theta}\left(\sigma_1 + \sigma_2\right) x_2 - \left[\hat{\theta}\left(\sigma_0 - \sigma_0 \sigma_1 |x_2| \alpha(x_2)\right) \hat{x}_3\right]'\right) / m_d\right]\right. \\ &\left. + m_d \dddot{x}_{ref} + m_d \lambda \ddot{x}_{ref} - k_d \left(-K_d s_1 - \frac{A_d}{m_d} \bar{s}_2\right)\right].\end{aligned} \tag{5.34}$$

This implies that

$$\begin{aligned}\dot{s}_2 &= -K_U s_2 + \left(-\frac{1}{m_d}\left(b_d + \hat{\theta}\left(\sigma_1 + \sigma_2\right) - \lambda m_d\right) - k_d \left(-\frac{1}{m_d} \hat{\theta}\left(\sigma_0 - \sigma_0 \sigma_1 |x_2| \alpha(x_2)\right)\right)\right) \varepsilon_3, \\ &\quad + \left(\frac{RT_{act}}{V_{act}}\left(a_1 + a_2(x_4 + \hat{x}_4)\right) + K_d \frac{A_d}{m_d} + K_U\right) \varepsilon_4.\end{aligned} \tag{5.35}$$

From here, u can be determined simply by solving the second order equation $b_2 u^2 + b_1 u + a_0 - U = 0$, and taking the positive value:

$$u = \frac{-b_1 + \sqrt{b_1^2 - 4 b_2 (a_0 - U)}}{2(b_2)}.$$

5.4.1.3 LYAPUNOV ANALYSIS

We will now demonstrate the exponential convergence of the closed-loop controller observer system. The Lyapunov function is as follows:
We recall $V_O = \varepsilon^T P \varepsilon$, the Lyaponov function associated with the observer as given in Equation (5.20), and introduce the function V_C, associated with the controller:

$$V_C = \frac{1}{2}\left[s_1^2 + s_2^2\right]. \tag{5.36}$$

Then the complete Lyapunov function for the controller and observer is given as

$$\begin{aligned}V &= V_C + K V_O, \\ &= \frac{1}{2}\left[s_1^2 + s_2^2\right] + K \varepsilon^T P \varepsilon.\end{aligned} \tag{5.37}$$

The term K is a positive constant, determined later on. For clarity and ease in calculation, we will analyze V_C and V_O separately. Starting with V_C, the derivative of this function is

$$\begin{aligned}
\dot{V}_C &= s_1\dot{s}_1 + s_2\dot{s}_2, \\
&= s_1\left(-K_d s_1 - \frac{A_d}{m_d}s_2 - \frac{1}{m_d}\hat{\theta}\left(\sigma_0 - \sigma_0\sigma_1|x_2|\alpha(x_2)\right)\varepsilon_3\right) \\
&\quad + s_2\left(\begin{array}{l} -K_U s_2 + \left(-\frac{1}{m_d}\left(b_d + \hat{\theta}\left(\sigma_1+\sigma_2\right) - \lambda m_d\right) - k_d\left(-\frac{1}{m_d}\hat{\theta}\left(\sigma_0 - \sigma_0\sigma_1|x_2|\alpha(x_2)\right)\right)\varepsilon_3\right) \\ + \left(\frac{RT_{act}}{V_{act}}\left(a_1 + a_2(x_4+\hat{x}_4)\right) + K_d\frac{A_d}{m_d} + K_U\right)\varepsilon_4 \end{array}\right), \\
&= -K_d s_1^2 - K_U s_2^2 - \frac{A_d}{m_d}s_1 s_2 + g_1 s_1\varepsilon_3 + g_2 s_2\varepsilon_3 + g_3 s_2\varepsilon_4.
\end{aligned} \tag{5.38}$$

where

$$\begin{aligned}
g_1 &= \frac{1}{m_d}\hat{\theta}\left(\sigma_0 - \sigma_0\sigma_1|x_2|\alpha(x_2)\right), \\
g_2 &= -\frac{1}{m_d}\left(b_d + \hat{\theta}\left(\sigma_1+\sigma_2\right) - \lambda m_d\right) - k_d\left(-\frac{1}{m_d}\hat{\theta}\left(\sigma_0 - \sigma_0\sigma_1|x_2|\alpha(x_2)\right)\right), \\
g_3 &= \left(\frac{RT_{act}}{V_{act}}\left(a_1 + a_2(x_4+\hat{x}_4)\right) + K_d\frac{A_d}{m_d} + K_U\right).
\end{aligned} \tag{5.39}$$

By using the inequality $|ab| \leq \frac{1}{2}a^2 + \frac{1}{2}b^2$, we get

$$\begin{aligned}
\dot{V}_C \leq\ & -\left(K_d - \frac{A_d}{2m_d} - \frac{|g_1|}{2}\right)s_1^2 - \left(K_U - \frac{A_d}{2m_d} - \frac{|g_2|}{2} - \frac{|g_3|}{2}\right)s_2^2 \\
& + \left(\frac{|g_1|}{2} + \frac{|g_2|}{2}\right)\varepsilon_3^2 + \left(\frac{|g_3|}{2}\right)\varepsilon_4^2.
\end{aligned} \tag{5.40}$$

Now, considering the function V_O, its derivative according to Equation (5.21) is given as

$$\dot{V}_O \leq -\bar{c}\,\|\varepsilon\|^2. \tag{5.41}$$

Using Equations (5.40) and (5.41), the derivative of the Lyapunov function V in Equation (5.37) becomes

$$\begin{aligned}
\dot{V} \leq\ & -\left(K_d - \frac{A_d}{2m_d} - \frac{|g_1|}{2}\right)s_1^2 - \left(K_U - \frac{A_d}{2m_d} - \frac{|g_2|}{2} - \frac{|g_3|}{2}\right)s_2^2 \\
& + \left(\frac{|g_1|}{2} + \frac{|g_2|}{2}\right)\varepsilon_3^2 + \left(\frac{|g_3|}{2}\right)\varepsilon_4^2 - K\bar{c}\,\|\varepsilon\|^2.
\end{aligned} \tag{5.42}$$

Then, for sufficiently large values of K_d, K_U and K, the inequality:

$$\dot{V} \leq -C_1 s_1^2 - C_2 s_2^2 - C_3\,\|\varepsilon\|^2 \tag{5.43}$$

holds true for some positive constants C_1, C_2 and C_3. Therefore the controller errors s_1 and s_2, and observer errors ε_3 and ε_4 converge exponentially to zero.

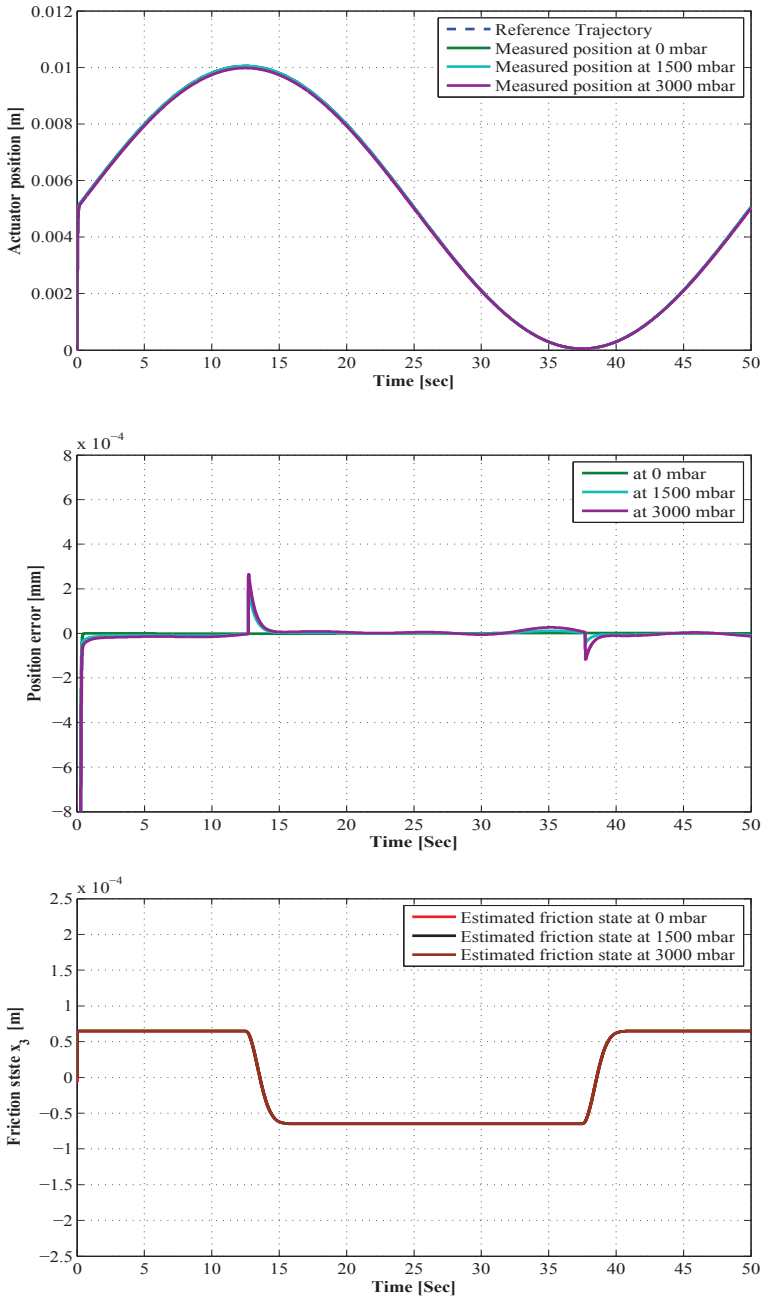

FIGURE 5.19. *Signal 1: (a) Trajectory tracking (b) Tracking error and (c) Observed friction state*

5.4.1.4 EXPERIMENTAL RESULTS

The experiments were performed on the industrial engine test bench presented in chapter 3. For validation of controllers with friction compensation, it is important to test them using trajectories with changing directions. This is because the characteristic nonlinear behavior of friction is most significant when velocity changes its sign. On the other hand, in real operation the actuator mainly performs positioning tasks, and trajectory track-

ing is rare. In the experiments, we have considered both these aspects and performed two types of tests. The first test is for validating friction compensation and the chosen reference is an offset sinusoid, given as follows,

$$Signal1 = 0.005sin(0.125t) + 0.005. \tag{5.44}$$

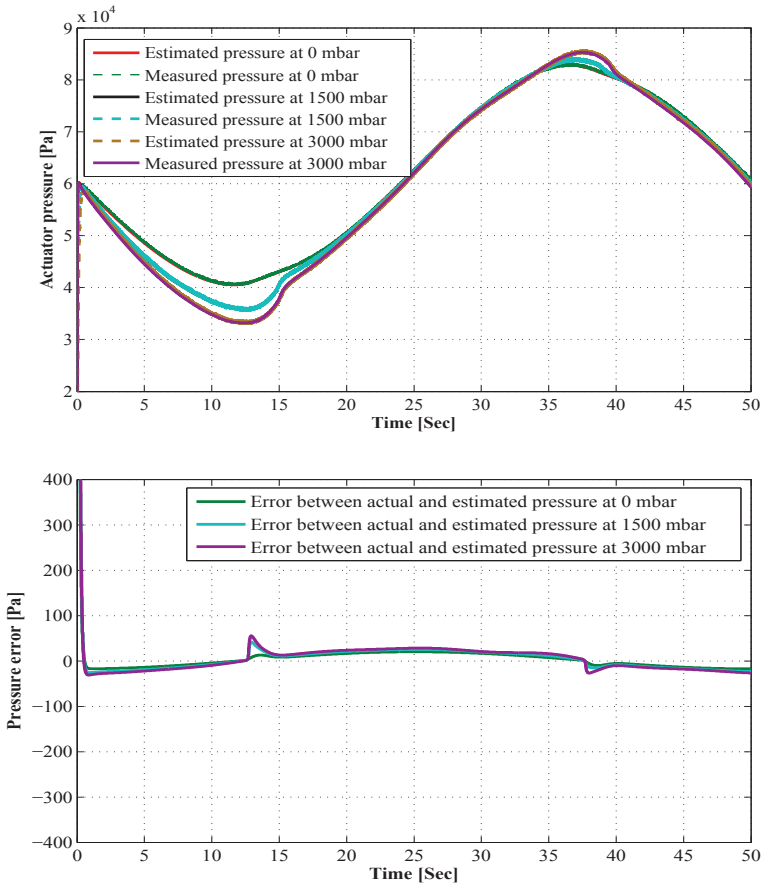

FIGURE 5.20. *Signal 1: (a) Estimated and measured pressures and (b) Pressure observer error*

The behavior of the closed-loop system is shown in Figure 5.19. It can be seen that the actuator tracks the reference trajectory closely, with a negligible error of the order of $10^{-3}mm$ for all turbine inlet pressures. The observed friction state is also shown in this figure. The aerodynamic force does not exist at $0mbar$ and friction is the only resistive force acting on the actuator. The behavior of this force changes significantly as the turbine inlet pressure increases and acts upon the VGT vanes, even though friction remains the same. This adaptive behavior of friction and aerodynamic force F_{ft} is already discussed in detail in chapter 3.

Figure 5.20 shows the output of the pressure observer. It is clear that the actuator requires more pressure to compensate the increasing composite force, which varies with changes

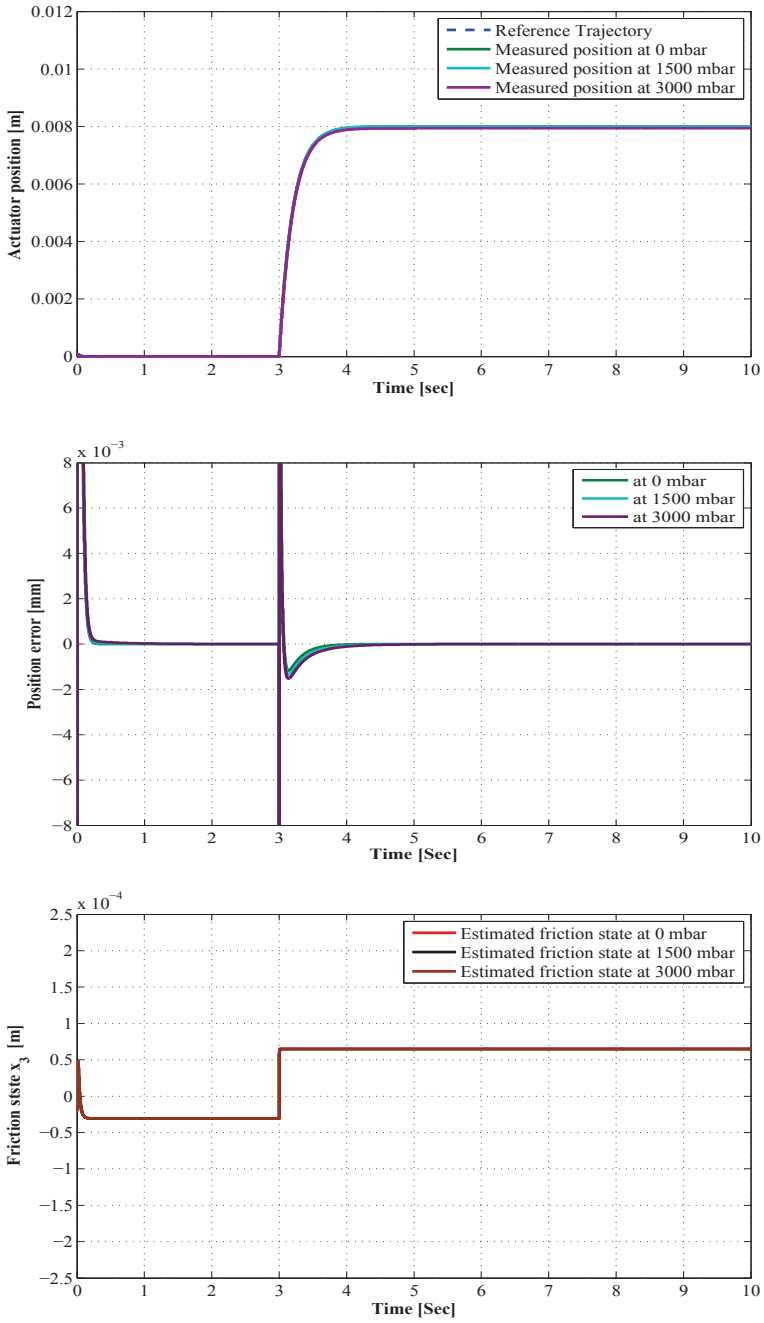

FIGURE 5.21. *Signal 2: (a) Actuator positioning (b) Positioning error and (c) Observed friction state*

in the aerodynamic force as the turbine inlet pressure changes. The observed pressure values are compared with the measured values obtained from the test bench sensor. This figure shows that the pressure observer converges rapidly and it accurately tracks the actual pressure. The error remains less than $100Pa$ after convergence.

The second test is for validating the positioning characteristics of the controller and the

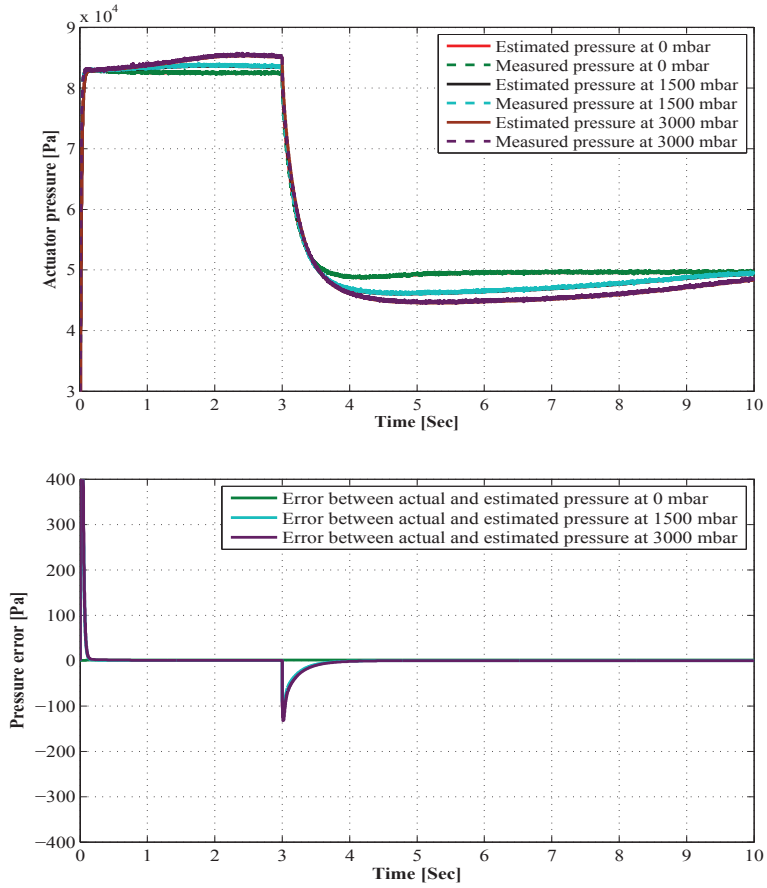

FIGURE 5.22. *Signal 2: (a) Estimated and measured pressures and (b) Observer error*

chosen position reference signal is a step, given as:

$$Signal2 = \begin{cases} 0 & 0 \leq t < 3 \\ 0.008 & t \geq 3 \end{cases} \tag{5.45}$$

Figure 5.21 shows the behavior of the closed-loop system as the reference changes its value. It can be seen that controller positions the actuator with a response time of $500msec$. The response is rapid and the error is negligible despite of the variation in the resistive force F_{ft}. The observed friction state is also shown in this figure for the second trajectory. There is no difference in the characteristics of total friction F_{ft} as compared to the sinusoidal test. In Figure 5.22, it can be seen that the pressure observer is not affected by the difference of trajectories. The observed pressure remains close to the actual pressure and the error remains at the negligible peak of $100Pa$.

These results show that the output feedback position control objective is achieved successfully and effectively using the proposed backstepping controller-observer system.

5.4.2 CONTROL DESIGN WITH ADAPTIVE FRICTION COMPENSATION

As described in chapter 3 that we may require expensive tests to obtain an adaptive friction model which could be used for model based control of VGT pneumatic actuator. However, to avoid this expensive and time consuming procedure, we can develop an adaptive controller for friction compensation. Adaptive friction compensation techniques have already been addressed in the literature for electric actuators [87, 96]. But, they are not considered yet for the pneumatic actuators to the best of author's knowledge. The system dynamics depends upon multiple states. As the actuator system is equipped with position and pressure sensor, the other state i.e. the friction state need to be observed. In the following section we will first present a dual friction observer. Based on this observer, the controller will be design by using backstepping technique which will be followed by the demonstration to show the convergence of the complete system with Lyapunov candidate function. The control objective is to force x_1 to follow a reference position trajectory x_{ref} in a robust manner such that the feedback error e_1 converge asymptotically to zero.

5.4.2.1 STATE SPACE MODEL FORMULATION

To simplify the control design, let us reformulate the system equations in (5.4) and (3.6) in chapter 3 by defining the following parameters

$$\begin{aligned}
a_0 &= \frac{p_{atm}A_d - F_0}{m_d} \quad , \quad a_1 = \frac{A_d}{m_d} \quad , \quad a_2 = \frac{k_{sm}}{m_d} \quad , \quad a_3 = \frac{b_d}{m_d} \\
\beta_0 &= \frac{\sigma_0}{m_d} \quad , \quad \beta_1 = \frac{\sigma_1 + \sigma_2}{m_d} \quad , \quad \beta_2 = \frac{\sigma_0\sigma_1}{m_d} \\
c_0 &= \frac{RT_{act}}{V_{act}}\phi(\delta p) \quad , \quad c_1 = \frac{RT_{act}}{V_{act}}\psi(\delta p) \quad , \quad c_2 = \frac{A_d}{V_{act}}
\end{aligned}$$

Using new notations for the parameters, we obtain the state space model of the actuator with the LuGre friction model which is shown in the equation set (5.46). Where x_1, x_2, x_3 and x_4 are the state variables for the diaphragm position, its velocity, the friction state and the actuator pressure, respectively.

$$\begin{aligned}
\dot{x}_1 &= x_2 \\
\dot{x}_2 &= a_0 - a_1 x_4 - a_2 x_1 - a_3 x_2 - \beta_0 x_3 - \beta_1 x_2 + \beta_2 \alpha(x_2)|x_2|x_3 \\
\dot{x}_3 &= x_2 - |x_2|\alpha(x_2)x_3 \\
\dot{x}_4 &= c_0 + c_1 u + c_2 x_2 x_4
\end{aligned} \tag{5.46}$$

5.4.2.2 FRICTION OBSERVER

As the internal state x_3 of the system is not measurable, so we will determine it with a dual friction observers, i.e. $\hat{z}_0$ and $\hat{z}_1$ which are given as under. A similar approach has been presented in [54], where friction observer is presented without parameters adaption.

$$\begin{aligned}\dot{\hat{z}}_0 &= x_2 - \sigma_0|x_2|\alpha(x_2)\hat{z}_0 + \jmath_0 \\ \dot{\hat{z}}_1 &= x_2 - \sigma_0|x_2|\alpha(x_2)\hat{z}_1 + \jmath_1\end{aligned} \tag{5.47}$$

where $\jmath_0$ and $\jmath_1$ are the compensation terms which will be defined later. By subtracting equation (3.6) from (5.47), we obtain following error dynamics for friction state.

$$\begin{aligned}\dot{\tilde{z}}_0 &= -\sigma_0|x_2|\alpha(x_2)\tilde{z}_0 - \jmath_0 \\ \dot{\tilde{z}}_1 &= -\sigma_0|x_2|\alpha(x_2)\tilde{z}_1 - \jmath_1\end{aligned} \tag{5.48}$$

with $\tilde{z}_i = x_3 - \hat{z}_i$ for $i = 1, 2$

5.4.3 CONTROL DESIGN WITH BACKSTEPPING

We will now use adaptive backstepping design method for developing the position controller for pneumatic actuator.

Step1: Let the position tracking error e_1 be defined as

$$e_1 = x_1 - x_{ref} \tag{5.49}$$

The derivative of the position error is computed as

$$\dot{e}_1 = x_2 - \dot{x}_{ref} \tag{5.50}$$

Our first objective is to design a feedback control x_2^* in order to stabilize the error $e_1 = 0$. Therefore, x_2^* is chosen as

$$x_2^* = -k_1 e_1 + \dot{x}_{ref} \tag{5.51}$$

Where k_1 is strictly positive constant.

Step2: Since x_2 is state of the system, therefore the variable shift is required until we obtain actual input applied to the system.

$$e_2 = x_2 - x_2^* \tag{5.52}$$

By replacing x_2 and x_2^* from equations (5.50) and (5.51) in equation (5.52), we get

$$\dot{e}_1 = -k_1 e_1 + e_2 \tag{5.53}$$

Now, taking the derivative of equation (5.52) we obtain

$$\begin{aligned} \dot{e}_2 &= a_0 - a_1 x_4 - a_2 x_1 - a_3 x_2 - \beta_0 x_3 - \beta_1 x_2 + \beta_2 \alpha(x_2)|x_2| x_3 + k_1 \dot{e}_1 - \ddot{x}_{ref} \\ &= a_0 - a_1 x_4 - a_2 x_1 - a_3 x_2 - \beta_1 x_2 - \beta_0 x_3 + \beta_1 |x_2| \alpha(x_2) x_3 + k_1 \left(x_2 - \dot{x}_{ref}\right) - \ddot{x}_{ref} \end{aligned} \tag{5.54}$$

By introducing the second virtual control input x_3^* and replacing $e_2 = x_2 + k_1 e_1 - \dot{x}_{ref}$ we get

$$\begin{aligned} x_3^* &= \frac{1}{a_1}\left[a_0 + \left(k_2 - a_3 - \hat{\beta}_1 + k_1\right) x_2 - \left(k_1 + k_2\right) \dot{x}_{ref} + k_1 k_2 e_1 - a_2 x_1 - \right. \\ &\quad \left. \hat{\beta}_0 \hat{z}_0 + \hat{\beta}_2 |x_2| \alpha(x_2) \hat{z}_1 - \ddot{x}_{ref}\right] \\ &= \frac{1}{a_1} \vartheta_1 \end{aligned} \tag{5.55}$$

where $\tilde{\beta}_i = \beta_i - \hat{\beta}_i \ \forall i = 1..3$. Moreover, by introducing the virtual control input x_3^* into equation (5.54) we get the following error dynamics

$$\dot{e}_2 = -k_2 e_2 - a_1 e_3 - \tilde{\beta}_1 x_2 - \tilde{\beta}_0 \hat{z}_0 - \beta_0 \tilde{z}_0 + \tilde{\beta}_2 |x_2| \alpha(x_2) \hat{z}_1 + \beta_2 |x_2| \alpha(x_2) \tilde{z}_1 \tag{5.56}$$

with

$$\begin{aligned} -\beta_0 x_3 + \hat{\beta}_0 \hat{z}_0 = -\beta_0 x_3 + \beta_0 \hat{z}_0 - \beta_0 \hat{z}_0 + \hat{\beta}_0 \hat{z}_0 &= -\tilde{\beta}_0 \hat{z}_0 - \beta_0 \tilde{z}_0 \\ -\beta_2 x_3 + \hat{\beta}_2 \hat{z}_1 = -\beta_2 x_3 + \beta_2 \hat{z}_1 - \beta_2 \hat{z}_1 + \hat{\beta}_2 \hat{z}_1 &= -\tilde{\beta}_2 \hat{z}_1 - \beta_2 \tilde{z}_1 \end{aligned} \tag{5.57}$$

Step3: At this point e_2 is not available for control so the recursive procedure is repeated to reach control variable u. We will introduce the third virtual input as the pressure in the actuator chamber x_3^*.

$$e_3 = x_4 - x_3^* \tag{5.58}$$

Taking the time derivative of the above equation

$$\dot{e}_3 = \dot{x}_4 - \dot{x}_3^* \tag{5.59}$$

By replacing the pressure dynamics and the derivative of the virtual input function x_3^*, we get

$$\dot{e}_3 = c_0 + c_1 u + c_2 x_2 x_4 - \frac{1}{a_1}\vartheta_2 + \frac{1}{a_1}\frac{\partial \vartheta_1}{\partial x_2}\left[a_0 - a_1 x_4 - a_2 x_1 - a_3 x_2 - \beta_1 x_2 - \beta_0 x_3 + \beta_2 |x_2| \alpha(x_2) x_3\right] \tag{5.60}$$

where term ϑ_2 is the derivative of the ϑ_1 with respect to time.

$$\begin{aligned}\vartheta_2 = \Big[&-\dot{\hat{\beta}}_1 x_2 - (k_1+k_2)\,\ddot{x}_{ref} + (1+k_1k_2)\,\dot{e}_1 - a_2 x_2 - \hat{\beta}_0\dot{\hat{z}}_0 - \dot{\hat{\beta}}_0\hat{z}_0 + \dot{\hat{\beta}}_2|x_2|\alpha(x_2)\hat{z}_1 + \\ &\hat{\beta}_2|x_2|\alpha(x_2)\dot{\hat{z}}_1 - \dddot{x}_{ref}\Big]\end{aligned} \tag{5.61}$$

The term $\partial\vartheta_1/\partial x_2$ can be obtain by taking the derivative of ϑ_1 with respect to actuator velocity. Its expression is given below

$$\frac{\partial\vartheta_1}{\partial x_2} = \left(k_2 - a_3 - \hat{\beta}_1 + k_1\right) + \hat{\beta}_2 sign(x_2)\alpha(x_2)\hat{z}_1 + \frac{2\left(\alpha(x_2)\right)^2 x_2|x_2|\left(F_s - F_c\right)}{v_s e^{(x_2/v_s)^2}} \tag{5.62}$$

Now, based on the stabilizing function if we choose the control input u, such that

$$\begin{aligned}u = \frac{1}{c_1}\Big\{&-k_3e_3 - c_0 - c_2x_2x_4 + \frac{1}{a_1}\vartheta_2 + \frac{1}{a_1}\frac{\partial\vartheta_1}{\partial x_2} \\ &\left[a_0 - a_1x_4 - a_2x_1 - a_3x_2 - \hat{\beta}_1x_2 - \hat{\beta}_0\hat{z}_0 + \hat{\beta}_2|x_2|\alpha(x_2)\hat{z}_1\right]\Big\}\end{aligned} \tag{5.63}$$

The dynamics of error can be expressed as

$$\dot{e}_3 = -k_3e_3 - \frac{1}{a_1}\frac{\partial\vartheta_1}{\partial x_2}\left[-\tilde{\beta}_1x_2 + \beta_0\tilde{z}_0 + \tilde{\beta}_0\hat{z}_0 - \tilde{\beta}_2|x_2|\alpha(x_2)\hat{z}_1 - \beta_2|x_2|\alpha(x_2)\tilde{z}_1\right] \tag{5.64}$$

5.4.3.1 Stability analysis with Lyapunov function

the convergence of the system (5.4) with the adaptive control law (5.63) can be ensured by using Lyapunov candidate function. The compensation terms e.g. $\jmath_0$ and $\jmath_1$ will also be defined during the development process. The Lyapunov function for the closed loop system with adaptive backstepping control is defined as under

$$V = \frac{1}{2}e_1^2 + \frac{1}{2}e_2^2 + \frac{1}{2}e_3^2 + \frac{1}{2\gamma_0}\tilde{\beta}_0^2 + \frac{1}{2\gamma_1}\tilde{\beta}_1^2 + \frac{1}{2\gamma_2}\tilde{\beta}_2^2 + \frac{1}{2}\beta_0\tilde{z}_0^2 + \frac{1}{2}\beta_2\tilde{z}_1^2 \tag{5.65}$$

By taking the time derivative of the Lyapunov function (5.65)

$$\dot{V} = e_1\dot{e}_1 + e_2\dot{e}_2 + e_3\dot{e}_3 + \frac{1}{\gamma_0}\tilde{\beta}_0\dot{\tilde{\beta}}_0 + \frac{1}{\gamma_1}\tilde{\beta}_1\dot{\tilde{\beta}}_1 + \frac{1}{\gamma_2}\tilde{\beta}_2\dot{\tilde{\beta}}_2 + \beta_0\tilde{z}_0\dot{\tilde{z}}_0 + \beta_2\tilde{z}_1\dot{\tilde{z}}_1 \tag{5.66}$$

where $\dot{\tilde{\beta}}_i = -\dot{\hat{\beta}}_i \;\forall\; i = 1..3$. By introducing the terms with error dynamics into (5.66) we obtain

$$\begin{aligned}&\dot{V} = e_1\left(-k_1e_1 + e_2\right) + \\ &e_2\left(-k_2e_2 - a_1e_3 - \tilde{\beta}_1x_2 - \tilde{\beta}_0\hat{z}_0 - \beta_0\tilde{z}_0 + \tilde{\beta}_2|x_2|\alpha(x_2)\hat{z}_1 + \beta_2|x_2|\alpha(x_2)\tilde{z}_1\right) \\ &+e_3\left(-k_3e_3 - \frac{1}{a_1}\frac{\partial\vartheta_1}{\partial x_2}\left[-\tilde{\beta}_1x_2 + \beta_0\tilde{z}_0 + \tilde{\beta}_0\hat{z}_0 - \tilde{\beta}_2|x_2|\alpha(x_2)\hat{z}_1 - \beta_2|x_2|\alpha(x_2)\tilde{z}_1\right]\right) \\ &-\frac{1}{\gamma_0}\tilde{\beta}_0\dot{\tilde{\beta}}_0 - \frac{1}{\gamma_1}\tilde{\beta}_1\dot{\tilde{\beta}}_1 - \frac{1}{\gamma_2}\tilde{\beta}_2\dot{\tilde{\beta}}_2 + \beta_0\tilde{z}_0\left(-|x_2|\alpha(x_2)\tilde{z}_0 - \jmath_0\right) + \beta_2\tilde{z}_1\left(-|x_2|\alpha(x_2)\tilde{z}_1 - \jmath_1\right)\end{aligned} \tag{5.67}$$

By rearranging the above equation

$$\begin{aligned}
&\dot{V} = -k_1 e_1^2 + e_1 e_2 - k_2 e_2^2 - k_3 e_3^2 - a_1 e_2 e_3 - \beta_0 |x_2|\alpha(x_2)\tilde{z}_0^2 - \beta_2 |x_2|\alpha(x_2)\tilde{z}_1^2 \\
&-\tilde{\beta}_0 \left[\frac{1}{\gamma_0}\dot{\hat{\beta}}_0 + \frac{e_3}{a_1}\frac{\partial \vartheta_1}{\partial x_2}\hat{z}_0 \right] - \tilde{\beta}_1 \left[e_2 x_2 + \frac{1}{\gamma_1}\dot{\hat{\beta}}_1 + \frac{e_3}{a_1}\frac{\partial \vartheta_1}{\partial x_2} x_2 \right] \\
&-\tilde{\beta}_2 \left[\frac{1}{\gamma_2}\dot{\hat{\beta}}_2 - e_2 |x_2|\alpha(x_2)\hat{z}_1 - \frac{e_3}{a_1}\frac{\partial \vartheta_1}{\partial x_2}|x_2|\alpha(x_2)\hat{z}_1 \right] - \beta_0 \tilde{z}_0 \left[e_2 + J_0 - \frac{e_3}{a_1}\frac{\partial \vartheta_1}{\partial x_2} \right] \\
&-\beta_2 \tilde{z}_1 \left[J_1 - \frac{e_3}{a_1}\frac{\partial \vartheta_1}{\partial x_2}|x_2|\alpha(x_2) - e_2 |x_2|\alpha(x_2) \right]
\end{aligned} \tag{5.68}$$

Now if we choose

$$\begin{aligned}
J_0 &= -e_2 + \frac{e_3}{a_1}\frac{\partial \vartheta_1}{\partial x_2} \\
J_1 &= \frac{e_3}{a_1}\frac{\partial \vartheta_1}{\partial x_2}|x_2|\alpha(x_2) + e_2 |x_2|\alpha(x_2) \\
\dot{\hat{\beta}}_0 &= -\gamma_0 \left[e_2 \hat{z}_0 + \frac{e_3}{a_1}\frac{\partial \vartheta_1}{\partial x_2}\hat{z}_0 \right] \\
\dot{\hat{\beta}}_1 &= -\gamma_1 \left[e_2 x_2 + \frac{e_3}{a_1}\frac{\partial \vartheta_1}{\partial x_2} x_2 \right] \\
\dot{\hat{\beta}}_2 &= \gamma_2 \left[e_2 |x_2|\alpha(x_2)\hat{z}_1 + \frac{e_3}{a_1}\frac{\partial \vartheta_1}{\partial x_2}|x_2|\alpha(x_2)\hat{z}_1 \right]
\end{aligned} \tag{5.69}$$

Then, the derivative of the Lyapunov function after simplification will become

$$\dot{V} = -k_1 e_1^2 - k_2 e_2^2 - k_3 e_3^2 + e_1 e_2 - a_1 e_2 e_3 - \beta_0 |x_2|\alpha(x_2)\tilde{z}_0^2 - \beta_2 |x_2|\alpha(x_2)\tilde{z}_1^2 \tag{5.70}$$

Using the inequality property $|ab| \leq (a^2 + b^2)/2$ and applying to equation (5.70), we get

$$\dot{V} \leq -\left(k_1 - \frac{1}{2}\right) e_1^2 - \left(k_2 - \frac{1 - a_1}{2}\right) e_2^2 - \left(k_3 + \frac{a_1}{2}\right) e_3^2 - \beta_0 |x_2|\alpha(x_2)\tilde{z}_0^2 - \beta_2 |x_2|\alpha(x_2)\tilde{z}_1^2 \tag{5.71}$$

which will be negative semi-definite if we choose $k_1 > 1/2$, $k_2 > (1 - a_1)/2$ and k_3 a positive constant, then the equation (5.71) will asymptomatically converge to zero by applying LaSalle's theorem with the errors e_1, e_2, e_3 and the control input given in (5.63).

5.4.3.2 EXPERIMENTAL RESULTS

As described in the earlier section that the experiments were performed on the industrial engine test bench presented in chapter 3. The same trajectories, as given in the previous section, are tested to validate the controller with adaptive friction compensation technique.

Unlike previous section we are directly using the information of pressure sensor to design the control law. However, the adaptive Lugre model is not used here for control design. Instead, the Lyapunov function based parameters adaption technique is used which ensures the stability of the controller.

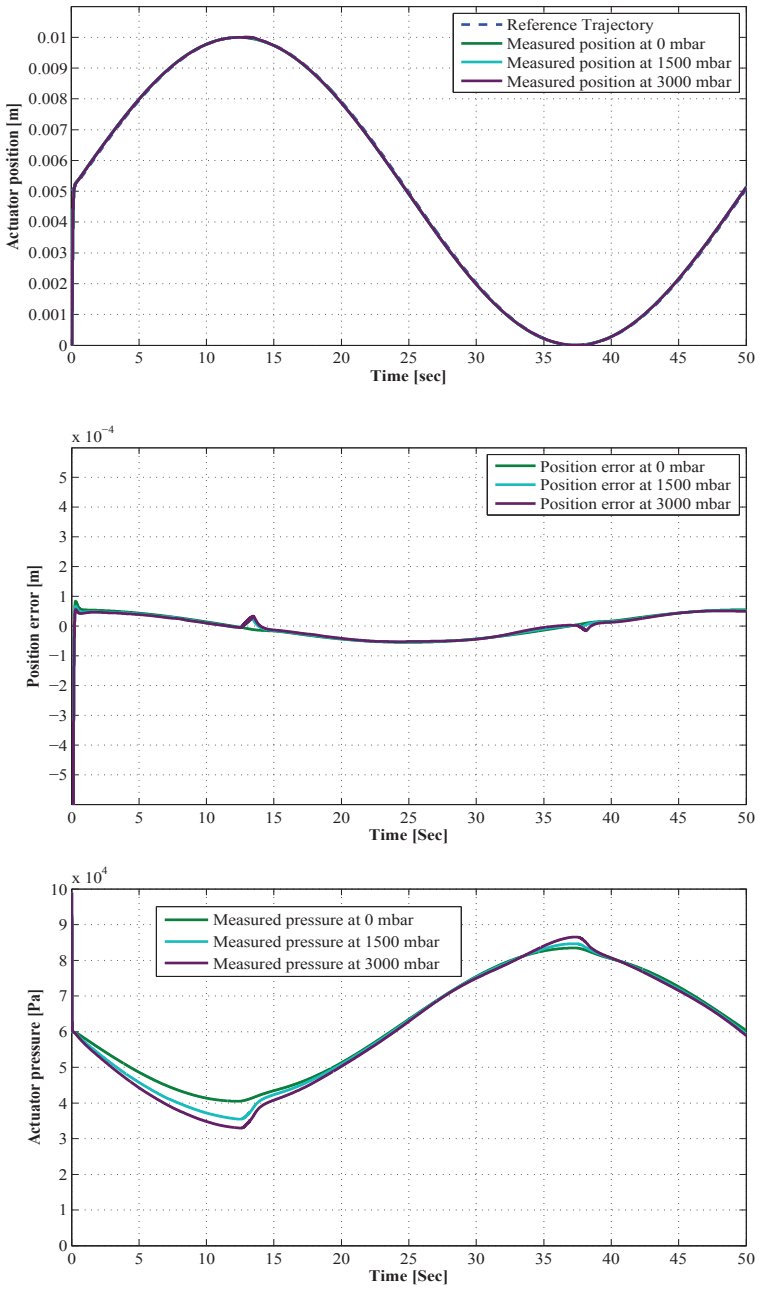

FIGURE 5.23. *Signal 1: (a) Trajectory tracking (b) Tracking error and (c) Observed friction state*

The response of the closed-loop system is shown in Figure 5.23. It can be seen that the actuator follows the reference trajectory with accuracy. The error signal is shown for three turbine inlet pressures and it is in the range of $\pm 0.05mm$ for all turbine inlet pressures. The measured pressure inside the pneumatic actuator's chamber is also shown in this figure. As the turbine inlet pressure increases, the required actuator pressure also increases to compensate the impact of aerodynamic forces.

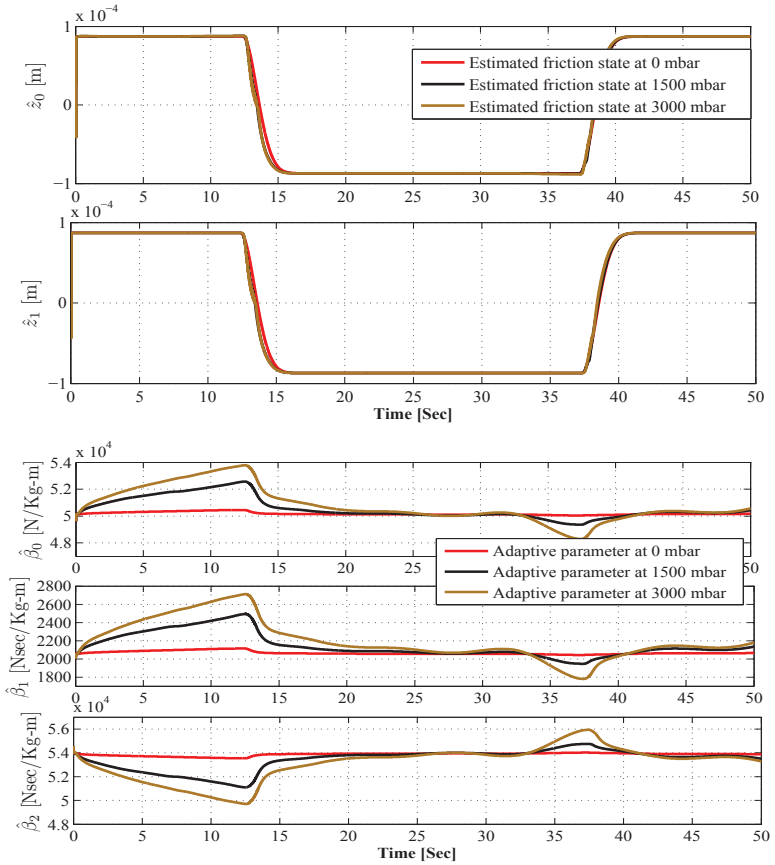

FIGURE 5.24. *Signal 1: (a) Estimated and measured pressures and (b) Pressure observer error*

Figure 5.24 shows the observed friction states $\hat{z}_0$ and $\hat{z}_1$. The duel friction observer is used to show asymptotic stability of the backstepping controller and adaptive friction observer [87]. The aerodynamic force does not exist at $0mbar$ and friction is the only resistive force acting on the actuator. The resistive force generated by the aerodynamic force does not influence duel observer for friction. Therefore, the variation in friction states is insignificant. However, the parameters of the friction model must be changed with external perturbation forces (e.g. aerodynamic forces in our case). In Fig. 5.24 all the three friction parameters are also shown for all turbine inlet pressures. The values of $\hat{\beta}_0$, $\hat{\beta}_1$ and $\hat{\beta}_2$ dynamically adapt under the conditions defined in equation (5.69) to minimize the output feedback error.

The second test is for validating the positioning characteristics of the controller with a step already defined in previous section. Figure 5.25 shows the behavior of the closed-loop system as the reference changes its value. The response is rapid and the error is negligible despite of the variation in the resistive force F_{ft}. It is clear that the actuator requires more pressure to compensate the increasing composite force, which varies with

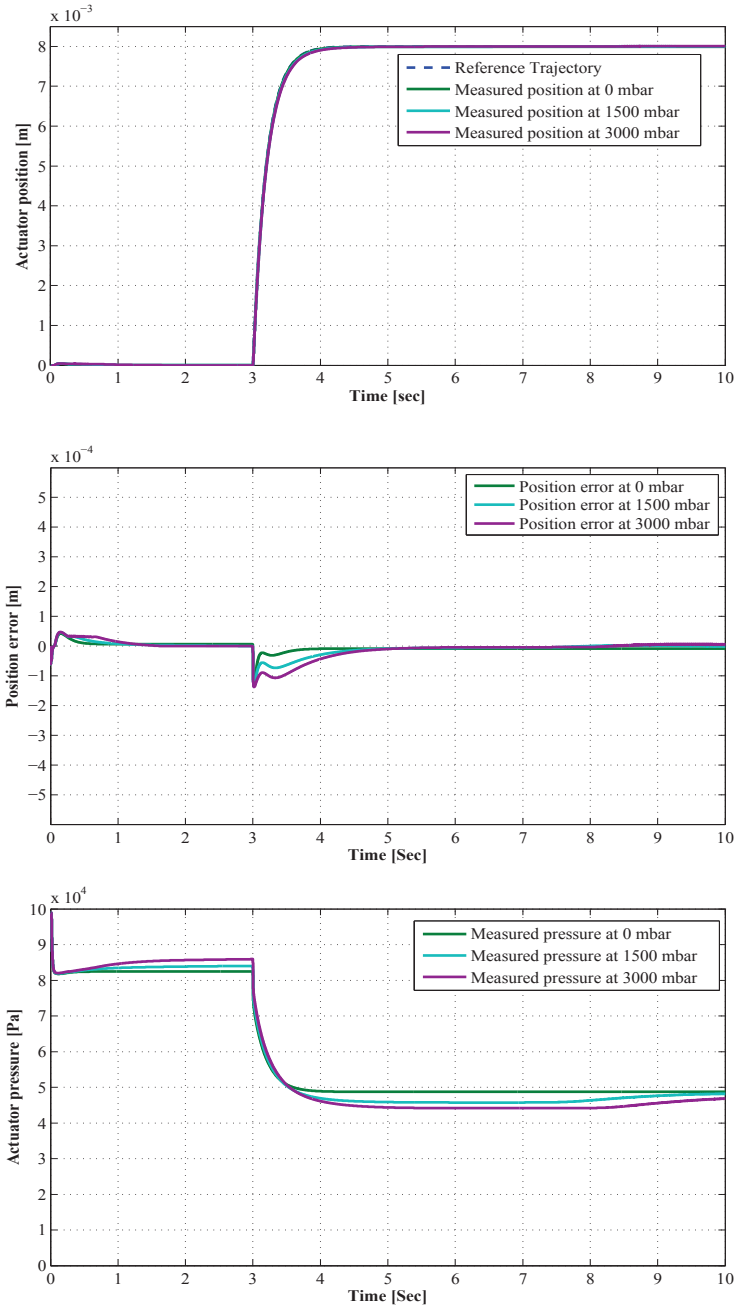

FIGURE 5.25. *Signal 2: (a) Actuator positioning (b) Positioning error and (c) Observed friction state*

changes in the aerodynamic force as the turbine inlet gauge pressure changes from $0mbar$ to $3000mbar$. The error signal between desired trajectory and actual position at three testing points is also shown in Fig. 5.25.

Figure 5.26 shows the observed friction states of the duel observer for all turbine pressures. The adaptive parameters $\hat{\beta}_0$, $\hat{\beta}_1$ and $\hat{\beta}_2$ are also shown in this figure. It can be seen that external forces only influence the adaptive parameters not the friction states. Hance,

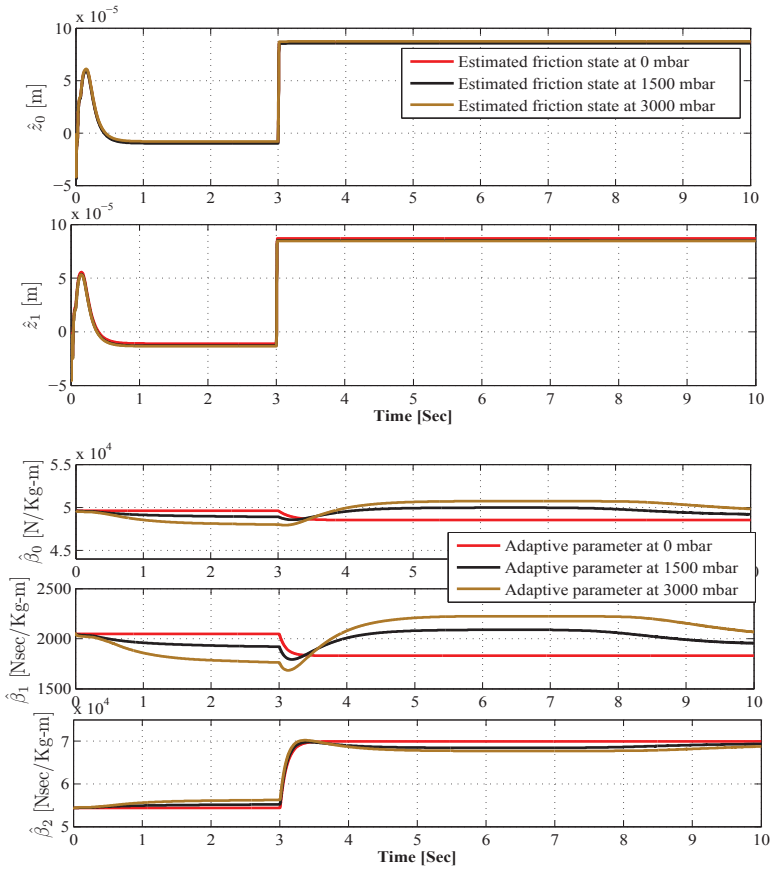

FIGURE 5.26. *Signal 2: (a) Estimated and measured pressures and (b) Observer error*

the proposed controller compensates both the friction and aerodynamic forces.

These results show that the output feedback position control objective is achieved successfully and effectively using the proposed backstepping adaptive controller. The advantage of this technique over the technique described in previous section is that we do not require an exact adaptive model for friction. Instead we can use an adaptive controller which will work for all classes of turbochargers.

5.5 CONCLUSION

This chapter concludes the research work conducted during the thesis. The VGT Actuator model was simplified for control design. Conventional control methods for actuator control were described and tested, and their drawbacks were highlighted. Based on recent advances in control theory, new nonlinear controllers were developed to overcome the drawbacks of conventional methods. In the new Lyapunov-based backstepping controllers, friction and aerodynamic force were taken into account and

observer based compensation methods were integrated during control design. The performance of these controllers was evaluated experimentally.

Conclusion and Perspectives

INTRODUCTION

This thesis considered the modeling of a VGT actuator from the perspectives of system design and control. The main focus was on detailed nonlinear physical modeling of the actuator dynamics including friction and repercussions of aerodynamic force on the VGT vanes. Then, simplifications were proposed in the detailed model, to make it suitable for control design and simulation purposes. The models were validated using experimental results. Most of the work presented in this thesis has already published in peer-reviewed journals and international conferences.

The role of the air path in modern diesel engines, the importance of its precise control and related challenges were presented in Chapter 1. A preliminary model was developed in Chapter 2, in which dynamic relationships that define the physical behavior of the actuator were presented. The nonlinear friction and exhaust aerodynamic forces were included in Chapter 3, and a complete physical model was developed. The influence of different parameters on the performance of the actuator was quantitatively evaluated in Chapter 4, using statistical sensitivity analysis methods. The detailed model was simplified in Chapter 5. Classical and advanced nonlinear control laws were also developed in this chapter, using the simplified model and they were implemented and tested on real time controllers and commercial VGT actuators.

CONCLUSIONS AND PERSPECTIVES

The challenge in VGT actuator control lies in the dynamic interaction of the pneumatic actuator and the EPC. In this work a complete physical model of a VGT actuator system was developed. The nonlinear effects such as the air compressibility, the friction force and the aerodynamic force were taken into account. The friction introduces hysteresis in the actuator characteristics and the width of the hysteresis loop varies with the amplitude

of aerodynamic forces. Three methods were considered for modeling aerodynamic force. Two of these approaches are based on experiments which involve force, position and pressure sensors. The first method requires a force sensor which directly measures the aerodynamic force with respect to turbine pressure and the VGT's vanes opening angle. The second method involves an adaptive friction model (LuGre model) which has been developed by analyzing the hysteresis curves between actuator pressure and position, at different turbine inlet pressures. The problem with above mentioned methods is that they require expensive experiments to characterize the aerodynamic force. Therefore, a generalized one dimensional CFD model for aerodynamic force was developed by using Euler equations.

The detailed model serves as an important tool for studying the behavior of actuator dynamics on the global performance of the air path, and also the effect of varying and pulsating gas flow on the actuator. However it is complex for use in control design. Therefore, two methods were proposed for model simplification. In the first approach, a static relationship between air mass flow, EPC plunger position, and pressure inside the actuator chamber is developed. This technique was found to be impractical because the plunger position is not measured in commercial EPCs. Therefore a second approach was proposed, in which a bi-polynomial function of the applied voltage and the pressure difference is presented to map the air mass flow rate. This function allow us in simplifying the actuator's model by eliminating the dynamics of the EPC. With the latter approach, two friction compensation techniques were tested with a conventional PI control. We also developed sliding mode observers for friction and pressure with the help of backstepping control method. Next, a dual friction observer was developed along with adaptive friction parameters technique to avert the requirement of a precise friction model which was, initially, obtained through an expensive experimental procedure. The estimation and control algorithms have been validated in simulation and experimentally on diesel engine test benches.

FUTURE RESEARCH

VGT is an essential element of the engine air path and its precise control is very crucial for engine performance. Until now the auto industry relies on the conventional control techniques based on static maps and simple PID control techniques. Therefore, it will be interesting to integrate new state of the art controllers in the diesel engine vehicles. The controller obtained for the variable geometry turbocharger is based upon state observers for pressure and friction as well as the sensing system for position. It is important to de-

velop a sensor-less control for the turbocharger as commercially available turbochargers are either sensor-less or they contain only position sensors.

To make it useful for all kind of turbochargers, two solutions are proposed here. One method is to develop adaptive friction controller, which is successfully implemented with measured pressure and position of the actuator. This controller need to be developed for only position sensor. The second approach is to develop a mechanistic one dimensional CFD model which could be adapted for model based friction compensation of all kind of turbochargers.

Bibliography

[1] F. S. Ahmed, S. Laghrouche, and M. El Bagdouri. An experimental comparative study of different second order sliding mode algorithms on a mechatronic actuator. *In Proc. IEEE american control conference ACC, San Francisco*, pages 5286–5291, 2011. [cited at p. 16]

[2] D. G. Ainley and G. C. R. Mathieson. *An examination of the flow and pressure losses in blade rows of axial flow turbines*. Ministry of supply technical memorandum no. 2891, Aeronautical Research Council, London, 1951. [cited at p. 46, 69, 70]

[3] F. Altpeter. Friction modeling, identification and compensation. *Phd Thesis, Ecole Polytechnique Federale de Lausanne*, 2004. [cited at p. 85]

[4] B. W. Andersen. *The analysis and design of pneumatic systems*. Publishers Wiley, ISBN-13: 978-1575241647, 1967. [cited at p. 29]

[5] B. Armstrong-Hélouvry, P. Dupont, and C. Canudas de Wit. A survey of models, analysis tools and compensation methods for the control of machines with friction. *Automatica*, 30(7):1083–1138, 1994. [cited at p. 45, 46, 48, 101]

[6] K.J. Astrom and C. Canudas de Wit. Revisiting the lugre model, stick-slip motion and rate dependence. *IEEE control systems Magazine*, 2008. [cited at p. 49]

[7] M. Belgharbi, S. Sesmat, S. Scavarda, and D. Thomasset. Analytical model of flow stage of an pneumatic servo-distributor for simulation and nonlinear control. *6th Scandinavian international conference on fluid power, Finland*, pages 847–860, 1999. [cited at p. 94]

[8] J.E. Bobrow and B. W. McDonell. Modeling, identification, and control of a pneumatically actuated, force controllable robot. *IEEE transactions on Robotics and Automation*, 14(5):732–742, 1998. [cited at p. 3]

[9] F. P. Bowden. *An Introduction to Tribology*. Publishers R.E. Krieger, ISBN-13: 978-0898744743, 1973. [cited at p. 45, 150]

[10] X. Brun, M. Belgharbi, S. Sesmat, D. Thomasset, and S. Scavarda. Control of an electropneumatic actuator: comparison between some linear and non-linear control laws. *Journal of Systems and Control Engineering*, 213(5):387–406, 1999. [cited at p. 3, 109]

[11] C. Canudas de Wit and P. Lischinsky. Adaptive friction compensation with partially known dynamic friction model. *Journal of adaptive control and signal processing*, 11:65–80, 1997. [cited at p. 60]

[12] C. Canudas de Wit, H. Olsson, J. K. Astrom, and P. Lischinsky. A new model for control of systems with friction. *IEEE Transactions on Automatic Control*, 40(3):419–426, 1995. [cited at p. 3, 49, 51, 101, 105, 109, 161]

[13] J. F. Carneiro and F. G. Almeida. Reduced-order thermodynamic models for servo-pneumatic actuator chambers. *Journal of Systems and Control Engineering*, 220:301–314, 2006. [cited at p. 22, 37]

[14] B. Challen and R. Baranescu. *Diesel Engine Reference Book*. Publishers Butterworth-Heinemann (2nd Edition), ISBN-13: 978-0750621762, 1999. [cited at p. 8, 10]

[15] N. Chen. Response sensitivity of electro- hydraulic actuator for hybrid vehicle engine. *IEEE Vehicle Power and Propulsion Conference (VPPC), China*, 2008. [cited at p. 81]

[16] S.B. Choi and S. K. Lee. A hysteresis model for the field-dependent damping force of a magnetorheological damper. *Journal of Sound and Vibration*, 245(2):375–383, 2001. [cited at p. 51]

[17] A. F. Contreras, I. P Quiroz, and C. C. Wit. Further results on modeling and identification of an electronic throttle body. *10th Mediterranean conference on control and automation, Lisbon Portugal*, 2002. [cited at p. 47, 48, 51]

[18] P.R Dahl. Measurement of solid friction parameters of ball bearings. *Sixth Annual Symposium on Incremental Motion Control Systems and Devices*, 1977. [cited at p. 49]

[19] W. Du and O. Leonard. Numerical simulation of surge in axial compressor. *International journal of rotating machinery*, 12:1–10, 2012. [cited at p. 46]

[20] P. Emanuele, E. Perez, X. Blasco J. V. Salcedo, M. Martinez, and J. M. Lujan. Characterization and control of the air management actuators in a variable geometry turbocharged diesel engine. *World automotive congress, FISITA Barcelona Spain*, 2004. [cited at p. 17]

[21] P. Eyabi and G. Washington. Modelling and sensorless control of an electromagnetic valve actuator. *Mechatronics (Elsevier)*, 16(9):159–175, 2006. [cited at p. 21]

[22] L. Freidovich, A. Robertsson, A. Shiriaev, and R. Johansson. Lugre-model-based friction compensation. *IEEE Transactions on Control Systems Technology*, 18(1):194 – 200, 2010. [cited at p. 109]

[23] N. Gaber, G. Foley, P. Pascual, N. Stiber, E. Sunderland, B. Cope, and Z. Saleem. Guidance on the development, evaluation, and application of environmental models. *Report, Council for Regulatory Environmental Modeling*, 2009. [cited at p. 81]

[24] J. Galindo, H. Climent, C. Guardiola, and J. Domenech. Modeling the vacuum circuit of a pneumatic valve system. *Journal of dynamic systems measurement and control*, 131(3), 2009. [cited at p. 3, 21, 22, 26, 32]

[25] C. Garcia. Comparison of friction models applied to a control valve. *Control Engineering Practice*, 16:1231–1243, 2008. [cited at p. 48]

[26] A. Girin. *Contribuition a la commande non lineaire d'un système électropneumatique pour une utilisation aéronautique*. Phd thesis (french), Universite de Nantes, France, 2007. [cited at p. 94, 96, 109]

[27] A. Girin, F. Plestan, X. Brun, and A. Glumineau. High-order sliding-mode controllers of an electropneumatic actuator: Application to an aeronautic benchmark. *IEEE transactions on control systems technology*, 17(3):633–645, 2009. [cited at p. 94]

[28] T. E. Graedel, D. T. Hawkins, and L. D. Claxton. *Atmospheric Chemical Compounds: Sources, Occurrence and Bioassay*. Publishers Academic Press, ISBN-13: 978-0122944857, 1986. [cited at p. 1]

[29] N. Gulati and E. J. Barth. A globally stable, load independent pressure observer for the servo control of pneumatic actuators. *IEEE Transactions on Mechatronics*, 14(3):295–306, 2009. [cited at p. 110]

[30] L. Guzzella and C. H. Onder. *Introduction to modeling and control of internal combustion engine system*. Publishers Springer, ISBN-13: 978-3540222743, 2004. [cited at p. 7, 8, 10, 11, 37]

[31] T. Hagglund. A friction compensator for pneumatic control valves. *Journal of process control*, 12:897–904, 2002. [cited at p. 101, 103]

[32] J. Heywood. *Internal Combustion Engine Fundamentals*. Publishers McGraw-Hill, ISBN-13: 978-0070286375, 1988. [cited at p. 7, 8, 28, 147]

[33] H. Hiereth and P. Prenninger. *Charging the Internal Combustion Engine*. Publishers Springer-Verlag, ISBN-13: 978-3211330333, 2007. [cited at p. 8]

[34] K. A. Hoffman and S. T. Chiang. *Computational fluid dynamics, volume 1*. Engineering Education System, ISBN-13: 978-0962373107, 2000. [cited at p. 63, 70, 71]

[35] T. Jacobs, D. Assanis, and Z. Filipi. The impact of exhaust gas recirculation on performance and emissions of a heavy duty diesel engines. *Journal Society of Automotive Engineers Inc.*, (SAE Paper 2003-01-1068), 2003. [cited at p. 11]

[36] D. Karnopp. Computer simulation of stick-slip friction in mechanical dynamic systems. *ASME Journal of Dynamic Systems, Measurement and Control*, 107(1):100–103, 1985. [cited at p. 46, 48]

[37] H. K. Khalil. *Nonlinear Systems*. Publishers Prentice Hall, ISBN-13: 978-0132280242, 1995. [cited at p. 105, 113]

[38] I.S. Kima, Y.J. Jeong, I.J. Son, I.J. Kima, J.Y. Kimb, I.K. Kimb, and Prasad K.D.V. Yaragada. Sensitivity analysis for process parameters influencing weld quality in robotic gma welding process. *journal of material processing technology*, 140:676–681, 2003. [cited at p. 81]

[39] R. D. Kopa and H. Kimura. Exhaust gas recirculation as a method of nitrogen oxides control in an internal combustion engine. *APCA 53rd Annual Meeting, Cincinnati, Ohio*, 1960. [cited at p. 11]

[40] A.J. kotwicki and J. Russell. Vacuum egr valve actuator model. *International Fuels & Lubricants Meeting & Exposition*, 107, 1998. [cited at p. 3, 21, 37, 148]

[41] M. Krzyzanowski and A. Cohen. Update of who air quality guidelines. *Air Qual Atmos Health*, 1:7–13, 2008. [cited at p. 1]

[42] S. Laghrouche, A. Mehmood, and M. El Bagdouri. Study of the nonlinear control techniques for single acting vgt pneumatic actuator. *International Journal of Vehicle Design (In press)*, 2012. [cited at p. 110]

[43] S Laghrouche, F. Plestan, and A. Glumineau. Higher order sliding mode control based on integral sliding mode. *Automatica*, 43:531–537, 2007. [cited at p. 3]

[44] S. Laghrouche, M. Smaoui, F.Plestan, and X. Brun. Higher order sliding mode control based on optimal approach of an electropneumatic actuator. *International journal of Control*, 79(2):119–131, 2005. [cited at p. 109]

[45] J. Lai and C. Menq. Accurate position control of a pneumatic actuator. *Transactions of the ASME*, 112, 1990. [cited at p. 48]

[46] O. Leonard and O. Adam. A quasi one dimensional cfd model for multistage turbomachines. *Journal of thermal science*, 16(2):1–15, 2007. [cited at p. 46, 66]

[47] A. Levant. Sliding order and sliding accuracy in sliding mode control. *International Journal of Control*, 58(6), 1993. [cited at p. 111]

[48] P.W. Lim, N.C Cheung, and M.F. Rahman. Proportional control of a solenoid actuator. *20th International Conference on Industrial Electronics, Control and Instrumentation*, 3:2045–2050, 1994. [cited at p. 21, 22]

[49] A. C. Love, G. Agnew, and B. Szczyrba. Adaptive variable geometry turbocharger strategy. *patent number: US 2009/0123272 A1*, 2009. [cited at p. 13, 90, 161]

[50] L. Marton and B. Lantos. Modeling, identification and compensation of stick-slip friction. *IEEE Trans. on Industrial Electronics*, 54(1):511–521, 2007. [cited at p. 47]

[51] G. Mattiazzo, S. Mauro, T. Raparelli, and M. Velardocchia. Control of a six-axis pneumatic robot. *Journal of Robotic systems*, 19(8):363–378, 2002. [cited at p. 109]

[52] E. A. Mayer. Electro-pneumatic control valve for egr/atc actuation. *SAE International*, (technical paper number: 810464), 1981. [cited at p. 3]

[53] A. Mehmood, S. Laghrouche, and M. El Bagdouri. Nonlinear modeling of electro-pneumatic actuator for variable nozzle turbocharger control. *In Proc. 49th IEEE conference on Decision and Control CDC 2010, Georgia*, 2010. [cited at p. 97]

[54] A. Mehmood, S. Laghrouche, and M. El Bagdouri. Control of the electro-pneumatic vgt actuator with friction compensator. *In Proc. 18th IFAC world congress, Milan*, 2011. [cited at p. 122]

[55] A. Mehmood, S. Laghrouche, and M. El Bagdouri. Modeling identification and simulation of pneumatic actuator for vgt system. *Sensors and actuators: A Physical*, 165:367–378, 2011. [cited at p. 93]

[56] A. Mehmood, S. Laghrouche, and M. El Bagdouri. Position tracking of the vgt single acting pneumatic actuator with 2nd order smc and backstepping control techniques. *In Proc. 12th International Workshop on Variable Structure Systems, Mumbai*, 2012. [cited at p. 110]

[57] A. Mehmood, S. Laghrouche, M. El Bagdouri, and F. S. Ahmed. Sensitivity analysis of lugre friction model for pneumatic actuator control. *In Proc. IEEE Vehicle Power and Propulsion Conference, Lille*, 2010. [cited at p. 85]

[58] A. Messina, N.I. Giannoccaro, and A. Gentile. Experimenting and modeling the dynamics of pneumatic actuators controlled by the pulse width modulation (pwm) technique. *Mechatronics*, 15(7):859–881, 2005. [cited at p. 22]

[59] P.E. Moraal, I.V. Kolmanovsky, and M.J. Nieuwstadt. Modeling and identification of a current to vacuum transducer and vnt actuator. *International conference on advanced intelligent mechatronics*, Atlanta, USA, 1999. [cited at p. 3, 21, 31]

[60] K. W. Morton and D. F. Mayers. *Numerical Solution of Partial Differential Equations: An Introduction*. Cambridge University Press, ISBN-13: 978-0521607933, 2005. [cited at p. 71]

[61] P. Moulin and J. Chauvin. Modeling and control of the air system of a turbocharged gasoline engine. *journal of Control engineering practice*, 19, 2009. [cited at p. 3]

[62] M. Muller, E. Hendricks, and S. C. Sorenson. Mean value modelling of turbocharged spark ignition engines. *SAE technical paper*, (980784):125–145, 1998. [cited at p. 10]

[63] M. Namba, H. Nakagawa, and A. Kuba. Lifting surface theory to predict aerodynamic force induced by oscillating blades under interaction of three bladerows. *Journal of sound and vibration*, 326:599–622, 2009. [cited at p. 54]

[64] S. Ning and G. M. Bone. High steady-state accuracy pneumatic servo positioning system with pva/pv control and friction compensation. *IEEE Intl. Conf. Robot. Autom*, pages 2824–2829, 2002. [cited at p. 109]

[65] H. Olsson, K.J. Astrom, C. Canudas de Wit, M. Gafvert, and P. Lischinsky. Friction models and friction compensation. *European Journal of Control*, 4(3):176–195, 1998. [cited at p. 47, 48, 49, 51, 101, 109]

[66] P.H. Oosthuizen and W. Carscallen. *Compressible Fluid Flow*. Publishers McGraw-Hill, ISBN-13: 978-0070481978, 1997. [cited at p. 28, 35, 147]

[67] S. R. Pandian, F. Takemura, Y. Hayakawa, and S. Kawamura. Pressure observer-controller design for pneumatic cylinder actuators. *IEEE Transactions on Mechatronics*, 7(4):490–499, 2002. [cited at p. 109]

[68] S. R. Parker. Sensitivity analysis and models of nonlinear circuits. *IEEE transection on circuit theory*, 16:443–447, 1969. [cited at p. 81]

[69] M. A. Perry, H. P. Wynn, and R. A. Bates. Principle components analysis in sensitivity studies of dynamic systems. *journal of probabilistic engineering mechanics*, 21:454–460, 2006. [cited at p. 81]

[70] F. Plestan, Y. Shtessel, V. Bregeault, and A. Poznyak. Sliding mode control with gain adaptation: Application to an electropneumatic actuator. *Control Engineering Practice, DOI: j.conengprac.2012.04.012*, 2012. [cited at p. 109]

[71] J. Pohl, M. Sethson, P. Kurs, and J. Palmberg. Modeling and simulation of a fast 2/2 switching valve. *Fifth International Conference on Fluid Power Transmission and Control, China*, 2001. [cited at p. 21, 109]

[72] W. W. Pulkrabek. *Engineering Fundamentals of the Internal Combustion Engine*. Publishers Prentice Hall (2 edition), ISBN-13: 978-0131405707, 2003. [cited at p. 9, 10, 147]

[73] Z. Rao and G.M. Bone. Nonlinear modeling and control of servo pneumatic actuators. *IEEE transactions on control systems technology*, 16(3):562–569, 2008. [cited at p. 94, 96, 109]

[74] E. Richer and Y. Hurmuzlu. A high performance pneumatic force actuator system: Part 1 - nonlinear mathematical model. *Journal of dynamic systems, measurement and control*, 122:416–425, 2000. [cited at p. 3, 21, 30, 31]

[75] Y. Rochdi, F. Giri, F. Z. Chaoui, F. Ikhouane, and J. Rodellar. Parameter identification of nonlinear hysteretic systems. *Journal of Nonlinear Dynamics*, 58(1):393–404, 2009. [cited at p. 49]

[76] D. Schindele and H. Aschemann. Adaptive friction compensation based on the lugre model for a pneumatic rodless cylinder. *Industrial Electronics, 2009. IECON '09. 35th Annual Conference of IEEE*, pages 1432 – 1437, 2009. [cited at p. 109]

[77] S. Sesmat. *Modelisation, Simulation et commande d'une servovalve pneumatique*. Phd thesis (french), INSA Lyon, France, 1996. [cited at p. 94]

[78] R. Singh and C. Kunt. A linear time varying model for on-off valve controlled pneumatic actuators. *Transactions of the ASME*, 30, 1990. [cited at p. 22, 48]

[79] M. Smaoui, X. Brun, and D. Thomasset. A study on tracking position control of an electropneumatic system using backstepping design. *Control Engineering Practice*, 14(8):923–933, 2006. [cited at p. 3]

[80] M. Smaoui, X. Brun, and D. Thomasset. High-order sliding mode for an electropneumatic system: A robust differentiator-controller design. *International journal of robust and nonlinear control*, 18:481–501, 2007. [cited at p. 3, 109]

[81] G. Song and Y. Wang. A sliding-mode based smooth adaptive robust controller for friction compensation. *American control conference*, 1995. [cited at p. 48]

[82] A. Soren, S. Anders, and B. Stefan. Friction models for sliding dry, boundary and mixed lubricated contacts. *Tribology international*, 40(4):580–587, 2007. [cited at p. 49]

[83] R. Stribeck. Die wesentlichen eigenschaften der gleit- und rollenlager ï£¡ the key qualities of sliding and roller bearings. *Zeitschrift des Vereines Seutscher Ingenieure*, 46(38,39):1342–48, 1432–37, 1902. [cited at p. 45]

[84] S.C. Subramanian, S. Darbha, and K.R. Rajagopal. Modeling the pneumatic subsystem of a s-cam air brake system. *Journal of dynamic systems measurement and control*, 126:36–46, 2004. [cited at p. 3]

[85] V. Szente and J. Vad. Computational and experimental investigation on solenoid valve dynamics. *IEEE conference on Advanced Intelligent Mechatronics*, 2001. [cited at p. 21]

[86] M. Taghizadeh, A. Ghaffari, and F. Najafi. Modelling and identification of a solenoid valve for pwm control applications. *Comptes Rendus Mecanique, Transactions of the Elsevier masson*, 337:131–140, 2009. [cited at p. 21]

[87] Y. Tan, J. Chang, and H. Tan. Adaptive backstepping control and friction compensation for ac servo with inertia and load uncertainties. *IEEE Transactions on Industrial Electronics*, 50(5):944–952, 2003. [cited at p. 109, 121, 127]

[88] S. Thiery. Modelisation et compensation de frottements dans un moteur lineaire. *Phd thesis, Ecole Polytechnique Federale de Lausanne*, 2005. [cited at p. 52]

[89] M. Tomizuka. Mechatronics: from the 20th to 21st century. *Control engineering practice*, 10:877–886, 2002. [cited at p. 2]

[90] E.E. Topcu, I. Yuksel, and Z. Kamis. Developement of electro-pneumatic fast switching valve and investigation of its characteristics. *Mechatronics*, 16:365–378, 2006. [cited at p. 21]

[91] V. I. Utkin, J. Guldner, and J. Shi. *Sliding Mode Control in Electro-Mechanical Systems*. Taylor and Francis, Philadelphia, USA, 1999. [cited at p. 112]

[92] R.B. van Verseveld and G. M. Bone. Accurate position control of pneumatic actuator using on/off solenoid valves. *IEEE/ASME Transactions on Mechatronics*, 2(3), 1997. [cited at p. 22]

[93] X. Wang, Y. Cheng, and G. Peng. Modeling and self tuning pressure regulator design for pneumatic-pressure load systems. *Journal of dynamic systems, measurement and control*, 15(9):1161–1168, 2007. [cited at p. 3]

[94] Z. Wenjing. Parameter identification of lugre friction model in servo system based on improved particle swarm optimization algorithm. *Proceedings of the 26th chinese control conference*, 2007. [cited at p. 52]

[95] F. White. *Fluid mechanics*. Publishers McGraw-Hill, ISBN-13: 978-0072281927, 1994. [cited at p. 22]

[96] W. F. Xie. Sliding-mode-observer-based adaptive control for servo actuator with friction. *IEEE Transactions on Industrial Electronics*, 54(3):1517–1527, 2007. [cited at p. 101, 121]

[97] N. Ye, S. Scavarda, M. Betemps, and A. Jutard. Models of a pneumatic pwm solenoid valve for engineering applications. *Journal of dynamic systems, measurement and control*, 114:680–688, 1992. [cited at p. 21]

[98] H. C. Yee. *Numerical approximation of boundary conditions with applications to inviscid equations of gas dynamics*. NASA Technical Memorandum 81265, Ames Research Center, Moffett Field, California, 1981. [cited at p. 46, 70, 71]

[99] M. K. Zavarehi and P. D. Lawrence. Nonlinear modeling and validation of solenoid-controlled pilot-operated servovalve. *IEEE transaction on mechatronics*, 4(3):324–334, 1999. [cited at p. 21]

[100] M. Zheng, G. T. Reader, and J. G. Hawley. Diesel engine exhaust gas recirculation - a review on advanced and novel concepts. *Energy Conversion and Management*, 45:883–900, 2004. [cited at p. 11]

[101] R. D. Zucker and O. Biblarz. *Fundamentals of Gas Dynamics*. Publishers Wiley, ISBN-13: 978-0471059677, 1987. [cited at p. 148]

Appendices

Appendix A

Appendix

A.1 Mass Flow Equation

The flow model determines the air mass flow through the valve. Air mass flow rate presented by equation (2.15) depends on upstream and downstream pressures, specific heat ratio, temperature and the throat area. The ideal gas equation can be written in the form [32], [72], [66].

$$P.V = \nu RT \tag{A.1}$$

$$\nu = \frac{m}{\mathbf{M}} \tag{A.2}$$

where ν is the molar mass. Equation (A.1) can be rewritten as

$$P.V = \frac{m}{\mathbf{M}} RT \tag{A.3}$$

By putting $R = R_0/\mathbf{M}$ and $\rho = m/V$ in equation (A.1), we get

$$P = \rho RT \tag{A.4}$$

The air mass flow rate is the amount of mass entering or leaving a reservoir in unit time and it is represented by $\dot{m}$

$$\dot{m} = \rho A v \tag{A.5}$$

$$v = Ma \tag{A.6}$$

$$a = \sqrt{\gamma RT} \tag{A.7}$$

$$R = C_p - C_v \tag{A.8}$$

The relationship between mass flow rate $\dot{m}$ and match number M is given below

$$\dot{m} = \rho AM\sqrt{\gamma RT} \tag{A.9}$$

For isentropic process (nighter the heat is entering nor leaving the system) the energy

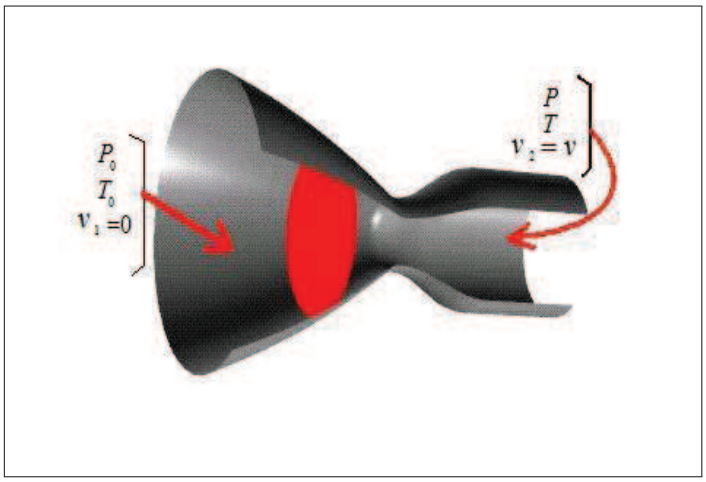

FIGURE A.1. *Stagnation fluid flow through a throat*

equation can be written as [101]

$$H_1 + \frac{{v_1}^2}{2} = H_2 + \frac{{v_2}^2}{2} \tag{A.10}$$

where $H = C_p T$ [40] we get the following relation

$$\frac{T_0}{T} = \left(1 + \frac{v^2}{2.C_p.T}\right) \tag{A.11}$$

The air flow is considered to be stagnation flow i.e. velocity of fluid at start is zero. As flow is also considered as an isentropic flow, relationship between temperature and pressure is given by

$$\frac{T_0}{T} = \left(\frac{P_0}{P}\right)^{(\gamma/\gamma-1)} \tag{A.12}$$

By putting the value of equation (A.5) in equation (A.12)

$$\frac{T_0}{T} = \left(1 + \frac{M^2.\gamma.R}{2.C_p}\right) \tag{A.13}$$

By using equation (A.9) we obtain

$$\frac{T_0}{T} = \left(1 + \frac{\gamma-1}{2}M^2\right) \tag{A.14}$$

$$\frac{P_0}{P} = \left(1 + \frac{\gamma-1}{2}M^2\right)^{(\gamma/\gamma-1)} \tag{A.15}$$

Now, by replacing ρ in equation (A.9) from equation (A.4).

$$\dot{m} = \frac{P}{\sqrt{\gamma RT}} AM\gamma \tag{A.16}$$

Rewriting above equation by using equation of match number M given in (A.13).

$$\frac{\dot{m}\sqrt{\gamma R}}{A} = P_0\left(\frac{T_0}{T}\right)^{(\gamma/\gamma-1)} \frac{1}{\sqrt{T_0}} M\gamma \tag{A.17}$$

Rearranging equation (A.17) we get

$$\frac{\dot{m}\sqrt{\gamma R}}{A} = P_0\left(\frac{T_0}{T}\right)^{(\gamma/\gamma-1)} \frac{1}{\sqrt{T_0}}\sqrt{\frac{T_0}{T}} M\gamma \tag{A.18}$$

Equation (A.18) can be rewritten as

$$\frac{\dot{m}\sqrt{\gamma R T_0}}{AP_0} = \left(\frac{T_0}{T}\right)^{-(\gamma/\gamma-1)+1/2} M\gamma \tag{A.19}$$

Rewriting equation (A.19) by using equation (A.14) we obtain

$$\frac{\dot{m}\sqrt{\gamma R T_0}}{AP_0} = \gamma M\left(1+\frac{\gamma-1}{2}M^2\right)^{-((\gamma+1)/2.(\gamma-1))} \tag{A.20}$$

The above equation can be written in the form of pressure ratio by using equation (A.15)

$$\frac{\dot{m}\sqrt{\gamma R T_0}}{AP_0} = \gamma M\left(\left(\frac{P}{P_0}\right)^{(-\gamma/\gamma-1)}\right)^{-((\gamma+1)/2.(\gamma-1))} = \gamma M\left(\frac{P}{P_0}\right)^{(\gamma+1/2\gamma)} \tag{A.21}$$

Replacing the value of $M = \left[\left\{\left(\frac{P}{P_0}\right)^{(-\gamma/\gamma-1)} - 1\right\}\frac{2}{\gamma-1}\right]^{1/2}$ in the above equation from equation (A.15);

$$\frac{\dot{m}\sqrt{\gamma R T_0}}{AP_0} = \gamma\left(\frac{P}{P_0}\right)^{(\gamma+1/2\gamma)}\left[\left\{\left(\frac{P}{P_0}\right)^{(-\gamma/\gamma-1)} - 1\right\}\frac{2}{\gamma-1}\right]^{1/2} \tag{A.22}$$

Rearranging the above equation

$$\frac{\dot{m}\sqrt{\gamma R T_0}}{AP_0} = \gamma\left(\frac{P}{P_0}\right)^{(\gamma+1/2\gamma)}\left(\frac{P}{P_0}\right)^{(-(\gamma-1)/2\gamma)}\left[\left\{\left(1-\frac{P}{P_0}\right)^{(\gamma-1/\gamma)}\right\}\frac{2}{\gamma-1}\right]^{1/2} \tag{A.23}$$

or

$$\frac{\dot{m}\sqrt{\gamma R T_0}}{AP_0} = \gamma\left(\frac{P}{P_0}\right)^{(1/\gamma)}\left[\left\{\left(1-\frac{P}{P_0}\right)^{(\gamma-1/\gamma)}\right\}\frac{2}{\gamma-1}\right]^{1/2} \tag{A.24}$$

Now, to determine the pressure dynamics and taking the time derivative of equation (A.4) we get the following equation

$$\dot{P} = \frac{\dot{m}}{V} RT \tag{A.25}$$

If we consider a reservoir where some mass of compressible fluid is entering and leaving at the same time from the system then change in pressure can be rewritten in the form

$$\dot{P} = \frac{RT}{V}\left(\dot{m}_{in} - \dot{m}_{out}\right) \tag{A.26}$$

A.1.1 CRITICAL PRESSURE RATIO

The maximum flow of the air occurs when its velocity at the throat is equal to the velocity of sound. In other words **Mach number** (Ratio of fluid velocity and velocity of sound) become equal to zero. Fluid flow can be divided into three types on the basis of Mach number

- If $M < 1$ Flow is called subsonic flow
- If $M = 1$ Flow is called sonic flow. Ratio of pressure at this point is called critical pressure ratio. The flow is also called **choked or critical flow**.
- If $M > 1$ Flow is called supersonic flow

The expression for critical pressure ratio can be calculated from equation (A.19) by putting $M = 1$.

$$\frac{P_0}{P} = \left(\frac{2+\gamma-1}{2}\right)^{(\gamma/\gamma-1)} \tag{A.27}$$

or

$$\frac{P}{P_0} = \left(\frac{2}{\gamma+1}\right)^{(\gamma/\gamma-1)} \tag{A.28}$$

The ideal mass flow rate at critical pressure ratio will be maximum and can be calculated from equation (A.29).

$$\frac{\dot{m}\sqrt{\gamma RT_0}}{AP_0} = \gamma\left(\frac{2}{\gamma+1}\right)^{(\gamma+1)/2(\gamma-1)} \tag{A.29}$$

A.1.2 ASSUMPTION

To derive this relationship some assumptions have been taken which are as under [9]

1. The gas is continuous and one dimensional. This assumption becomes invalid when pressure of gas and its density is low.
2. The gas is perfect and it obeys the perfect gas law and specific heats at constant pressure and volume are constant i.e. the gas is calorically perfect.
   $P = \rho RT$ and $\gamma = C_p/C_v$
   This assumption may not apply there are very large temperature changes in the flow or gas temperature is very high.
3. Gravitational effects on the flow are negligible. This assumption is justifiable for gas flow.
4. The effect of viscosity is negligible. This assumption becomes invalid when density of the fluid is high and near the solid walls.

Appendix B

Appendix

B.1 Actuator Parameters

The identified parameters for the electro-pneumatic pressure converter are provided in Table. B.1. Whereas, the parameters used for the pneumatic actuator are given in Table. B.2.

TABLE B.1: *Parameters values for the EPC*

Parameter	abbreviation	Value
Plunger mass	m_p	$0.01kg$
Membrane constant	k_{mem}	$2000N/m$
Spring constant	k^*_{s1}	$2400N/m$
Damping constant	b_p	$22N-s/m$
Actuator area	A_{act}	$1.7425e-4m^2$
Atmospheric area of solenoid	A_{atm}	$1.7652e-4m^2$
Reservoir area of solenoid	A_{res}	$3.1416e-6m^2$

Polynomial for the Magnetic force F_{mag} is given as a function of applied PWM signal.

$$F_{mag} = \left(9.1355e-8\langle pwm\rangle^4\right) - \left(3.5733e-5\langle pwm\rangle^3\right) + \left(0.0039\langle pwm\rangle^2\right) + \left(0.0022634\langle pwm\rangle\right) + 0.021731 \tag{B.1}$$

Effective flow area between actuator chamber and source reservoir is identified as function of plunger position

$$A_{eff(act-res)} = \begin{cases} 0.360e-3|x_p| & ,0 \geq x_p \geq -2.5e-3 \\ 0.90e-6 & ,x_p < -2.5e-3 \end{cases} \tag{B.2}$$

Effective flow area between actuator chamber and atmosphere is identified in the form of polynomial of plunger position for $x_p \geq 0$.

$$A_{eff(atm-act)} = 0.342x_p^2 + 1.68e-4x_p + 2.299e-8 \tag{B.3}$$

TABLE B.2: *Parameters values for the Diaphragm*

Parameter	abbreviation	Value
Diaphragm mass	m_d	0.63 kg
Spring preloaded force	F_0	49.46 N
Spring(+membrane) constant	k_{sm}	12000 N/m
Diaphragm volume	V_0	$60e-6m^3$
Diaphragm cross sectional area	A_d	$2.9224e-3m^2$
Gas constant for air	R	$286.7J/Kg-K$
Specific heat ratio	γ	1.396
Atmospheric pressure	p_{atm}	$1.01013e5Pa$
Static friction Force	F_s	$3.2N$
Coulomb friction force	F_c	$2.8N$
Bristle Stiffness constant	σ_0	43135
Bristle damping constant	σ_1	429.77
Damping constant	b_d, σ_2	$206N-s/m$
Stribeck velocity	v_s	$0.001m/s$

Polynomial function ($\phi(\delta p)$ and $\psi(\delta p)$) for air mass flow are given below. Where δp is in mBar

$$\phi(\delta p) = -7.94 * 10^{-6} - 4.92 * 10^{-7}\delta p - 5.94 * 10^{-10}\delta p^2 - 2.48 * 10^{-12}\delta p^3 + 5.65 * 10^{-15} \delta p^4 + 1.59 * 10^{-18}\delta p^5$$

$$\psi(\delta p) = 5.19 * 10^{-7} - 5.27 * 10^{-8}\delta p + 3.13 * 10^{-10}\delta p^2 - 1.13 * 10^{-13}\delta p^3 - 4.42 * 10^{-16}\delta p^4 \quad \text{(B.4)}$$

B.2 DV6 MODEL PARAMETERS

The unknown parameters for the turbine map are given in Table. B.3. Whereas, the parameters for the Jensen & Kristensen model for the compressor are provided in Table. B.4.

TABLE B.3: *Identified parameters for the turbine map*

Parameter	Value	Parameter	Value
a	1.1615	b	5.81698
c	1	d	1.59935e-4
e	6.93e-3		

TABLE B.4: *Identified parameters for the compressor map*

Parameter	Value	Parameter	Value
a	1.1615	b	5.81698
c	1	d	1.59935e-4
e	6.93e-3		

B.2.1 ENGINE INTERNAL GEOMETRY

To determine the pulsating flow we may require the exact internal geometry of the engine. With known internal geometry we can determine the displaced volume V_d which is responsible for the pulsations in the exhaust air. To determine engine displaced volume we require following parameters

Engine	
$B = 75mm$	Cylinder bore diameter
$a = 45.5mm$	Crank radius
$l = 136.5mm$	Connecting rod length
$V_c = 4417.8mm^3$	Clearance volume

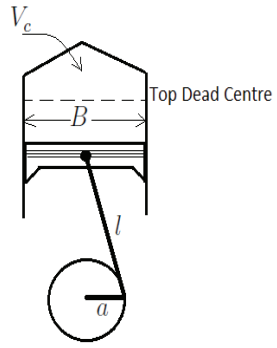

Parameters	Description
Turbocharger	
$J_t = 3.92e-6kg-m^2$	Turbocharger inertia
Exhaust manifold	
$V_x = 0.00092m^3$	Exhaust manifold volume
Intake manifold	
$V_i = 0.00192m^3$	Intake manifold volume
Engine	
$J_e + J_{dr} = 0.126Kg-m^2$	Engine and drive line inertia
$T_{l-max} = 260Nm$	Maximum load torque in Nm (100% charge)

List of Figures

Index

Résumé :

Le Turbocompresseur à Géométrie Variable (TGV) joue un rôle très important dans la détermination des performances de la boucle d'air du moteur. Le comportement dynamique non linéaire des actionneurs pneumatiques du TGV, causé par les forces de frottement et les forces aérodynamiques, rend les méthodes de contrôle classiques inappropriées. Ainsi, dans cette thèse, nous nous sommes intéressés à l'étude de ces différents aspects en proposant de nouveaux modèles et en appliquant de nouvelles commandes robustes à l'actionneur électropneumatique de la turbo. Notre démarche pour traiter le problème se déroule en deux temps. Dans un premier temps, nous avons commencé par établir un nouveau modèle de simulation pour l'actionneur. Ensuite, nous lui avons élaboré un nouveau modèle physique détaillé ; en prenant en compte les caractéristiques non linéaires provenant de la compressibilité de l'air et des forces de frottement. Puis, nous avons proposé deux modèles pour les forces aérodynamiques agissant sur l'actionneur. Enfin, Le modèle global de l'actionneur a été validé expérimentalement et une analyse complémentaire de sensibilité a été menée afin d'identifier les paramètres ayant le plus d'impact sur les performances de l'actionneur. Puis, dans un second temps, nous avons proposé une simplification du modèle élaboré afin de le rendre plus adéquat pour lui appliquer une action de contrôle. La commande robuste, que nous avons mise en place pour ce modèle, se base sur le retour de sortie de l'actionneur. Les algorithmes de contrôle et d'estimation élaborés ont été validés par simulations, puis expérimentalement sur un banc d'essai pour le moteur.

Abstract:

Variable Geometry Turbocharger (VGT) is an important part of the engine air path which is responsible for intake and exhaust air quality and exhaust emissions control. Nonlinear dynamic behavior of the VGT pneumatic actuators caused by friction and varying aerodynamic forces in the VGT render classical control methods ineffective. Therefore, we have addressed this problem, using model based control complemented with robust control methods to overcome operational uncertainties and parametric variations. In the first step, a detailed physical model of an electro-pneumatic actuator has been developed; taking into account the nonlinear characteristics originating from air compressibility and friction. Means to compensate for aerodynamic force have been studied and implemented in the next step. These include model parametric adaptation and one dimensional CFD (Computational Fluid Dynamics) modeling. The complete model has been experimentally validated and a sensitivity analysis has been conducted to identify the parameters which have the greatest impact upon the actuator's behavior. The detailed simulation model has then been simplified to make it suitable for control purposes while keeping its essential behavioral characteristics (i.e. transients and dynamics). Next, robust controllers have been developed around the model for the control objective of accurate actuator positioning in presence of operational uncertainty. An important constraint in commercial actuators is that they provide output feedback only, as they are only equipped with low-cost position sensors. This hurdle has been overcome by introducing observers in the control loop, which estimate other system states from the output feedback. The estimation and control algorithms have been validated in simulation and experimentally on diesel engine test benches.

SPIM

■ École doctorale SPIM - Université de Technologie Belfort-Montbéliard
F - 90010 Belfort Cedex ■ tél. +33 (0)3 84 58 31 39
■ ed-spim@univ-fcomte.fr ■ www.ed-spim.univ-fcomte.fr

utbm
université de technologie Belfort-Montbéliard